INVESTIGATING OPERATION OF ATOM INTERFEROMETERS IN DYNAMIC INERTIAL CONDITIONS

by

DAVID SEDLAK

A thesis submitted to

the University of Birmingham

for the degree of

DOCTOR OF PHILOSOPHY



UNIVERSITY OF BIRMINGHAM

Cold Atoms Research Group

School of Physics and Astronomy

College of Engineering and Physical Sciences

University of Birmingham

September 2023

UNIVERSITY OF
BIRMINGHAM

University of Birmingham Research Archive

e-theses repository

This unpublished thesis/dissertation is copyright of the author and/or third parties. The intellectual property rights of the author or third parties in respect of this work are as defined by The Copyright Designs and Patents Act 1988 or as modified by any successor legislation.

Any use made of information contained in this thesis/dissertation must be in accordance with that legislation and must be properly acknowledged. Further distribution or reproduction in any format is prohibited without the permission of the copyright holder.

To my parents, Alena and Jake (a.k.a. Waldemar)

I have knowledge progress.

Abstract

This thesis investigates the operation of atom interferometers in dynamic inertial conditions. As such, the cross-coupling effect of an accelerating sensor head on the output of an interferometer has been simulated, showing a contrast drop to 59% for $T = 80$ ms and 49% for $T = 40$ ms if the centre-of-mass of the atoms is within the waist radius of the Raman laser beam. Two ways to combat dynamic conditions are presented. Firstly, a model that is able to simulate phase shear fringes using fluorescence coupled with camera imaging is presented, helping to pave way towards extracting contrast and interferometer phase in one experimental shot. Secondly, a preliminary investigation of multi-modal measurements of gravity, magnetic field and magnetic field gradient is presented. Atom shot noise uncertainties for a $T = 50$ ms interferometer with 10^6 atoms are estimated as 3×10^{-8} ms^{-2} per shot for gravity and 4×10^{-6} Gm^{-1} per shot for magnetic field gradient.

Experimentally, gravity gradiometer based on atom interferometry has been built. It is capable of producing over 10^8 atoms in the MOT, with cloud temperatures of 7.3 $\pm$ 0.2 μK for the top chamber and 7.4 $\pm$ 1.7 μK for the bottom chamber following molasses and state preparation. Interferometry is demonstrated, able to obtain short T gravity fringes without vibration isolation platform. Implementation steps required for phase shear readout are investigated, implementing a beam tilting Raman telescope, camera imaging and building an analysis technique using principal component analysis. The system is integrated with a classical accelerometer and tiltmeter (as well as a linear rail) and is able to obtain Rabi oscillations while moving.

Acknowledgements

PhD is a strenuous process, and definitely not a single-person endeavour. As such, I would like to thank Michael Holynski for his vision and optimism as well as technical advice during the PhD. I have enjoyed being involved in some of your wilder ideas, even the unsuccessful FlyYourThesis application.

A special thanks has to go to my other supervisor, and lab partner, Andrew Lamb. Thank you for showing me the ropes of the experiment and your patience. Thanks for your lambastings (the best word I have learnt during the last four years) and billionaire discussions. I have no doubt that you will make your start-up successful.

I would also like to thank Kai Bongs for taking an interest in my PhD application and offering me a position. This has been an experience of a lifetime, which I would not have the opportunity to explore otherwise.

A massive thanks also goes to the entire research group, past and present, with particular mention to the various people who have occupied the same lab as me. Thank you also to the people who helped to build a part of my experiment, even though I didn't have the opportunity to meet a lot of them.

I would like to thank all my family and friends for their support. Special thanks to my parents, Alena and Jake, for supporting me and pushing me to improve myself. I would never have been here if it were not for you. Last but definitely not least, I would like to thank Yuqi for her support (e.g. hard disk recovery), as well as putting up with me, especially in the last few months. You have been a bright spot of my PhD.

Contents

Abbreviations **x**

List of Figures **xii**

List of Tables **xxiii**

1 Introduction **1**

1.1 Historical Overview 3

1.2 Atom Interferometry for Inertial Sensing 5

1.3 Motivation 8

1.4 State of the Art 11

1.5 Thesis Outline 14

2 Theory **15**

2.1 Stimulated Raman Transitions 15

2.1.1 Rabi Oscillations 22

2.1.2 Velocity Selection 23

2.2 Mach-Zehnder Interferometer 27

2.2.1 Quantum Projection Limits 32

2.3 MOT and Molasses 33

2.4 Rubidium-87 35

2.4.1 Interferometry with ^{87}Rb 36
2.5 Phase Contributions 42
2.5.1 Inertial Shifts 42
2.5.2 Atomic Frequency Shifts 50
2.5.3 Summary 54

3 Experimental Setup **56**
3.1 Sensor Head 58
3.1.1 Vacuum Science Chamber 59
3.1.2 Magnetic Field Control 61
3.1.3 Optical Delivery 65
3.2 Laser System 68
3.2.1 Optical System 69
3.2.2 RF System 72
3.2.3 Physical Layout 75
3.3 Control Package 76
3.4 Cold Atoms 80
3.4.1 MOT 81
3.4.2 Optical Molasses (and State Preparation) 82

4 Moving Platform Techniques **89**
4.1 Phase Shear 90
4.1.1 Fluorescence and Camera Imaging 107
4.2 Multi-modal Measurements 114
4.2.1 Magnetic Energy Levels 114
4.2.2 Quadratic Zeeman Effect 118
4.2.3 Analytical κ 121

4.2.4 Numerical κ . . . 123
4.2.5 Quantum Projection Uncertainties . . . 127
4.2.6 Summary . . . 128

5 Cross-coupling **130**
5.1 Introduction . . . 130
5.2 Method . . . 132
5.3 Results . . . 137
5.4 Compensation Technique . . . 140
5.5 Conclusion . . . 144
5.6 Outlook . . . 144

6 Atom Interferometry **147**
6.1 Standard Interferometry . . . 147
6.1.1 Raman Polarisation . . . 147
6.1.2 Detection Scheme . . . 148
6.1.3 Rabi Oscillations . . . 150
6.1.4 Spectrum Scans . . . 153
6.1.5 Gravity Fringes . . . 156
6.2 Phase Shear . . . 158
6.2.1 Raman Telescope . . . 158
6.2.2 Imaging Detection . . . 169
6.2.3 Initial Interferometry . . . 172
6.3 Moving Platform . . . 178

7 Conclusion and Outlook **188**

Appendices **193**

A Additional Theory **194**

B Phase Noise **196**

B.1 Sensitivity Function 196

B.2 Laser Phase Noise 198

B.3 Vibrational Phase Noise 201

B.4 Response Function 203

C ^{87}Rb Transitions **206**

C.1 $\sigma^- - \sigma^-$ Raman Transitions 206

C.2 $\pi - \pi$ Raman Transitions 207

D Barrell Connectors Cleaning Procedure for Vacuum **208**

E Doubler Response and 1560 nm AOM **209**

F ARTIQ Characterisation **213**

F.1 Trigger 213

F.2 Variable Voltage 214

F.3 RF Frequency 216

F.4 Summary 217

G Analytical Solution of Mach-Zehnder **219**

G.1 Atomic State Evolution 219

G.1.1 First Pulse 219

G.1.2 First Free Evolution 219

G.1.3 Second Pulse 220

G.1.4 Second Free Evolution 220

G.1.5 Third Pulse 220

G.2 Probabilities 221
G.2.1 Probability of Excited State After First Pulse 221
G.2.2 Probability of Excited State After First Free Evolution 221
G.2.3 Testing $\pi/2$ and π times 221
G.2.4 Probability of Excited State After Second Pulse 221
G.2.5 Probability of Excited State After Second Free Evolution 222
G.2.6 Probability of Excited State After Third Pulse 223
G.2.7 Recovering Mach-Zehnder Equation 226

Bibliography **228**

Abbreviations

ADU Analog-to-Digital Units

AOM Acousto-Optical Modulator

ARTIQ Advanced Real-Time Infrastructure for Quantum physics

BNC Bayonet Neill–Concelman

BS Beam Splitter

CAD Computer-Aided Design

DAC Digital-to-Analog Converter

DC Direct Current

EDFA Erbium-Doped Fiber Amplifier

EOM Electro-Optical Modulator

FPGA Field-Programmable Gate Array

IP Internet Protocol

MOT Magneto-Optical Trap

MTS Modulation Transfer Spectroscopy

NI-DAQ National Instruments Data Acquisition

PCA Principal Component Analysis

PC Personal Computer

PSD Power Spectral Density

Rb Rubidium

RF Radio-Frequency

RMS Root Mean Square

RWA Rotating-Wave Approximation

SHG Second-Harmonic Generator (Frequency Doubler)

SMA SubMiniature version A

TTL Transistor-Transistor Logic

List of Figures

1.1 Schematic of an optical Mach-Zehnder interferometer with a sample providing a phase shift in one of the arms compared to the other one. . . . 6

2.1 **(a)** Internal energy diagram of a three-level system, depicting the atomic states and the Raman frequencies. **(b)** Momentum conservation diagram when the atoms interact with the Raman beams. 16

2.2 Rabi oscillations against $\Omega_{\text{eff}}\tau$ for a series of δ, assuming $a_a(t_0) = 1$ and $\delta_{\text{AC}} = 0$. 22

2.3 The effect of velocity selection. The dashed orange line shows the Maxwell-Boltzmann distribution of a 7 μK atomic cloud before a pulse (with all atoms in the $|a\rangle$ state). The solid orange and blue lines show the probabilities of the $|a\rangle$ and $|b\rangle$ states after a π pulse. 26

2.4 Mach-Zehnder sequence, with the atoms depicted in blue circles with the states $|a\rangle$ and $|b\rangle$ illustrated inside of these circles. The first $\pi/2$ pulse creates a superposition of states $|a\rangle$ and $|b\rangle$. After time T, the π pulse inverts the states, which are allowed to propagate for another T time. When these two states recombine, the final $\pi/2$ pulse creates interference between the states. 27

2.5 Laser phases under the influence of gravity, neglecting the slightly different phases of the two atomic wavepackets. 30
2.6 Chirp rate scans showing α_0 that exactly cancels the Doppler shift by finding the point at which scans at different T times are minimum at the same point. 31
2.7 Level structure of the D_2 transition of ^{87}Rb, highlighting the transitions that are used to cool the atoms (and keep them out of the dark state) as well as the ones used for stimulated Raman transitions. 36
2.8 $\sigma^+ - \sigma^+$ transitions between $|5^2S_{1/2}; F = 1\rangle$ and $|5^2S_{1/2}; F = 2\rangle$ via $|5^2P_{3/2}; F' = 1\rangle$ and $|5^2P_{3/2}; F' = 2\rangle$. 38
2.9 A plot of the intensity ratio of the Raman laser beams required to cancel out the AC Stark shift for a range of Δ_1. 41
2.10 Vertical vibrations as measured with a Nanometrics Titan accelerometer placed on a stationary and moving linear rail. The linear rail motion is along the horizontal direction, i.e. perpendicular to the vertical vibrations. 44
2.11 Phase shift due to Coriolis as a function of the orientation of the sensor. 47
2.12 Sensitivity function, $g_s(t)$, as a function of time, showing a symmetric behaviour around the middle pulse. Therefore, for constant systematics that scale with the sensitivity function, the phase shift during the interferometer is cancelled. 53

3.1 Gravity gradiometer at the University of Birmingham that was built and utilised as part of this work. 57
3.2 CAD diagram of the top gravimeter. 58
3.3 Illustration of both of the vacuum chambers of the gradiometer. 60

3.4 Magnetic shielding factors for the **(a)** top and **(b)** bottom outer magnetic shields. 63
3.5 **(a)** The full optical delivery for the top chamber. **(b)** Schematic diagram of the top chamber telescope, with all the relevant components annotated. 67
3.6 Schematic diagram of the optical part of the laser system. 70
3.7 Schematic diagram of the RF part of the laser system. 73
3.8 ARTIQ control package used in our setup, with the parts used in our experimental sequence annotated. 77
3.9 Fitted loading curve with dispenser current of 4 A, indicative of the upper performance limits of both of the chambers. 83
3.10 Molasses and state preparation sequence for our setup. This sequence allows us us to further cool the atoms following the MOT and then prepare them in the clean $|F = 1\rangle$ state. For clarity, the repump power has been increased by 1% while the MOT coils have been reduced by 1%. 84
3.11 **(a)** Temperature after molasses without state preparation as opposed to **(b)** temperature after molasses with state preparation; showing the increase in temperature and reduction in amplitude. 86
3.12 Temperature stability measurement after molasses without state preparation. 88

4.1 Phase shear beam pointing setup. The left diagram shows the standard interferometer setup with no beam tilting while the right one shows the application of beam tilting. Note that the propagation of the laser beams further is not shown for illustration purposes. 91
4.2 Absolute horizontal spatial frequency as a function of the tilt angle with $t_3 = 152$ ms and $t_d = 178$ ms. 94

4.3 Absolute horizontal spatial frequency due to Coriolis as a function of the orientation of the sensor, given $t_d = 178$ ms. 96

4.4 Absolute horizontal spatial frequency due to residual Coriolis effect as a function of the angle between the true North and x-axis, given $t_d = 178$ ms. 97

4.5 The atomic transition probability of the fringes as a function of both the horizontal displacement of the atoms and the angle of beam pointing applied (including the maximum possible effect of Coriolis, i.e. orientation of 0°). The following parameters are used: $t_3 = 52$ ms, $t_d = 178$ ms, $T = 1$ ms, $g = 9.81$ ms^{-2}, $\alpha = 2\pi\times25.1538$ MHz/s and $C = 1$. The chirp rate chosen cancels the value of gravity exactly, hence with no tilt angle applied, this leads to no atoms in the upper state being present at the end of the Mach-Zehnder sequence. 98

4.6 Absolute vertical spatial frequency due to timing asymmetry with $t_d = 178$ ms. 99

4.7 Vertical spatial frequency due to the gravity gradient and T, given $t_d = 178$ ms. The black line represents the Earth's gravitational gradient at 3×10^{-6} s^{-2}. 101

4.8 **(a)** Atomic cloud with no beam tilting or timing asymmetry and with $\Phi_0 = \pi$. **(b)** The same atomic cloud with the application of $\delta\theta = 500$ μrad and $\delta T = 10$ μs. For both of these, $A_y = A_z = C = 1$, $t_3 = 52$ ms and $t_d = 178$ ms. 103

4.9 Level structure of the D_2 line of ^{87}Rb. 108

4.10 **(a)** Atomic cloud with no beam tilting or timing asymmetry. **(b)** The same atomic cloud with the application of $\delta\theta = 500$ μrad tilt. For both of these, $A_y = A_z = C = 1$, $T = 1$ ms, $t_3 = 52$ ms and $t_d = 178$ ms; with $\Phi_0 = \pi$. 113

4.11 Energies of the ^{87}Rb $|5^2S_{1/2}\rangle$ state as a consequence of the magnetic field. For weak fields, F is a good quantum number while for strong fields, m_J is a good quantum number. 118

4.12 Numerically-calculated energy differences between the $m_{|F=2\rangle}$ and $m_{|F=1\rangle}$ sub-states. These are the remaining energy differences after the subtraction of the hyperfine splitting and the linear Zeeman effect. The black solid lines are the fits of these energy differences that have been used to calculate ξ and κ, which are the coefficients of the B and B^2 dependencies, respectively. 126

5.1 **(a)** Three-level atom diagram, showing the ground states $|a>$ and $|b>$ and the excited state $|e>$ and the two laser frequencies ω_1 and ω_2. These are detuned from $|e>$ by Δ and δ from the state $|b>$. **(b)** Diagram illustrating the acceleration, a_x, acting on the sensor head while the atoms (blue circle) are in free-fall. The atoms will not feel the force producing this acceleration during their free-fall. **(c)** If $a_x = 0$, the atomic cloud (blue circles) does not move horizontally and remains in the centre of the Gaussian intensity profile. In the case of $a_x > 0$, the atomic cloud moves in the intensity profile of the beams, reducing the contrast seen at the output. The size of the pulses is for illustrative purposes to explain the movement in the intensity profile. **(d)** α scans showing the outputs of our simulations for $a_x = 0$, $a_x = 2$ ms^{-2} and $a_x = 4$ ms^{-2} for a number of T times - 10 ms (blue), 20 ms (red) and 40 ms (green). These are plotted with a single atom and no thermal expansion. α_0 represents the value at which g is cancelled exactly and is the first value of the α scan to help with the "apparent" phase shift calculation. The shape of these will be discussed in section 5.3. 133

5.2 A plot showing contrast loss due to a_x for $T = 10$ ms (blue), 20 ms (red), 40 ms (green) and 80 ms (yellow) - using both the analytical (dashed line) and numerical (crosses) simulation approaches. The vertical lines show when the centre of mass of the atomic cloud at the third pulse reaches 16.95 mm, i.e. w_0. 138

5.3 A plot showing "apparent" phase shift due to a_x for $T = 10$ ms (blue), 20 ms (red), 40 ms (green) and 80 ms (yellow) - using both the analytical (dashed line) and numerical (crosses) simulation approaches. The vertical lines show when the centre of mass of the atomic cloud at the third pulse reaches 16.95 mm, i.e. w_0. 140

5.4 Contour plots showing the (a) contrast, and (b) "apparent" phase shift for a typical range of horizontal atomic cloud temperatures with the effect of a_x for $T = 80$ ms. The vertical line shows when the centre of mass of the atomic cloud at the third pulse reaches 16.95 mm, i.e. w_0. . 141

5.5 Comparison of uncompensated and compensated (a) contrast and (b) "apparent" phase shift for $T = 10$ ms (blue), 20 ms (red), 40 ms (green) and 80 ms (yellow). Analytical (dashed line for uncompensated and solid line for compensated) and numerical (crosses for uncompensated and circles for compensated) solutions are shown. 143

5.6 Rabi oscillations 150 ms after molasses for an atomic cloud with 10^3 atoms and horizontal temperature of 2.5 μK for a range of a_x. 146

6.1 Top and bottom Raman beam linear polarisation levels prior to being fed into the telescopes. A stable and high level of linear polarisations is observed for a measurement time of about an hour. 149

6.2 Two-state detection scheme. 150

6.3 Vertical detection start time characterisation. 151

6.4 Rabi oscillations at different heights. The dashed lines are the fits using an exponentially damped sinusoidal function used to obtain the π-times. The π-times are increasing with time, implying that the Raman beams are not perfectly aligned. 152

6.5 Spectrum scans at different heights with a bias coil current of 450 mA and Raman pulse length of 8 μs. The solid lines are the Lorentzian fits of these peaks. 154
6.6 Chirp rate calculation using the $m_F = 0$ state. The calculated chirp rate values differ from the expected result, likely due to other systematic effects apart from the gravitational field. 155
6.7 Magnetic field profile as calculated using the atoms with bias coil currents of 450 mA. While largely uniform in the central region, small variations in the magnetic field seen by the atoms is observed, most probably due to background magnetic fields and practical limitations of designing and building the bias coils. 156
6.8 Measured gravity fringes, with the first pulse being 50 ms after molasses and with $T = 1$ ms. 157
6.9 Upgraded telescope design for the implementation of beam tilting. The x- and $y-$axes will be used throughout this chapter to differentiate between the two axes that can be controlled using the piezo-actuated mirror mount. 160
6.10 Angle as a function of the control voltage for the **(a)** x-axis and **(b)** y-axis of the Polaris K05P2 piezo-actuators, featuring hysteresis loops. 161
6.11 **(a)** Piezo controller response of outputting a voltage once it receives an input voltage. **(b)** Piezo-actuated mount response following the controller signal. 163
6.12 Piezo-actuated mount switching off response. 164
6.13 Performance of Rabis for a number of times after molasses following the Raman telescope upgrade. 166

6.14 **(a)** Chirp rate and **(b)** magnetic field profile for the two chambers following the Raman telescope upgrade. 167
6.15 Raman intensity stability analysis using 100 shots with a pulse length of 5 μs. 168
6.16 Camera background measurements of a mean of 50 images for 20 dB gain. 170
6.17 Preliminary estimate of **(a)** size per pixel and **(b)** the horizontal atomic temperature at different detection times. 171
6.18 Single-state detection scheme. 173
6.19 Gravity fringes using single-state detection for $T = 1$ ms with the first pulse being 40 ms after molasses as obtained with **(a)** photodiode and **(b)** camera, where the camera fringes have been filtered to ignore outliers. 175
6.20 Gravity fringes utilising two-state detection **(a)** without and **(b)** with the isolation platform enabled for $T = 10$ ms and the first pulse being 50 ms after molasses. The reduction of vertical vibrations is the reason for being able to observe these fringes in **(b)** but not in **(a)**. 176
6.21 Phase shear attempts for $T = 1$ ms. **(a)** First pulse 50 ms after molasses and no beam tilt. **(b)** First pulse 50 ms after molasses and maximum beam tilts along both axes. **(c)** First pulse 150 ms after molasses and no beam tilt. **(d)** First pulse 150 ms after molasses and maximum beam tilts along both axes. The solid black lines are the fits to both of the principal components used to obtain the parameters in the legends. . . 177
6.22 Atomic cloud image with first pulse 150 ms after molasses **(a)** without application of beam tilting and **(b)** with the application of beam tilting. 179
6.23 Still images of the sensor head moving on the rail. 180

6.24 **(a)** Rabi oscillations 150 ms after molasses and **(b)** gravity fringes with $T = 1$ ms with the first pulse being 150 ms after molasses. Both of these show the results before and after moving the sensor head. 182

6.25 **(a)** Chirp rate and **(b)** magnetic field profile calculations at different locations along the rail. 183

6.26 **(a)** Maximum and **(b)** minimum tilts as measured by the tiltmeter when the sensor is moving along both of the axes measured. The error bars are the standard deviation of a set of 10 measurements. A clear correlation is seen between the applied acceleration of the rail and the tilt seen by the tiltmeter. 184

6.27 Maximum accelerations measured by the Nanometrics Titan accelerometer compared against the ones set by the rail software. 186

6.28 Rabi oscillations while the rail is stationary and moving. 187

B.1 Sensitivity function, $g_s(t)$, as a function of time, showing the odd symmetry. 198

B.2 Plot of $|H_\phi(\omega)|^2$ for $T = 50$ ms and $\tau = 15$ μs. 200

B.3 Vibration-induced phase noise. The relative phase between the two lasers changes depending on the displacement. 201

B.4 Plot of $|H_a(\omega)|^2$ for $T = 50$ ms and $\tau = 15$ μs. 202

B.5 Triangle-shaped response function of an atom interferometer. 205

C.1 $\sigma^- - \sigma^-$ transitions (and their Clebsch-Gordan coefficients) between $|5^2S_{1/2}; F = 1\rangle$ and $|5^2S_{1/2}; F = 2\rangle$ via $|5^2P_{3/2}; F' = 1\rangle$ and $|5^2P_{3/2}; F' = 2\rangle$.206

C.2 $\pi-\pi$ transitions (and their Clebsch-Gordan coefficients) between $|5^2S_{1/2}; F = 1\rangle$ and $|5^2S_{1/2}; F = 2\rangle$ via $|5^2P_{3/2}; F' = 1\rangle$ and $|5^2P_{3/2}; F' = 2\rangle$. 207

E.1 Frequency doubler testing setup. 210

E.2 Frequency doubler power response as a function of the input power. . . 210
E.3 **(a)** 780 nm AOM setup and **(b)** 1560 nm AOM setup. 211
E.4 **(a)** 780 nm AOM results and **(b)** 1560 nm AOM results. The error bars represent the standard deviation of a set of five measurements. 212

F.1 Characterisation of the ARTIQ triggering response. 214
F.2 **(a)** Variable voltage response and **(b)** variable voltage ramps. 215
F.3 **(a)** RF spectrum of Urukul output of 216 MHz. **(b)** Frequency ramps characterisation, where frequency number refers to the position of the frequency in the ramps (105 frequencies feature in the two ramps). . . . 216

List of Tables

2.1 Phase shift contribution terms due to the different transitions. 23

2.2 Phase shift contributions to the output of an interferometer. 55

4.1 Parameters needed to calculate κ for the $|F = 1, m_F = 0\rangle \rightarrow |F = 2, m_F = 0\rangle$ transition of ^{87}Rb D_2 line. 120

Chapter 1

Introduction

Gravity is one of the four known fundamental forces affecting matter in our Universe. It is the weakest of these forces but usually dominates for large masses over long distances because of its position dependence. However, "small" matter also creates gravitational force. In simple terms, the law of gravitation states that every object in the Universe attracts every other object. For any two bodies, the force between them is proportional to the mass of each and inversely proportional to the square of the distance between them. Mathematically, this can expressed as [1]:

$$\boldsymbol{F} = \frac{Gm_1m_2}{r^2}\hat{\boldsymbol{r}}, \tag{1.1}$$

where G is the gravitational constant, m_1 and m_2 are the masses of the two objects acting on each other and r is the distance between them. If we let $m_1 = M$, where M is the mass of a macroscopic object such as the Earth, and $m_2 = m$ as the mass of an object on Earth, the force seen by this object can be expressed as:

$$\boldsymbol{F} = m\boldsymbol{g}, \tag{1.2}$$

where $\boldsymbol{g}$ is the gravitational acceleration. Therefore, this equation allows us to calculate the force experienced by an object in the Earth's gravitational field.

Gravimetry is a field of study that is interested in the measurement of the local gravitational acceleration, $\boldsymbol{g}$, and its gradient. The field takes advantage of the fact that the Earth's mass distribution is not constant but that there are changes in various places around the Earth. The leading order effect is due to Earth's irregular mass distribution, which is a result of the ellipsoidal shape of the Earth (caused by the rotation around its own axis) and causes the value of $\boldsymbol{g}$ to change from 9.78 ms^{-2} at the equator to 9.83 ms^{-2} at the poles. However, other spatial and temporal changes that affect M locally have an effect on $\boldsymbol{g}$, such as mountain ranges, tides, volcanic activities, large constructions, water variations, buried tunnels, etc. A lot of these are relatively small, especially given the value of $\boldsymbol{g}$ provided by Earth, and hence instruments with high sensitivity need to be used to be able to detect them [2].

The observation of the gravitational variations enables us to study the structure of the Earth and due to the fact that these gravitational effects span many orders of magnitude, they can be used for a wide range of applications; including geodesy [3], monitoring water [4] and tides [5], cartography [6], and navigation map matching [7]. In principle, any physical process that involves gravity can be used to measure $\boldsymbol{g}$ and instruments used for this purpose are called gravimeters. Gravimeters are generally categorised into one of two groups, namely absolute or relative. Absolute gravimeters are able to measure $\boldsymbol{g}$ in units of length and time (ms^{-2}); examples of absolute gravimeters include a pendulum [8] or a free-falling object whose trajectory can be tracked [9]. Relative gravimeters work on counter-balancing the gravitational force, for example, the displacement of a proof mass suspended from a spring can be observed to obtain the variation of $\boldsymbol{g}$ [10]. This means that relative gravimeters can only measure the changes in $\boldsymbol{g}$ while absolute gravimeters can give an accurate value of $\boldsymbol{g}$ [11–13].

1.1 Historical Overview

The earliest theory of gravitation, using the Aristotle principle that the velocity of free falling body is proportional to its weight, was refuted by Galileo Galilei in 1604. He discovered, by means of rolling balls down inclined planes, that in free fall the acceleration is actually constant and independent of the mass. Isaac Newton was later able to explain this phenomenon to be a consequence of the gravitational force exerted by the Earth, publishing his results in Philosophiæ Naturalis Principia Mathematica in 1678.

The first instrument able to measure the acceleration due to gravity was the pendulum, whose oscillation period relates gravitational acceleration to the pendulum's length. While the concept was simple, this method was used until the end of the nineteenth century and this instrument even played a key role in proving that Earth is a prolate ellipsoid and not a sphere. Building on this simple instrument, a number of more advanced instruments were developed. Examples include the reversible pendulum, in which a rigid pendulum is swung from two opposing pivot points, and the torsion balance [11, 14].

One of the milestones in the field was the discovery that for some applications we do not need to know the precise values of $\boldsymbol{g}$ but rather we only need to know changes of $\boldsymbol{g}$. Due to having to deal with fewer parameters, the sensitivity of these instruments is enhanced. This idea was the birth of the field of relative gravimetry. This realisation paved the way for the development of spring-type relative gravimeters. These work by using weighing devices where the force of gravity on the mass is counter-balanced by the restoring force of the spring. Three types of these devices exist: linear devices, where the equilibrium conditions are between two forces (e.g. elastic and gravitational); astatic, in which a condition close to equilibrium is reached by equating the momentum

of the gravitational and elastic forces; and the least common one, where gas functions as the spring element [11].

Another breakthrough in relative gravimetry came from the development of the zero-length spring. In this instrument, the restoring force is proportional to the entire length of the spring and in certain conditions this instrument could have, at least in principle, infinite sensitivity. This gravimeter dominated the scene of relative gravimetry for about 50 years from its first use by LaCoste in 1934. Later on, a new kind of "spring-type" gravimeter, which could, in principle, be drift-free, was introduced following the discovery of superconductivity. This uses a test mass made from, or layered with, a superconducting material that is levitated by a magnetic field, produced by a current in the superconducting coil. The changes in the current needed to levitate the mass are then proportional to $\boldsymbol{g}$ [11].

These developments have resulted in a number of commercial gravimeters that are available for numerous applications. These include the relative spring gravimeters from Scintrex: CG5 and CG6 for outdoor applications [15–17], RG1 for underwater or terrain vehicles [18] and Gravilog for slim holes [19]. Micro-g LaCoste also has a suite of gravimeters, specifically the free-falling corner cube absolute gravimeter FG5-X [20–22], optical falling cube absolute gravimeter A10 [23, 24], zero length spring relative gravimeter gPhoneX [25, 26], and zero length spring gravimeters Sea III [27] for sea applications and TAGS 7 [28] for air applications. The Dynamic Gravity Systems have also created zero length spring relative gravimeters AT1A [29], AT1M [30], AT1U [31] and AT1L [32] for airborne, marine, underwater and land applications, respectively. Other instruments include GF Instruments' spring relative land gravimeter LG-1 Galileo [33], GWR Instruments' superconducting gravimeter iGrav [34–36], CSRI Elektropribor's torsion Chekan Shelf [37, 38], and MEMS gravimeters being developed by research organisations, e.g. University of Glasgow [39].

Later, it became possible to measure $\boldsymbol{g}$ through the motion of free-falling objects and the last half of the twentieth century has seen the development of these instruments. At first, measurements were made using geometrical optics to define the position of the falling object. The last few decades have seen the rise of the use of laser and atom interferometry [11].

However, gravimeters suffer from a major disadvantage - this is due to vertical vibrations affecting the measurements. It might not necessarily be obvious to the reader but vertical vibrations are present everywhere and are quite prominent. This means that if we are measuring gravity, which is essentially "vertical" acceleration, these vibrations will couple with the gravity measurements. As they are indistinguishable due to Einstein's equivalence principle, these cannot be separated. Therefore, these need to be taken into account when designing and using these instruments. How this is done in the case of atom interferometery will be discussed later.

1.2 Atom Interferometry for Inertial Sensing

Wave-particle duality means that matter and light are able to display similar phenomena. This means, for example, that sometimes matter is able to behave as light. In fact, matter-wave interference has been demonstrated for a number of different systems. However, one of the most promising ones, especially for precision matter-wave interferometry, are atoms. This is due to the fact that they have a relatively simple internal structure that can be manipulated with electromagnetic fields [40].

This makes gravimeters utilising atom interferometry promising for precision measurements as they use clouds of cold atoms as free-falling objects. Their lack of moving mechanical parts makes them ideal for field applications because atoms are identical and hence will behave the same way from shot to shot if the external environment and

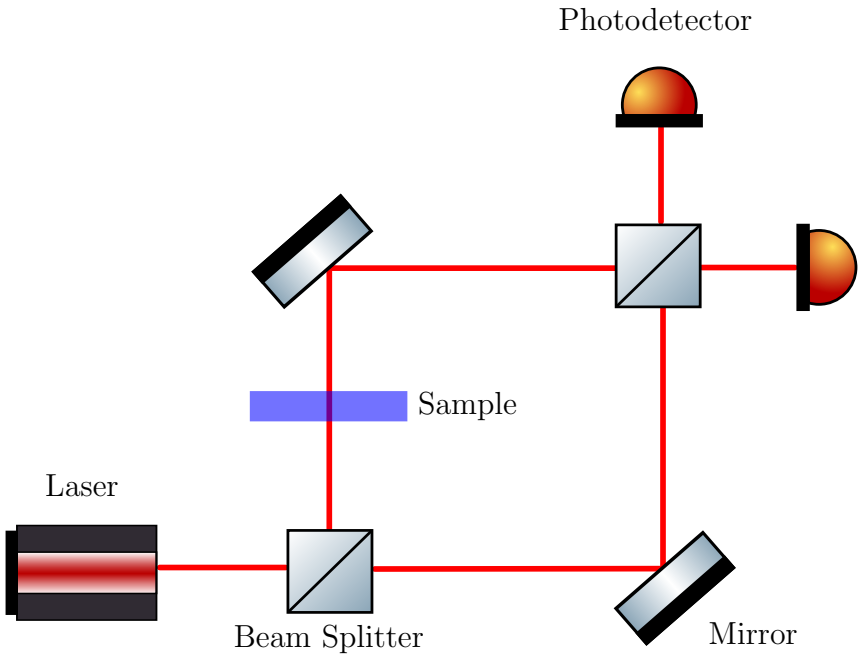


Figure 1.1: Schematic of an optical Mach-Zehnder interferometer with a sample providing a phase shift in one of the arms compared to the other one.

the processes acting on them are identical between the shots. These instruments utilise laser pulses to create interference between atomic states, effectively making the laser beam the ruler with which to measure how fast the atoms move in a certain distance in a certain time. After the first demonstration of this technique by Mark Kasevich and Steven Chu, these instruments became very popular with many research groups around the world developing their own devices [14].

More theory of atom interferometry will be explained in chapter 2 but in simple terms, the setup used is equivalent to an optical Mach-Zehnder sequence, which can be seen in Figure 1.1. In this setup, a laser light is incident onto a beam splitter that splits the light beam into two paths. Both of these paths have a mirror that reflects the lights back onto a final beam splitter, where the two beams interfere. The interference pattern can be detected by photodetectors on the output of a final beam

splitter. If a sample is present in one of the arms of this interferometer, this will result in a phase shift that can be observed by measuring the intensities of the light at the two photodetectors.

In atom interferometry, the roles of light and matter are reversed. The cloud of cold atoms is allowed to free-fall under gravity. As these atoms fall, a series of laser pulses with specific frequencies, tuned to be on resonance with specific atomic transitions, is applied. These pulses are, therefore, able to change the populations of the atoms. In addition, as these transitions occur via the simultaneous absorption and emission of two photons, the pulses also change the momenta of the atoms. Therefore, if we start with atoms in the ground state, applying a pulse to transfer these into the excited state will also impart a momentum kick to the atoms, making the atoms in the excited state move away from the atoms in the ground state. These pulses have an oscillatory behaviour, referred to as Rabi oscillations.

These oscillations can be used to create pulses with certain characteristics. If the atoms are all in the ground state, a pulse that is timed to have a length of a quarter of a full oscillation period creates an equal superposition of momentum and energy states (of the ground and excited states), in analogy with an optical beam splitter. This pulse is referred to as a $\pi/2$ pulse. This is followed by a π pulse, which is timed to stop after half an oscillation, hence inverting the energy and momentum states and acting as a mirror. Finally, a last $\pi/2$ pulse closes the interferometer and creates interference on the two output ports. As this is actually a superposition, the atoms travel along both of these trajectories, with the final interference pattern being dependent on the gravitational potential difference experienced by the atoms during the trajectories. This makes it possible to use these atoms and pulses as gravity sensors, with the simplest sequence of pulses being this $\pi/2 - \pi - \pi/2$ pulse sequence, separated by an interrogation time T between each of the pulses [40]. Due to the fact that this technique uses a quantum

superposition of states, it is also commonly referred to as 'quantum technology' and as a 'quantum sensor'. The measurement of the number of atoms in each of the states at the end of the interferometer sequence allows for the determination of $\boldsymbol{g}$ using [41]:

$$P_{\text{excited state}} \propto C\cos(\boldsymbol{k}\cdot\boldsymbol{g}-\alpha)T^2, \tag{1.3}$$

where C is the contrast of the interferometer, $\boldsymbol{k}$ is the wavevector of the laser pulses and α is the chirp rate, i.e. the time-dependent shift in laser frequency, required to offset the changing Doppler shift as the atoms accelerate under gravity.

1.3 Motivation

While offering the aforementioned advantages, the other big selling point of these instruments is also their relatively high sensitivity (or low uncertainty), expressed as [42, 43]:

$$\sigma_g = \frac{1}{kT^2\sqrt{N}}, \tag{1.4}$$

where N is the number of atoms and $k = |\boldsymbol{k}|$, the value of which is constrained by the lasers. The lasers are chosen in line with the atomic element used in the experiment so that the laser frequency matches the internal structure of the atom. The interrogation time, T, is therefore the more flexible parameter. As is clear, increasing this time improves the sensitivity. However, this usually comes at the expense of the size of the instrument. Therefore, a compromise needs to be taken as to the sensitivity that can be achieved. This is driven by the desired application - as is obvious some applications require a higher sensitivity than others. One of the key focuses of the work at the University of Birmingham is to demonstrate transportable instruments utilising atom

interferometry. This means that not only sensitivity, but also size, weight, power and cost are of paramount concern. The sensitivity possible is extraordinary even for reasonable parameters of T and hence these instruments have a huge potential in a wide range of applications. These range all the way from fundamental physics, such as testing of equivalence principle, dark matter searches; to real-world applications, such as space applications, civil engineering and non-GPS navigation [40].

As has been mentioned, gravimeters have limitations due to vertical vibrations being present. In terms of of atom interferometers, there are several ways to combat the effect of these vibrations. A common solution is is to use a passive or active vibration suppression (for example, by placing it on an vibration isolation platform) or to use a hybrid sensor, in which a classical accelerometer is attached to an atom interferometer to measure these vertical vibrations separately and couple them into the measurements appropriately, as will be discussed later. These are limited by the vibrations that can be compensated for due to the limits of the isolation platforms or classical accelerometers - for example, hybrid sensors do not remove microseism as classical accelerometers do not operate at low enough frequency. The other potential workaround is to use gravity gradiometers. These instruments are able to detect the gravity gradient by placing two gravimeters on top of each other but separated by a distance between them (termed baseline). If they are run simultaneously, the gravity gradient can be measured by taking the difference between the outputs of the interferometers. As the signals are subtracted, the vertical vibrations will also be cancelled via common mode rejection. However, this common mode rejection requires certain conditions to be fulfilled. Firstly, the measurements between the chambers in one experimental shot have to be sufficiently common, which for cold atoms-based instruments is obtained by using a single laser. Secondly, there must be no significant drift between two measurements, which is achieved by using atoms. This is harder to implement using classical gravime-

ters and hence similar advantages are not necessarily possible. Cold atom gravity gradiometers also offer an added bonus as the effect of tilt is suppressed - a sensitivity to tilt three times less than an ideal gravimeter has been shown in [44]. This is because the reference point for tilts of these instruments is different. For a gravimeter, the measured tilt needs to be referenced to the direction of Earth's radius. In the case of a gradiometer, the measured tilt actually has to be referenced to the baseline of the instrument. This has the effect that a larger tilt is needed for a gradiometer than for a gravimeter to see the same uncertainty on the output of the instrument [44].

Therefore, gravity gradiometers offer promise to perform measurements outside laboratories, including in dynamic conditions, because of the systematic effects having suppressed effect on the final output due to common mode rejection. As a result, the main aim of our group at the University of Birmingham is to demonstrate gravity gradiometers in real-world applications. This means that sensitivity has to be compromised to a certain degree (based on application) in order to make them transportable, compact, and dynamic. Field demonstrations with quantum gravity gradiometers have been demonstrated [6], being able to detect an underground tunnel using this type of instrument. While only a demonstration, this achievement shows the potential of these instruments in creating robust instruments that can work outside the laboratories. However, the demonstration mentioned was done in a stop-start measurement routine - the instrument stands still while taking measurements with the instrument only being moved in-between the measurements. Therefore, while gravity and gravity gradient sensors based on cold atoms have demonstrated useful measurements in static conditions, such as moving sensors from point to point or for long-term static monitoring, the majority of practical applications would drastically benefit from enabling the sensors to operate at high sensitivity on moving or dynamic platforms.

Barriers to this shift in operation remain. The first, and one of the dominant

ones, is due to the sinusoidal relation in equation (1.3). Multiple experimental shots have to be performed to obtain both C and the value of $\boldsymbol{g}$ (or even the change in $\boldsymbol{g}$). Obtaining C and a change in $\boldsymbol{g}$ requires a scan of α values. If the exact value of $\boldsymbol{g}$ is to be obtained, α scans at multiple T values are required. Additionally, multiple measurements are also needed to improve the sensitivity of the instrument by averaging out white noise effects. This low data rate of standard interferometer operation does not offer itself to dynamic operation. Secondly, an instrument that is moving and taking measurements during this movement, specifically if it is accelerating, might experience this acceleration during the atoms' free fall. This means that the atoms would not feel the force providing this acceleration and would actually move within the instrument and hence within the intensity profile of the laser beams. This movement has an effect on the final output of an interferometer that needs to be understood. Thirdly, movement in the outside world means that the external environment that the atoms might experience changes. While the atoms' environment is kept as constant and uniform as possible, this is not fully possible. One of the leading effects affecting interferometers is the magnetic field, providing an extra phase shift in equation (1.3), which will be discussed in more detail in Chapter 2. This means that additional measurements may be needed at each measurement location to measure the magnetic field to ensure that $\boldsymbol{g}$, rather than the magnetic field, is causing the phase shift. The theme of this thesis is to investigate, understand and start overcoming these barriers of operating in dynamic inertial conditions.

1.4 State of the Art

A number of quantum sensors are present throughout the world. The commercial ones include the Muquans Absolute Quantum Gravimeter [45, 46], AOSense Compact

Gravimeter [47] and the Lockheed Martin full tensor gradiometer [48, 49]. The experimental quantum sensors include Humboldt-Universitat zu Berlin - GAIN [20, 50, 51], LNE-SYRTE - CAG [52–55], LNE-SYRTE - MiniAtom [56], ONERA - GIRAFE [57], Zhejiang University Hangzhou [58–60] and Institue d'Optique - ICE [61–64]. However, not all of these are currently investigating dynamic applications. We will now present some of the research being performed in this area, concentrating on quantum sensors.

One of the approaches at increasing the data rate of interferometers is high-bandwidth operation, which can be achieved by recapturing atoms, rather than loading them from background, in the cooling part of the experiment [7]. While laboratory instruments have demonstrated high data rates [65, 66] (of up to 330 Hz [67]), these have not yet been demonstrated in the field. This technique has certain limitations as to sensitivity because the T times have to be constrained to be able to perform atom recapture.

In terms of demonstrating and investigating moving atom interferometers, research is being carried out in a number of contexts, such as air, sea as well as on rockets [68]. The most amount of research in dynamic conditions has been done with hybrid gravimeters in combination with classical accelerometers and using fringe reconstruction by accelerometer correlation. Some of these experiments have involved testing different implementations of this technique [56, 69–71] while others have involved more advanced trials. These have included experiments on parabolic flights simulating microgravity to investigate the possibility of using these instruments to measure universality of free-fall [72]. However, some of these parabolic flight experiments, such as with ICE, have involved testing the ability of quantum gravimeters to measure the plane acceleration with good results [62, 73]. One of the most extensive and promising trials were done by ONERA on sea [13] and in air [74]. In both of these instances, they were able to create gravity maps that matched other methods of mapping, showing good correlation between the different approaches.

The technique of phase shear readout to perform single-shot measurements is the theme of this thesis and also holds promise in dynamic applications. This work was pioneered by Stanford in [75], where it was shown that this technique can be used to obtain the interferometer contrast and phase in one experimental shot. The Stanford group have developed this method further, using it (in some cases alongside other techniques such as large momentum transfer) to show that it can be used to enable multi-axis (two rotations, one acceleration) detection [76], and to investigate space-time curvature [77] and the equivalence principle [78, 79]. Since their initial demonstrations, other groups have also demonstrated phase shear readout, including NIST [80] that showed a new data analysis technique, Weizmann Institute of Science that demonstrated a dual T interferometer in combination with phase shear to obtain a thousand-fold increase in dynamic range [81] as well using it for rotation measurements with schemes to suppress measurement drifts [82], Zhejiang University of Technology that have investigated and enhanced the principal component analysis method [83], and Northwestern University who investigated the combination of phase shear readout and large momentum transfer [84].

As can be seen from these examples, effort is currently underway to start increasing the data rate of measurements of quantum sensors as well as testing these in dynamic conditions. However, most of the work in dynamic conditions involves gravimeters, rather than gravity gradiometers; and the technique of phase shear readout has been largely implemented in laboratory conditions rather than being used in the outside world. The aim of this thesis is to start bridging that gap, helping to move phase shear readout to the outside world, with the eventual goal being the use of this technique in a gravity gradiometer due to the benefits offered by these instruments over gravimeters.

1.5 Thesis Outline

This thesis is split the following way. Chapter 2 introduces the general theory behind atom interferometry and how this can be used to measure gravity. The effect of the external environment on the measurements is also analysed. In essence, this chapter introduces the main theoretical background behind atom interferometers that is used throughout the rest of the thesis. Chapter 3 outlines the build and characterisation of the atom interferometer that was built as part of this PhD, including the cold atoms preparation. Chapter 4 concentrates on techniques that can be used on moving platforms. The first part of this chapter explains the technique of phase shear readout that can, in principle, be used to obtain the atom interferometer phase and contrast in one experimental shot. This chapter introduces the theoretical background of this technique and the initial model that has been built to simulate the expected output of these fringes, using fluorescence and camera imaging for detection. The second part of this chapter investigates a way to perform multi-modal measurement of gravity, magnetic field and magnetic field gradient using a standard atom interferometer and estimates the potential atom shot noise limited uncertainties of gravity and magnetic field gradient measurements. Chapter 5 presents the simulations created to understand the expected output of a standard accelerating atom interferometer while the atoms are in free-fall, as well as proposing a simple compensation technique. Chapter 6 describes the atom interferometry obtained using the setup of chapter 3 and describes some of the steps that need to be taken to move from a static interferometer to implementing phase shear readout and moving platform operation, highlighting the lessons learnt when attempting these steps. Finally, Chapter 7 closes off the thesis with the conclusion of this work as well as future outlook. Contributions of the work are presented as appropriate throughout the thesis, otherwise all the work is the author's own.

Chapter 2

Theory

2.1 Stimulated Raman Transitions

Stimulated Raman transitions are a two-photon process that couple two hyperfine states together. The energy diagram for this process can be seen in Figure 2.1(a). Let us consider a three-level atom with two ground states $|a\rangle$ and $|b\rangle$, and an intermediate/excited state $|e\rangle$; with ω_{ba} denoting the angular frequency of the splitting of the ground states and ω_{ea} indicating the splitting between states $|a\rangle$ and $|e\rangle$. In order to drive the stimulated Raman transitions, a pair of counter-propagating lasers with optical frequencies ω_1 and ω_2 are also introduced. These angular frequencies are close to the optical transition with $|e\rangle$ but different by an amount close to ω_{ba}. Therefore, atoms in state $|a\rangle$ can absorb a photon of energy $\hbar\omega_1$ from the first light field and emit a photon of energy $\hbar\omega_2$ (via stimulated emission) in the second light field, at the end of which the atoms are in state $|b\rangle$. If we want to prevent populating state $|e\rangle$, and hence prevent the effect of spontaneous emission, the light fields should also be detuned from ω_{ea} [14, 43].

The resonance condition for the transfer of an atom from $|a\rangle$ to $|b\rangle$ can be obtained

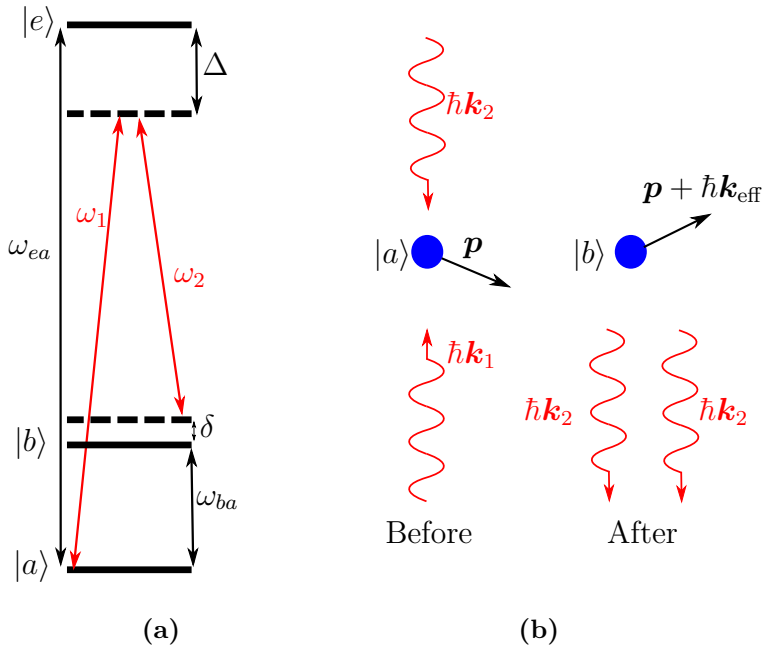


Figure 2.1: **(a)** Internal energy diagram of a three-level system, depicting the atomic states and the Raman frequencies. **(b)** Momentum conservation diagram when the atoms interact with the Raman beams.

using conservation of energy and momenta between initial and final states - the conservation of momentum diagram can be seen in Figure 2.1(b). During an interaction with the light, an atom can absorb or emit a photon, which changes the atom's external state by one photon momentum [14, 43] due to conservation of momentum [41]. If the atom starts in state $|a\rangle$ with momentum $\boldsymbol{p}$, an interaction with a photon from the first laser beam will impart momentum $\hbar\boldsymbol{k}_1$ to the atom, followed by an emission of a photon using the second laser beam with a recoil of $\hbar\boldsymbol{k}_2$. Therefore, the transition from $|a\rangle$ to $|b\rangle$ can be expressed by an effective wavevector, $\boldsymbol{k}_{\text{eff}} = \boldsymbol{k}_1 - \boldsymbol{k}_2$ [14, 41]. Using the conservation of momentum and energy, this process is described by [43]:

$$\hbar\omega_1 + \hbar\omega_a + \frac{|\boldsymbol{p}|^2}{2m} = \hbar\omega_2 + \hbar\omega_b + \frac{(\boldsymbol{p}+\hbar\boldsymbol{k}_{\text{eff}})^2}{2m}. \tag{2.1}$$

Using this relation, it is possible to derive definitions of the various parameters as

well as set the requirements of the experiment. For example, the difference in the frequencies of the lasers is given by [43]:

$$\omega_1 - \omega_2 = \omega_b - \omega_a + \frac{\boldsymbol{p} \cdot \boldsymbol{k}_{\text{eff}}}{m} + \frac{\hbar |\boldsymbol{k}_{\text{eff}}|^2}{2m} = \omega_{ba} + \omega_{\text{D}} + \omega_{\text{rec}}, \tag{2.2}$$

where ω_{D} is the Doppler shift and ω_{rec} is the recoil shift [43]. The two two-photon detuning, δ, is expressed as [14]:

$$\delta = \omega_1 - \omega_2 - \omega_{ba} + \frac{|\boldsymbol{p}|^2}{2m\hbar} - \frac{(\boldsymbol{p} + \hbar \boldsymbol{k}_{\text{eff}})^2}{2m\hbar}, \tag{2.3}$$

while the single-photon detuning, Δ, is defined as [14]:

$$\Delta = \omega_{ea} - \omega_1 - \frac{|\boldsymbol{p}|^2}{2m\hbar} + \frac{(\boldsymbol{p} + \hbar \boldsymbol{k}_1)^2}{2m\hbar}. \tag{2.4}$$

Having dealt with the frequencies of the lasers and the atomic structure, let us now further the discussion by including the actual fields of these Raman beams. The Raman beams tend to have high intensity, meaning that they can be represented as classical plane waves of the form [14, 43, 51]:

$$\boldsymbol{E}(\boldsymbol{r}, t) = \boldsymbol{E}_1 \cos(\boldsymbol{k}_1 \cdot \boldsymbol{r} - \omega_1 t + \phi_{1\text{L}}) + \boldsymbol{E}_2 \cos(\boldsymbol{k}_2 \cdot \boldsymbol{r} - \omega_2 t + \phi_{2\text{L}}), \tag{2.5}$$

where $\boldsymbol{E}_1$ and $\boldsymbol{E}_2$ represent the amplitudes and polarisations of the two laser beams, and $\phi_{1\text{L}}$ and $\phi_{2\text{L}}$ are the phase offsets, which are assumed constant during the interaction with the atom [14, 43, 51]. In general, both of these fields could interact with all three of the energy levels, creating quite a complicated situation. However, the fact that $\omega_{ba} > \Delta$ means that this is not fully the case, and it can be assumed that the first field couples $|a\rangle$ to $|e\rangle$ only and the second field only couples $|b\rangle$ to $|e\rangle$ [14]. As mentioned,

as $\Delta >> \Gamma$ (where Γ is the linewidth of the transition), spontaneous emission effects can also be ignored as we can assume that this transition does not actually populate $|e\rangle$. This results in the following Hamiltonian for the stimulated Raman transitions [43, 51]:

$$\begin{aligned}\hat{H} &= \hat{H}_{\text{momentum}} + \hat{H}_{\text{atom}} + \hat{H}_{\text{interaction}} \\ &= \frac{\hat{\boldsymbol{p}}^2}{2m} + \hbar\omega_a \left|a\right\rangle \left\langle a\right| + \hbar\omega_b \left|b\right\rangle \left\langle b\right| + \hbar\omega_e \left|e\right\rangle \left\langle e\right| - \hat{\boldsymbol{d}} \cdot \boldsymbol{E},\end{aligned} \tag{2.6}$$

where $\hat{\boldsymbol{p}}$ is the momentum operator. $\hat{\boldsymbol{d}}$ is the dipole moment operator and the last term in this equation is due to the interaction between the atom and the light [14, 43].

As has been shown, these stimulated Raman transitions not only change the internal energy structure of the atoms but also change their external momenta. Therefore, the atomic states can be written as a tensor product of these two Hilbert spaces: $|a\rangle \otimes |\boldsymbol{p}\rangle, |b\rangle \otimes |\boldsymbol{p} + \hbar\boldsymbol{k}_{\text{eff}}\rangle$ and $|e\rangle \otimes |\boldsymbol{p}_e\rangle$ [41, 85]. This one-to-one correspondence between the internal energy state and the external momentum allows for the coupling of these basis sets to obtain [14, 85]:

$$\begin{aligned}|a, \boldsymbol{p}_a\rangle &= |a\rangle \otimes |\boldsymbol{p}\rangle, & \hbar\omega_a + \frac{|\boldsymbol{p}|^2}{2m}, \\ |b, \boldsymbol{p}_b\rangle &= |b\rangle \otimes |\boldsymbol{p} + \hbar\boldsymbol{k}_{\text{eff}}\rangle, & \hbar\omega_b + \frac{|\boldsymbol{p} + \hbar\boldsymbol{k}_{\text{eff}}|^2}{2m}, \\ |e, \boldsymbol{p}_{ej}\rangle &= |e\rangle \otimes |\boldsymbol{p}_{ej}\rangle, & \hbar\omega_e + \frac{|\boldsymbol{p} + \hbar\boldsymbol{k}_{\text{j}}|^2}{2m}.\end{aligned} \tag{2.7}$$

Due to the coupling of $|e\rangle$ with $|a\rangle$ and $|b\rangle$ via the two light fields, the following three different momenta are possible: $\boldsymbol{p}_{e1} = \boldsymbol{p} + \hbar\boldsymbol{k}_1$, $\boldsymbol{p}_{e2} = \boldsymbol{p} + \hbar\boldsymbol{k}_2$ and $\boldsymbol{p}_{e3} = \boldsymbol{p} + \hbar(\boldsymbol{k}_{\text{eff}} + \boldsymbol{k}_1)$. These can be eliminated adiabatically if $\Delta >> \Gamma$ to obtain a simple two-level atom. We will only use $\boldsymbol{p}_{e1}$ in our calculations as this is the main momentum of interest and the elimination of the other two states, $\boldsymbol{p}_{e2}$ and $\boldsymbol{p}_{e3}$, follows the same procedure [43, 86].

For completeness sake, it should be mentioned that additional states are possi-

ble by coupling the aforementioned states with the light fields further. An atom that is in the $|e, \boldsymbol{p} + \hbar\boldsymbol{k}_2\rangle$ state can transition to the $|b, \boldsymbol{p}\rangle$ state via an emission of photon with $\boldsymbol{k}_2$, while an emission of a photon with $\boldsymbol{k}_1$ can lead to $|a, \boldsymbol{p} - \hbar\boldsymbol{k}_{\text{eff}}\rangle$ or $|b, \boldsymbol{p} - \hbar\boldsymbol{k}_{\text{eff}}\rangle$. Similarly, an atom in $|e, \boldsymbol{p} + \hbar(\boldsymbol{k}_{\text{eff}} + \boldsymbol{k}_1)\rangle$ can transition to the following states: $|a, \boldsymbol{p} + \hbar\boldsymbol{k}_{\text{eff}}\rangle$, $|a, \boldsymbol{p} + 2\hbar\boldsymbol{k}_{\text{eff}}\rangle$ and $|b, \boldsymbol{p} + 2\hbar\boldsymbol{k}_{\text{eff}}\rangle$. The fortunate thing with these states is that they can be neglected for a number of reasons, including the fact that their detuning from the two-photon resonance condition is high, resulting in low populations [86].

Consequently, the evolution of the states from equation (2.7) can be expressed in the time-dependent wavefunction as [43]:

$$|\Psi(t)\rangle = a_a(t)\,|a, \boldsymbol{p}_a\rangle + a_b(t)\,|b, \boldsymbol{p}_b\rangle + a_{e1}(t)\,|e, \boldsymbol{p}_{e1}\rangle\,, \tag{2.8}$$

which can be used alongside the Hamiltonian in the Schrödinger equation:

$$i\hbar\frac{\mathrm{d}}{\mathrm{d}t}\,|\Psi(t)\rangle = \hat{H}\,|\Psi(t)\rangle \tag{2.9}$$

to derive the following set of equations [14, 85]:

$$i\hbar\dot{a}_a(t) = \left(\hbar\omega_a + \frac{|\boldsymbol{p}|^2}{2m}\right)a_a + V_{ea}^* a_e, \tag{2.10a}$$

$$i\hbar\dot{a}_b(t) = \left(\hbar\omega_b + \frac{|\boldsymbol{p} + \hbar\boldsymbol{k}_{\text{eff}}|^2}{2m}\right)a_b + V_{eb}^* a_e, \tag{2.10b}$$

$$i\hbar\dot{a}_{e1}(t) = \left(\hbar\omega_e + \frac{|\boldsymbol{p} + \hbar\boldsymbol{k}_1|^2}{2m}\right)a_{e1} + V_{ea}a_a + V_{eb}a_b, \tag{2.10c}$$

where the following parameters are defined [14, 85]:

$$V_{ea} = \hbar\Omega_{ea}\left(\frac{e^{i(\omega_1 t+\phi_{1\mathrm{L}})} + e^{-i(\omega_1 t+\phi_{1\mathrm{L}})}}{2}\right), \tag{2.11a}$$

$$V_{eb} = \hbar\Omega_{eb}\left(\frac{e^{i(\omega_2 t+\phi_{2\mathrm{L}})} + e^{-i(\omega_2 t+\phi_{2\mathrm{L}})}}{2}\right), \tag{2.11b}$$

$$\Omega_{ea} = \frac{-\langle e|\, \boldsymbol{d}\cdot\boldsymbol{E}_1\, |a\rangle}{\hbar}, \tag{2.11c}$$

$$\Omega_{eb} = \frac{-\langle e|\, \boldsymbol{d}\cdot\boldsymbol{E}_2\, |b\rangle}{\hbar}. \tag{2.11d}$$

To help with the derivation, the coefficients $a_n(t)$ can be split into fast oscillation terms and slow oscillation terms, $c_k(t)$, allowing for the elimination of the time-dependent factors [14, 43, 85]:

$$a_n(t) = c_k(t)\exp\left(-i\Big(\omega_k + \frac{|\boldsymbol{p}_k|^2}{2m\hbar}\Big)t\right). \tag{2.12}$$

Note that coefficients $c_k(t)$ are also a function of the momentum $\boldsymbol{p}$ but we have ignored this dependency for ease of writing. They are slowly varying if $\Omega_{ba} << \omega_b, \omega_a$. Using this substitution of variables in equation (2.8) yields [14]:

$$\begin{aligned}|\Psi(t)\rangle = {} & c_a(t)\exp(-i(|\boldsymbol{p}|^2/2m\hbar + \omega_a)t)\,|a,\boldsymbol{p}\rangle \\ & + c_b(t)\exp(-i(|\boldsymbol{p}+\hbar\boldsymbol{k}_{\mathrm{eff}}|^2/2m\hbar + \omega_b)t)\,|b,\boldsymbol{p}+\hbar\boldsymbol{k}_{\mathrm{eff}}\rangle \\ & + c_{e1}(t)\exp(-i(|\boldsymbol{p}+\hbar\boldsymbol{k}_1|^2/2m\hbar + \omega_e)t)\,|e,\boldsymbol{p}+\hbar\boldsymbol{k}_1\rangle\,.\end{aligned} \tag{2.13}$$

Steps to solve this this system can be seen in Appendix A, with the final result [87]:

$$c_a(t_0+\tau) = e^{i(-\Omega_{\rm AC}+\delta)\tau/2}\Bigg\{-i\frac{\Omega_{\rm eff}}{\Omega_{\rm R}}\sin\left(\frac{\Omega_{\rm R}\tau}{2}\right)e^{i(\delta t_0+\phi_{\rm eff})}c_b(t_0)+ \left[\cos\left(\frac{\Omega_{\rm R}\tau}{2}\right)+i\frac{(\delta_{\rm AC}-\delta)}{\Omega_{\rm R}}\sin\left(\frac{\Omega_{\rm R}\tau}{2}\right)\right]c_a(t_0)\Bigg\}, \tag{2.14a}$$

$$c_b(t_0+\tau) = e^{i(-\Omega_{\rm AC}-\delta)\tau/2}\Bigg\{-i\frac{\Omega_{\rm eff}}{\Omega_{\rm R}}\sin\left(\frac{\Omega_{\rm R}\tau}{2}\right)e^{-i(\delta t_0+\phi_{\rm eff})}c_a(t_0)+ \left[\cos\left(\frac{\Omega_{\rm R}\tau}{2}\right)-i\frac{(\delta_{\rm AC}-\delta)}{\Omega_{\rm R}}\sin\left(\frac{\Omega_{\rm R}\tau}{2}\right)\right]c_b(t_0)\Bigg\}, \tag{2.14b}$$

where:

$$\begin{aligned} &\Omega_a^{\rm AC} = \frac{|\Omega_{ea}|^2}{4\Delta}, && \Omega_b^{\rm AC} = \frac{|\Omega_{eb}|^2}{4(\Delta-\delta)}, && \Omega_{\rm eff} = \frac{\Omega_{eb}^*\Omega_{ea}}{2\Delta}, \\ &\phi_{\rm eff} = \phi_{\rm 1L}-\phi_{\rm 2L}, && \delta_{\rm AC} = \Omega_b^{\rm AC}-\Omega_a^{\rm AC}, && \Omega_{\rm AC} = \Omega_b^{\rm AC}+\Omega_a^{\rm AC}, \\ &\Omega_{\rm R} = \sqrt{|\Omega_{\rm eff}|^2+(\delta_{\rm AC}-\delta)^2}. \end{aligned} \tag{2.15}$$

Finally, coefficients $a_n(t)$ can be expressed as [87]:

$$a_a(t_0+\tau) = e^{-i(|\boldsymbol{p}|^2/2m\hbar+\omega_a)(t_0+\tau)}e^{i(-\Omega_{\rm AC}+\delta)\tau/2}\Bigg\{-i\frac{\Omega_{\rm eff}}{\Omega_{\rm R}}\sin\left(\frac{\Omega_{\rm R}\tau}{2}\right)e^{i(\delta t_0+\phi_{\rm eff})}c_b(t_0)+ \left[\cos\left(\frac{\Omega_{\rm R}\tau}{2}\right)+i\frac{(\delta_{\rm AC}-\delta)}{\Omega_{\rm R}}\sin\left(\frac{\Omega_{\rm R}\tau}{2}\right)\right]c_a(t_0)\Bigg\}, \tag{2.16a}$$

$$a_b(t_0+\tau) = e^{-i(|\boldsymbol{p}+\hbar\boldsymbol{k}_{\rm eff}|^2/2m\hbar+\omega_b)(t_0+\tau)}e^{i(-\Omega_{\rm AC}-\delta)\tau/2}\Bigg\{-i\frac{\Omega_{\rm eff}}{\Omega_{\rm R}}\sin\left(\frac{\Omega_{\rm R}\tau}{2}\right)e^{-i(\delta t_0+\phi_{\rm eff})}c_a(t_0)+ \left[\cos\left(\frac{\Omega_{\rm R}\tau}{2}\right)-i\frac{(\delta_{\rm AC}-\delta)}{\Omega_{\rm R}}\sin\left(\frac{\Omega_{\rm R}\tau}{2}\right)\right]c_b(t_0)\Bigg\}. \tag{2.16b}$$

2.1.1 Rabi Oscillations

If the atom is in state $|a, \boldsymbol{p}\rangle$ at t_0 then $a_a(t_0) = 1$ and $a_b(t_0) = 0$ and consequently the probability of detecting the atom in each of the states at a time $t = t_0 + \tau$ is given by:

$$P_a(t_0 + \tau) = \cos^2\left(\frac{\Omega_{\mathrm{R}}\tau}{2}\right) + \left|\frac{\delta_{\mathrm{AC}} - \delta}{\Omega_{\mathrm{R}}}\right|^2 \sin^2\left(\frac{\Omega_{\mathrm{R}}\tau}{2}\right), \tag{2.17a}$$

$$P_b(t_0 + \tau) = \left|\frac{\Omega_{\mathrm{eff}}}{\Omega_{\mathrm{R}}}\right|^2 \sin^2\left(\frac{\Omega_{\mathrm{R}}\tau}{2}\right). \tag{2.17b}$$

These are called Rabi oscillations and can be seen depicted in Figure 2.2. The ideal

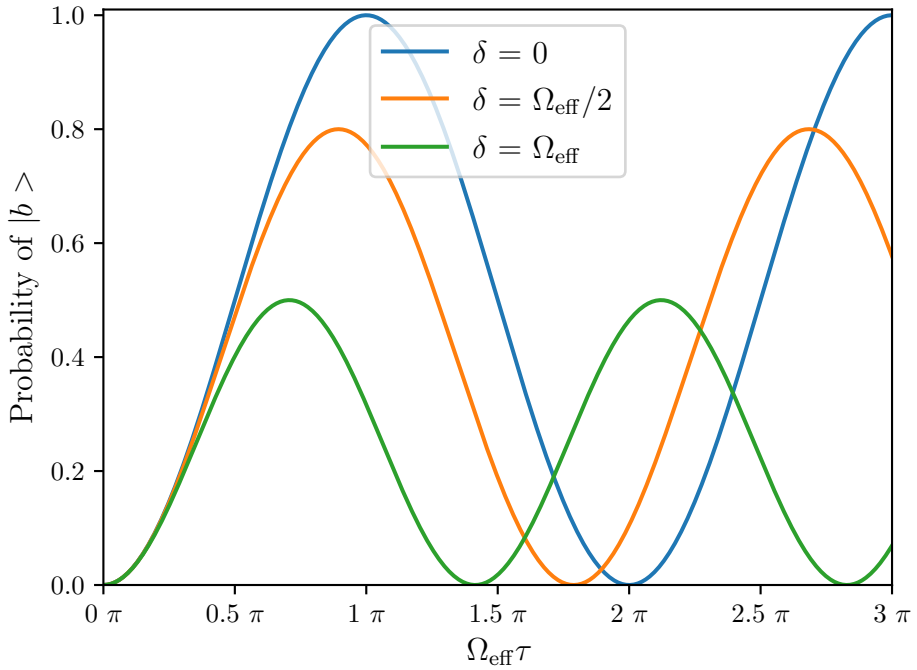


Figure 2.2: Rabi oscillations against $\Omega_{\mathrm{eff}}\tau$ for a series of δ, assuming $a_a(t_0) = 1$ and $\delta_{\mathrm{AC}} = 0$.

case for these oscillations is when $\delta = \delta_{\mathrm{AC}}$ and hence $\Omega_{\mathrm{R}} = \Omega_{\mathrm{eff}}$, resulting in a perfect population transfer. However, this means that the differential AC Stark shift, δ_{AC},

would have to be compensated by δ. To avoid this in actual experiments, δ_{AC} is cancelled by setting an appropriate ratio of the two Raman beams that depends on Δ. This will be discussed further in section 2.4.1.3.

The useful thing about the Rabi oscillations is that they allow us to understand the interferometry pulses. For example, a $\pi/2$ pulse is defined as $\tau_{\frac{\pi}{2}} = \pi/(2\Omega_{\mathrm{eff}})$, creating a superposition of the states $|a\rangle$ and $|b\rangle$ (and their momenta). This can be thought of as an optical beam splitter. On the other hand, a π pulse is defined as $\tau_{\pi} = \pi/\Omega_{\mathrm{eff}}$ and can be used to invert the states, acting in analogy with an optical mirror. These two pulses are the building blocks of gravity sensors using atom interferometry, as will be shown later [14, 43]. Apart from affecting the populations of the states, these pulses also attach phases to the atoms, and gravity can be obtained from these pulses as a consequence of these phases. The phases for the possible transitions can be seen in Table 2.1 with [51]:

$$\theta^0 = \cos\left(\frac{\Omega_{\mathrm{R}}\tau}{2}\right) + \frac{i(\delta - \delta_{\mathrm{AC}})}{\Omega_{\mathrm{R}}} \sin\left(\frac{\Omega_{\mathrm{R}}\tau}{2}\right). \tag{2.18}$$

Table 2.1: Phase shift contribution terms due to the different transitions.

Transition	**Phase Shift**
$\lvert a, \boldsymbol{p}\rangle \rightarrow \lvert a, \boldsymbol{p}\rangle$	$(-\Omega_b^{\mathrm{AC}} - \Omega_a^{\mathrm{AC}} + \delta)\tau/2 - \theta^0$
$\lvert a, \boldsymbol{p}\rangle \rightarrow \lvert b, \boldsymbol{p} + \hbar\boldsymbol{k}_{\mathrm{eff}}\rangle$	$(-\Omega_b^{\mathrm{AC}} - \Omega_a^{\mathrm{AC}} - \delta)\tau/2 - \pi/2 - \delta t_0 - \phi_{\mathrm{eff}}$
$\lvert b, \boldsymbol{p} + \hbar\boldsymbol{k}_{\mathrm{eff}}\rangle \rightarrow \lvert b, \boldsymbol{p} + \hbar\boldsymbol{k}_{\mathrm{eff}}\rangle$	$(-\Omega_b^{\mathrm{AC}} - \Omega_a^{\mathrm{AC}} - \delta)\tau/2 + \theta^0$
$\lvert b, \boldsymbol{p} + \hbar\boldsymbol{k}_{\mathrm{eff}}\rangle \rightarrow \lvert a, \boldsymbol{p}\rangle$	$(-\Omega_b^{\mathrm{AC}} - \Omega_a^{\mathrm{AC}} + \delta)\tau/2 - \pi/2 + \delta t_0 + \phi_{\mathrm{eff}}$

2.1.2 Velocity Selection

Another important effect of stimulated Raman transitions is a consequence of the Doppler shift of the atoms as they fall with respect to these beams, as well as the

temperature of the cloud. To explain this, let us first discuss the possible configurations of Raman beams. The two most obvious configurations are co- and counter-propagating beams that are in parallel with each other. One of the differences between these configurations is the momentum kick applied. The wave-vectors $\boldsymbol{k}_1$ and $\boldsymbol{k}_2$ are very close in magnitude. In the case of co-propagating lasers, the momentum kick on the atom is $\hbar|\boldsymbol{k_1}|-\hbar|\boldsymbol{k_2}|$, which leads to a recoil velocity of around 0.10 μms^{-1} for rubidium-87. For counter-propagating beams, the momentum kick is $\hbar|\boldsymbol{k_1}|+\hbar|\boldsymbol{k_2}|$, which leads to a recoil velocity of about 12 mms^{-1} ($\sim 2\hbar|\boldsymbol{k}_1|$) for rubidium-87. Larger momentum kick leads to larger separation of the atomic clouds during the fall, improving sensitivity [14].

The choice of beam configuration turns out to have a profound impact on these transitions in a cloud of atoms. The atomic cloud has a finite velocity spread due to thermal effects, given by the Maxwell-Boltzmann distribution [14]:

$$f_v(v_z) = \frac{1}{\sigma_{v,z}\sqrt{2\pi}} \exp\left[-\frac{(v_z - \overline{v}_z)^2}{2\sigma_{v,z}^2}\right], \tag{2.19}$$

where $\overline{v_z}$ is the mean velocity of the atoms along z-axis, and $\sigma_{v,z} = \sqrt{k_B T_{\text{temp}}/m}$, where k_B is the Boltzmann constant, T_{temp} is the temperature of the cloud and m is the mass of the atoms. In the co-propagating case, the Doppler shifts experienced by the atoms are almost identical because the wave-vectors of the beams are almost identical and in the same direction - the effective wave-vector is very small. This means that these Raman transitions are almost Doppler-insensitive. This is not the case for the counter-propagating case. In this configuration, the resonance condition cannot be met for all of the atoms at the same time as each of the atoms has different Doppler shift because of their velocities. This means that Raman transition will only select a narrow velocity band of atoms, determined by the length of the Raman pulse, with

longer pulses resonant with narrower velocity class [14, 44].

If the Raman beams are also along the z-axis, the resonance equation (2.3) can be rewritten as [14]:

$$\delta = \omega_{\text{eff}} - \omega_{ba} - \frac{\hbar|\boldsymbol{k}_{\text{eff}}|^2}{2m} - \frac{p_z|\boldsymbol{k}_{\text{eff}}|}{m} = (v_{\text{R}} - v_z)|\boldsymbol{k}_{\text{eff}}|, \tag{2.20}$$

where v_{R} is the atomic velocity at which this resonance condition is satisfied. This resonant velocity is given by [14]:

$$v_{\text{R}} = \frac{\omega_{\text{eff}} - \omega_{ba}}{|\boldsymbol{k}_{\text{eff}}|} - \frac{\hbar|\boldsymbol{k}_{\text{eff}}|}{2m}, \tag{2.21}$$

where the last term in this equation is half of the recoil velocity. The generalised Rabi frequency can be expanded on with the relation of δ as [14]:

$$\Omega_{\text{R}}(v_z) = |\Omega_{\text{eff}}|\sqrt{1 + \frac{(v_z - v_{\text{R}})^2|\boldsymbol{k}_{\text{eff}}|^2}{|\Omega_{\text{eff}}|^2}}. \tag{2.22}$$

As a consequence, atoms with different velocities along the z-axis experience different Rabi frequencies. This means that the pulses cannot be resonant with all the atoms, leading to a reduction of efficiencies of the pulses when transferring the atoms from one state into another [14].

Using the π pulse as a reference, the inclusion of the velocity selective Raman transitions means that the state population after this pulse has to be modified by substituting equation (2.22) into equation (2.17)(b) to obtain [14]:

$$P_b\left(v_z, t_0 + \frac{\pi}{|\Omega_{\text{eff}}|}\right) = \frac{\pi^2}{4}\text{sinc}^2\left(\frac{\pi}{2}\sqrt{1 + \frac{(v_z - v_{\text{R}})^2|\boldsymbol{k}_{\text{eff}}|^2}{|\Omega_{\text{eff}}|^2}}\right). \tag{2.23}$$

To obtain the number of atoms transferred from $|a\rangle$ to $|b\rangle$, a convolution of equations

(2.19) and (2.23) needs to be calculated. The largest transfer is possible if $v_{\mathrm{R}} = \overline{v_z}$, i.e. the Raman frequencies are tuned to be around the mean velocity of the atoms [14, 44].

An example of the effect of the velocity selection can be seen in Figure 2.3, with $T_{\mathrm{temp}} = 7\ \mu$K and $\Omega_{\mathrm{eff}} = 2\pi\times10$ kHz. The effect of this velocity selection is clearly seen in this figure, with only a small fraction of the atoms able to transfer from state $|a\rangle$ to state $|b\rangle$. As is clear, decreasing the temperature as well as increasing the Rabi frequency is able to increase the number of atoms that are transferred. However, a compromise is needed, especially with the latter, as an interferometer should only select a narrow band of atoms to avoid a loss of contrast in the interferometer [14, 44].

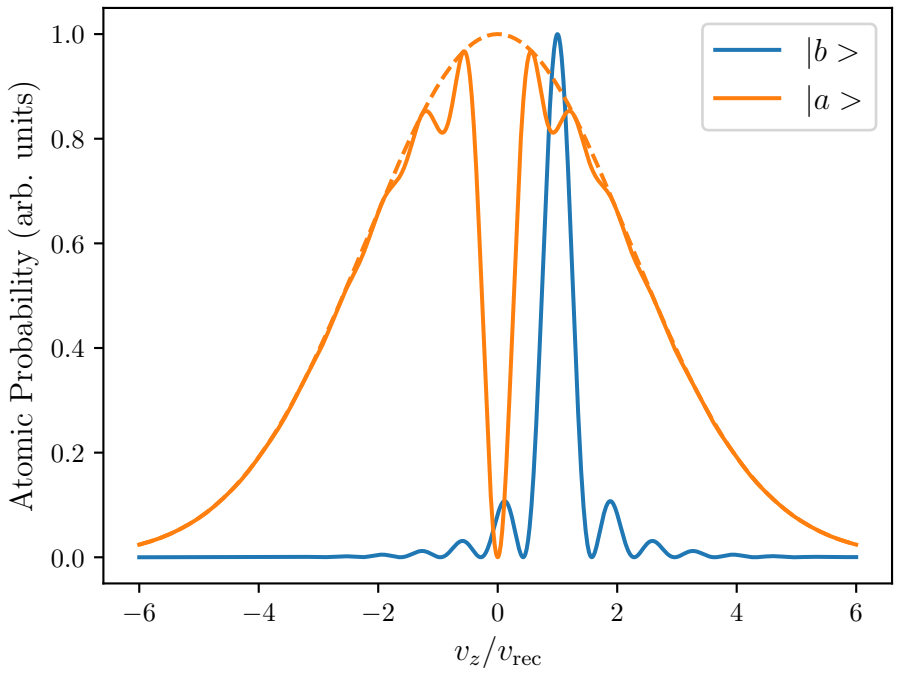


Figure 2.3: The effect of velocity selection. The dashed orange line shows the Maxwell-Boltzmann distribution of a 7 μK atomic cloud before a pulse (with all atoms in the $|a\rangle$ state). The solid orange and blue lines show the probabilities of the $|a\rangle$ and $|b\rangle$ states after a π pulse.

2.2 Mach-Zehnder Interferometer

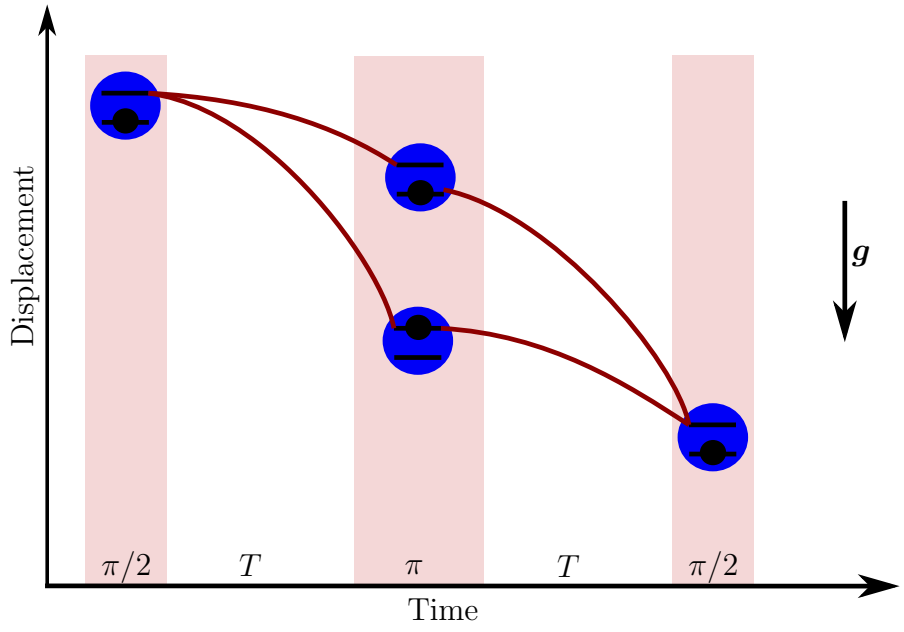


Figure 2.4: Mach-Zehnder sequence, with the atoms depicted in blue circles with the states $|a\rangle$ and $|b\rangle$ illustrated inside of these circles. The first $\pi/2$ pulse creates a superposition of states $|a\rangle$ and $|b\rangle$. After time T, the π pulse inverts the states, which are allowed to propagate for another T time. When these two states recombine, the final $\pi/2$ pulse creates interference between the states.

To utilise the Raman transitions to measure $\boldsymbol{g}$, a specific sequence of π and $\pi/2$ pulses is used. The most common sequence used in current atom interferometers is comprised of $\pi/2 - \pi - \pi/2$ pulses, referred to as Mach-Zehnder interferometer in analogy with its optical equivalent. The schematic diagram of this type of atom interferometer can be seen in Figure 2.4. These pulses coherently divide, deflect and recombine the atomic wavepackets, respectively. The first $\pi/2$ pulse excites an atom initially in state $|a, \boldsymbol{p}\rangle$ into a coherent superposition of states $|a, \boldsymbol{p}\rangle$ and $|b, \boldsymbol{p} + \hbar\boldsymbol{k}_{\text{eff}}\rangle$. The two wavepackets drift apart for time T before the π pulse then inverts the states

by inducing transitions $|a, \boldsymbol{p}\rangle \rightarrow |b, \boldsymbol{p} + \hbar \boldsymbol{k}_{\text{eff}}\rangle$ and $|b, \boldsymbol{p} + \hbar \boldsymbol{k}_{\text{eff}}\rangle \rightarrow |a, \boldsymbol{p}\rangle$. After another interval T, the wavepackets once again overlap. A final $\pi/2$ pulse causes the two wavepackets to interfere. This interference can be detected by measuring the atoms in one state as opposed to the other state, as will be discussed later [41, 88]. In order to deduce the output at the end of the Mach-Zehnder interferometer, we can set up the matrix formalism as [89]:

$$\begin{pmatrix} C_a(t_f) \\ C_b(t_f) \end{pmatrix} = M_{\text{total}} \begin{pmatrix} C_a(t_i) \\ C_b(t_i) \end{pmatrix}, \tag{2.24}$$

where $M_{\text{total}} = M_{\text{third pulse}} M_{\text{second evolution}} M_{\text{second pulse}} M_{\text{first evolution}} M_{\text{first pulse}}$ are the matrices for the three pulses and the two free evolutions [89]. The separate matrices are obtained using the equations (2.16). Assuming there is no AC Stark shift (which can be achieved by setting an appropriate ratio of Raman laser beams as discussed later in section 2.4.1.3), these equations can be simplified and cast into matrix form as [89]:

$$M_p(t_0, t, \Omega_R, \phi) = \begin{pmatrix} e^{-i\omega_a(t-t_0)} \cos(\frac{\Omega_{\text{R}}}{2}[t-t_0]) & -ie^{-i\omega_a(t-t_0)} e^{i(\omega_{\text{eff}} t_0 + \phi)} \sin(\frac{\Omega_{\text{R}}}{2}[t-t_0]) \\ -ie^{-i\omega_b(t-t_0)} e^{-i(\omega_{\text{eff}} t_0 + \phi)} \sin(\frac{\Omega_{\text{R}}}{2}[t-t_0]) & e^{-i\omega_b(t-t_0)} \cos(\frac{\Omega_{\text{R}}}{2}[t-t_0]) \end{pmatrix}, \tag{2.25}$$

where $\omega_{\text{eff}} = \omega_1 - \omega_2$ is the frequency difference of the lasers and ϕ is the effective phase of the lasers. $M_{\text{third pulse}}, M_{\text{second pulse}}$ and $M_{\text{first pulse}}$ can be deduced by appropriate setting of the Rabi frequencies in these equations. $M_{\text{second evolution}}$ and $M_{\text{first evolution}}$ can be obtained by setting setting $\Omega_{\text{R}} = 0$ since there is no light pulse [89].

Assuming that the atoms are initially in the lower state at the beginning of the interferometer, i.e. $C_a(t_i) = 1$ and $C_b(t_i) = 0$, and all pulses are perfectly efficient, it is possible to use matrix multiplication to obtain the well-known result [14]:

$$P_b = \frac{1}{2}[1 - \cos(\phi_3 - 2\phi_2 + \phi_1)]. \tag{2.26}$$

To aid in latter discussion, the phase difference between the two arms of the interferometer, Φ, is defined as [90]:

$$\Phi = \phi_3 - 2\phi_2 + \phi_1. \tag{2.27}$$

As can be seen, the output of the interferometer is proportional to the phase change imparted to the atoms during the three Raman pulses - the free evolutions in a uniform gravity potential do not contribute to the interference seen at the end [12, 51].

The vertical position of an atom at time t during the free-fall is given by:

$$z(t) = z_0 + v_0 t + \frac{1}{2} g t^2, \tag{2.28}$$

where z_0 is its initial position, v_0 is its initial velocity and $g = |\boldsymbol{g}|$ is assumed to have the same direction as the atom (downwards is taken as positive). The phase of the laser beams with angular frequency, ω_{eff}, and phase offset, ϕ_0, is [14]:

$$\phi(t) = k_{\text{eff}} z(t) - \left(\omega_{\text{eff}} + \frac{1}{2}\alpha t\right) t + \phi_0, \tag{2.29}$$

where $k_{\text{eff}} = |\mathbf{k}_{\text{eff}}|$ and α is the applied chirp rate, i.e. rate of change of frequencies of the two lasers that allows them to stay on resonance as the atom experience a Doppler shift during the free-fall. Equation (2.29) can be used in equation (2.27), with the contributions for each of the phases seen picture in Figure 2.5. The final result is given by [14]:

$$\begin{aligned}
&\phi_3 - 2\phi_2 + \phi_1 = k_{\text{eff}}\left(z_0 + 2v_0 T + 2gT^2\right) - 2\omega_{\text{eff}} T - 2\alpha T^2 + \phi_0 \\
&- 2\left[k_{\text{eff}}\left(z_0 + Tv_0 + \frac{1}{2}gT^2\right) - \omega_{\text{eff}} T - \frac{1}{2}\alpha T^2 + \phi_0\right] + k_{\text{eff}}\left(z_0\right) + \phi_0 \\
&= k_{\text{eff}} g T^2 - \alpha T^2.
\end{aligned} \tag{2.30}$$

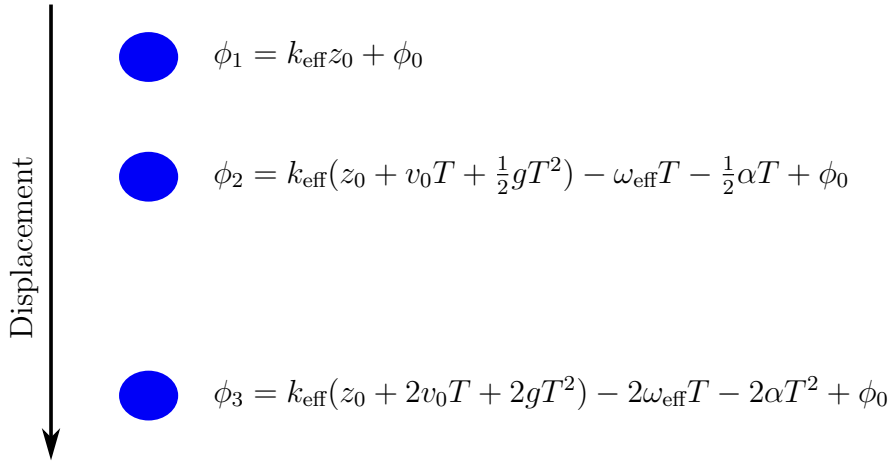


Figure 2.5: Laser phases under the influence of gravity, neglecting the slightly different phases of the two atomic wavepackets.

Therefore, the phases of the three laser pulses acting on the atoms during the sequence allow us to map the value of gravity onto the probability of the atomic states. In general, this dependence becomes [14, 51]:

$$P_{|b,\boldsymbol{p}+\hbar\boldsymbol{k}_{\text{eff}}\rangle} = \frac{1}{2}\{1 - C\cos[(\boldsymbol{k}_{\text{eff}} \cdot \boldsymbol{g} - \alpha)T^2]\}, \tag{2.31}$$

where C is the contrast of the interferometer. The determination of local gravity can be obtained by measuring the population ratio at the output of the interferometer [14, 51].

Gravity can be obtained by measuring the chirp rate, α_0, that exactly cancels the Doppler shift such that $\boldsymbol{k}_{\text{eff}} \cdot \boldsymbol{g} T^2 - \alpha_0 T^2 = 0$ [43]. This is done by performing chirp rate scans at multiple T times and finding when all of these intersect at the minimum value at the same point, as is shown in Figure 2.6. To avoid aliasing, these T times should not be integer multiples of one another. These oscillations are commonly referred to as interference or gravity fringes.

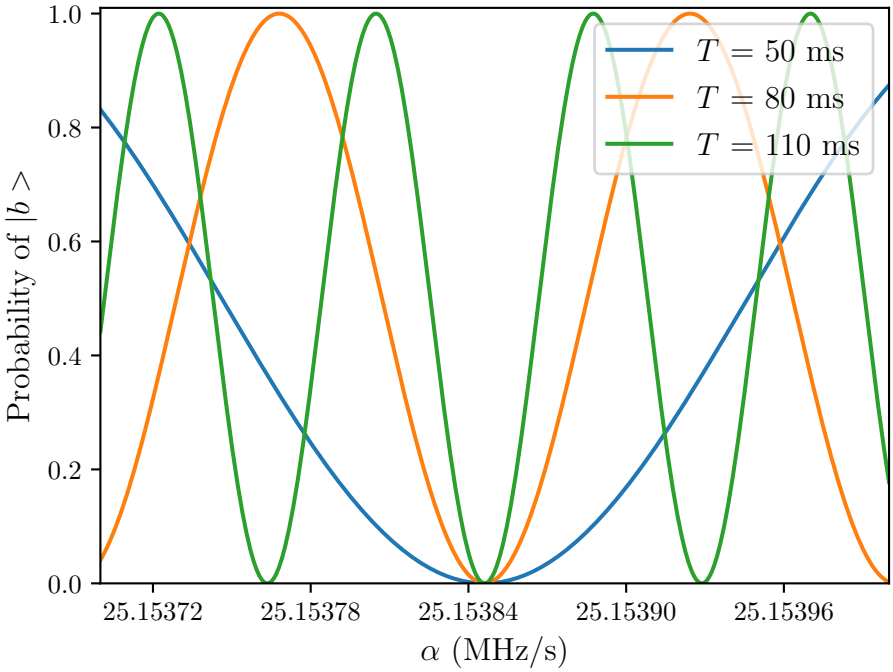


Figure 2.6: Chirp rate scans showing α_0 that exactly cancels the Doppler shift by finding the point at which scans at different T times are minimum at the same point.

A gravity gradiometer is composed of a pair of Mach-Zehnder atom interferometers, separated by a baseline, that are running simultaneously. Due to the height difference, it is able to measure the gravity gradient effects along the vertical direction:

$$(\nabla \boldsymbol{g})_{zz} = \frac{\boldsymbol{g}_1 - \boldsymbol{g}_2}{b}, \tag{2.32}$$

where $\boldsymbol{g}_1$ and $\boldsymbol{g}_2$ are the values of gravity measured by each of the interferometers and b is the baseline between them. This configuration has the advantage that it reduces the effect of vertical vibrations, which are common to both chambers, due to common mode rejection, as well as tilt. More information on the mathematical treatment of common mode rejection of vertical vibrations can be seen in Appendix B.

2.2.1 Quantum Projection Limits

In an actual experiment, the probability at the end of the interferometer is obtained by using multiple atoms. The upper state population can be obtained by measuring the number of atoms in each of the states and using [14]:

$$P_b = \frac{N_b}{N_a + N_b}, \tag{2.33}$$

where N_a and N_b are the number of atoms in the $|a\rangle$ and $|b\rangle$ states at the end of the Mach-Zehnder sequence.

The precision of the phase difference measurement of an atom interferometer is fundamentally limited by the total number of atoms, N. The atom shot noise (or quantum projection noise) causes an uncertainty in the measurement due to the statistical fluctuations in the atom number. Assuming perfect contrast, the fluctuations on the final probability are given by $\sigma_P = \sqrt{\frac{P_b(1-P_b)}{N}}$, which corresponds to the following uncertainty in the phase difference [42]:

$$\sigma_\Phi = \sigma_P \left|\frac{\mathrm{d}\Phi}{\mathrm{d}P_b}\right| = \sqrt{\frac{P_b(1-P_b)}{N}}\frac{2}{|\sin\Phi|} = \frac{1}{2}\sqrt{\frac{1-\cos^2\Phi}{N}}\frac{2}{|\sin\Phi|} = \sqrt{\frac{1}{N}}. \tag{2.34}$$

Since $\sigma_\Phi = k_{\mathrm{eff}} T^2 \sigma_g$ [12], the interferometer sensitivity is then given by:

$$\frac{\sigma_\Phi}{\Phi} = \frac{\sigma_g}{g} = \frac{1}{k_{\mathrm{eff}} g T^2 \sqrt{N}} \tag{2.35}$$

for single shot. Extending to a gravity gradiometer, the uncertainty in gravity gradient in vertical direction, σ_{grad}, may be calculated by propagation of errors of the two

interferometers of equation (2.32) [44]. The result is:

$$\sigma_{\text{grad}} = \frac{1}{k_{\text{eff}} T^2 b} \sqrt{\frac{N_2 + N_1}{N_1 N_2}}. \tag{2.36}$$

Assuming identical atom numbers in both interferometers, $N_1 = N_2 = N$, leads to shot noise limited uncertainty of a gravity gradiometer as:

$$\sigma_{\text{grad}} = \frac{\sqrt{2}}{k_{\text{eff}} T^2 b \sqrt{N}} \tag{2.37}$$

for a single shot. To be limited by this atomic fluctuation noise, other sources of noise must be lower than this. This is difficult practically and requires extensive optimisation.

2.3 MOT and Molasses

The velocity selection of the Raman transitions implies that a colder atomic cloud is favourable to perform interferometry. Therefore, interferometers use a cloud of cold atoms so that the atoms have a small velocity spread. The full theory of laser cooling and trapping is beyond the scope of this work and can be seen in [91]. The main effect behind this technique is the damping experienced by atoms as they interact with a pair of counter-propagating laser beams, which are red detuned from a closed atomic transition. The repeated absorption and emission cycles experienced by these atoms make them lose energy through spontaneous emission. To ensure that the cooling is done in all three dimensions, three pairs of these counter-propagating beams have to be applied. This technique is referred to as optical molasses [92].

In order to not just slow down the atoms but also trap them, a magnetic quadrupole field needs to be applied. This produces an energy shift in the magnetic sub-states (due to the Zeeman effect) that is dependent on the location of the atoms in this field. If

circularly-polarised laser beams are applied, these atoms are forced towards the centre of the quadrupole field where the magnetic field is zero. This creates a magneto-optical trap (MOT). Typical temperatures of the MOT are on the order of what is referred to as Doppler temperature, $T_{\text{Doppler}} = (\hbar\Gamma)/(2k_B)$ [92], where Γ is the natural linewidth of the atomic transition (for rubidium-85, $T_{\text{Doppler}} = 143.41$ μK [91]). One problem with applying the magnetic field, however, is the fact that it counteracts somewhat against sub-Doppler cooling mechanisms [14] due to the spatially varying force of the MOT. Lower temperatures are obtained when the magnetic field is reduced so that the Zeeman energy shift is of the order or below the single-photon recoil energy, in which case it is possible to reach what is referred to as recoil temperature. This temperature is limited by the recoil from a single photon, $T_{\text{recoil}} = (\hbar^2 k^2)/(mk_B)$ [92], where k is the wavevector magnitude of the photon and m is the mass of the atom (for rubidium-85, $T_{\text{recoil}} = 0.370$ μK [91]). Circularly-polarised light is needed for the MOT due to the allowed transitions given by the selection rules. For the sub-Doppler cooling (also referred to as optical molasses), two light polarisation configurations can be used. These are the "$\sigma^+ - \sigma^-$ polarisation gradient cooling" or "lin perp lin cooling" (commonly referred to as Sisyphus cooling) [91]. While the latter is theoretically able to reach slightly lower temperatures, the former is easier to implement since circularly-polarised light is needed for the MOT. For full theoretical treatment of sub-Doppler cooling, see [93].

In summary, to obtain the lowest possible temperatures of atoms, a MOT is created to capture atoms from background vapour, given its larger velocity capture range, followed by optical molasses, with smaller velocity capture range, to cool the atoms further [91].

2.4 Rubidium-87

So far, the discussion has been fairly theoretical, with an imaginary three-level atom. In real-life, real atoms have to be used. Alkali atoms are the most common elements used for these types of experiments as they have a simple electronic structure because of the single valence electron. Additionally, their states also have long lifetimes given the length of the experiments, avoiding spontaneous emission. Rubidium (Rb) is often favoured as it also has a relatively high mass, meaning that long interrogation times are possible. Rb is also advantageous for portable applications as the splitting of interest for cooling and Raman interactions is on the order of 780 nm, with light at this wavelength easily available due to the commercially-available telecomunnications lasers at 1560 nm. The two most abundant Rb isotopes are ^{85}Rb ($\sim$72% abundant) and ^{87}Rb ($\sim$28% abundant), with the latter favoured for interferometry due to higher possible suppression of spontaneous emission [14, 51, 86].

Figure 2.7 shows the level structure of the D_2 line of ^{87}Rb used in our experiments. Starting with ^{87}Rb at room temperature, the atoms are loaded into a MOT using the $|F = 2\rangle \rightarrow |F' = 3\rangle$ closed transition - selection rules mean that the atoms in $|F' = 3\rangle$ can only decay back to $|F = 2\rangle$. However, the MOT requires a red-detuned laser, meaning there is a possibility to induce the $|F = 2\rangle \rightarrow |F' = 2\rangle$ transition as well. As the atoms undergoing this transition can decay back to $|F = 1\rangle$, they could leave the cooling cycle and be lost. To avoid this, a repump light is introduced to enable the $|F = 1\rangle \rightarrow |F' = 2\rangle$ transition. Thanks to this, the atoms can decay back to $|F = 2\rangle$ and hence once again enter the cooling cycle. Once the atoms are cooled to an appropriate temperature, stimulated Raman transitions are performed using $|F = 1\rangle$ as state $|a\rangle$ and $|F = 2\rangle$ as state $|b\rangle$, ignoring the m_F states for now. To do this, two lasers, Raman 1 and Raman 2, are introduced, which are detuned from resonance [14].

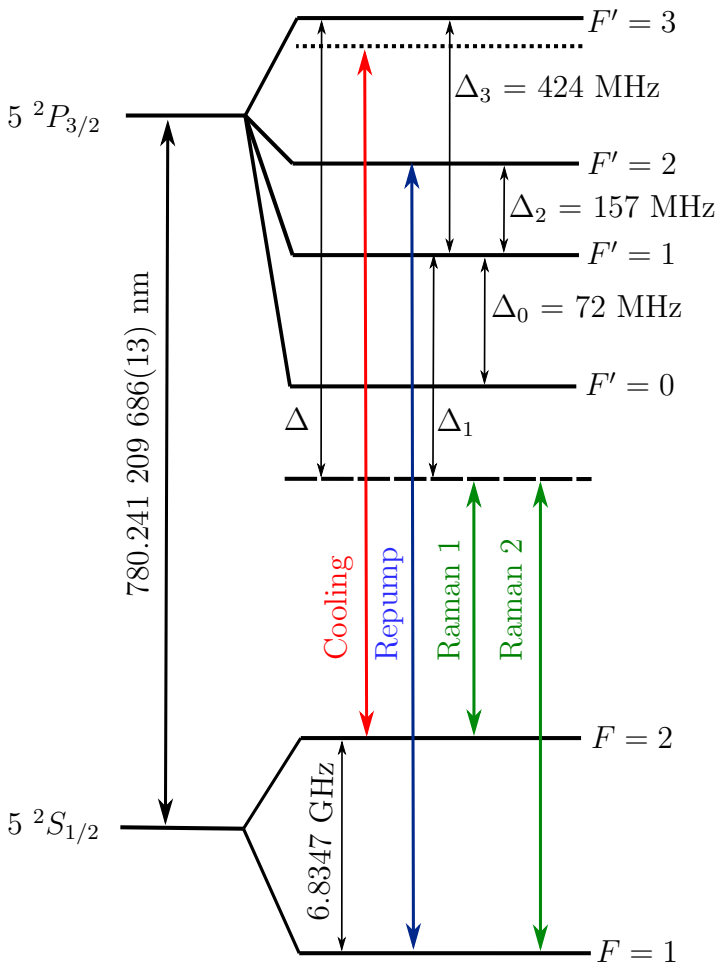


Figure 2.7: Level structure of the D_2 transition of ^{87}Rb, highlighting the transitions that are used to cool the atoms (and keep them out of the dark state) as well as the ones used for stimulated Raman transitions.

2.4.1 Interferometry with ^{87}Rb

The question that now needs answering is whether the theoretical treatment of a three-level atom can be used with a real atom, i.e. is it possible to obtain an interferometer using Rb. The next sections will briefly explain how the aforementioned theory can be applied in real-life as well as additional complexities that have so far not been addressed. More detail of this can be found in [14] while the full mathematical background can be found in [94].

2.4.1.1 Rabi Frequencies

The first task is to identify which states from the simple three-level model correspond to which of the states in ^{87}Rb. The inclusion of the m_F states creates more complexities when defining the various states but it is possible to obtain the following equivalents [14]:

$$\begin{aligned} |a\rangle &= |5^2S_{1/2}; F = 1; m_F\rangle \,, \\ |b\rangle &= |5^2S_{1/2}; F = 2; m_F + q_1 - q_2\rangle \,, \\ |e\rangle &= |5^2P_{3/2}; F' = 1, 2; m_{F'} + q_1\rangle \,, \end{aligned} \tag{2.38}$$

where $q_{1,2}$ are the polarisations of the Raman lights. As can be seen, two F states in the $|5^2P_{3/2}\rangle$ state can act as $|e\rangle$, with the m_F states also needing to be included.

In order to be able to coherently drive these transitions, a clearly-defined quantisation axis is required. This ensures that the polarisation of the light relative to the atoms is clearly defined, allowing us to drive specific transitions. This is achieved by including a magnetic field along the Raman beam axis, termed bias field [44]. Once the quantisation axis is defined, different light polarisations can drive different transitions, with σ^+ and σ^- transitions corresponding to $q_{1,2} = \pm 1$ and π transitions corresponding to $q_{1,2} = 0$ [14]. The transitions possible with $\sigma^+ - \sigma^+$ polarisations can be seen in Figure 2.8, along with their Clebsch-Gordan coefficients [14]. The equivalent $\sigma^- - \sigma^-$ and $\pi - \pi$ transitions can be seen in Appendix C.

The next step in understanding interferometry with a multi-level atom is the ability to calculate the Rabi frequencies of the relevant transitions. This is done by combining the Rabi frequencies of equation (2.11) with the Clebsch-Gordan coefficients of the appropriate transitions. It has been shown that the Winger-Eckart theorem can be

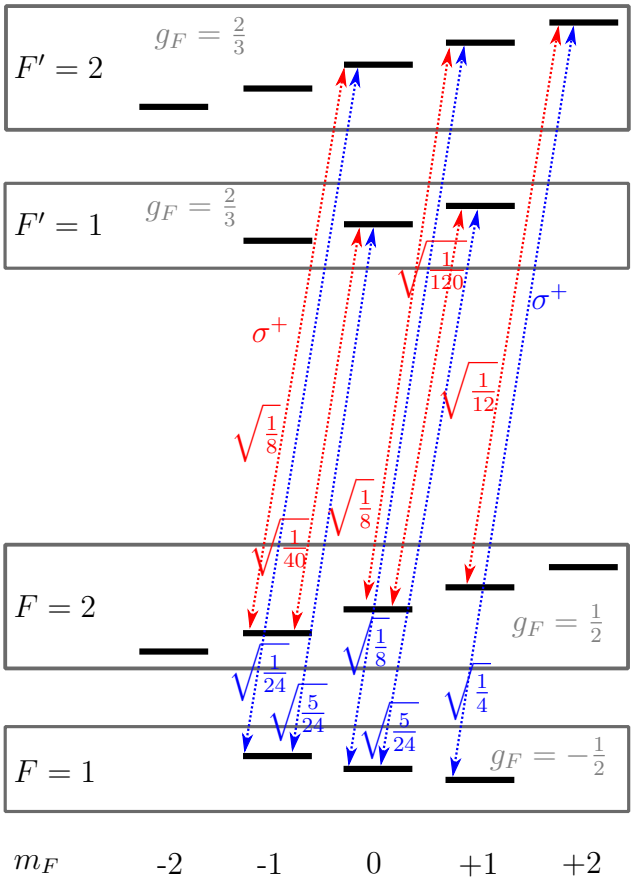


Figure 2.8: $\sigma^+ - \sigma^+$ transitions between $|5^2S_{1/2}; F = 1\rangle$ and $|5^2S_{1/2}; F = 2\rangle$ via $|5^2P_{3/2}; F' = 1\rangle$ and $|5^2P_{3/2}; F' = 2\rangle$.

used to obtain these as [14, 95]:

$$\Omega_{1,2} = \frac{|\boldsymbol{E}_{1,2}|}{2\hbar} DG_{1,2} = \sqrt{\frac{I_{1,2}}{2c\epsilon_0\hbar^2}} DG_{1,2}, \tag{2.39}$$

where $I_{1,2}$ are the intensities of the Raman beams, c is the speed of light, ϵ_0 is the electric constant, D is the transition dipole matrix element ($D = 3.584 \times 10^{-29}$ Cm for ^{87}Rb D_2 line) [96]. $G_{1,2}$ is the dimensionless geometric factor that depends on the specific transition and is equivalent to the Clebsch-Gordan coefficients [14].

However, the stimulated Raman transitions are a consequence of a two-photon

process and hence these Rabi frequencies have to be combined to produce an overall Rabi frequency for the transition. This effective Rabi frequency can be obtained by multiplying the Rabi frequencies of the single-photon transitions to produce the Rabi frequency of the overall two-photon transition using the equation above. This is followed by summation over all of the possible transitions. Alternatively, this full effective Rabi frequency has been shown in the literature to have the form [14, 94]:

$$\Omega_{\text{eff}} = \frac{D^2}{c\epsilon_0\hbar^2}\frac{\sqrt{I_1 I_2}}{\Delta}\Big|\sum_i G_1 G_2\Big|, \tag{2.40}$$

ignoring the hyperfine splitting of the $|5^2P_{3/2}\rangle$ state because it is much smaller than the hyperfine splitting of $|5^2S_{1/2}\rangle$, a valid approximation if $\Delta >> \Omega_{1,2}$ [14]. In the case of equal polarisations, the sum of the geometric factors can be simplified further due to symmetry [14, 94]:

$$\Big|\sum_i G_1 G_2\Big| = \frac{\sqrt{4 - m_F^2}}{12}. \tag{2.41}$$

2.4.1.2 Zeeman Effect

The inclusion of the m_F sub-states as well as the bias field causes additional considerations. If no magnetic field is present, all of the m_F states of a particular F state are degenerate. However, introduction of the bias field breaks the degeneracy of these m_F sub-states, due to the Zeeman splitting, with the shift of energy given by [96, 97]:

$$\Delta E_{|F,m_F\rangle} = \mu_B g_F m_F B, \tag{2.42}$$

which is valid in the weak-field regime [96, 97]. These energy shifts for the various m_F states can also be seen illustrated in Figure 2.8.

As the Zeeman energy shift is m_F-dependent, it is desirable to use an m_F state which

is not affected by magnetic field as much as possible, to ensure that that Raman frequencies are on resonance regardless of B and that any B variations have a minimal effect on the Raman transitions. This makes the the $|F = 1, m_F = 0\rangle \leftrightarrow |F = 2, m_F = 0\rangle$ transition desirable. As this transition does not depend on B, it is said to be insensitive to magnetic field to first order [14, 44, 51]. Unfortunately, this is not quite the end of the story. Even for this transition, an energy shift due to the external magnetic field remains due to the quadratic Zeeman shift, which is a consequence of the energy shift of the states because of B^2 dependence. This shift dependence can be calculated using the intermediate-field regime (Breit-Rabi formula) [96, 97]:

$$\frac{\Delta\omega}{B^2} = \frac{(g_J - g_I)^2 \mu_B^2}{2\hbar \Delta E_{|F=1\rangle \to |F=2\rangle}} = 2\pi\kappa, \tag{2.43}$$

which is evaluated as $2\pi\times$ 575.15 Hz/G^2 for the transition in question [96]. Therefore, this bias field comes at a price, inducing additional phase contributions to our final interferometer output, which will be discussed in more detail in section 2.5.1.5.

2.4.1.3 AC Stark Shift

The final topic of discussion for real atoms is the AC Stark shift and how it can be cancelled. As seen in equation (2.16), the stimulated Raman transitions have a dependence on the energy shift of the energy levels as a consequence of the Raman lights. These lights are detuned by Δ, which needs to be relatively large to suppress spontanous emissions (on the order of or even larger than the hyperfine splitting of the $|5^2P_{3/2}\rangle$ state). Therefore, when considering the AC Stark shift in ^{87}Rb, this multi-level structure of the $|5^2P_{3/2}\rangle$ state needs to be taken into account but keeping in mind that only the $|F' = 1\rangle$ and $|F' = 2\rangle$ states can act as state $|e\rangle$ [51].

This means is that the definitions of Ω_a^{AC} and Ω_b^{AC} in equation (2.15) need to be

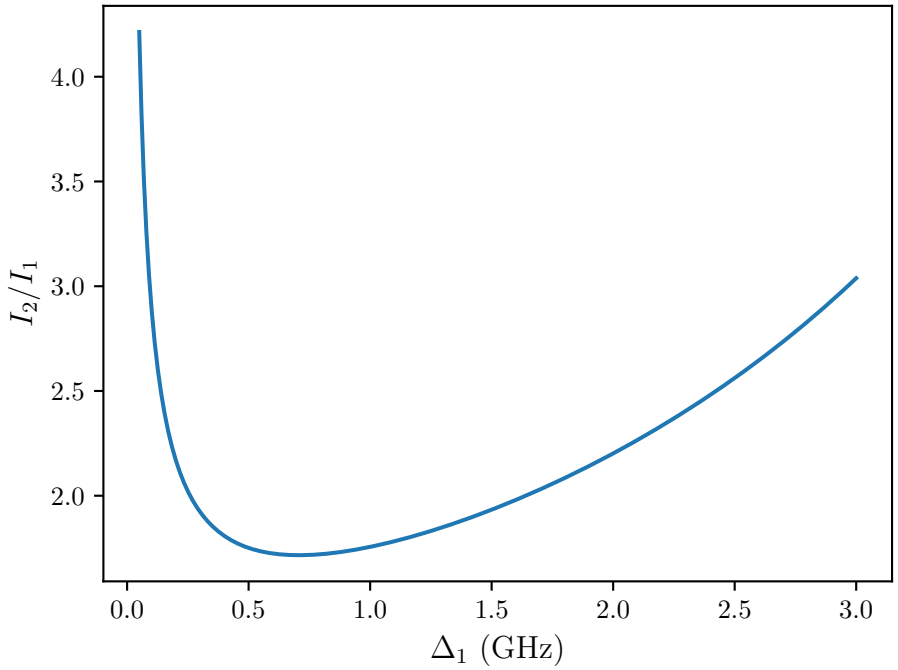


Figure 2.9: A plot of the intensity ratio of the Raman laser beams required to cancel out the AC Stark shift for a range of Δ_1.

modified to take into account the other states that cannot be considered as $|e\rangle$. This can be done by defining new detuning parameters Δ_0, Δ_1, Δ_2 and Δ_3 with respect to the $|F' = 1\rangle$, as seen in Figure 2.7. In the case of orthogonal linear polarisations of the Raman beams, taking into account all of the corresponding Clebsch-Gordan coefficients, it is possible to derive an equation for the ratio of intensities of the two Raman beams that cancels out this AC Stark shift [51]:

$$\frac{I_2}{I_1} = \frac{\left(\frac{1}{60(\Delta_1+\omega_{ba})} + \frac{1}{4(\Delta_1-\Delta_2+\omega_{ba})} + \frac{2}{5(\Delta_1-\Delta_3+\omega_{ba})}\right) - \left(\frac{5}{12\Delta_1} + \frac{1}{4(\Delta_1-\Delta_2)}\right)}{\left(\frac{5}{12(\Delta_1-\omega_{ba})} + \frac{1}{4(\Delta_1-\Delta_2-\omega_{ba})}\right) - \left(\frac{1}{60\Delta_1} + \frac{1}{4(\Delta_1-\Delta_2)} + \frac{2}{5(\Delta_1-\Delta_3)}\right)}. \tag{2.44}$$

Satisfying this ratio results in $\Omega_a^{\mathrm{AC}} = \Omega_b^{\mathrm{AC}}$ and $\delta_{\mathrm{AC}} = 0$, allowing us to drive Raman transitions on resonance. This ratio of I_2/I_1 is plotted against Δ_1 in Figure 2.9 [51].

2.5 Phase Contributions

The relation of the probability of upper state being only the consequence of $\boldsymbol{g}$ and α, as indicated in equation (2.31), is only valid in the ideal case of no other forces acting on the atoms during their free-fall. This is not a valid approximation in the real-world. This section deals with other phase contributions, concentrating on ones with relevance to dynamic conditions. While both inertial and atomic frequency phase shifts will be considered for gravimeters and gradiometers, the latter ones will only be discussed briefly.

2.5.1 Inertial Shifts

2.5.1.1 Gravity & Gravity Gradient

As mentioned, $\boldsymbol{g}$ is the most obvious contribution to the interferometer output. As already mentioned in equation (2.31), the term due to gravity for a gravimeter is [98]:

$$\Phi_{\text{g-g}} = \boldsymbol{k}_{\text{eff}} \cdot \boldsymbol{g} T^2. \tag{2.45}$$

For $T = 50$ ms, this term contributes $\Phi_{\text{g-g}} \simeq 4 \times 10^4$ rad/(ms^{-2}) and provides a huge phase shift given the value of $\boldsymbol{g}$ of the Earth.

This term can be modified for the gradiometer configuration to obtain [99, 100]:

$$\Phi_{\text{g-grad}} = \boldsymbol{k}_{\text{eff}} \cdot (\boldsymbol{g_1} - \boldsymbol{g_2}) T^2, \tag{2.46}$$

where $\boldsymbol{g}_1 - \boldsymbol{g}_2$ is the difference in gravitational acceleration between the two clouds. In the case of a constant $\boldsymbol{g}$, this term disappears, which is not the case on Earth. This term can be rewritten to take into account the baseline of the gradiometer, b, as

[90, 101]:

$$\Phi_{\text{grad-grad}} = b\boldsymbol{k}_{\text{eff}} \cdot (\nabla \boldsymbol{g})_z T^2, \tag{2.47}$$

where $(\nabla \boldsymbol{g})_z$ is the gravity gradient between the two atomic clouds along the vertical direction (and assuming this gradient only changes along the vertical axis and not the horizontal axes). For $T = 50$ ms, this calculates, as before, to $\Phi_{\text{grad-grad}} \simeq b|(\nabla \boldsymbol{g})_z| \cdot 4 \times 10^4$ rad/(ms^{-2}). However, in this case, the values that can be measured (and hence phase shifts) are considerably smaller. For example, $|(\nabla \boldsymbol{g})_z| \simeq 3 \times 10^{-6}$ s^{-2} on Earth [90, 101] and hence only a small phase shift will be observed as a consequence of a gradiometer of $b = 1$ m.

These terms provide the signals of interest for both gravimeters and gradiometers. To detect small changes in these, and hence allow us to detect smaller features of interest, it is important to ensure that this phase shift effect is the dominating factor and that any other phase shifts are kept as small as possible. Since $\boldsymbol{g}$ is a special case of acceleration, a force that creates acceleration along the same axis as $\boldsymbol{g}$ will contribute a phase shift that is indistinguishable, manifesting as uncertainty on the measurement.

2.5.1.2 Vertical Vibrations

Vertical vibrations, i.e. vibrations along the Raman beams/gravity axis, are pronounced on Earth and can often destroy the signal of a gravimeter. They couple onto the phase of the atom interferometer as [70, 98, 99, 102, 103]:

$$\Phi_{\text{vib-g}} = \boldsymbol{k}_{\text{eff}} \cdot \boldsymbol{a}_{\text{vib}} T^2, \tag{2.48}$$

where $\boldsymbol{a}_{\text{vib}}$ is the vertical acceleration due to vibrations. It might not be obvious to the reader but moving along a horizontal axis can actually produce vertical vibrations as well; the level of this correlation depends on the mounting used. An example of this can

be seen in Figure 2.10, where a Nanometrics Titan accelerometer placed on a linear rail was used to measure the vertical vibrations on the said rail when it was stationary and when it was moving. The measured acceleration is along the vertical axis, i.e. along the axis of $\boldsymbol{g}$. $\Phi_{\text{vib-g}}$ has the same scaling with acceleration as $\Phi_{\text{g-g}}$ and hence has substantial contribution. The data is an example but it shows that vertical vibrations can approach order of magnitude of $\boldsymbol{g}$ and this effect could potentially be even more pronounced on vehicles such as ships or planes. Therefore, this term is of huge importance when it comes to moving gravimeters. One way to combat this is to use a hybrid sensor, where a gravimeter coupled with a classical accelerometer utilises a technique called fringe reconstruction by accelerometer correlation [13, 56, 62, 69, 73, 74].

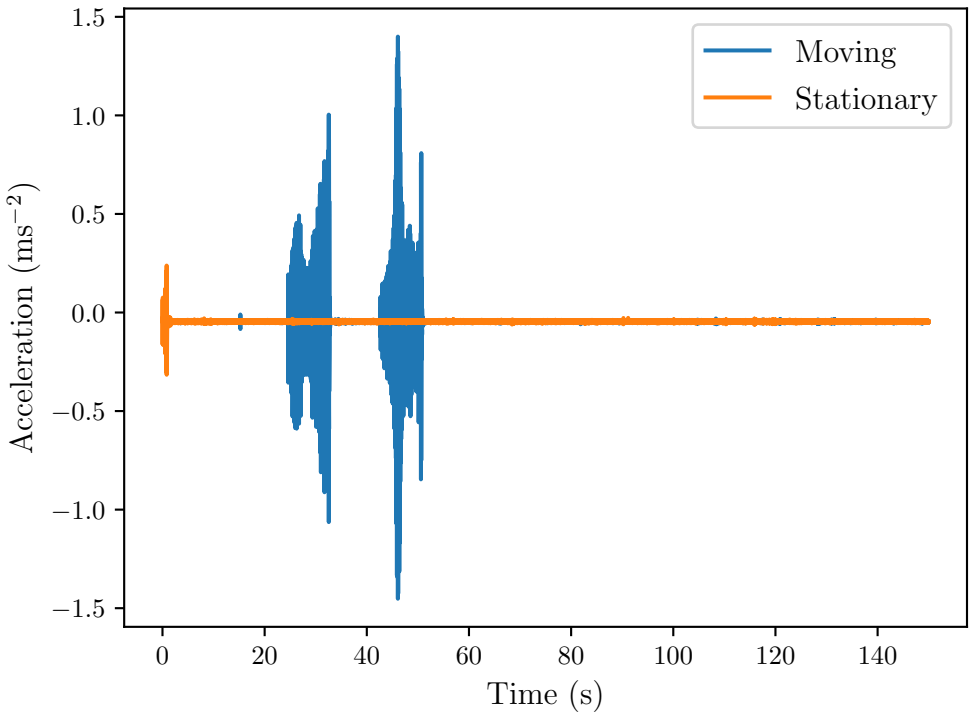


Figure 2.10: Vertical vibrations as measured with a Nanometrics Titan accelerometer placed on a stationary and moving linear rail. The linear rail motion is along the horizontal direction, i.e. perpendicular to the vertical vibrations.

As has been mentioned numerous times, this is where the advantage of a gravity

gradiometer becomes apparent, with the term for this contribution being [99]:

$$\Phi_{\text{vib-grad}} = \boldsymbol{k}_{\text{eff}} \cdot (\boldsymbol{a}^1_{\text{vib}} - \boldsymbol{a}^2_{\text{vib}})T^2, \tag{2.49}$$

where $(\boldsymbol{a}^1_{\text{vib}} - \boldsymbol{a}^2_{\text{vib}})$ is the difference in vertical accelerations due to vibrations between the two atomic clouds. Gradiometer is advantageous as it is able to suppress the effect of vertical vibrations due to common mode rejection, with the degree of this suppression being somewhat dependant on the structural support and the length of the baseline [104]. With a rigid structure and reasonable baseline, almost perfect common mode rejection can be achieved, meaning $\Phi_{\text{vib-grad}} \simeq 0$. More discussion about the effects of vibrations on gravimeters and gradiometers can be seen in Appendix B.

2.5.1.3 Rotation

Rotation of the sensor will cause a phase shift given by [76, 90, 98, 101, 105, 106]:

$$\Phi_{\text{rot-g}} = 2\boldsymbol{k}_{\text{eff}} \cdot (\boldsymbol{\Omega} \times \boldsymbol{v})T^2, \tag{2.50}$$

where $\boldsymbol{\Omega}$ is the rotation rate and $\boldsymbol{v}$ is the centre of mass velocity of the atomic cloud. Due to practical limitations of atomic cooling, atoms will have a component of velocity that depends on their temperature. The amount of rotation that an interferometer will experience on a move depends on the application that it is being used for, as well as engineering of mounting and support. Therefore, this term needs to be considered when operating in dynamic conditions.

This term can be modified for the gradiometer to obtain:

$$\Phi_{\text{rot-grad}} = 2\boldsymbol{k}_{\text{eff}} \cdot (\boldsymbol{\Omega} \times (\boldsymbol{v_1} - \boldsymbol{v_2}))T^2, \tag{2.51}$$

where $(\boldsymbol{v_1} - \boldsymbol{v_2})$ is the difference in centre of mass velocities of the two atomic clouds. This means that gradiometer configuration could in principle have a higher rotation term than a standard gravimeter of the same atomic cloud speeds if they are in opposite directions.

Coriolis effect is an extension of the rotation term but in this case the rotation is a result of the Earth spinning around its axis. The equation above can be used to derive the phase shift as a consequence of this [5]:

$$\Phi_{\text{coriolis-g}} = 2\Omega_E k_{\text{eff}} v_{\text{hor}} \cos\phi_{\text{lat}} \cos\theta_{\text{or}} T^2, \tag{2.52}$$

where Ω_E is the Earth's rotation angular velocity, v_{hor} is the horizontal velocity of the atomic cloud, ϕ_{lat} is the latitude of the point of interest and θ_{or} is the orientation of the atomic motion to the East-West direction. Usually, Earth's rotation rate can be considered as a constant, with $\Omega_E = 72.9\ \mu$rad/s [90, 101] and the latitude of University of Birmingham (UK) is 52.45°. For $T = 50$ ms, this calculates as $\Phi_{\text{coriolis-g}} \simeq v_{\text{hor}} \cdot 3.58$ rad/(ms^{-1}), which is not insignificant. While this phase shift can be compensated for via an appropriate orientation of the sensor, as seen in Figure 2.11, it presents a challenge in the field as it might not be possible to characterise and re-orient the instrument if large areas of the Earth are to be covered.

As with the normal rotation term, the equation for Coriolis can be modified for a gradiometer to obtain:

$$\Phi_{\text{coriolis-grad}} = 2\Omega_E k_{\text{eff}} (v^1_{\text{hor}} - v^2_{\text{hor}}) \cos\phi_{\text{lat}} \cos\theta_{\text{or}} T^2, \tag{2.53}$$

where $(v^1_{\text{hor}} - v^2_{\text{hor}})$ is the difference in horizontal velocities of the two atomic clouds.

Another phase shift due to rotation is as a consequence of the centrifugal accelera-

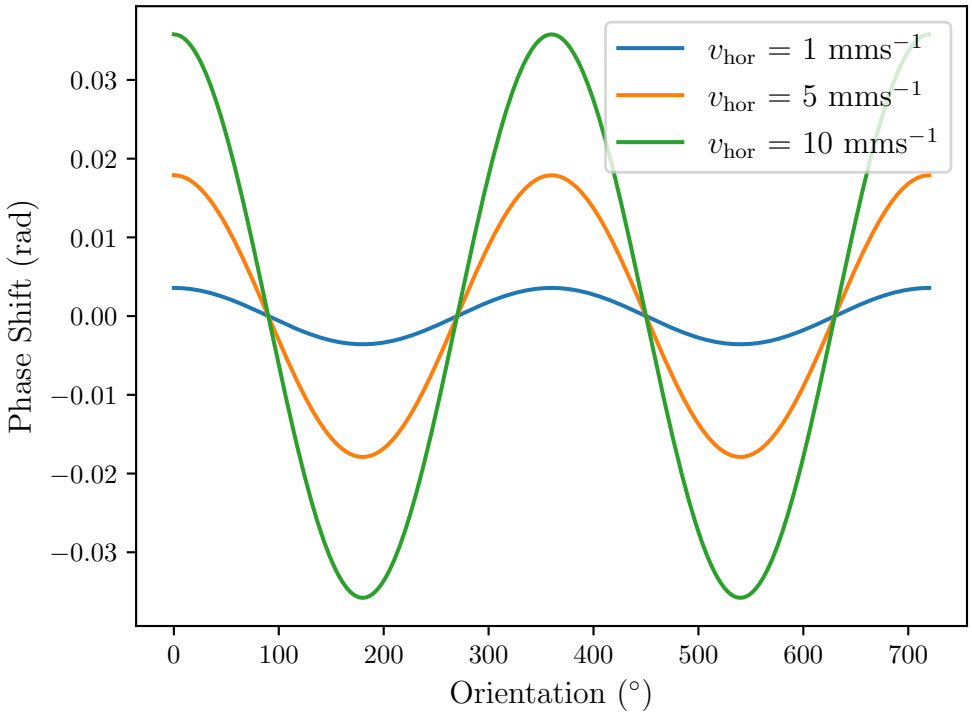


Figure 2.11: Phase shift due to Coriolis as a function of the orientation of the sensor.

tion generated. In general terms, this produces a phase shift of [107, 108]:

$$\Phi_{\text{centrifugal-g}} = \boldsymbol{k}_{\text{eff}} \cdot (\boldsymbol{\Omega} \times (\boldsymbol{\Omega} \times \boldsymbol{r}))T^2, \tag{2.54}$$

where $\boldsymbol{r}$ is the distance from the centre of rotation. In the case of Earth's rotation, $\boldsymbol{r}$ becomes the cloud's displacement from the centre of the Earth. A simplified version of this expression is given by [102]:

$$\Phi_{\text{centrifugal-g}} = k_{\text{eff}} R\Omega^2 T^2, \tag{2.55}$$

where R is interferometer distance from the centre of the rotation and Ω is the rotation

rate. For the gradiometer configuration, similar terms can be obtained [102, 104]:

$$\Phi_{\text{centrifugal-grad}} = \boldsymbol{k}_{\text{eff}} \cdot \{\boldsymbol{\Omega} \times [\boldsymbol{\Omega} \times (\boldsymbol{r}_1 - \boldsymbol{r}_2)]\} T^2 = k_{\text{eff}} \delta R \Omega^2 T^2, \tag{2.56}$$

where $(\boldsymbol{r}_1 - \boldsymbol{r}_2)$ or δR is the distance between the interferometers, hence equal to b.

2.5.1.4 Tilt

While the Raman beams can be oriented along the vertical direction relatively well, for example by using a liquid mirror, small fluctuations in the propagation direction of the Raman beams would couple as a consequence of the Coriolis effect:

$$\Phi_{\text{tilt-g}} = -2\Omega_E k_{\text{eff}} v_{\text{hor}} \cos\phi_{\text{lat}} \sin\theta T^2, \tag{2.57}$$

where θ is a small inclination along the East-West direction. For $T = 50$ ms at our altitude, this calculates as $\Phi_{\text{tilt-g}} \simeq v_{\text{hor}}\theta \cdot 3.58$ rad/(ms^{-1}) for small tilts. For gradiometer, the difference in the cloud velocities is of consequence and hence the tilt phase shift is given by [101, 109]:

$$\Phi_{\text{tilt-g}} = -2\Omega_E k_{\text{eff}} (v^1_{\text{hor}} - v^2_{\text{hor}}) \cos\phi_{\text{lat}} \sin\theta T^2. \tag{2.58}$$

2.5.1.5 Magnetic Field

As was shown in section 2.4.1.2, a magnetic field causes energy shifts of the m_F substates. One consequence of these shifts is an inertial effect, causing a linear Zeeman phase shift of [90, 101]:

$$\Phi_{\text{linear-g}} = \frac{\mu_B}{m} \left(m_{|F=2\rangle} g_{|F=2\rangle} - m_{|F=1\rangle} g_{|F=1\rangle} \right) \boldsymbol{k}_{\text{eff}} \cdot \nabla B T^2, \tag{2.59}$$

where ∇B is the gradient of the magnetic field. This term will cause a shift if there are magnetic field variations along the direction of $\boldsymbol{k}_{\text{eff}}$. As has been mentioned, a way to combat this term is to use atoms in the $m_F = 0$ state [101], meaning that it can be usually assumed that $\Phi_{\text{linear-g}} \simeq 0$.

For completeness, this term can be modified for the gradiometer to obtain:

$$\Phi_{\text{linear-grad}} = \frac{\mu_B}{m} \left(m_{F=2} g_{F=2} - m_{F=1} g_{F=1}\right) \boldsymbol{k}_{\text{eff}} \cdot \left(\nabla B_1 - \nabla B_2\right) T^2, \tag{2.60}$$

where $(\nabla B_1 - \nabla B_2)$ is the difference in the magnetic field gradients of the two interferometers. If the magnetic field variations are the same for both, this term cancels.

While the $m_F = 0$ state is magnetically insensitive to first order, there is still a shift due to the quadratic Zeeman shift even for this state. The frequency shift is shown in equation (2.43), which leads to a phase shift of [43, 110]:

$$\Phi_{\text{quadratic-g}} = \frac{2h\kappa}{m} \boldsymbol{k}_{\text{eff}} \cdot (B \nabla B) T^2, \tag{2.61}$$

where B is the magnetic field and $\kappa = 575.15$ Hz/G^2 for the $|F = 1, m_F = 0\rangle \leftrightarrow |F = 2, m_F = 0\rangle$ transition. This calculates as $\Phi_{\text{quadratic-g}} \simeq B \nabla B \times 0.2$ rad/(G^{2}m^{-1}) but if the field is uniform then this effect is cancelled.

Once again, for gradiometer, this can be modified to be:

$$\Phi_{\text{quadratic-grad}} = \frac{2h\kappa}{m} \boldsymbol{k}_{\text{eff}} \cdot \left(B_1 \nabla B_1 - B_2 \nabla B_2\right) T^2, \tag{2.62}$$

with B_1 and B_2 being the magnetic fields in the two interferometers. Assuming a uniform magnetic field is a reasonable assumption in laboratory conditions, where the external magnetic environment is the same. In portable applications, the instrument is placed in different locations, meaning that the external magnetic environment could

change if it is not dealt with adequately. Therefore, additional steps can be taken to try and reduce the magnetic field that the atoms experience - this is via the use of magnetic shielding. This will be discussed further in chapter 3.

2.5.1.6 Electric Field

Electric fields cause an acceleration proportional to qE/m, shifting the energy of the ground state, and causing a phase shift of [90, 101]:

$$\Phi_{\text{electric-g}} = \frac{4\pi\epsilon_0\alpha_{\text{pol}}}{m}\boldsymbol{k}_{\text{eff}} \cdot (E\nabla E)T^2, \tag{2.63}$$

where ϵ_0 is the permittivity of space, E is the electric field, ∇E is the gradient of the electric field and α_{pol} is the scalar polarisability of the state given by $\alpha_{\text{pol}} = h \cdot 0.13408$ Hz/(V/cm)^2 for the D_2 transition of ^{87}Rb. Similarly to magnetic field, if the electric field is uniform, this term can be ignored [96, 111].

This term can be modified for gradiometer to obtain:

$$\Phi_{\text{electric-grad}} = \frac{4\pi\epsilon_0\alpha_{\text{pol}}}{m}\boldsymbol{k}_{\text{eff}} \cdot (E_1\nabla E_1 - E_2\nabla E_2)\, T^2, \tag{2.64}$$

where $E_1(\nabla E_1)$ and $E_2(\nabla E_2)$ are the electric fields (and their gradients) inside of the two interferometers. This term can be ignored based on the same argument as above. However, as with magnetic fields, this might not be the case in non-laboratory conditions and hence should be remembered in portable applications.

2.5.2 Atomic Frequency Shifts

We will now discuss the other types of interferometer phase shifts, namely the atomic frequency phase shifts. During the first $\pi/2$ pulse interaction between the light and

atom, the Raman light, oscillating at ω_{eff}, induces a dipole oscillation in the atom, oscillating at ω_0. If these two oscillations are identical for the full interferometer sequence, or even if they are not but $\delta = 0$ for the entire interferometry sequence, no phase shift contribution will be observed. However, a change of δ after the π pulse as opposed to before the π pulse would cause a phase shift contribution. Therefore, any processes that change the difference in frequencies of these oscillations have a potential to introduce phase shift to the interferometer output [90, 101].

2.5.2.1 Light Shift

To perform stimulated Raman transitions, interferometers use $\Delta >> \delta$. Due to this detuned light, an energy shift of $\Delta E_{\text{AC}} = \pm\hbar\Omega_{\text{R}}/2$ [90] is introduced, where an increase in energy is observed if negative detuning is present. Due to the symmetry of the Mach-Zehnder, if the atom-light interactions are the same before and after the π pulse then there will be no resulting phase shift contribution. However, if this light were to be introduced only after the π pulse, the following phase shift would be seen [90]:

$$\Phi_{\text{AC-g}} = \int_{t_i}^{t_f} \Omega_{\text{R}} \, \mathrm{d}t \tag{2.65}$$

for gravimeters, and:

$$\Phi_{\text{AC-grad}} = \int_{t_i}^{t_f} (\Omega_{\text{R}}^1 - \Omega_{\text{R}}^2) \, \mathrm{d}t \tag{2.66}$$

for gradiometers, where Ω_{R}^1 and Ω_{R}^2 are the Rabi frequencies of the two interferometers. Since we assume that the atom-light interaction is the same on either side of the π pulse as well as the fact that the AC Stark shift is compensated by an appropriate ratio of the intensities of the laser beams, this phase shift can be ignored.

2.5.2.2 Zeeman Shift

Once again, the magnetic field has yet another phase shift contribution to the interferometer output. If the magnetic field changes during the interferometry sequence, this results in a change of energies of the m_F sub-states. This has the consequence of changing the resonance frequency of the atomic levels during the sequence. However, the frequencies of the pulses will remain the same. This mismatch between the shifted resonance frequency and the unshifted Raman frequencies causes a phase shift on the $m_F = 0$ sub-state of [43, 101]:

$$\Phi_{\text{Zeeman-g}} = 2\pi\kappa \int_{-\infty}^{\infty} g_s(t)|\boldsymbol{B}(t)|^2 \, \mathrm{d}t, \tag{2.67}$$

where $g_s(t)$ is the sensitivity function, seen plotted in Figure 2.12, with more discussion in Appendix B. For completeness, the gradiometer term is given by:

$$\Phi_{\text{Zeeman-grad}} = 2\pi\kappa \int_{-\infty}^{\infty} g_s(t)(|\boldsymbol{B_1}(t)|^2 - |\boldsymbol{B_2}(t)|^2) \, \mathrm{d}t. \tag{2.68}$$

If the magnetic field is stable during the interferometry then this term vanishes due to the shape of $g_s(t)$ [43].

2.5.2.3 DC Stark Shift

In a similar manner to the magnetic field, the electric field can also change the energies of the states, shifting the atomic frequencies compared to the Raman frequencies. In the case of an electric field, this energy shift is $\Delta E_{\text{DC}} = h a_{\text{DC}} |\boldsymbol{E}|^2$ for the $m_F = 0$ sub-state [90, 101]. Also similarly to magnetic field, this effect is cancelled in the case of a static and uniform electric field [101] because of the reversal of the internal states

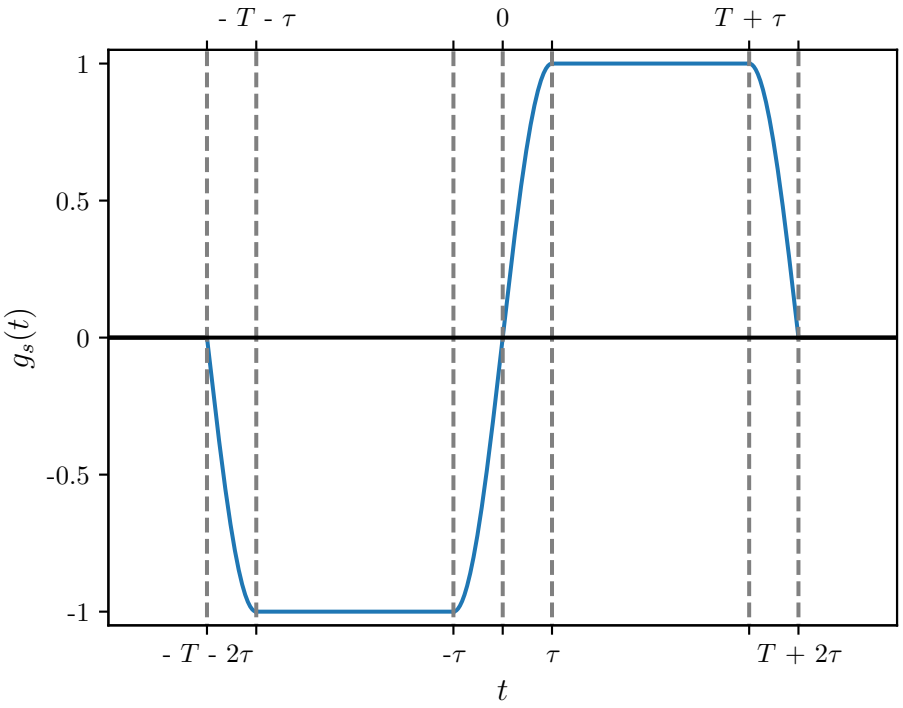


Figure 2.12: Sensitivity function, $g_s(t)$, as a function of time, showing a symmetric behaviour around the middle pulse. Therefore, for constant systematics that scale with the sensitivity function, the phase shift during the interferometer is cancelled.

before and after the π pulse [90], with a similar expression for phase shift observed:

$$\Phi_{\text{DC-g}} = 2\pi a_{\text{DC}} \int_{-\infty}^{\infty} g_s(t) |\boldsymbol{E}(t)|^2 \, \mathrm{d}t, \tag{2.69}$$

where $a_{\text{DC}} = -3.97 \times 10^{-10}$ Hz/(V/m)^2. However, this shift is far more negligible compared to the other shifts. For example, using a $T = 50$ ms interferometer, and switching on an electric field of 1 kV/m after the π pulse, produces a phase shift of only $\sim$0.1 mrad. For completeness, for gradiometer this effect is:

$$\Phi_{\text{DC-grad}} = 2\pi a_{\text{DC}} \int_{-\infty}^{\infty} g_s(t) (|\boldsymbol{E}_1|^2 - |\boldsymbol{E}_2|^2) \, \mathrm{d}t. \tag{2.70}$$

2.5.3 Summary

A summary of the phase shifts discussed can be seen in Table 2.2. This is not a full list of all phase contributions - more comprehensive lists can be found in literature, for example in [107].

Table 2.2: Phase shift contributions to the output of an interferometer.

	Contribution	Gravimeter	Gradiometer	Comments
Inertial	Gravity and Gravity Gradient	$\boldsymbol{k}_{\text{eff}} \cdot \boldsymbol{g} T^2$	$b\boldsymbol{k}_{\text{eff}} \cdot (\nabla \boldsymbol{g})_z T^2$	Gravimeter cannot obtain the gravity gradient.
	Vibrations	$\boldsymbol{k}_{\text{eff}} \cdot \boldsymbol{a}_{\text{vib}} T^2$	$\boldsymbol{k}_{\text{eff}} \cdot (\boldsymbol{a}^1_{\text{vib}} - \boldsymbol{a}^2_{\text{vib}}) T^2$	Negligible for gradiometer due to common mode rejection.
	Rotation	$2\boldsymbol{k}_{\text{eff}} \cdot (\boldsymbol{\Omega} \times \boldsymbol{v}) T^2$	$2\boldsymbol{k}_{\text{eff}} \cdot (\boldsymbol{\Omega} \times (\boldsymbol{v}_1 - \boldsymbol{v}_2) T^2$	Relevant for dynamic gravimeter and gradiometer.
	Coriolis	$2\Omega_E k_{\text{eff}} v_{\text{hor}} \cos\phi_{\text{lat}} \cos\theta_{\text{or}} T^2$	$2\Omega_E k_{\text{eff}} (v^1_{\text{hor}} - v^2_{\text{hor}}) \cos\phi_{\text{lat}} \cos\theta_{\text{or}} T^2$	Relevant for dynamic gravimeter and gradiometer but can be suppressed with appropriate orientation.
	Centrifugal	$\boldsymbol{k}_{\text{eff}} \cdot (\boldsymbol{\Omega} \times (\boldsymbol{\Omega} \times \boldsymbol{r})) T^2$	$\boldsymbol{k}_{\text{eff}} \cdot \{\boldsymbol{\Omega} \times [\boldsymbol{\Omega} \times (\boldsymbol{r}_1 - \boldsymbol{r}_2)]\} T^2$	Relevant for dynamic gravimeter and gradiometer.
	Tilt	$-2\Omega_E k_{\text{eff}} v_{\text{hor}} \cos\phi_{\text{lat}} \sin\theta$	$-2\Omega_E k_{\text{eff}} (v^1_{\text{hor}} - v^2_{\text{hor}}) \cos\phi_{\text{lat}} \sin\theta$	Relevant for dynamic gravimeter and gradiometer.
	Linear Zeeman	$\frac{\mu_B}{m} (m_{F=2} g_{F=2} - m_{F=1} g_{F=1}) \boldsymbol{k}_{\text{eff}} \cdot \nabla B T^2$	$\frac{\mu_B}{m} (m_{F=2} g_{F=2} - m_{F=1} g_{F=1}) \boldsymbol{k}_{\text{eff}} \cdot (\nabla B_1 - \nabla B_2) T^2$	Negligible due to using $m_F = 0$.
	Quadratic Zeeman	$\frac{2h\kappa}{m} \boldsymbol{k}_{\text{eff}} \cdot (B \nabla B) T^2$	$\frac{2h\kappa}{m} \boldsymbol{k}_{\text{eff}} \cdot (B_1 \nabla B_1 - B_2 \nabla B_2) T^2$	Negligible if uniform magnetic field.
	Electric Field	$\frac{4\pi\epsilon_0 \alpha_{\text{pol}}}{m} \boldsymbol{k}_{\text{eff}} \cdot (E \nabla E) T^2$	$\frac{4\pi\epsilon_0 \alpha_{\text{pol}}}{m} \boldsymbol{k}_{\text{eff}} \cdot (E_1 \nabla E_1 - E_2 \nabla E_2) T^2$	Negligible if uniform electric field.
Frequency	Light Shift	$\int_{t_i}^{t_f} \Omega_{\text{R}} \, \text{d}t$	$\int_{t_i}^{t_f} (\Omega^1_{\text{R}} - \Omega^2_{\text{R}}) \, \text{d}t$	Negligible if light and atom interactions are constant during interferometry.
	Zeeman Shift	$2\pi\kappa \int_{-\infty}^{\infty} g_s(t) \lvert\boldsymbol{B}(t)\rvert^2 \, \text{d}t$	$2\pi\kappa \int_{-\infty}^{\infty} g_s(t) (\lvert\boldsymbol{B_1}(t)\rvert^2 - \lvert\boldsymbol{B_2}(t)\rvert^2) \, \text{d}t$	Negligible if uniform magnetic field.
	DC Stark Shift	$2\pi a_{\text{DC}} \int_{-\infty}^{\infty} g_s(t) \lvert\boldsymbol{E}(t)\rvert^2 \, \text{d}t$	$2\pi a_{\text{DC}} \int_{-\infty}^{\infty} g_s(t) (\lvert\boldsymbol{E}_1\rvert^2 - \lvert\boldsymbol{E}_2\rvert^2) \, \text{d}t$	Negligible if uniform electric field.

Chapter 3

Experimental Setup

The full image of the gravity gradiometer setup utilised during this work can be seen in Figure 3.1 and it comprises of the following sub-systems:

- **Sensor head** that houses two vacuum science chambers containing the ^{87}Rb atoms. It is built to be able to provide the required magnetic control using magnetic shielding and magnetic coils. The light for the cooling and interferometry is delivered into the chamber vertically by optical delivery telescopes. The sensor head was built as part of previous work within the group [112] and has only been upgraded during this work, with the upgrades being primarily implemented by Andrew Lamb.

- **Laser system**, composed of radio-frequency (RF) and optical components, that produces the necessary light of appropriate frequencies to perform the experiment. The laser utilises frequency-doubled 1560 nm telecommunications fibre seed lasers. This light is transferred to the sensor head using a flexible umbilical cord, which means that the sensor head can be moved while the laser and control package remain stationary. The laser system was designed by Andrew Lamb and built by the author alongside him.

- **Control package**, composed of a personal computer (PC) and the Advanced Real-Time Infrastructure for Quantum physics (ARTIQ) system. This package is used to control the experimental sequence. Data collected at the end of the experiment is collected by the National Instruments Data Acquisition system (NI-DAQ), which can be transferred back to the PC via the umbilical cord.

- **Peripherals** to help with performing of the experiments, including linear rail, accelerometer and tiltmeter. These will be discussed in chapter 6 as appropriate.

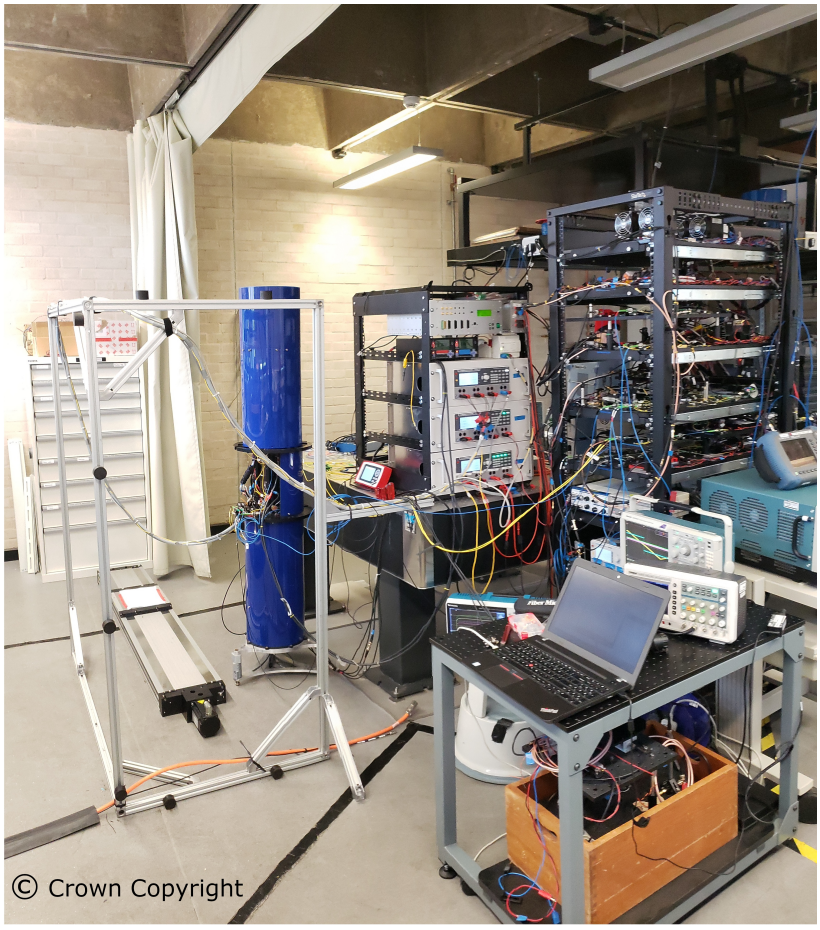


Figure 3.1: Gravity gradiometer at the University of Birmingham that was built and utilised as part of this work.

3.1 Sensor Head

The sensor head was built prior to this work by past members of the group, including one of the author's supervisors, Andrew Lamb. This section will summarise the important parts of this system, with more information to be found in [112].

The sensor head is composed of two independent gravimeters, with the cross-section of one of these seen in Figure 3.2 (adapted from [112]), placed one above the other in a gradiometer configuration. This can function as a gravimeter by itself; using two of these in combination produces a gravity gradiometer. They are mounted separately in a rigid structure that allows them to be coupled together by the light. The structural geometry can be modified with small changes to the system, for example allowing for a change in baseline, total sensor height as well as enabling atom launch that takes advantage of the full chamber length. However, neither of these capabilities have been utilised during this PhD. The sensor head has been left in its default state, with a height of 175 cm and an outer diameter of ∼30 cm (with weight just under 50 kg) [112].

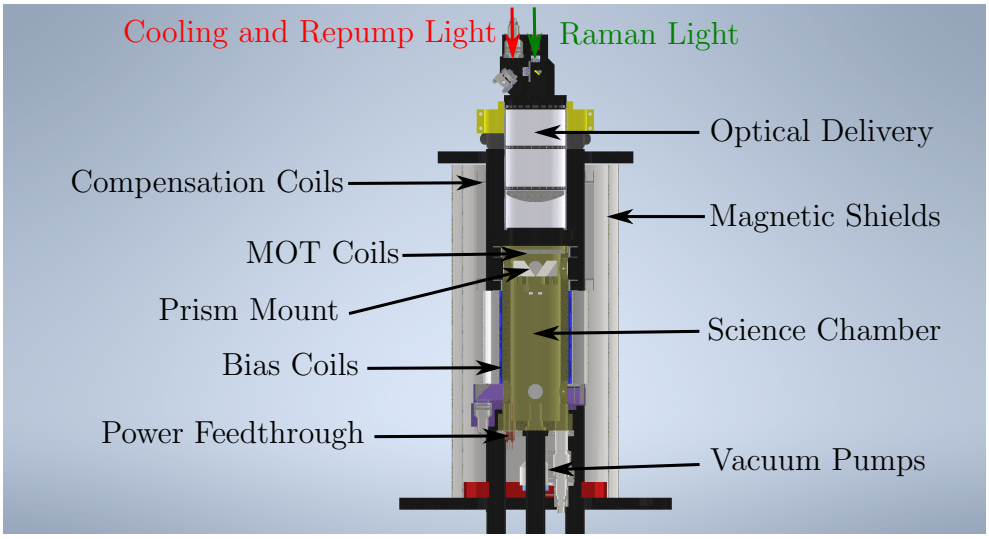


Figure 3.2: CAD diagram of the top gravimeter.

3.1.1 Vacuum Science Chamber

A science chamber is a container which can hold atoms inside of a vacuum, isolating them from as much of the external environment as possible. This helps us to cool the atoms down and to perform interferometry because these atoms do not collide with hot atmospheric gas (or other unwanted material), enabling them to maintain coherence during the free-fall. A simplistic diagram of both of the science chambers can be seen in Figure 3.3, which has been adapted from [112]. Both of these are largely the same apart from the positions of the prisms [112].

A four-pin power feedthrough supplies current to the in-vacuum rubidium dispensers from SAES group [113]. Dispensers are small rods that keep the alkali metal pure in the form of a stable salt. Upon heating of these rods, this salt is turned into Rb atoms. Appendix D describes the cleaning procedure required to clean the barrell connectors used to mount the dispensers inside of the chamber. The vacuum environment is maintained by two components. Firstly, the ion pumps in both chambers are used to help maintain the vacuum by pumping out the noble gases (e.g. Helium). Due to the fact that these pumps contain a strong permanent magnet, they are placed as far away from the atoms as possible. Secondly, a getter is also present to pump out any other material not addressed by the ion pumps.

The vacuum also houses prisms mounted inside of it; this is to enable the cooling light to be reflected along all three axes to create the six beam configuration required for the creation of the MOT. Special grooves inside of the chamber were made to glue the prism mounts to the wall, helping to position the prisms inside of the chambers. The sensor head also contains ten windows; these were included to allow for monitoring of the atoms as well as the delivery of the light. The windows have been fixed to chamber using a soft metal indium seal, which allows the windows to be attached to the chamber

without sticking out from the surface, helping to maintain the cylindrical form factor of the sensor head [112].

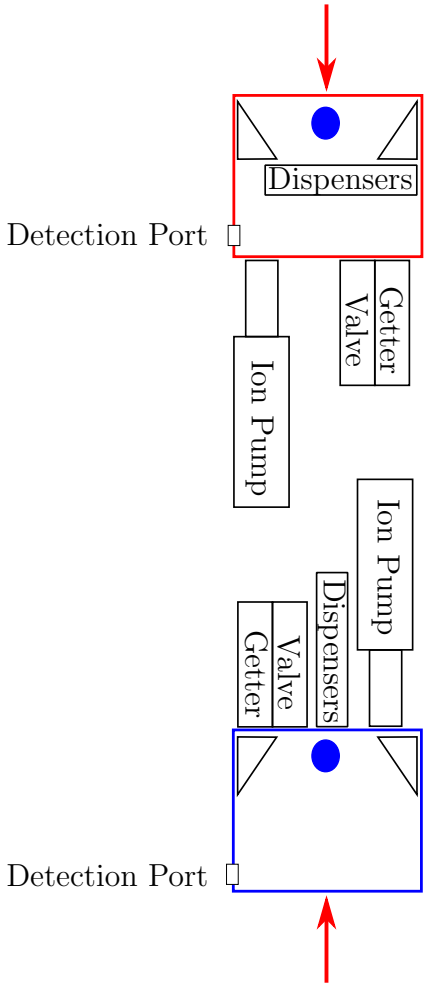


Figure 3.3: Illustration of both of the vacuum chambers of the gradiometer.

The preparation of the vacuum needs to be done with a high degree of cleaning, ensuring that any unwanted material is removed. If this is not done properly, this could result in an increase in pressure, limiting the performance of the system due to collisions between the Rb atoms and unwanted material. Once cleaned, the system is heated while attached to an external vacuum pump, referred to as baking, to remove water as well as any residual gas. More details about the steps taken to perform the cleaning required during the build of the sensor head can be seen in [112].

3.1.2 Magnetic Field Control

Due to the numerous effects of the magnetic fields highlighted in chapter 2, the magnetic environment that the atoms are placed in needs to be carefully controlled. This is the case for both cooling and interferometry. To provide passive magnetic shielding from external fields, magnetic shields surround both of the chambers. Firstly, a double-layered magnetic shield over the full length of each of the gravimeters is present to help with both cooling and interferometry. In addition, a second double-layered shield encompassing the interferometry region is also included, further limiting the external fields during the interferometry (these are placed within the aforementioned shields). A number of coils are also present. Firstly, the MOT coils create a position-dependent magnetic field needed for the MOT. Secondly, the bias coils provide a uniform field that defines a quantisation axis for the Raman transitions to ensure that we can precisely manipulate the m_F states. Lastly, a set of compensation coils have also been added to deal with any systematics that cause the atomic cloud to be off-centre in the MOT region [112].

3.1.2.1 Magnetic Shields

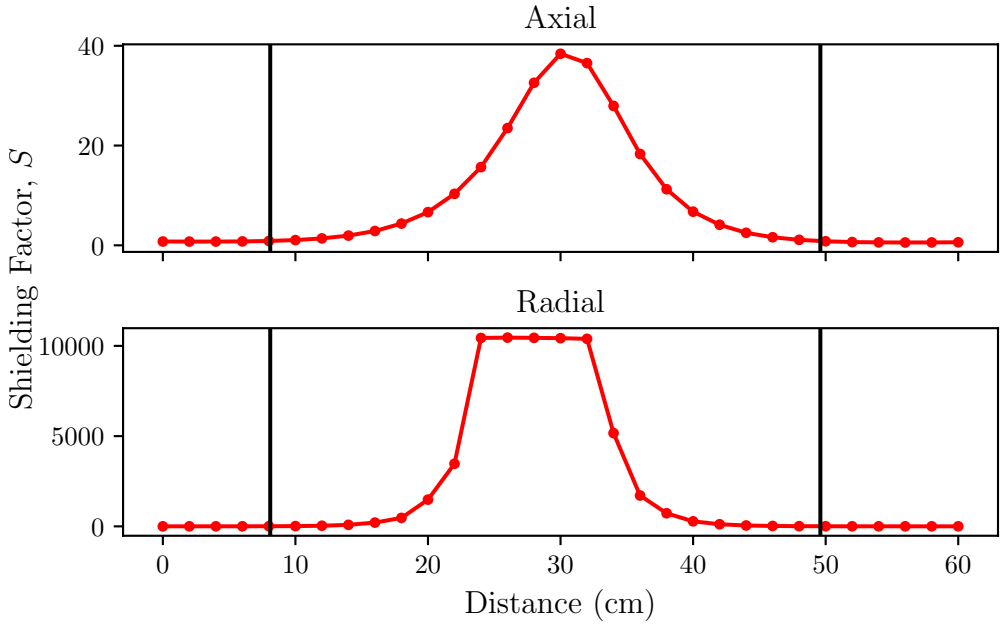
In order to isolate the system (and hence atoms) from the external environment, the vacuum science chambers are enclosed within a pair of double-layered MuMetal shields [114]. This is the most widely used alloy for magnetic shielding purposes. Its composition of 80% nickel, 4.5 % molybdenum and varying composition of iron gives the material a high susceptibility to magnetic field, accepting the flow of magnetic field easily. It is possible to take advantage of this property by redirecting the field away from the experimental area. Building a hollow structure from MuMetal sheet that encompasses the experimental area creates a region that is relatively unaffected by

external magnetic fields as they are directed to the shield, leaving experimental area without any external field [114].

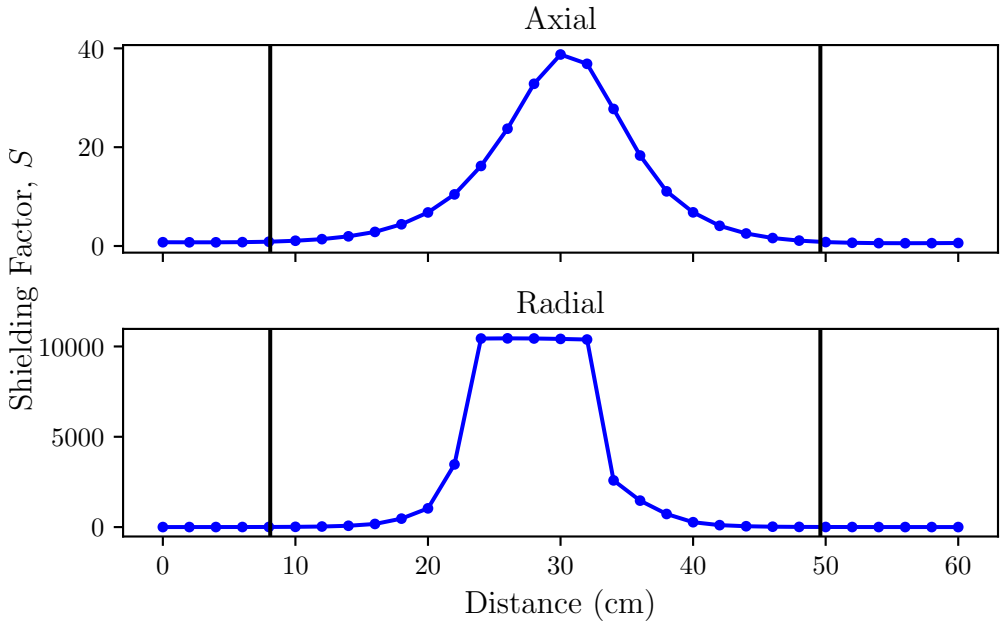
This experiment uses open-ended cylinder-shaped magnetic shields; meaning that the shielding along the shield's central axis is significantly lower than along the radial axes [112]. The magnetic shielding factor, S, is a measure of this shielding, which was investigated for the outer shields to ensure that they were providing significant shielding, especially along the axial direction. To do this, a setup for creating a Helmholtz field was created. This is achieved by using a pair of coils with currents in the same direction. Square coils were used for this purpose, with the optimum spacing for maximum field calculated using [115]. The shields/coils combination was oriented in such a way as to have the largest magnetic field along the axis of investigation. A limit of the testing was the safe operation due to the current limits of the wires - the upper limit of these was 3.5 A. The shielding factor can be calculated by adapting the equation from [116]:

$$S = \frac{B_{\text{without shields \& with coils}} - B_{\text{without shields \& without coils}}}{B_{\text{with shields \& with coils}} - B_{\text{with shields \& without coils}}}, \tag{3.1}$$

where $B_{\text{without shields \& without coils}}$ and $B_{\text{with shields \& without coils}}$ act as the background measurements. The results of this testing (with the measurements done with Stefan Mayer Instruments Fluxmaster [117]) can be seen in Figure 3.4. The black vertical lines represent the boundaries of the shields. The plateau in the radial directions is due to the fact that all of the magnetic field applied by the coils had been attenuated by the shields, producing a value of 0.00 μT. This was changed to 0.01 μT (smallest resolution of the magnetometer) to avoid infinities. In the axial direction, along the axis of the open ended cylinder, the shielding factors in this central region reached 38.4 ± 0.3 and 38.8 ± 0.3 for the top and bottom shields, respectively.



(a)



(b)

Figure 3.4: Magnetic shielding factors for the **(a)** top and **(b)** bottom outer magnetic shields.

3.1.2.2 MOT Coils

MOT coils create the required MOT field. This is essentially a magnetic field with a linear gradient. This field is zero at the central point, with opposite directions either side of this central point. The MOT coils are placed on separate mounts that allow them to be attached or detached from the system as well as allowing easier winding than on the chamber itself. The required field is generated using one pair of coils in quadrupole configuration, to provide a gradient magnetic field. Each coil has an inner diameter of 90 mm, outer diameter of 106 mm and there are 75 turns per coil. The resulting magnetic field can be modelled using the Biot-Savart law [118]. The model of these coils had been created and verified experimentally in previous work in [112]. The resulting linear gradient in the central region was found to be $\sim$3.9 G/(cmA).

3.1.2.3 Bias Coils

As has been mentioned, interferometry requires a bias field to define the quantisation axis and to break the m_F degeneracy. The breaking of the m_F degeneracy means that it is possible to perform experiments using the $m_F = 0$ sub-states of $|5^2S_{1/2}, F = 1\rangle$ and $|5^2S_{1/2}, F = 2\rangle$, eliminating any first-order Zeeman effects on the final interferometer output. The remaining magnetic field effect will only be the quadratic Zeeman effect (or effects arising from the distant wings of the other sub-states).

The bias field in our instrument is created using a single-layered, 18-turn solenoid. This is placed inside all of the magnetic shields and creates the bias field along the axial direction (along the direction of the open ends of the magnetic shields). As it is placed inside all of these shields, it has to be compact but also needs to create the required magnetic field within the interferometry region, with minimal spatial variations. This has been achieved by manufacturing a solenoid with a high number of turns at the edge

and a decreased number of turns in the centre. This should enable the field to reach the desired strength within 1 cm of the edge and stay uniform in the central region [112].

The simulated bias field using the Biot-Savart law with a current of 200 mA can be seen in [112]. The simulated field shows good uniformity over the interferometry region. This field profile had been verified experimentally in [112] and a field uniformity of $<0.2\%$ over the central shielded region had been observed. The actual magnetic profile as measured by atoms will be discussed in section 6.1.4.

3.1.2.4 Compensation Coils

The sensor head has been upgraded with new compensation coils to be able to compensate for any of the remaining external magnetic fields that might remain in the MOT region. There are three pairs of coils along each of the principal axes. They have a rectangular shape, with the shorter side of $\sim$73 mm, longer side of $\sim$120 mm and a thickness of 12 mm. Each pair of coils are $\sim$132 cm apart and have 91 turns each. These were designed to provide the best fields within the space available.

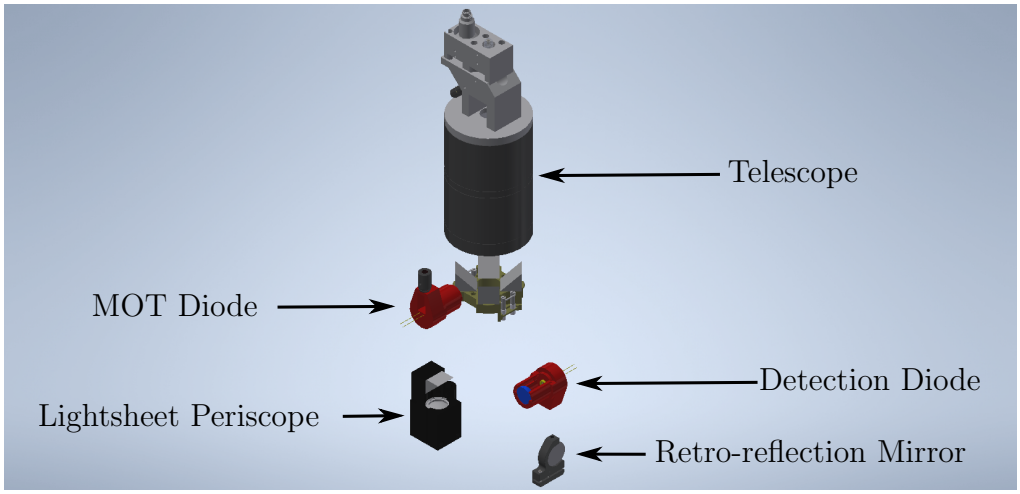
3.1.3 Optical Delivery

Laser light needed to interact with the atoms in the vacuum chamber is delivered via the umbilical cord. An optical delivery system allows us to couple the Raman and cooling/repump lights into the chamber. The system is designed to deliver the light along the chamber's common central axis vertically, with the light being input from both the top and bottom chambers as previous work using this sensor head has found that better performance is obtained by not using a retro-reflection mirror in the middle [112].

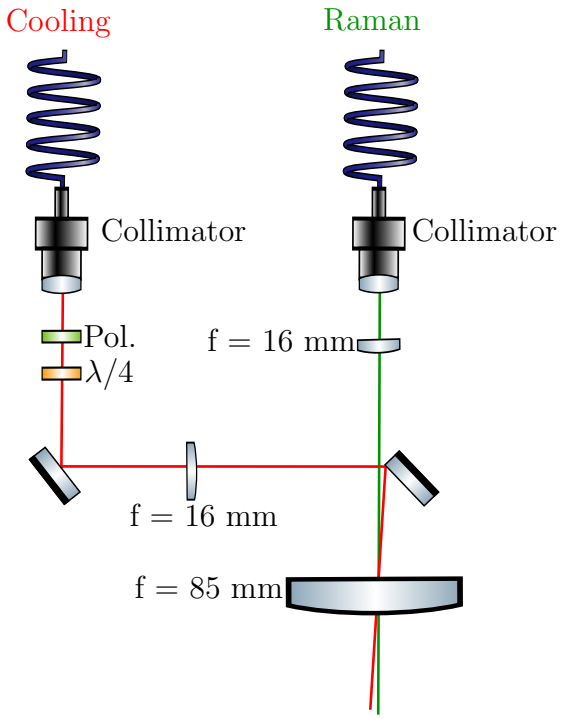
The optical delivery is shown in Figure 3.5(a), which is adapted from [112]. The

top part of the diagram is the telescope that enables us to couple the cooling/repump and Raman lights from a fibre to create a collimated beam that can be fed into the chamber. The prism mount along with the two input telescopes create the six beam configuration needed for MOT; the MOT can be monitored with the MOT photodiode (e.g. loading curves). Some distance further down the chamber is the detection region, which contains the detection photodiode to image the cloud using fluorescence as well as a lightsheet periscope and mirror to obtain time of flight (i.e. temperature) measurements. These temperature measurements can once again be imaged with the detection photodiode [112]. An optical switch in the laser system delivers the bottom cooling light to either the bottom telescope, or top and bottom lightsheet periscopes, as required. This diagram shows the optical delivery for the top chamber, with the bottom chamber being largely similar apart from the telescope position and orientation, which would sit at the bottom and face upwards.

The schematic diagram of the telescope itself can be seen in Figure 3.5(b), once again adapted from [112]. The light from the laser system is delivered via an umbilical cord into polarising fibres to eliminate polarisation noise. These polarising fibres are then used to couple the light into the telescope. One of these fibres is used for the cooling/repump light and is fed into the cooling collimator. This has an output beam size of $\sim$19 mm. Once outside of the collimator, the light passes through a polariser and a quarter waveplate to allow us to control the polarisation of the cooling light. This beam is then reflected from a 0.5" mirror. This mirror is mounted to a kinematic mount and is actually the primary way to control the alignment of the cooling beam into the chamber. This beam then passes through another lens and is incident on a *D*-mirror. It is important to ensure that the focus of this beam is along the edge of the *D*-mirror to ensure that it reflects correctly into the chamber. Upon this reflection, the beam passes through a 3" collimating lens, finally producing a beam with a $1/e^2$



(a)



(b)

Figure 3.5: **(a)** The full optical delivery for the top chamber. **(b)** Schematic diagram of the top chamber telescope, with all the relevant components annotated.

diameter of ∼53 mm that is incident on the atoms. The other polarising fibre is coupled into the Raman arm, which is a bit simpler than the cooling arm. The light enters

the Raman collimator and exits with $1/e^2$ diameter of $\sim$7 mm. Upon passing through a lens, the beam is focused near the edge of the D-mirror. The beam should be as close to edge of this mirror as possible to ensure that minimal angle offset between the Raman and cooling beams is present. Upon passing through the same 3" collimating lens as the cooling beam, this beam exits with a $1/e^2$ diameter of $\sim$20 mm into the chamber [112]. Both the top and the bottom telescopes operate in exactly the same way.

A part of the work done as part of this PhD involved the investigation of implementing phase shear readout technique that can obtain the interferometer contrast and phase in one experimental shot. This technique will be explained more fully in chapter 4 but it requires a Raman beam that can be tilted, which this telescope design could not deliver. Therefore, this telescope had to be upgraded for the top chamber but this was not done for the bottom chamber, with this design still being applicable for the latter. The top chamber telescope upgrade will be discussed in chapter 6.

3.2 Laser System

The optical part of the laser system utilises a two-seed design, with the Raman laser seed being used to drive the stimulated Raman transitions and the cooling laser seed used for laser cooling and trapping. These seeds are the commercially-available 1560 nm telecommunication laser seeds from NKT Photonics [119], showing the ability to build these instruments using existing technology. The Raman laser seed is locked to a ^{85}Rb transition via modulation transfer spectroscopy (MTS), the mechanics of which are beyond the scope of this thesis but can be seen in [120]. The cooling seed is slaved to the Raman laser via an offset lock. Lastly, the repump laser is locked to the cooling light that allows it to stay on resonance whilst the cooling light is scanned during

molasses. The laser utilises four optical arms that allow independent intensity control of each of the arms. The RF system is used to provide the necessary frequencies at the required powers for the optical components.

The next few sections describe the various parts of this laser system. Throughout these, diagrams are used to illustrate the setup. Different colours are used within these to easily distinguish between the different components - the colours of components are arbitrarily chosen. The colours of the arrows do have a meaning - a black arrow signifies 1560 nm connection, a red arrow signifies 780 nm connection and a blue arrow signifies an RF signal. The following abbreviations for the optical components will be used throughout: Acousto-Optical Modulator (AOM), Beam Splitter (BS), Electro-Optical Modulator (EOM), Erbium-Doped Fiber Amplifier (EDFA), and Second-Harmonic Generator (SHG), also referred to as a frequency doubler.

3.2.1 Optical System

The full optical laser system schematic can be seen in Figure 3.6, where the original component numbering has been retained for historical reasons. The Raman laser is a single seed locked to the ^{85}Rb D_2 $|F = 3\rangle \rightarrow |F' = 4\rangle$ transition (384,229,241,690,064 Hz) via sideband lock and using MTS, making the Raman laser the master of this setup. The exact frequency of the Raman light is controlled using the sideband generated by EOM 1. As the locking transition is higher than the desired frequency in ^{87}Rb, the MTS is locked to the higher sideband so that the Raman is red detuned from the desired transition. To make this sideband sufficiently large, EOM 1 is purposefully over-driven to suppress the carrier and to maximise the sidebands. EDFA 5 ensures that there is a sufficient optical power to seed both of the lasers and controls the amount of light into the spectroscopy cell as not to saturate the transition.

Two arms deliver the Raman light to the top and bottom chambers. Each of these

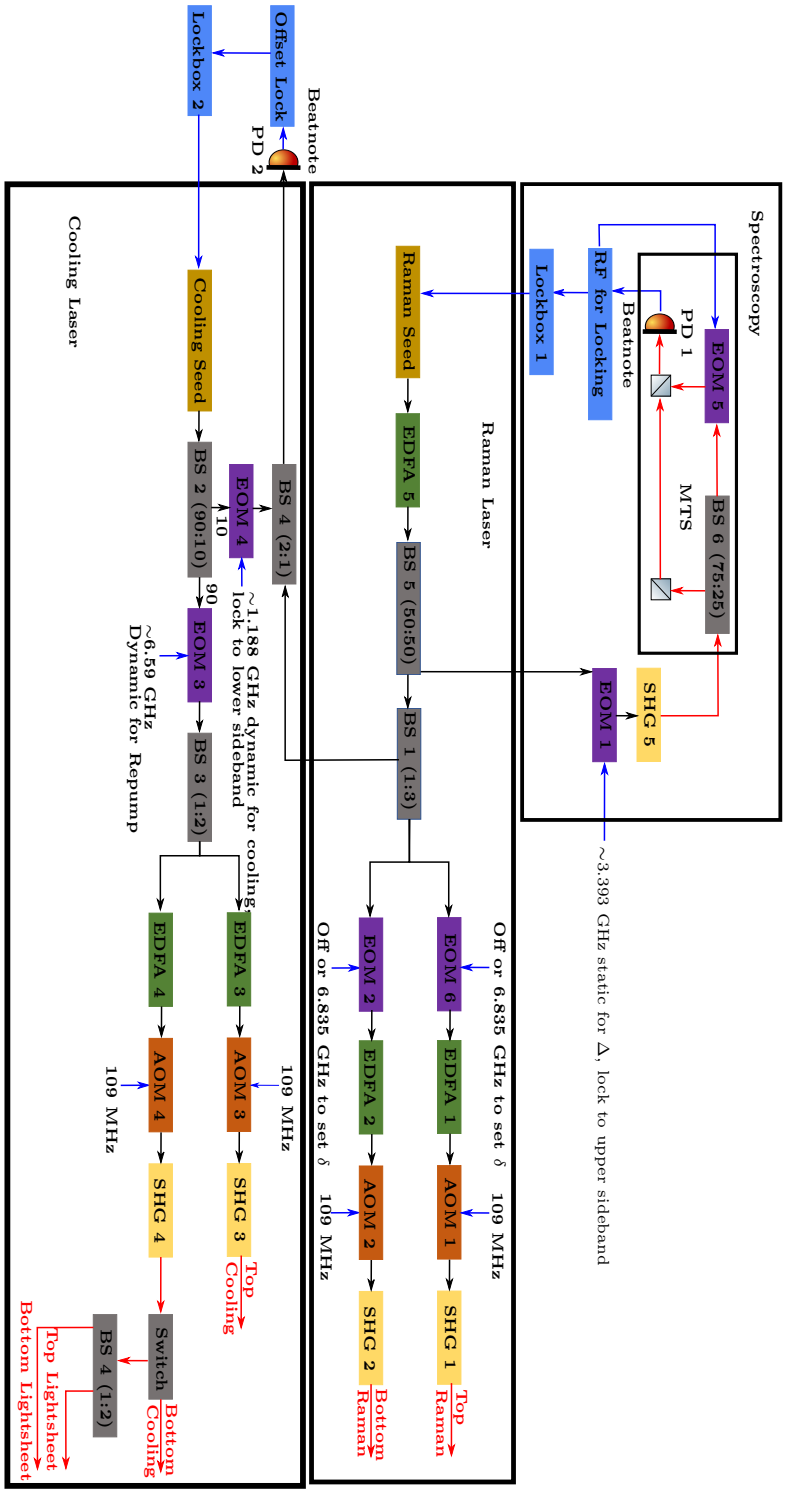


Figure 3.6: Schematic diagram of the optical part of the laser system.

arms is composed of an EOM, EDFA, AOM and SHG. The EOMs on both arms can be used to create the sideband to be able to perform the stimulated Raman transitions. This is done by creating a sideband at ∼6.835 GHz, which is the same as the hyperfine separation between $|F = 1\rangle$ and $|F = 2\rangle$ in ^{87}Rb. The addition of EOMs on both of the arms allows the system to perform k_{eff}-reversal. In order to avoid parasitic Raman transitions, only one of the two EOMs (EOM 2 or 6) is driven at any one time. The use of two EOMs also allows upgrades for the future, e.g. phase locking between arms or fringe reconstruction techniques. The two arms contain two independent AOMs in both of the Raman arms, allowing full intensity control over both of the Raman arms as well as fast switching of the laser output. The frequencies of these AOMs were optimised for maximum power, which was found to be 109 MHz. The arms are finished off with the SHGs, enabling us to double the frequency from 1560 nm to 780 nm, which is required for the D_2 line of ^{87}Rb. As explained before, a significant single-photon detuning, Δ, of the Raman is desirable to suppress spontaneous transitions, which given our setup is ∼2 GHz from the $|F = 2\rangle \rightarrow |F' = 3\rangle$ transition.

The cooling light is slaved to the Raman master via an offset lock and is controlled by locking to an optical sideband, in this case the lower sideband. A small percentage of the cooling seed (∼10%) is taken out to be used for locking. The offset lock uses a beatnote between the Raman and cooling lights (∼171.2 MHz) to lock the cooling light to the Raman master. It uses a comparator board that utilises a side of filter lock, in line with [121]. The approach uses the overlap and offset between two asymmetrically attenuated and filtered arms of the same signal to generate an error signal. This is then fed onto Lockbox 2, which in turn feeds onto the cooling seed to keep the cooling light slaved to the Raman light.

The majority of the power (∼90%) is used in the laser cooling arms. EOM 3 is present prior to the splitting of the light into the two cooling arms with ∼6.59 GHz

applied onto EOM 3 with RF adjusted to obtain carrier/sideband ratio of roughly 10:1, which is achieved with RF power into EOM 3 of ∼5 - 6 dBm. This creates the repump light using the $|F = 1\rangle \rightarrow |F' = 2\rangle$ transition. The advantage of this setup is the fact that the repump light is dynamic as well, therefore when the cooling seed is ramped, as is for example the case in molasses, the repump light stays on resonance.

Following this repump creation, the light is split up into two cooling arms, similar to the Raman laser. These two arms deliver the cooling light to the top and bottom chambers, with the static MOT detuning of ∼15 MHz. Each of the arms is composed of EDFA, AOM and SHG; with the AOMs being optimised for maximum power output at 109 MHz. One additional step in this setup is the addition of the optical switch in the bottom arm. This allows us to switch between either all light going into the bottom cooling, or delivering 50% into the top lightsheet periscope and 50% into the bottom lightsheet periscope for time of flight measurements to measure temperature. This switch is a mechanical switch, meaning that the time taken to switch between the channels should be kept in mind; this is on the order of a few ms with asymmetric behaviour when switching in different channel directions.

Prior to committing to this final design, an investigation of two areas of this laser design was carried out. The first was the response of SHG 5 with low input powers. The second investigation involved the use of the 1560 nm AOMs as opposed to the 780 nm alternatives, which is the common mode of operation within our group. More on this can be seen in Appendix E.

3.2.2 RF System

The RF system is designed to provide the driving frequencies at the required powers for all optical components, with the dynamic capability required for both the cooling and the Raman frequencies. The design has kept as much as possible of the design

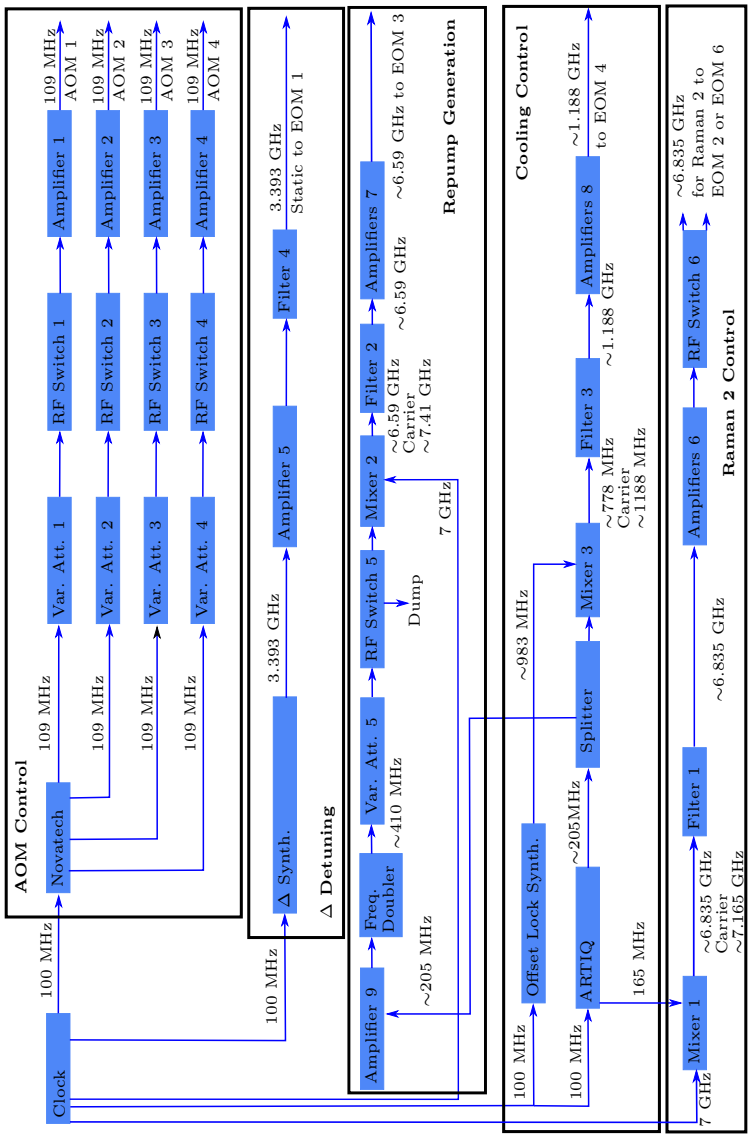


Figure 3.7: Schematic diagram of the RF part of the laser system.

either passive or slaved to appropriate sources, e.g. the single photon detuning is static and the repump is slaved to the cooling such that the frequency scans in the opposite direction. The full RF system required can be seen in Figure 3.7, where numbering of some components has been retained due to historical reasons.

The frequency generation components (Novatech, synthesiser boards ("Synth.") and the ARTIQ) all require a stable 100 MHz external reference. This is provided by

the clock using splitters (and an amplifier). These are not pictured in Figure 3.7 for simplicity. The 7 GHz output of the clock has been used to create the required frequencies for the repump and Raman 2, as will be explained in the next few paragraphs.

All the AOMs within the setup require independent RF sources. Novatech was used as the static frequency source due to its convenience. Independent source and arm for each of the AOMs means that there is independent control of the top and bottom Raman AOMs, and top and bottom cooling AOMs. The addition of the variable attenuators in these arms also allows independent control of the power output of all of these arms. Future modifications are also available - one obvious one is the possibility of the launch capability, which could be implemented by replacing the Novatech with a dynamic frequency synthesiser, such as another ARTIQ port.

As the single photon detuning can remain static during the sequence, a single synthesiser and amplifier is required to provide the 3.393 GHz EOM driving frequency. This allows for sideband locking to the ^{85}Rb D_2 line to generate Raman light with $\sim$2 GHz detuning out of the two Raman arms. Detuning limits are placed on the setup by the operational bandwidth of the components used; however, these can be replaced.

One ARTIQ port provides RF signal at $\sim$165 MHz, which when mixed with the 7 GHz reference from the system clock, generates a controllable frequency at $\sim$6.835 GHz for Raman 2. Filter 1 is a cavity band pass filter with an incredibly narrow pass band with a high attenuation. ARTIQ allows for control of the size of the Raman sideband and allows for optimisation for any differences between the Raman EOMs (EOM 2 and EOM 6). Three amplifiers 6 are used to generate frequency at the required power. RF switch 6 is connected to both EOM 2 and EOM 6 and allows either the top or bottom Raman arm to become Raman 2.

The offset lock needs to account for the detuning between the Raman and cooling transitions; this value can be changed by modifying the output of Offset Lock Synth.

(with default at ∼983 MHz). The frequency of ARTIQ at ∼205 MHz should stay constant for steady state. These frequencies are mixed, filtered and amplified (using two amplifiers) to generate a signal at ∼1.188 GHz for EOM 4. Similarly to the Raman detuning, the possible values of MOT detuning are limited by the bandwidths of the components used although this is not such a big issue here as this tends to be relatively close to resonance.

The ∼205 MHz signal is also used in the repump generation. Upon splitting this signal, it is amplified followed by passing through a frequency doubler. Variable attenuator 5 is used to control the power for optimisation of molasses and detection schemes. If the sideband is not needed on the cooling light, as is the case towards the end of the molasses sequence, RF switch 5 allows for complete removal of the sideband within a few ns. Mixer 2 mixes this signal with clock 7 GHz output. As the beatnote is proportional to the sum of the two input frequencies, variable attenuator 5 provides power control of the RF output by modifying the power of the dominant low frequency arm. Upon mixing and filtering (using a cavity bandpass), a clean signal is obtained, which is amplified with Amplifiers 7 (two amplifiers). The result is a clean signal at ∼6.59 GHz with ∼17 dBm of controllable power into EOM 3. Mixing the dynamic cooling frequency in this manner means that as the cooling light frequency scans up (down), the repump frequency will decrease (increase), allowing the light to stay resonant with the repump transition without having to scan the repump light frequency independently.

3.2.3 Physical Layout

The whole laser system is built onto separate breadboards and placed into a standard 19" server rack, which can be seen in Figure 3.1. This provides the system with two advantages. Firstly, it allows some flexibility in the placement of this system - either

within the lab or if moving it outside of the lab. Secondly, the server rack allows for better cooling with airflow as the breadboards are far apart (about 20 cm) and so little heat is trapped, meaning that components stay relatively cool. If more airflow is needed in the future, or if more modules are added, a bigger server rack could be obtained. Since the different parts of the laser system are on separate breadboards, the system could be placed into a different server rack by moving the entire breadboards while not having to worry about re-arranging individual components.

The physical layout has as little connections as possible between levels, therefore keeping the individual sub-systems together as much as possible. The RF and optical components are mainly kept separate. In the case of Raman 2 control, the RF was placed as close to the EOMs as possible to reduce the loss of the high frequency $\sim$6.8 GHz through the cables. Different levels are joined by connections that go outside of the server rack and are secured in place with cable ties. Optical and RF outputs go out from the front of the rack while power cables go out from the back. The power supplies are placed at the bottom of the rack to keep them as far away from the rest of the components as not to heat them up. The PC and the control package are also placed towards the bottom of the server rack.

3.3 Control Package

The whole experimental setup is controlled using PC and the commercially-available control package ARTIQ (Advanced Real-Time Infrastructure for Quantum physics) manufactured by M-Labs [122]. The ARTIQ used in this setup is shown in Figure 3.8. ARTIQ is a leading-edge control system for quantum information experiments. It is now used and supported by a growing number of research institutions worldwide, mainly within the atomic physics community [122].

Within our institution, and specifically within our research group, this experiment is one of the earliest adopters of ARTIQ. Therefore, a large part of the build of this instrument was the build of the infrastructure to control the experiment using ARTIQ, including the creation and setup of the software as well as characterising the functions of the various components that make up the ARTIQ system. While ARTIQ is composed of components that can be purchased separately, its selling point is that it creates the underlying infrastructure to communicate with all of these components using an integrated Python software package. Our software builds on this underlying infrastructure to create a bespoke experimental sequence code. However, the ARTIQ software source code has been modified at the source level to be able to integrate it easily with the existing software within our group, increasing the rate of progress.

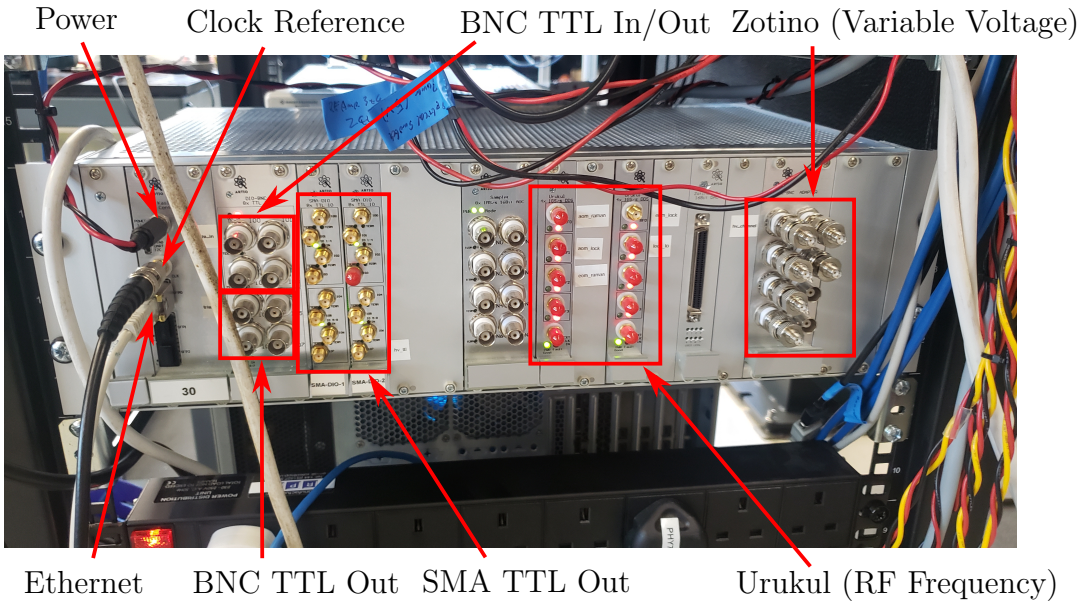


Figure 3.8: ARTIQ control package used in our setup, with the parts used in our experimental sequence annotated.

ARTIQ is externally powered via a standard UK socket. Connection between the ARTIQ and a PC is provided by an ethernet cable and the PC has to have a fixed Internet protocol (IP) address on the same network as ARTIQ. Lastly, it also requires

an external clock input of 100 MHz at ∼0 - 10 dBm as a reference. The main control chip of the ARTIQ that connects to the other boards is called Kasli. This is a field-programmable gate array-based (FPGA-based) hardware designed for ARTIQ as part of the Sinara family of boards [123]. The rest of the components can be chosen in line with the experimental requirements when ordering the system from M-Labs. The characterisations of ARTIQ performed can be seen in Appendix F. We will only discuss the final results.

The ARTIQ module used in this instrument contains four Bayonet Neill–Concelman (BNC) input/output transistor-transistor logic connections (TTLs). These can be configured to be either "IN" or "OUT". By default, these four TTLs are configured to be "IN" - changing them to be "OUT" is possible but would require some hardware changes. As this capability was not required, these have been left unused for now. In addition to the four TTLs mentioned, there are also four BNC TTL outputs. These are specifically output channels and hence do not require any hardware changes. These four channels were used to switch on and off the dispensers and the MOT coils during the experimental sequence. Lastly, there are also 16 SubMiniature version A (SMA) TTL outputs. These were used to trigger various parts of our laser, such as RF switches, data collection triggers, etc. The triggering of these was found to be fast enough with the only issue noted that the voltages reach ∼3 V (reaching ∼4 V on the order of a few ms), which is not always enough for all devices, although it has been found to be sufficient for our components.

This ARTIQ also includes Zotino (model: AD5372BCPZ), which is a 32 channel, 16-bit digital-to-analog converter (DAC) with eight analogue channel outputs able to provide voltages up to ±10 V [124]. The time taken to reach the desired voltage is not instant but it is short given our experimental timeframes, with the full timing depending on the desired voltage. There are two things to note with the Zotino. Firstly,

while the data specifications for Zotino say that the range of output voltages is ±10 V [124], in actuality setting the value of the Zotino to +10 V produces negative voltages. Therefore, a voltage of +9.9 V was used as the maximum output possible from the Zotino. Secondly, an issue was identified when connecting the Zotino to standard Mini-Circuits RF variable attenuators - a significant voltage drop was observed when the Zotino output was connected to these RF components and a non-zero voltage was programmed. This is thought to be a consequence of impedance mismatch - the impedance of Zotino is 470 Ω [124]. For example, programming one of the Zotino channels to have 0 V output produced an actual voltage out of the socket of -0.008 V, and when connected to the variable attenuator, a voltage of -0.004 V was measured. Setting the channel output to +9.9 V, actual voltage out of the socket was measured as +9.89 V, but this dropped to +5.930 V once connected to the variable attenuator. As a result, for the time-being, RF variable attenuators 1 and 2 are controlled with standard power supplies and only variable attenuators 3, 4 and 5 are controlled by ARTIQ. A possible upgrade in the future would be the inclusion of voltage amplifiers. The second use of the Zotino is to perform power ramps for molasses, as will be explained in section 3.4.2. A characterisation of the voltage ramps using ARTIQ showed smooth ramps in the required times.

Lastly, our ARTIQ has the ability to generate RF frequencies using its own synthesiser board Urukul. This board utilises either the AD9910 or AD9912 synthesiser boards. Our ARTIQ uses the former of these boards and has 10 RF output channels able to provide frequencies of up to 400 MHz [125]. This meant that ARTIQ was chosen as the low frequency generation source in the RF. This has simplified the work as it has meant that no bespoke code needed to be programmed to be able to integrate individual boards with the experimental sequence, which has accelerated the development progress. Characterisation of this frequency generation showed that a clean spectrum

could be obtained, with a stable frequency output. Similarly to the variable voltages, frequency ramps are also needed for the molasses sequence. While Urukul should have the capability to perform frequency ramps with internal commands, this was found to not work. Therefore, bespoke code for frequency ramps was created and characterised. Frequency ramps lasting over ∼14 hours were analysed and showed good stability of frequency outputs for the entirety of the run.

3.4 Cold Atoms

The cold atoms preparation consists of three main steps:

1. MOT creation,
2. optical molasses, and
3. state preparation.

The first step involves heating up the dispensers to expel the ^{87}Rb atoms into the vacuum chamber. Applying a quadrupole magnetic field - by applying a current across the MOT coils placed in quadrupole configuration - as well as applying counter-propagating cooling beams using the prisms - cools the atoms down to hundreds of μK. Once a cloud of these cool atoms is produced, the magnetic coils are switched off, making the sub-Doppler cooling mechanisms the dominating effect. This mechanism can reduce the temperatures even lower, to a few μK in practice. The state preparation is completed by preparing the majority of the atoms in the $|F = 1\rangle$ state and blowing away the remaining $|F = 2\rangle$ atoms. This ensures that all of the starting atoms are in the clean $|F = 1\rangle$ state.

3.4.1 MOT

A MOT loading curve can be used to estimate the Rb atom number and the MOT loading rate. This measurement is done by switching on the MOT and recording the corresponding signal using the MOT photodiode. The voltage measured by the photodiode can be converted into atom number using [44, 126]:

$$N = \frac{V}{eR_{\text{scat}}\Omega_{\text{angle}}QG}, \tag{3.2}$$

where V is the photodiode voltage, e is the electron charge, R_{scat} is the photon scattering rate, Ω_{angle} is the fractional solid angle, Q is the quantum efficiency of the photodiode and G is the gain resistance [126]. Our MOT photodiodes are standard Thorlabs FDS100 photodiodes with home-built circuits. For this setup, $G = 1{\times}10^7\ \Omega$ and $Q \sim 0.50$ [127]. The fractional solid angle can be estimated as:

$$\Omega_{\text{angle}} = \frac{r^2_{\text{aperture}}}{4 \cdot d^2}, \tag{3.3}$$

where for our system $r_{\text{aperture}} = 8.6$ mm from window clear aperture and $d = 35.293$ mm, which is the distance from the centre of the chamber to the window/aperture. Using these estimates, $\Omega_{\text{angle}} \simeq 0.015$ in our case. The scattering rate, R_{scat}, is given by [14, 126]:

$$R_{\text{scat}} = \frac{\Gamma}{2}\frac{s}{(1 + s + (\frac{2\delta}{\Gamma})^2)}, \tag{3.4}$$

where Γ is the natural linewidth of the transition, which in the case of our cooling transition is $\Gamma = 2\pi \times 6.066$ MHz [126]. s is the saturation parameter and is given by I/I_{sat}, where I_{sat} is the saturation intensity of the transition (1.67 mWcm^{-2} for ^{87}Rb [126]) and δ is the detuning from the cooling transition. For our measurements, I has

been estimated as 15.9 mWcm^{-2} (estimated by measuring the power/intensity of the two beams in the middle of the sensor head and multiplying by 3 for the three axes) and hence $s = 9.52$ with $\delta = 2\pi\times15$ MHz. The loading curve can then be fit using [14]:

$$N(t) = R_{\mathrm{MOT}}\tau_{\mathrm{load}}\left[1 - \exp\left(\frac{-(t-t_0)}{\tau_{\mathrm{load}}}\right)\right] + y_0, \tag{3.5}$$

where R_{MOT} is the MOT loading rate, τ_{load} is the MOT loading time, t_0 is the time the loading started and y_0 is to account for background light levels. The equilibrium atom number, N_{eq}, can be calculated using $N_{\mathrm{eq}} = R_{\mathrm{MOT}}\tau_{\mathrm{load}}$.

A fitted loading curve can be seen in Figure 3.9, which is indicative of the atom number possible in both of the chambers at best performance. From the fit, we are able to estimate $N_{\mathrm{eq}} \simeq 1.7 \times 10^9$ atoms with a loading time constant of 3.6 s. This should not be taken as the normal operation atom number of our chambers. Firstly, it is an estimate and the object distance could be different to the estimated one. Secondly, these measurements were taken just after the dispenser currents were increased. Lastly, the MOT is usually not loaded for the calculated loading time, and hence this atom number would usually not be reached. What is obvious though is that a good atom number is possible in our chambers, more than sufficient for interferometry.

3.4.2 Optical Molasses (and State Preparation)

The next step in cooling the atoms is to cool them even further using optical molasses, followed by preparation in the $|F = 1\rangle$ state. The molasses sequence for our setup can be seen in Figure 3.10. This sequence starts at the end of the MOT. At this point, the MOT coils, as well as the cooling and repump lights, are switched off for 7 ms, referred to as dark time. This is to ensure that any eddy currents from the coils dissipate. This has been found to improve the final temperature in this sensor head in previous work,

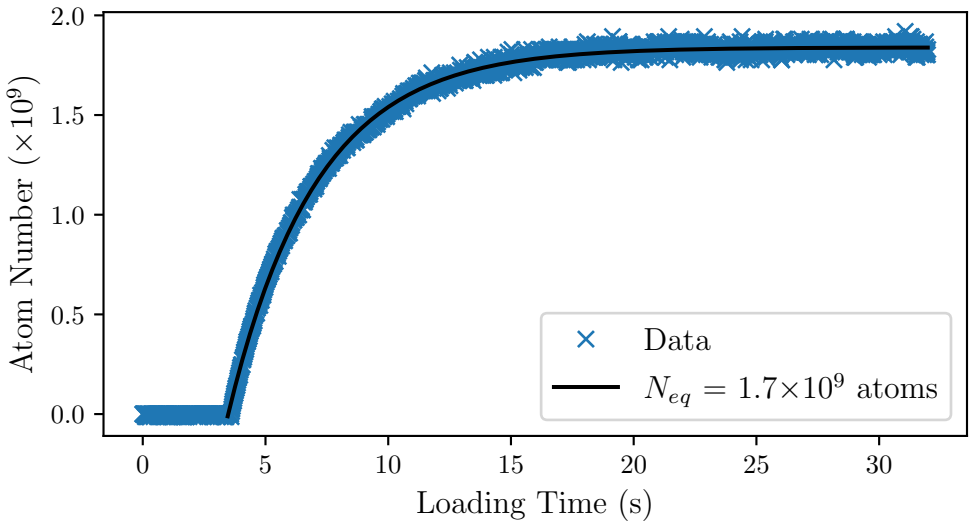


Figure 3.9: Fitted loading curve with dispenser current of 4 A, indicative of the upper performance limits of both of the chambers.

as outlined in [112]. After this dark time, the cooling and repump lights are switched on again, immediately followed by frequency ramping. Firstly, the cooling detuning is quickly ramped from 15 MHz to 85 MHz in 1.5 ms (in 20 steps), followed by slow ramping from 85 MHz to 140 MHz in 5 ms (in 30 steps). To start the state preparation, the repump light is then switched off, leaving only the cooling light for 750 μs. This means that all of the atoms fall into the dark $|F = 1\rangle$. The cooling power is then ramped from maximum to minimum power. In actual experiment this means that the RF variable attenuator 3 is ramped down from the maximum 88% power output to 0% power output while the RF variable attenuator 4 is ramped from maximum 83% power output to 0% power output. These ramps are done simultaneously in 100 μs (in 40 steps). The cooling light is left off for 2 ms during which the cooling detuning is brought to resonance. The cooling light is then pulsed for a final time of 1 ms, acting as a blowaway on the $|F = 2\rangle$ atoms. Therefore, the final result is that all of the remaining atoms are in the clean $|F = 1\rangle$ state.

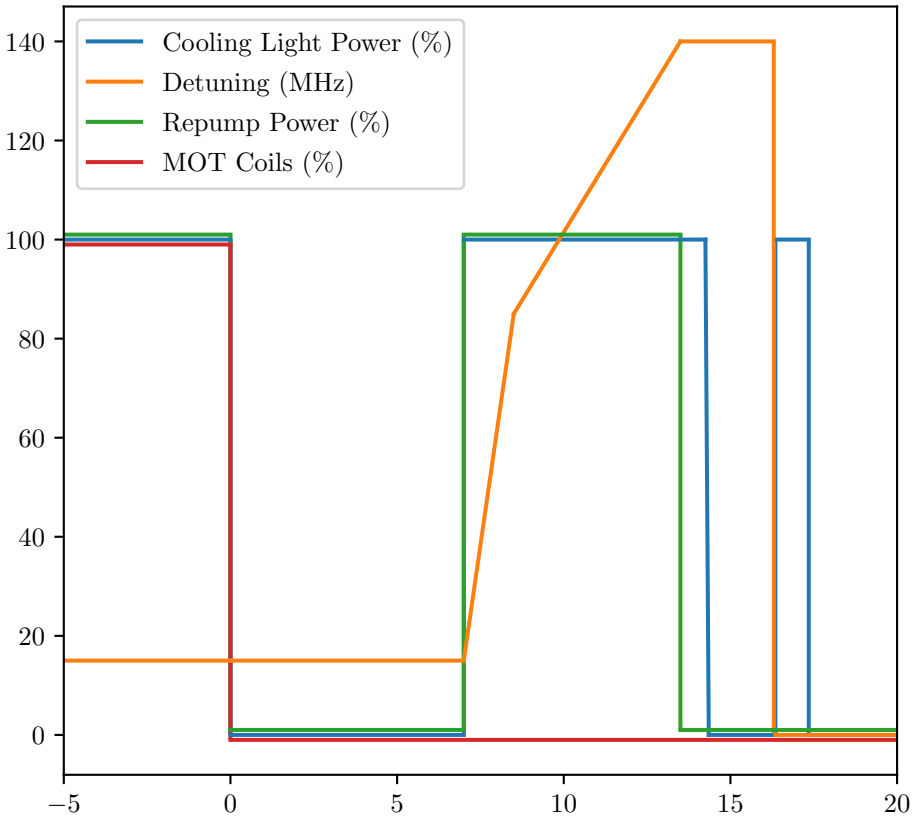


Figure 3.10: Molasses and state preparation sequence for our setup. This sequence allows us us to further cool the atoms following the MOT and then prepare them in the clean $|F = 1\rangle$ state. For clarity, the repump power has been increased by 1% while the MOT coils have been reduced by 1%.

The final temperature of the atomic cloud can be estimated using a lightsheet measurement. This uses laser light to create a thin sheet of light perpendicular to the free-falling atoms. As the atoms fall through this sheet of light, they can be seen on the detection photodiode, allowing us to measure the size of this cloud. If this cloud is left to expand for sufficient expansion times, the size of the cloud is primarily a consequence of its temperature (rather than its initial size) and hence its temperature

can be estimated. As the lightsheet can be assumed to be a flat probe beam, the signal can be fit with the following function [128]:

$$g(t) = \frac{A}{\sqrt{\sigma_a^2 + \sigma_v^2 t^2}} \exp\left[-\left(\frac{g(t_0^2 - t^2)}{2\sqrt{2}\sqrt{\sigma_0^2 + \sigma_v^2 t^2}}\right)^2\right], \tag{3.6}$$

where A is the signal amplitude, σ_0 is the initial Gaussian radius of the atomic cloud, t_0 is the average arrival time of the atoms, σ_v is the Gaussian radius of the velocity distribution and $\sigma_a = \sqrt{\sigma_0^2 + \sigma_l^2}$ is the effective width of the cloud and the probe team due to the definition of σ_l as the Gaussian beam radius of the lightsheet. The temperature, T_{temp}, can be obtained using [128]:

$$T_{\text{temp}} = \frac{m_{\text{Rb}}}{k_B}\sigma_v^2, \tag{3.7}$$

where m_{Rb} is the mass of the Rb atom and k_B is the Boltzmann constant. The thickness of the lightsheet in our sensor head has been designed to be 300 μm [112] and so it will be assumed that $\sigma_l = 150$ μm. The value of σ_0 is assumed to be 1 mm, which has been observed as the initial size of the MOT using a camera in the MOT region, as is mentioned in [112]. As σ_0 is over 3 times larger than σ_l, this is the dominating contribution to σ_a [128] but at the free-fall times we are considering, σ_0 also has very little effect on the final output, which is mainly the consequence of the ballistic expansion due to thermal effects. The time of arrival of atoms with no initial velocity, t_0, has been taken as 178 ms in line with the design of the experiment.

One disadvantage of the state preparation had been that the amplitudes of the lightsheet signals have suffered as have the temperatures of both of the clouds. The comparison of the lightsheets without and with state preparation can be seen in Figure 3.11. These signals have been fit as described above to estimate the temperatures of

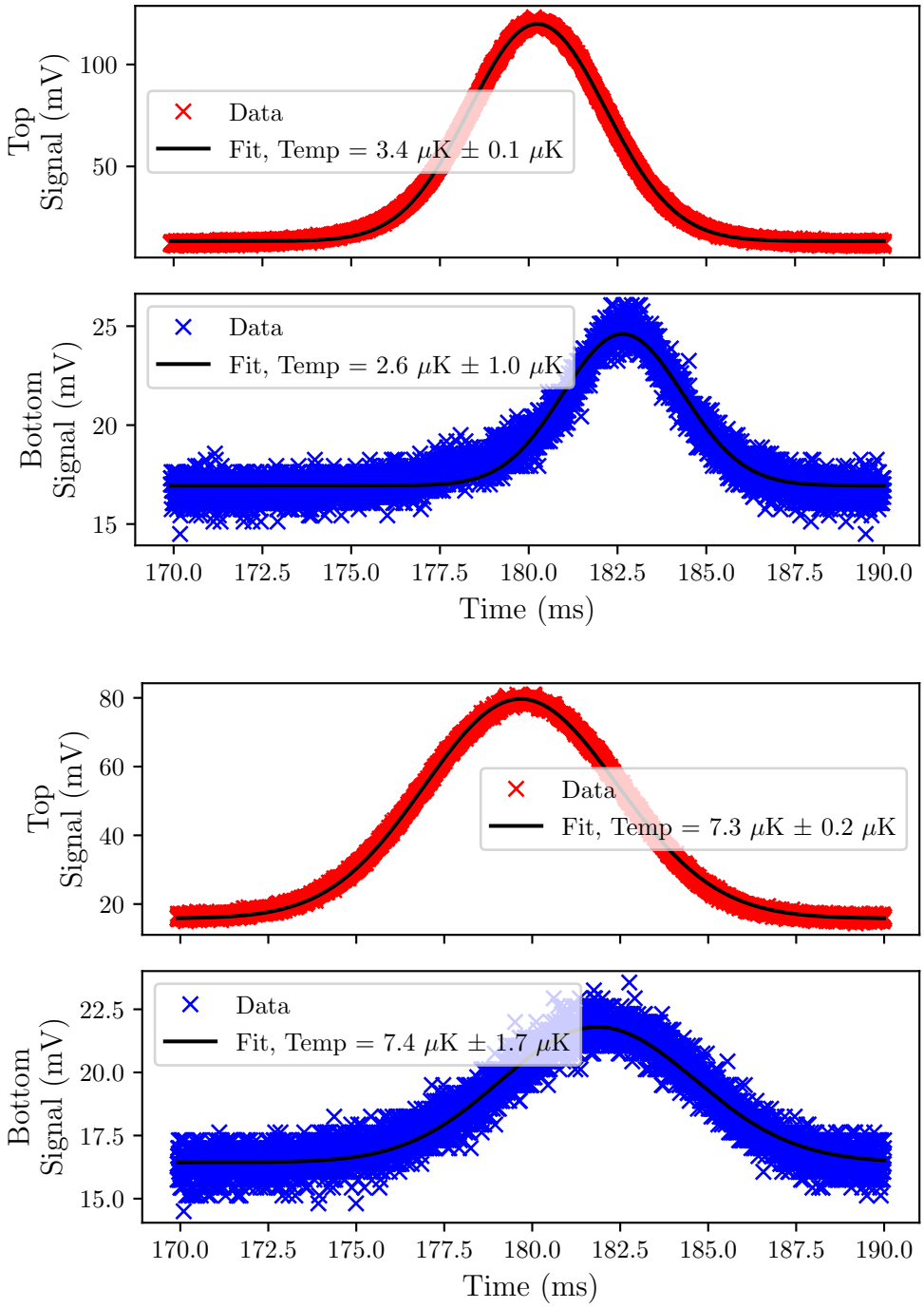


Figure 3.11: **(a)** Temperature after molasses without state preparation as opposed to **(b)** temperature after molasses with state preparation; showing the increase in temperature and reduction in amplitude.

the clouds. The temperatures without state preparation are 3.4 ± 0.1 μK for the top chamber and 2.6 ± 1.0 μK for the bottom chamber. State preparation has increased these to 7.3 ± 0.2 μK for the top chamber and 7.4 ± 1.7 μK for the bottom chamber. Additionally, the signal of these has also been reduced to about half of the amplitude, which makes sense given the fact that the blowaway pulse will get rid of some of the atoms. While not as good as without state preparation, the temperatures after state preparation are still acceptable for interferometry and provide the atoms in the clean $|F = 1\rangle$ state. It is of note to mention that the system has been designed for the atoms to be at the detection region at 178 ms after molasses. As can be seen from these plots, these times are slightly shifted, especially for the bottom chamber, indicating that there is lightsheet misalingment.

Finally, the stability of the temperatures of the atomic clouds after the molasses sequence, without state preparation, for over an hour has been analysed and can be seen in Figure 3.12. The temperatures in both chambers show good stability for over 1.5 hours, with ∼4.9% maximum variation from the mean for the top chamber and ∼7.6% for the bottom chamber. These temperatures are limited because of the open shields and the lack of intensity stabilisation of the light.

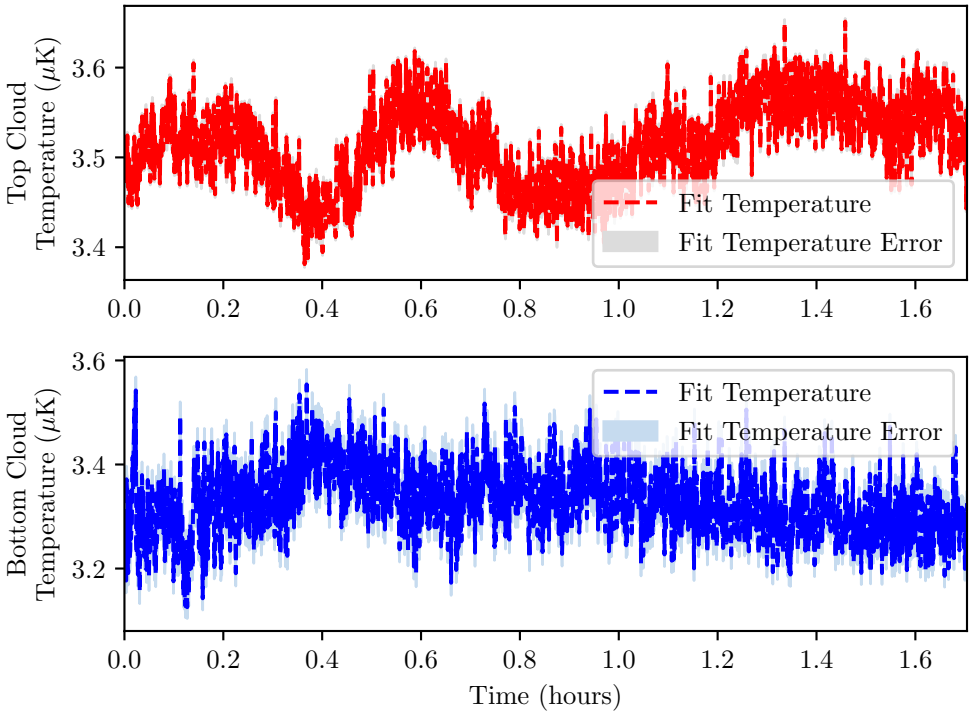


Figure 3.12: Temperature stability measurement after molasses without state preparation.

Chapter 4

Moving Platform Techniques

In standard atom interferometers, contrast and interferometer phase can be obtained by performing a chirp rate scan. This works well in static or semi-static cases when it is possible to take multiple experimental shots at the same location to build up this scan. This becomes problematic once the sensors start moving towards dynamic applications. It is then no longer possible to perform this chirp rate scan as each of the measurement points would be at a different location. One way to combat this is to obtain the contrast and interferometer phase in one experimental shot. A technique to enable this is to apply a phase shear across the atomic ensemble [75, 129] and will be discussed in the first part of this chapter.

The changing external magnetic field in different locations causes a challenge, even in static and semi-static cases. This effect of magnetic fields can be negated using a technique of k_{eff}-reversal. This works by changing the direction of the k_{eff} kick applied by the lasers onto the atoms. It is possible to cancel out the magnetic field systematics by subtracting a pair of of measurements with k_{eff} in opposite direction. However, this becomes ineffective in dynamic conditions as it requires the external magnetic field to be identical for all measurements, which is not the case as the interferometer moves. Simultaneous gravity, magnetic field and magnetic field gradient measurements using

a Mach-Zehnder interferometer based on Bragg transitions that utilise a Bose-Einstein condensate have been proposed and demonstrated [130]. In the second part of this chapter, we present an initial investigation of performing simultaneous measurements of gravity, magnetic field and magnetic field gradient with Mach-Zehnder interferometer using stimulated Raman transitions with a molasses-cold atom cloud.

4.1 Phase Shear

A cold atom cloud is a spatially localised atomic source that can expand due to its ballistic thermal expansion. If the atomic cloud size at detection is much larger than its initial size then the atoms' position is dominated by its initial velocity. This means that its final size can be assumed to be only a consequence of its initial velocity and not its initial size. If there are initial velocity-dependent phase shifts affecting the interferometer, these manifest as a spatial variation of the interferometer phase across the cloud, resulting in position-dependent population difference between the $|F = 1\rangle$ and $|F = 2\rangle$ states across the cloud. This effect can be imaged using a spatially-resolved detection. This means that rather than temporally scanning the phase and contrast using multiple shots, it is possible to scan this phase spatially, where the depth of the modulation is related to the contrast of the fringes and the phase of the spatial fringe is related to the interferometer phase. The two main ways to purposefully enable the introduction of laser phase shear into the experiment is by the use of beam pointing and by pulse timing asymmetry, with other effects also contributing to this shear. We will now discuss these in turn and use this background to build a simple model of these phase shear fringes [75, 129].

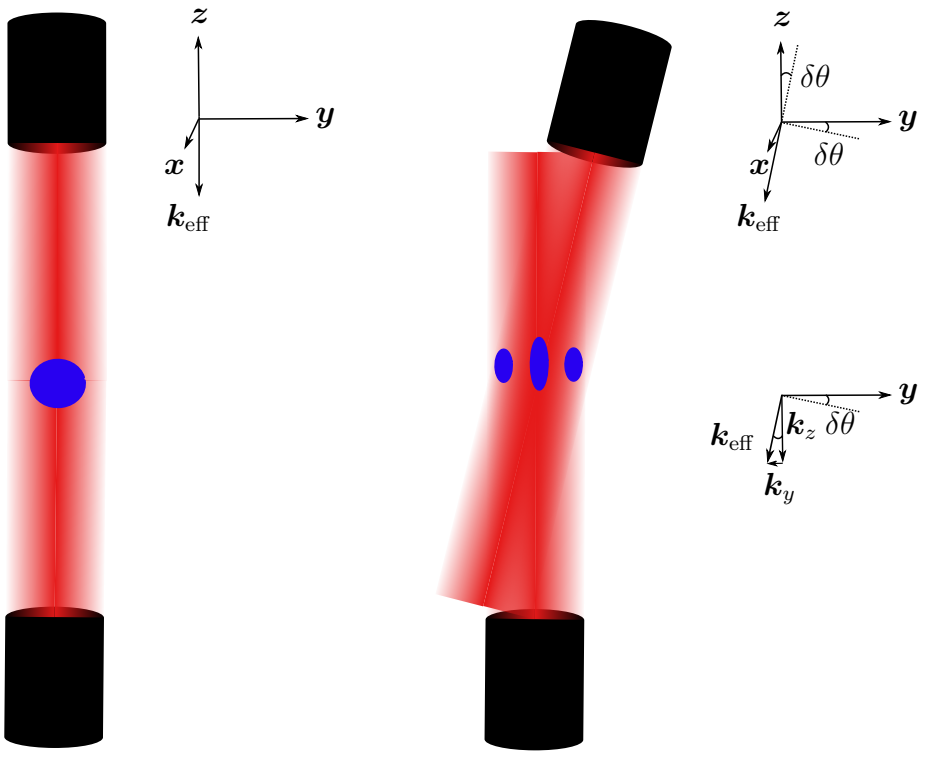


Figure 4.1: Phase shear beam pointing setup. The left diagram shows the standard interferometer setup with no beam tilting while the right one shows the application of beam tilting. Note that the propagation of the laser beams further is not shown for illustration purposes.

4.1.0.1 Beam Pointing

The simplest way to introduce this phase shear is to tilt the final $\pi/2$ pulse by an angle $\delta\theta$ with respect to the initial two pulses (ignoring any other effects) [129]. This can be seen illustrated in Figure 4.1. The z-axis is taken as the vertical axis for ease of discussion. If tilting is introduced, the final probability of the atomic cloud that was shown in equation (2.26) can be modified to (taking into account the 2D Gaussian shape of the imaged cloud along the z and y axes) [131, 132]:

$$P_b(\boldsymbol{r}) = A_{\boldsymbol{r}} e^{-\frac{r^2}{2\sigma^2}} \left(\frac{1}{2} - \frac{C}{2} \cos[\Phi(\boldsymbol{r})] \right), \tag{4.1}$$

where $\Phi(\boldsymbol{r}) = \boldsymbol{\kappa} \cdot \boldsymbol{r} - \alpha T^2$, $\boldsymbol{\kappa}$ is the wavevector of the spatially varying phase, $\boldsymbol{r}$ is the vector position of the atom, $A_{\boldsymbol{r}}$ is the amplitude and C is the contrast of the fringe [129]. In the semi-classical limit [75, 129]:

$$\boldsymbol{\kappa} \cdot \boldsymbol{r} = \boldsymbol{k}_1 \cdot \boldsymbol{r}_1 - 2\boldsymbol{k}_2 \cdot \boldsymbol{r}_2 + \boldsymbol{k}_3 \cdot \boldsymbol{r}_3, \tag{4.2}$$

where $\boldsymbol{k}_i \equiv \boldsymbol{k}_{\text{eff, i}}$ is the effective propagation vector at the time of the ith pulse and $\boldsymbol{r}_i$ is the classical position of the atom at the ith pulse [75, 129]. For standard interferometers, i.e. no tilting, $\boldsymbol{k}_{\text{eff}}$ is along the z-axis and hence $\boldsymbol{k}_1 \cdot \boldsymbol{y}_1 = \boldsymbol{k}_2 \cdot \boldsymbol{y}_2 = \boldsymbol{k}_3 \cdot \boldsymbol{y}_3 = 0$ as there is no wavevector component along the non-vertical axes, leading to:

$$\Phi(\boldsymbol{r}) = \boldsymbol{\kappa} \cdot \boldsymbol{r} - \alpha T^2 = \boldsymbol{k}_{\text{eff}} \cdot \boldsymbol{z}_1 - 2\boldsymbol{k}_{\text{eff}} \cdot \boldsymbol{z}_2 + \boldsymbol{k}_{\text{eff}} \cdot \boldsymbol{z}_3 - \alpha T^2 = (\boldsymbol{k}_{\text{eff}} \cdot \boldsymbol{g} - \alpha) T^2 = \Phi_0, \tag{4.3}$$

where Φ_0 is the standard interferometer phase. Introducing very small tilting means that there are components of $\boldsymbol{k}_{\text{eff}}$ along the non-vertical axes. Introducing a tilt around the x-axis, as per Figure 4.1, these components become:

$$\begin{aligned} |\boldsymbol{k}_x| &= 0, \\ |\boldsymbol{k}_z| &= |\boldsymbol{k}_{\text{eff}}| \cos(\delta\theta) \simeq k_{\text{eff}}, \\ |\boldsymbol{k}_y| &= |\boldsymbol{k}_{\text{eff}}| \sin(\delta\theta) \simeq k_{\text{eff}} \delta\theta, \end{aligned} \tag{4.4}$$

for small $\delta\theta$ for the last pulse. As no tilts have been introduced on the first two pulses, there are no horizontal components for $\boldsymbol{k}_1$ and $\boldsymbol{k}_2$:

$$\Phi(\boldsymbol{r}) = \boldsymbol{k}_y \cdot \boldsymbol{y}_3 + \boldsymbol{k}_{\text{z}} \cdot \boldsymbol{z}_1 - 2\boldsymbol{k}_{\text{z}} \cdot \boldsymbol{z}_2 + \boldsymbol{k}_{\text{z}} \cdot \boldsymbol{z}_3 - \alpha T^2 = k_{\text{eff}} \delta\theta y_3 + \Phi_0. \tag{4.5}$$

The normal interferometer phase is present ($\Phi_0 = [kg - \alpha]T^2$) but with an extra term due to the tilting that is dependent on the horizontal position of the atoms at the point

of tilting, creating the spatially varying phase modulation.

The cloud expands from a point source due to the thermal expansion. Therefore, this means that each of the atoms has a horizontal component of velocity, v_y. Assuming significant expansion, the atom position, y_3, can be assumed to be only a consequence of v_y at the time at which this third pulse is applied, t_3, meaning $y_3 \simeq v_y t_3$ [129]. However, detection of the cloud occurs at a time later than t_3. Hence even after the tilt has been applied, the cloud still keeps expanding, separating the fringes further. This means that this expansion between the application of the tilt and the detection time needs to be taken into account. If the atoms are detected after time t_d, the position of atoms at this point is $y_d \simeq v_y t_d$ [75, 129]. Using these two positions and timings, the following relationship can be derived:

$$y_3 = \frac{t_3}{t_d} y_d, \tag{4.6}$$

leading to:

$$\Phi_{\text{tilt}} = k_{\text{eff}} \delta\theta y_3 + \Phi_0 = k_{\text{eff}} \delta\theta \frac{t_3}{t_d} y_d + \Phi_0, \tag{4.7}$$

where the dependence of Φ on $\boldsymbol{r}$ is not explicitly stated from now on.

The horizontal fringe spatial frequency due to the tilting, κ_{tilt}, can then be obtained using [75, 129]:

$$\kappa_{\text{tilt}} \simeq \delta_y \Phi_{\text{tilt}} = k_{\text{eff}} \delta\theta \frac{t_3}{t_d}. \tag{4.8}$$

As can be seen, this fringe spatial frequency can be controlled using the beam tilting angle, $\delta\theta$. An example of the absolute spatial frequency for different angles can be seen in Figure 4.2. This spatial frequency is independent of the T chosen, and is only dependent on the tilt angle and the timing of the third pulse compared to the detection time. In order to understand what this means in terms of the actual fringes,

when imaging one of the two states, a bright spot will be seen every $(2\pi \cdot 1/|\kappa_{\text{tilt}}|)$ m.

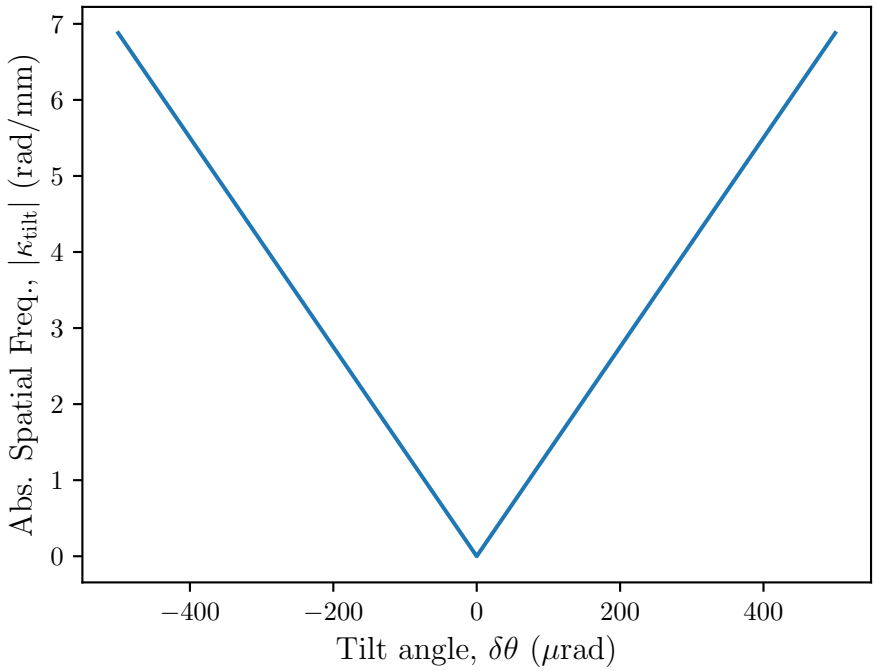


Figure 4.2: Absolute horizontal spatial frequency as a function of the tilt angle with $t_3 = 152$ ms and $t_d = 178$ ms.

4.1.0.2 Coriolis Effect

In addition to the phase shift applied by beam tilting, more shear will be introduced as a result of the Coriolis effect (a consequence of Earth's rotation). In line with section 2.5.1.3, the phase shift due to Coriolis can be written as [5]:

$$\Phi_{\text{cor}} = \frac{2k_{\text{eff}}T^2\Omega_E \cos(\theta_{\text{or}})\cos(\theta_{\text{lat}})y_d}{t_d}, \tag{4.9}$$

where v_y has been substituted for v_{hor} together with the identity $v_y \simeq y_d/t_d$. Therefore, the horizontal spatial frequency due to the Coriolis effect can be expressed as:

$$\kappa_{\text{cor}} \simeq \delta_y \Phi_{\text{cor}} = \frac{2k_{\text{eff}} T^2 \Omega_E \cos(\theta_{\text{or}}) \cos(\theta_{\text{lat}})}{t_d}. \tag{4.10}$$

In order to only see the phase shear due to the beam pointing, the Coriolis effect can be compensated by introducing extra beam pointing during the three pulses that counteracts this effect. As per section 2.5.1.3, $\Omega_E = 72.9$ μrad/s and the latitude of University of Birmingham (UK) is 52.45°. A plot showing the absolute spatial frequency due to Coriolis as a function of the orientation can be seen in Figure 4.3. Unlike beam pointing, this term is independent of t_3 but it strongly dependent on T. An increase of T from 1 ms to 51 ms results in three orders of magnitude increase in the absolute spatial frequency.

4.1.0.3 Residual Coriolis

Given that the Coriolis effect is strongly T-dependent, it is useful to compensate for it. However, Coriolis compensation does leave residual effects arising from small misalignment of the rotation axis and the true North. Assuming that the local true North vector is at angle ϕ_E with respect to the x-axis, a small misalignment $\delta\phi_E << 1$ between the rotation axis of the telescope and true North results in a residual rotation:

$$\delta\boldsymbol{\Omega} \simeq \delta\phi_E \Omega_E \cos(\theta_{\text{lat}})(\sin\phi_E \hat{\boldsymbol{x}} - \cos\phi_E \hat{\boldsymbol{y}}), \tag{4.11}$$

that leads to a residual Coriolis phase shift of [75, 129]:

$$\Phi_{\text{cor-res}} = 2\boldsymbol{k}_{\text{eff}} \cdot (\delta\boldsymbol{\Omega} \times \boldsymbol{v}) T^2 = 2k_{\text{eff}} \delta\phi_E \Omega_E \cos\theta_{\text{lat}} \sin\phi_E v_y T^2. \tag{4.12}$$

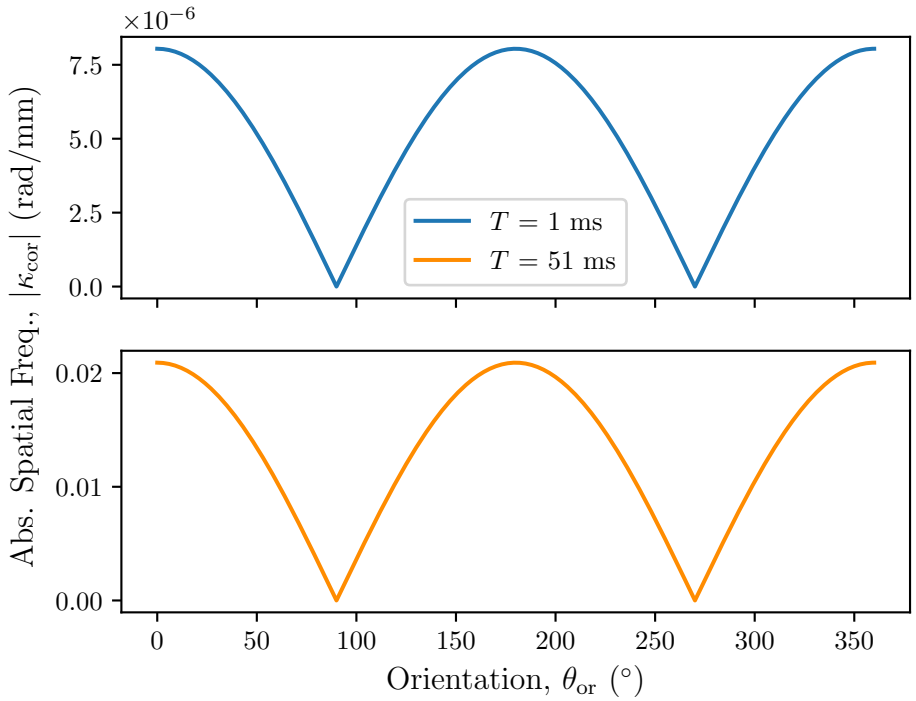


Figure 4.3: Absolute horizontal spatial frequency due to Coriolis as a function of the orientation of the sensor, given $t_d = 178$ ms.

Using the identity $v_y \simeq y_d/t_d$ once again, the residual Coriolis phase gradient becomes:

$$\kappa_{\text{cor-res}} \simeq \delta_y \Phi_{\text{cor-res}} = \frac{2k_{\text{eff}}\delta\phi_E \Omega_E \cos\theta_{\text{lat}} \sin\phi_E T^2}{t_d}. \tag{4.13}$$

A big challenge with this effect is that it relies on being able to estimate and/or calculate the misalignment between the sensor and the true North. There are ways to do this, for example, ϕ_E can be estimated cartographically [129] while it is possible to identify the true North by scanning $\delta\phi_E$ to identify the angle at which $\kappa_{\text{cor-res}} = 0$.

Seeing as this effect is just the artefact of the Coriolis effect, this residual Coriolis term will be ignored in the following sections. If needed, only the Coriolis term will be included in the following models. Figure 4.4 shows the absolute spatial frequency as a result of this effect for a range of ϕ_E. An example of $\delta\phi_E = 0.1$ produces an effect which

is about an order of magnitude lower than the potential effect due to uncompensated Coriolis.

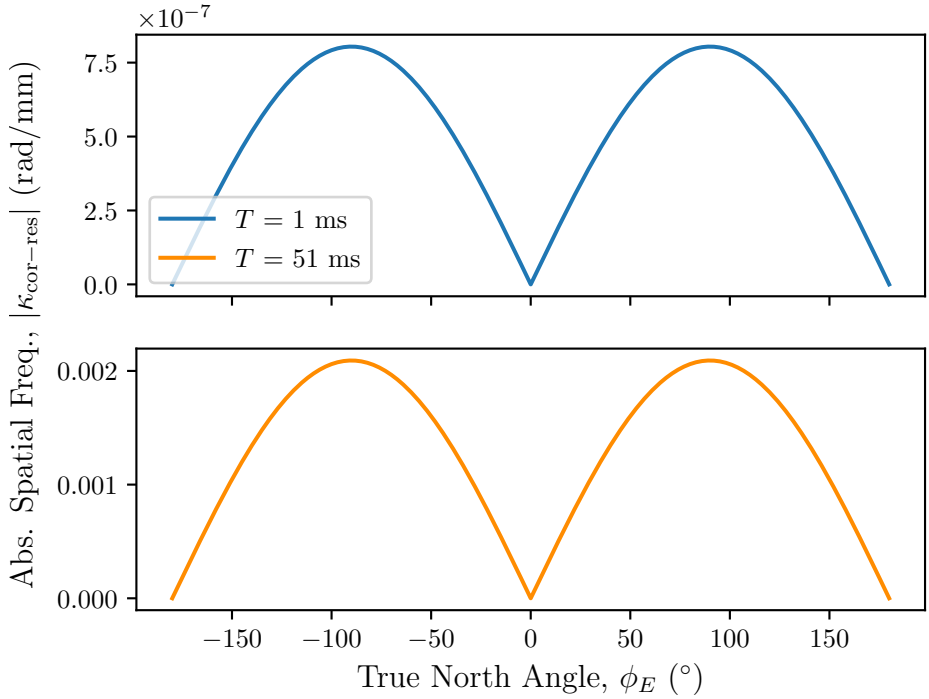


Figure 4.4: Absolute horizontal spatial frequency due to residual Coriolis effect as a function of the angle between the true North and x-axis, given $t_d = 178$ ms.

A contour plot of the interference fringes for a range of horizontal displacements for a range of tilt angles can be seen in Figure 4.5. These indicate how the atomic transition probability would vary depending on the size of the cloud. The interferometer phase, Φ_0 has been calculated with $g = 9.81$ ms^{-2} and $\alpha = 2\pi\times25.1538$ MHz/s. The Coriolis effect is included (with orientation chosen to obtain the maximum Coriolis effect). As the spatial frequency due to this effect is orders of magnitude smaller than that of the beam pointing, it has a negligible contribution and so no asymmetry between positive and negative tilt angles is seen.

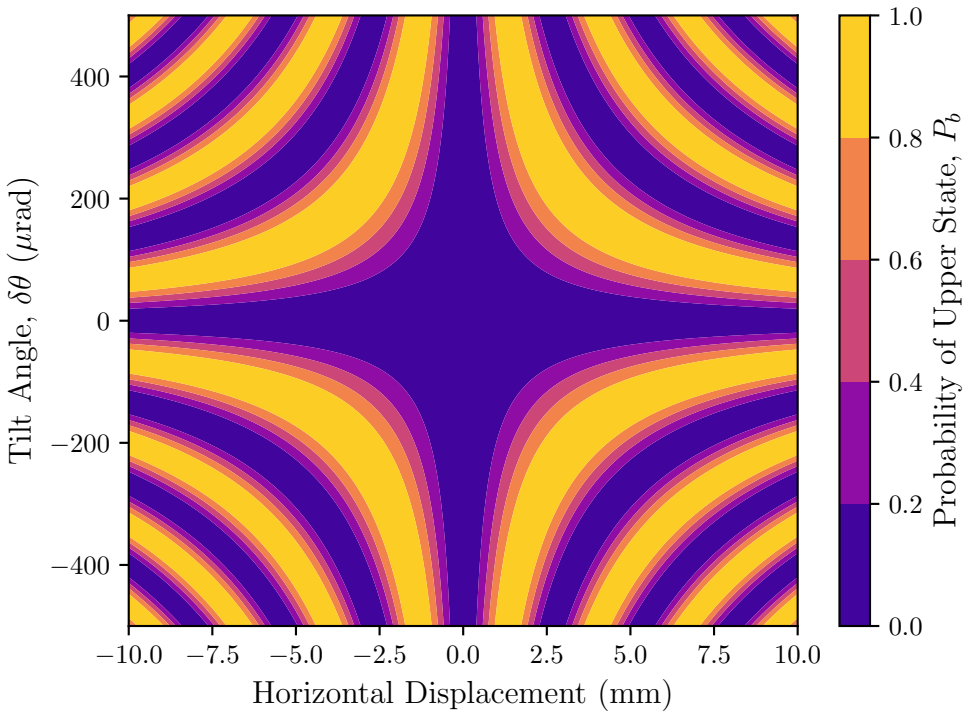


Figure 4.5: The atomic transition probability of the fringes as a function of both the horizontal displacement of the atoms and the angle of beam pointing applied (including the maximum possible effect of Coriolis, i.e. orientation of 0°). The following parameters are used: $t_3 = 52$ ms, $t_d = 178$ ms, $T = 1$ ms, $g = 9.81$ ms^{-2}, $\alpha = 2\pi\times25.1538$ MHz/s and $C = 1$. The chirp rate chosen cancels the value of gravity exactly, hence with no tilt angle applied, this leads to no atoms in the upper state being present at the end of the Mach-Zehnder sequence.

4.1.0.4 Timing Asymmetry

While beam pointing creates a shear transverse to the interferometer axis, timing asymmetry yields a shear parallel to the beam axis. This timing asymmetry can be created by offsetting the central π pulse. This is done by extending the T-time between the first and second pulse and reducing the T-time between the second and third pulse. This results in the timing between the first and second pulse being, $T_{1-2} = T + \delta T/2$, while the timing between the second and third pulse becomes $T_{2-3} = T - \delta T/2$. The

resulting phase in the vertical direction as a result of this timing asymmetry is:

$$\Phi_{\text{asy}} = k_{\text{eff}} v_z \delta T, \tag{4.14}$$

which results in a phase shear along the vertical direction (using $y_d \simeq v_z t_d$):

$$\kappa_{\text{asy}} \simeq \delta_z \Phi_{\text{asy}} = k_{\text{eff}} \delta T / t_d. \tag{4.15}$$

The vertical absolute spatial frequency as a result of this timing asymmetry can be seen in Figure 4.6. It only depends on t_d and the level of asymmetry [75, 129].

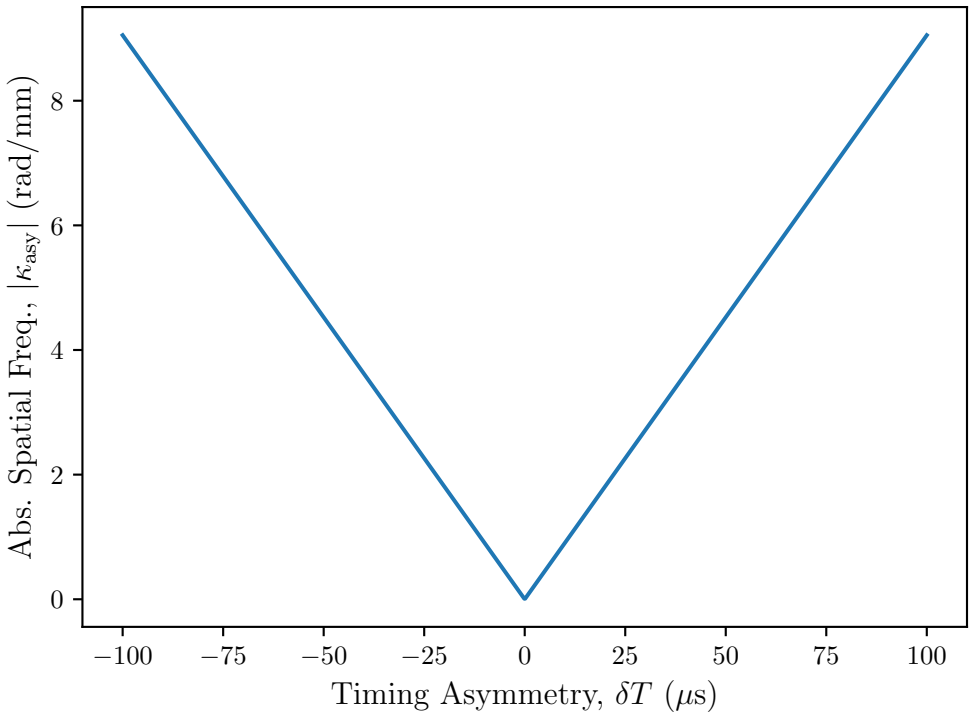


Figure 4.6: Absolute vertical spatial frequency due to timing asymmetry with t_d = 178 ms.

4.1.0.5 Gravity Gradient

The last term that will be discussed is the effect of the gravity gradient on the fringes. Gravity gradient also has an effect in creating the fringes along the vertical axis:

$$\Phi_{\text{gradient}} = k_{\text{eff}}(\nabla \boldsymbol{g})_{zz} v_z T^3, \tag{4.16}$$

where $(\nabla \boldsymbol{g})_{zz}$ describes how the vertical gravity gradient changes along the vertical direction. The spatial frequency as a result is given by [75, 129]:

$$\kappa_{\text{gradient}} \simeq \delta_z \Phi_{\text{gradient}} = k_{\text{eff}}(\nabla \boldsymbol{g})_{zz} T^3 / t_d. \tag{4.17}$$

The vertical spatial frequency as a result of the gravity gradient for various T times and for various gravity gradient signals can be seen in Figure 4.7. The vertical black line is the typical Earth's gravity gradient ($\sim 3 \times 10^{-6}$ s^{-2}) and has been included for reference. While this term has a strong T^3 dependence, the low typical value of gravity gradient of the Earth means that this contributes a small amount to the spatial frequency in the vertical axis and hence this would not be easily observed, becoming more pronounced if large gradients are present, or if long T is used.

4.1.0.6 Composite Fringes

It is possible to create fringes at any arbitrary angle, Θ. This creates the possibility to create composite fringes, composed of both horizontal and vertical components:

$$\Theta = \arctan\left[\frac{\delta T - (\nabla \boldsymbol{g})_{zz} T^3}{\delta\theta t_3 + 2T^2 \Omega_E \cos(\theta_{\text{or}}) \cos(\theta_{\text{lat}})}\right]. \tag{4.18}$$

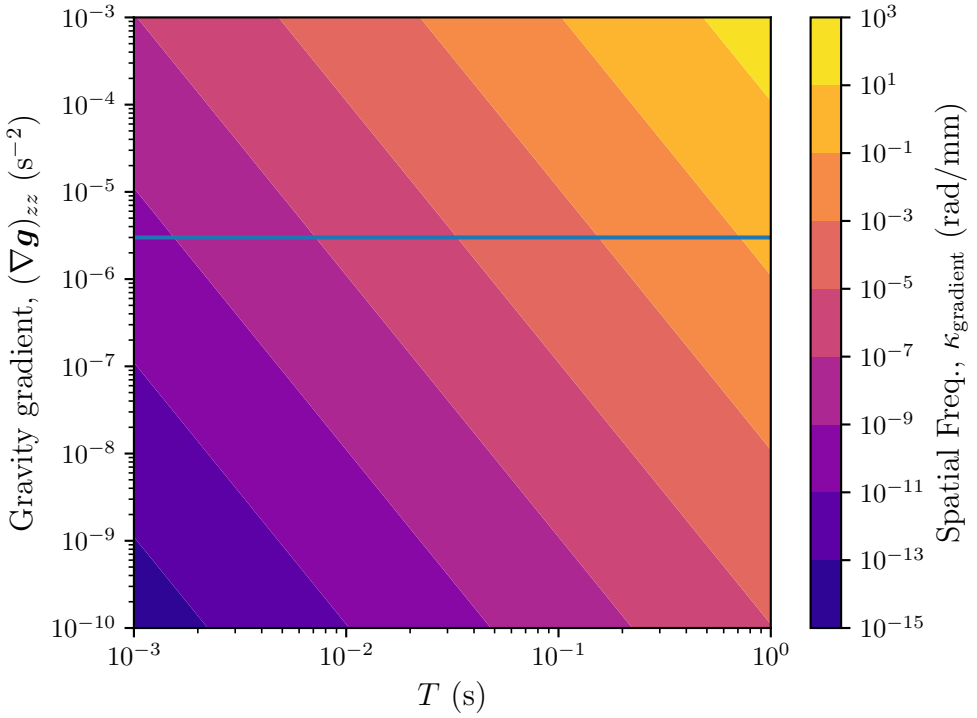


Figure 4.7: Vertical spatial frequency due to the gravity gradient and T, given $t_d = 178$ ms. The black line represents the Earth's gravitational gradient at 3×10^{-6} s^{-2}.

The final output of an interferometer can be expressed as two 1D Gaussians combined with these composite fringes (in analogy with equation (4.1)):

$$P_b(y,z) = A_y A_z e^{\frac{-y^2}{2\sigma_y^2}} e^{\frac{-z^2}{2\sigma_z^2}} \cdot \left(\frac{1}{2} - \frac{C}{2}\cos[\kappa_H y + \kappa_V z + \Phi_0]\right), \tag{4.19}$$

where $\kappa_H = \kappa_{\text{tilt}} + \kappa_{\text{cor}}$, $\kappa_V = \kappa_{\text{asy}} - \kappa_{\text{gradient}}$, and σ_y and σ_z are the Gaussian radii calculated using [133]:

$$\sigma_{y/z}^2 = \sigma_0^2 + \frac{T_{\text{temp}} k_B}{m_{\text{Rb}}} t_d^2, \tag{4.20}$$

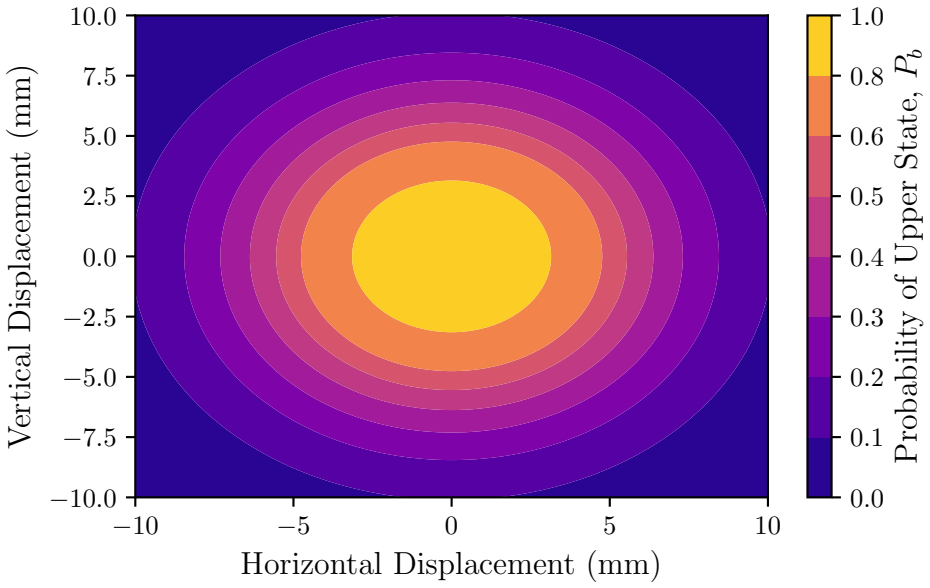
where σ_0 is the initial Gaussian radius (taken as 1 mm), T_{temp} is the temperature of the cloud (taken as 7 μK), m_{Rb} is the mass of ^{87}Rb and k_B is the Boltzmann constant.

In the case of $T = 1$ ms with no beam tilting or timing asymmetry, and setting $\Phi_0 = \pi$ for maximum P_b, a standard 2D Gaussian is observed, as seen in Figure 4.8(a). This is the case even when Coriolis and gravity gradient spatial frequencies are present. However, introducing $\delta\theta = 500$ μrad and $\delta T = 10$ μs, a composite fringe pattern is observed in Figure 4.8(b), clearly highlighting the effect of intentional application of phase shear. The choice of $\Phi_0 = \pi$ has been for illustrative purposes only. If $\Phi_0 = 0$ were chosen, no cloud would be observed with no beam tilt or timing asymmetry; however, the fringes would still be visible in the latter case, the only difference would be that the fringe pattern would be shifted in space.

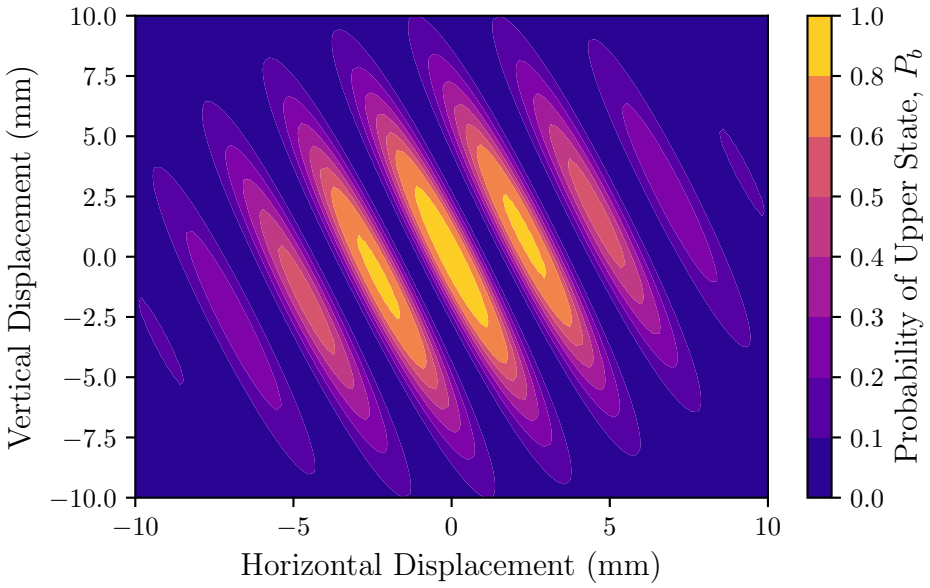
More complex schemes of introducing phase shear are also possible. For example, it is possible to tilt the first and last pulses beams by the same angle (with the central pulse taken as reference) but in opposite directions as well as shift the frequency of the pulses (on top of the chirp rate). This has the effect of being able to compensate additional degrees of freedom, especially in dual-species interferometers [79]. These more complex techniques are beyond the scope of this work.

4.1.0.7 Analysis

While the main focus of this part of the chapter is in developing the model for simulating the phase shear fringes to aid in our experimental implementation of beam tilting, this section will briefly describe a way to analyse the fringes once they have been obtained. The method that we will concentrate on is the one that was used in the first demonstration of phase shear, referred to as principal component analysis (PCA) [75]. Other methods have been demonstrated, including the "Simple, High dynamic range, and Efficient Extraction of Phase map" method in [80] but this is beyond the scope of this work. The full mathematical treatment of PCA can be seen in [134]. We will use the work performed in [134] to briefly explain the concepts in relatively simple terms



(a)



(b)

Figure 4.8: **(a)** Atomic cloud with no beam tilting or timing asymmetry and with $\Phi_0 = \pi$. **(b)** The same atomic cloud with the application of $\delta\theta = 500$ μrad and $\delta T = 10$ μs. For both of these, $A_y = A_z = C = 1$, $t_3 = 52$ ms and $t_d = 178$ ms.

to gain an understanding of this analysis method.

PCA is a statistical image analysis. In this method, each image can be represented as a p dimensional vector, with p being the number of pixels in the image. The projection of p along dimension j represents the pixel j of the actual image. Let us denote an image as $\boldsymbol{X}_i$. This image is a combination of a set of, what is termed as "basis", images:

$$\boldsymbol{X}_i = \boldsymbol{M} + Y_{1i}\boldsymbol{u}_1 + Y_{2i}\boldsymbol{u}_2 + ... + Y_{pi}\boldsymbol{u}_p, \tag{4.21}$$

where $\boldsymbol{M}$ is the mean image of the set. The other terms are the basis images of the PCA and they are orthonormal to each other.

If we have a set of N image vectors that can be represented in the PCA, the requirement of this method is that coefficients of one basis image are statistically uncorrelated with coefficients of another image, which mathematically can be written as:

$$\sigma_{jk}^2 = \frac{1}{N-1}\sum_{i=1}^{N} Y_{ji}^{(P)} Y_{ki}^{(P)} = 0, \tag{4.22}$$

where $Y_{ji}^{(P)}$ is the coefficient of the principal component basis image j in the representation of image i. PCA ensures that image-to-image variation is preserved, meaning that the variance of the overall image is conserved. What this means in non-mathematics expert terms is that the variance of a given principal component coefficient is actually a measure of its importance in reconstructing the image and can be used to quantify how much of the data variation is accounted for by that particular principal component.

In the PCA basis, the image can therefore be represented as a linear combination of a new orthornormal set of N vectors/images:

$$\boldsymbol{X}_i = \boldsymbol{M} + Y_{1i}^{(P)}\boldsymbol{u}_1^{(P)} + Y_{2i}^{(P)}\boldsymbol{u}_2^{(P)} + ... + Y_{Ni}^{(P)}\boldsymbol{u}_N^{(P)}, \tag{4.23}$$

where it is assumed that $N < p$, which is a valid assumption for CCD cameras. These basis images can be written as a $p \times N$ orthonormal matrix, $P = [\boldsymbol{u}_1^{(P)} \boldsymbol{u}_2^{(P)} ... \boldsymbol{u}_p^{(P)}]$, and are referred to as principal components of the data set. These principal components have been sorted in order of decreasing strength - therefore each subsequent principal component accounts for smaller variation in the data. The main idea of PCA is that the majority of the image can be reconstructed using only the first l principal components:

$$\boldsymbol{X}_i \simeq \boldsymbol{M} + Y_{1i}^{(P)} \boldsymbol{u}_1^{(P)} + Y_{2i}^{(P)} \boldsymbol{u}_2^{(P)} + ... + Y_{li}^{(P)} \boldsymbol{u}_l^{(P)}, \tag{4.24}$$

thereby reducing the dimensionality of the image. If each of the principal components can be identified with a particular experimental parameter then its placing in the principal component order is a reflection of its importance in the experimental results. This can be useful in calibration and optimisation of the experiment due to the ability to quantify each of these effects independently.

What all of this means in an atom interferometer is that PCA can be used as a filter to distinguish between the constant overall shape of the cloud, the interfering atom populations, and sources of technical and systematic noises. Using the images obtained, PCA can be used to decompose the image, with the different principal components holding information about different aspects of the cloud. The first principal component is the general shape of the atomic cloud. The second and third principal components are due to the fringe and any possible interferometer phase can be represented as a weighted sum of these two components (they can be thought of as sine and cosine terms). If it were possible to obtain an infinite number of images with uniformly distributed phase then the variance of the second and third components would be the same. However, with a finite number of images, one of these terms will dominate over the other by chance. Alternatively, given a set of images with a fixed interferometer

phase, the spatial fringes would appear on the first principal component as a common feature of all the images [131].

Therefore, as a result of this analysis, equation (4.19) can be decomposed into:

$$P_b(y,z) = P_{\text{cloud}}(y,z) + P_{\text{fringe}}(y,z), \tag{4.25}$$

where:

$$P_{\text{cloud}}(y,z) = \frac{A_y A_z}{2} e^{-\frac{y^2}{2\sigma_y^2}} e^{-\frac{z^2}{2\sigma_z^2}}, \tag{4.26}$$

and:

$$P_{\text{fringe}}(y,z) = -\frac{A_y A_z C}{2} e^{-\frac{y^2}{2\sigma_y^2}} e^{-\frac{z^2}{2\sigma_z^2}} \cos[\kappa_H y + \kappa_V z + \Phi_0]. \tag{4.27}$$

Equations (4.26) and (4.27) can be fit independently, where the contrast C is calculated using the ratio of the amplitudes of the fits while the fit to the spatial frequency of the fringe of the second/third components is a direct measurement of the phase gradient and allows for the determination of the interferometer phase. By being able to do these fits separately, the fits are more robust as there is reduced cross-talk between the fitting parameters [131].

The question arises as to how to use the phase shear technique in real-life applications. The spatial frequency fit of the fringes can be used to obtain the phase gradient together with the interferometer phase. The effect of the interferometer phase is to shift the fringes in the horizontal direction (if beam tilting is applied). Due to the sinusoidal relation, these fringes have a periodicity of 2π. Therefore, one way would be to perform scans similarly to standard interferometers to obtain the absolute value of g. Alternatively, the fringes could be used to monitor the changes in gravity by monitoring the shifts of these fringes in real space. For example, it is common for atom interferometers to sit at $P_b = 0.5$ for maximum sensitivity and monitor the change in

interferometer phase as a result of anomalies. For a scanning/dynamic system, therefore, this technique could be used to monitor this interferometer shift and to use it to calculate the changes in g. One advantage of phase shear readout over this standard interferometer technique is the fact that it is able to obtain both the contrast and the interferometer phase in one experimental shot.

4.1.1 Fluorescence and Camera Imaging

The building blocks of the phase shear fringes and their dominant contributions have now been shown. The aim of this section is to build on the work in the literature to simulate these fringes in a more realistic scenario, specifically using fluorescence imaging with a camera. This will make these simulations more useful for the experimental work being carried out within our group.

While numerous types of detection are possible (for a brief introduction of different detection types see [135]), our detection uses fluorescence. For phase shear, this is aided with camera imaging. This introduces real-life considerations on the output of the fringes that have been neglected so far. When considering fluorescence detection, one needs to consider the multi-level structure of ^{87}Rb, atom number, and detection beam intensity. When imaging with a camera, the noise of the camera as well as how photons are converted into electrons, and eventually into a pixel signal, need to be considered.

For reference, Figure 4.9 shows the level structure of ^{87}Rb D_2 line but with new symbol definitions that will be used in this section that has been adapted from [136] with values obtained from [96]. A detection/cooling beam that is red-detuned by an amount of Δ_{cooling} from the cooling $|F = 2\rangle \rightarrow |F' = 3\rangle$ transition also induces the undesirable $|F = 2\rangle \rightarrow |F' = 2\rangle$ and $|F = 2\rangle \rightarrow |F' = 1\rangle$ transitions. Therefore, some of the atoms in the $|F' \neq 3\rangle$ states can spontaneously decay to the $|F = 1\rangle$ state, and

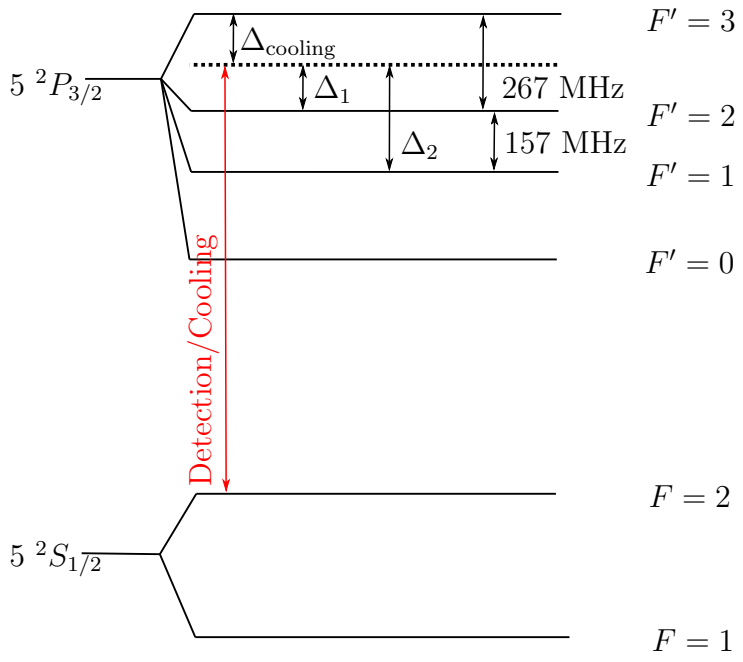


Figure 4.9: Level structure of the D_2 line of ^{87}Rb.

enter the dark state. As single-state detection (which will be used with camera imaging) cannot make the atoms re-enter the closed transitions, these atoms are effectively lost and will not be imaged as a signal by the camera. Therefore, the multi-level energy structure of ^{87}Rb has an effect on the number of scattered photons, n_s, which can be calculated using [136]:

$$n_s(t) = \frac{N\gamma_d}{\gamma_{\text{lost}}}\left(1 - \exp\left[-t_{\text{pulse}}\frac{I}{2I_{\text{sat}}}\Gamma\gamma_{\text{lost}}\right]\right), \tag{4.28}$$

where N is the atom number, Γ is the natural linewidth of the cooling transition ($\Gamma = 2\pi \times 6.06$ MHz), I is the intensity of the cooling beam and I_{sat} is the saturation intensity ($I_{\text{sat}} = 1.67$ mW/cm^{-2} for ^{87}Rb [91]).

The parameters $\gamma_d = \gamma(\Delta_{\text{cooling}})$ and $\gamma_{\text{lost}} = \sum_i \gamma(\Delta_i)\text{br}_i$ are proportional to the scattering cross-sections of the cooling transition and of all the lost non-closed transitions, respectively. The lost non-closed transitions in this case are $|F' = 2\rangle \rightarrow |F = 1\rangle$

and $|F' = 1\rangle \rightarrow |F = 1\rangle$. In general, the function $\gamma(\Delta_{\text{cooling}})$ is given by [136]:

$$\gamma(\Delta_{\text{cooling}}) = \left(1 + \frac{I}{I_{\text{sat}}} + 4\frac{\Delta_{\text{cooling}}^2}{\Gamma^2}\right)^{-1}, \tag{4.29}$$

where Δ_{cooling} has been assumed as $2\pi \times 0$ MHz, i.e. the transition is assumed to be on resonance. In the case of γ_{lost}, Δ_{cooling} can be replaced with $\Delta_i = \Delta_{di} - \Delta_{\text{cooling}}$. In this case, Δ_i is the detuning with respect to the non-detection hyperfine transitions, and Δ_{di} is the frequency difference of these transitions with respect to the cooling transition. These detunings can be seen in Figure 4.9 and calculate as $\Delta_1 = 2\pi \times 267$ MHz and $\Delta_2 = 2\pi \times 424$ MHz. br_i refers to the spontaneous emission branching ratios to the non-closed transitions, which is 50% for $|F' = 2\rangle \rightarrow |F = 1\rangle$ and 83.3% for $|F' = 1\rangle \rightarrow |F = 1\rangle$ [136].

Our modelling composes of creating an array of shape 1224 $\times$ 1024, in line with the number of pixels of a camera. Equation (4.19) is used with this array to calculate the probability of the atomic transition. To convert between the pixel number and actual size, a magnification of $\sim$6.4 has been assumed (each pixel has a size of 3.45 μm along one side). This magnification is in roughly in line with our setup as will be seen in chapter 6. As seen from equation (4.19), in standard atom interferometers with no phase shear across the cloud, the maximum signal is obtained when $\Phi_0 = n\pi$ (where n = 1, 3, 5...). We have assumed that the total atom number at this point is 1×10^4 atoms with the distribution being a consequence of the atomic probabilities. This represents the maximum atom number that can be seen in the cloud. Therefore, any calculated atomic probabilities are normalised with respect to the sum of the atomic probabilities when $\Phi_0 = \pi$ with no phase shear present. This ensures that the total atom number for any interferometer phase or phase shear does not exceed 1×10^4 atoms as well as ensuring that changing these parameters changes the total atom number (and hence the

signal) seen. The resulting atom number distribution is subsequently used in equation (4.28) to calculate n_s. The cooling intensity, I, has been assumed as 5.3 mW/cm^2, in line with our setup. The length of time for which the detection beam is applied for is taken as $t_{\text{pulse}} = 100$ μs.

n_s can be used to estimate the number of photons that reach the photodetector, n_d, using [136]:

$$n_d = n_s \Omega, \tag{4.30}$$

where Ω is the fraction of solid angle intercepted by the imaging lens of numerical aperture, NA, given by $\Omega \simeq \text{NA}^2/4$ [136]. The numerical aperture of the lens has been taken as 0.36 (Computar 35 mm 1:1.4 2/3" [137]).

For completeness, we will state that the limitations of these equations as outlined in [136]. These are derived assuming that all of the light polarisations are present and that all of the m_F states are equally occupied, and excluding optical pumping. Stimulated transitions to the lost states have also been excluded because if Δ_{cooling} is small, they are only a second-order correction [136].

Each of the values of n_d in the array is randomised with Poisson statistics to simulate photon shot noise on the individual pixels. Upon hitting the pixels, these photons are converted into electrons, n_e, using:

$$n_e = \eta n_d, \tag{4.31}$$

where η is the quantum efficiency of the pixel and is assumed as $\sim$0.6 (for our DZK 33UX250 camera [138]). Therefore, the equation above gives the mean electrons per pixel that will be produced as a result of the scattered photons due to fluorescence, with the photons of each pixel obeying Poisson statistics.

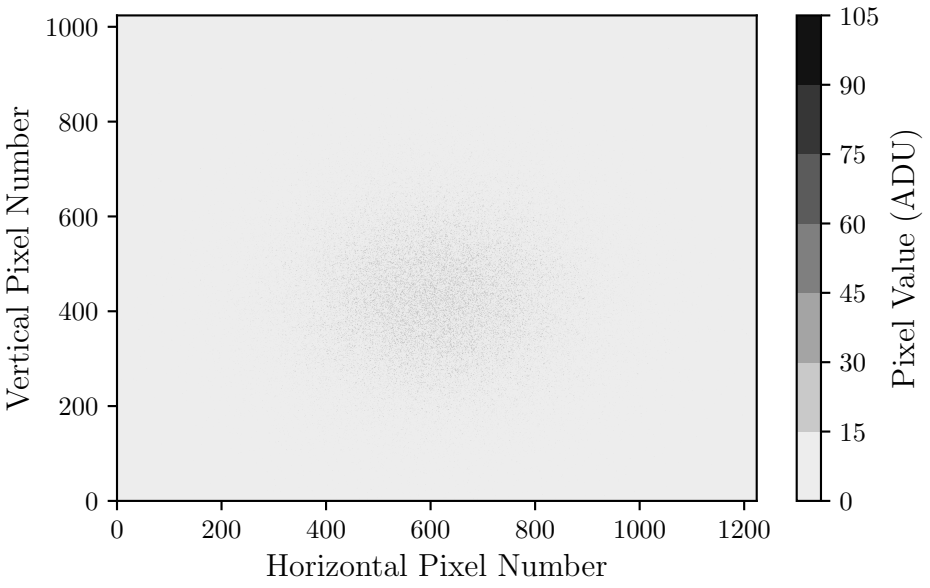
Apart from this photon shot noise, other sources of error also affect a camera sig-

nal. One of them is the dark shot noise due to dark current. Dark current occurs due to the thermal effect of valence electrons being thermally excited into the conduction band and hence registering as a signal on the pixel. As such, this occurs even when no photons are incident on the camera. The amount of dark electrons collected during the exposure is the dark shot noise. While independent of the signal level, it is dependent on the temperature of the sensor. Another source of error is the read noise, which is constant for all temperatures [139, 140]. We have taken estimates of both of these noises from [141] as an estimate for our sensor. This reference has a different camera to ours but it does contain the Sony IMX250 sensor (our sensor is Sony IMX250MZR) - we were unable to obtain an estimate of these values for our camera/sensor specifications. The read noise is taken as 2.32 electrons/(pixel s) while the dark noise is 3.9 electrons/(pixel s) at operating temperature of 50 °C. Using an exposure time of 400 μs, we obtain $n_{\text{read noise}} \simeq 9.3 \times 10^{-4}$ electrons/pixel and the readout $n_{\text{dark noise}} \simeq 1.6 \times 10^{-3}$ electrons/pixel. These are taken as the mean values of these noises at each element of the n_e array, with their variation obeying Poisson statistics. Therefore, these are added as extra noises to each element of the n_e array on top of the photon shot noise. However, due to their small sizes, they are largely negligible. The only noise that has been ignored is the fixed pattern noise, caused by spatial non-uniformities of the pixels, making it independent of the signal seen or the temperature. Fortunately, no fixed pattern noise is a valid assumption for CCD cameras and hence can be ignored [140].

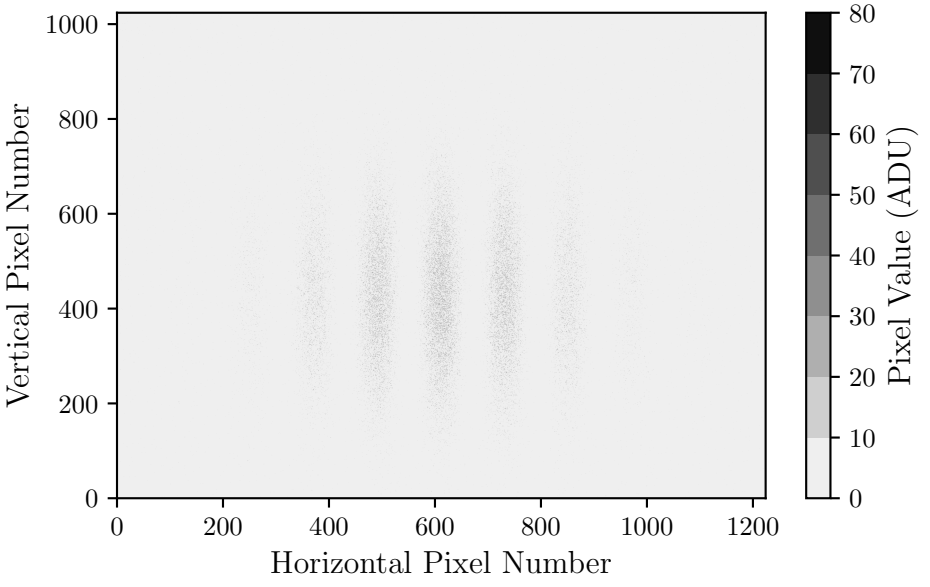
The number of electrons calculated for each of the pixels needs to be converted from electrons to analog-to-digital units (ADUs). ADUs are the units of grey scale that are output by monochrome cameras. Once again, this number could not be obtained from the camera and sensor manuals and hence a value of 6 electrons/ADU has been assumed [142]. As will be discussed in chapter 6, the camera also has a gain setting

that affects how much signal is seen. We have used a gain of 20 dB, which translates as an increase of the signal by a factor of 100. Hence the ADUs calculated for each pixel are multiplied by this factor. Finally, these ADUs are turned into discrete numbers with the maximum upper values set to 2^k-1, where k is the camera's bit-depth (k = 8 for our setup). This ensures that the saturation of the pixels is correctly modelled [139].

Including all of these effects in our simulation, we have derived a simple mathematical treatment to estimate what the atomic cloud would look like when using fluorescence detection combined with camera imaging. Examples of these images can be seen in Figure 4.10 for the same parameters as before - the Coriolis and gravity gradient terms have been included. This is a simple model and it is the author's hope that this work can be built on. Estimating some of the parameters for camera imaging is not a trivial matter, with manufacturers not necessarily providing all of the required information. Therefore, these parameters need further investigation to ensure that they are appropriate and to provide better estimates. Additionally, the atom number has been estimated using working knowledge of interferometers with good performance - this is obviously not always the case. This model can be built on further to include different effects that could affect the fringes, one obvious one is the inclusion of a lens and the effect of depth of field as well as other blurring mechanisms. Nevertheless, this model serves as a first step to model the expected output of an interferometer following the introduction of phase shear and can help to investigate different cameras before acquiring them. With more advanced model that includes the aforementioned effects due to the lens, different configurations of cameras and lenses could be investigated.



(a)



(b)

Figure 4.10: **(a)** Atomic cloud with no beam tilting or timing asymmetry. **(b)** The same atomic cloud with the application of $\delta\theta = 500$ μrad tilt. For both of these, $A_y = A_z = C = 1$, $T = 1$ ms, $t_3 = 52$ ms and $t_d = 178$ ms; with $\Phi_0 = \pi$.

4.2 Multi-modal Measurements

In this second part of the chapter we investigate the possibility of performing multi-modal measurements of both gravity, magnetic field and magnetic field gradient with a Mach-Zehnder interferometer utilising stimulated Raman transitions. This is an initial investigation at the end of which we will outline the possible next steps to validate this work. The work done in this chapter has been performed using information from [96] and [97]. These will not be referenced throughout this section. Any other references will be referenced as appropriate.

4.2.1 Magnetic Energy Levels

The effect of magnetic field on an atom interferometer is via the shifting of the energies of the m_F sub-states. The strength of the field has a profound effect on the resulting dependence of the energy levels on this field. For example, if the energy shift due to the magnetic field is small compared to the hyperfine splitting, F is a good quantum number. However, if the energy shift due to the magnetic field is larger than the hyperfine splitting but smaller than the fine structure, then F ceases to be a good quantum number and J becomes a good quantum number. This leads to three possible regimes for the energy shifts due to magnetic field:

1. Weak magnetic field,
2. Intermediate magnetic field, and
3. Strong magnetic field.

4.2.1.1 Weak Magnetic Field

The weak magnetic field regime is also called referred to as anomalous Zeeman shift. In this regime, energy of the m_F states is given by:

$$E = \frac{1}{2} A_{\text{hfs}} K + \mu_B g_F m_F B, \tag{4.32}$$

where:

$$K = F(F+1) - I(I+1) - J(J+1), \tag{4.33}$$

and μ_B is the Bohr magneton, g_F is the Landé factor, m_F is the sub-state and B is the magnetic field. It has been assumed that $\boldsymbol{B}$, ∇B, $\boldsymbol{g}$ and $\boldsymbol{k}_{\text{eff}}$ are parallel with each other, with their vector directions being in the same direction and only in the z-axis. The Landé g_F factor is known for the different states but can also be calculated using:

$$g_F \simeq g_J \frac{F(F+1) + J(J+1) - I(I+1)}{2F(F+1)}. \tag{4.34}$$

For ^{87}Rb $|5^2S_{1/2}\rangle$ state, $J = 1/2$ and $I = 3/2$. A_{hfs} is the magnetic dipole constant and for the $|5^2S_{1/2}\rangle$ state, $A_{\text{hfs}} = h \cdot 3.417$ GHz. This weak-field regime is valid if $A_{\text{hfs}} >> g_J \mu_B B$, where g_J is the fine structure Landé factor ($g_J = 2.002$ for $|5^2S_{1/2}\rangle$). This is usually satisfied with magnetic fields of less than 10^{-3} T. If the magnetic field term is ignored, this equation yields the hyperfine splitting of the $|5^2S_{1/2}\rangle$ state that agrees with [96].

4.2.1.2 Intermediate Magnetic Field

The intermediate magnetic field regime is a more difficult regime to calculate. However, for the $|J = 1/2\rangle$ state, this can be solved relatively easily, with the final energy of the

state being calculable using the Breit-Rabi formula:

$$E = -\frac{E_{\text{hfs}}}{2(2I+1)} + g_I \mu_B m B \pm \frac{E_{\text{hfs}}}{2}\left(1 + \frac{4mx}{2I+1} + x^2\right)^{1/2}, \tag{4.35}$$

where $E_{\text{hfs}} = A_{\text{hfs}}(I + 1/2)$ is the hyperfine splitting, g_I is the nuclear g-factor (g_I = -0.000995 in our case) and $m = m_I \pm m_J = m_I \pm 1/2$ (where $\pm$ sign in the equation above is taken to be the same as the one in this equation of the sub-state). The symbol x is given by:

$$x = \frac{(g_J - g_I)\mu_B B}{E_{\text{hfs}}}. \tag{4.36}$$

For weaker magnetic fields, the m state becomes the m_F state. As the magnetic field gets stronger, the m_J states start to dominate.

As our interferometers are likely to work in the weak and intermediate regimes, it is useful to understand how this intermediate-field regime fits in with the weak-field regime. The first step is to recognise that as $B \to 0$, F becomes a good quantum number. This means that the state m can be rewritten as m_F. The last term of equation (4.35) contains an equation of the form $(1+ax+x^2)^{1/2}$. This can be expanded around $x = 0$:

$$(1+ax+x^2)^{1/2} = 1 + \frac{ax}{2} + \frac{1}{8}(4-a^2)x^2 + \frac{1}{16}a(a^2-4)x^3 + \frac{1}{128}(-5a^4+24a^2-16)x^4 + ... \tag{4.37}$$

As $B \to 0$, $x \to 0$ and so the higher order terms can be ignored:

$$(1 + ax + x^2)^{1/2} \simeq 1 + \frac{ax}{2}. \tag{4.38}$$

Equation (4.35) can be simplified using this expansion (together with $I = 3/2$ for ^{87}Rb

and $g_I \simeq 0$):

$$E = -\frac{E_{\text{hfs}}}{8} \pm \frac{E_{\text{hfs}}}{2} \pm \frac{E_{\text{hfs}} m_F x}{4}, \tag{4.39}$$

where the $\pm$ is set depending on whether it is the higher or the lower state. Since $g_{|F=2\rangle} = +1/2$ and $g_{|F=1\rangle} = -1/2$, this can be simplified further:

$$E = -\frac{E_{\text{hfs}}}{8} + g_F E_{\text{hfs}} + \frac{g_F E_{\text{hfs}} m_F x}{2}. \tag{4.40}$$

The last step is to substitute the expression for x together with $(g_J - g_I) \simeq 2$ to obtain:

$$E = -\frac{E_{\text{hfs}}}{8} + g_F E_{\text{hfs}} + g_F m_F \mu_B B, \tag{4.41}$$

as $B \to 0$. While the notation of this equation is not the same as of the weak-field regime, calculating the energy shifts of the $|F = 1\rangle$ and $|F = 2\rangle$ states without any magnetic field produces the same energy shifts as the weak-field regime. Additionally, the energy shift due to the magnetic field has the same dependence as the weak-field regime.

4.2.1.3 Strong Magnetic Field

The last regime is the strong magnetic field regime, which satisfies the relation $g_J \mu_B B >> A_{\text{hfs}}$. In this regime, J (rather than F) becomes a good quantum number. The expression for the energy of the states is given by the Paschen-Back effect:

$$E = A_{\text{hfs}} m_J m_I + \mu_B (g_J m_J + g_I m_I) B. \tag{4.42}$$

4.2.1.4 Summary

The resulting graph of all of these regimes can be seen in Figure 4.11. The coupling of the magnetic field onto the energy levels of an atom is not a trivial matter, resulting in three different regimes depending on the strength of the magnetic field. The regimes of importance for atom interferometers are the weak- and intermediate-field regimes.

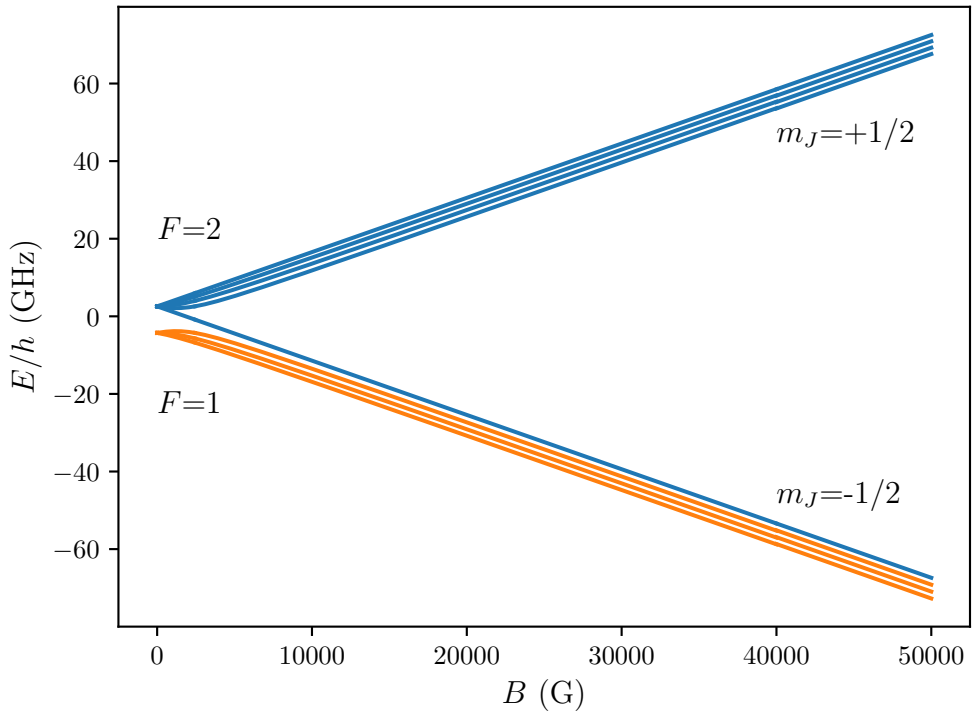


Figure 4.11: Energies of the ^{87}Rb $|5^2S_{1/2}\rangle$ state as a consequence of the magnetic field. For weak fields, F is a good quantum number while for strong fields, m_J is a good quantum number.

4.2.2 Quadratic Zeeman Effect

As was seen in sections 2.4.1.2 and 2.5.1.5, the magnetic fields mainly contribute phase contributions to the phase measurement of the interferometer via the linear and quadratic Zeeman effects. The linear Zeeman effect discussed can be seen as a

consequence of the weak-field regime, which can be countered by using the $m_F = 0$ sub-state. However, the same sections also discussed the quadratic Zeeman effect, which is also of relevance even when $m_F = 0$. The quadratic effect dependence is set by the constant of proportionality κ. This is well-known for the $m_F = 0$ state but has not been calculated for the $m_F = \pm 1$ states (to the best of the author's knowledge). We will show how the Breit-Rabi formula (intermediate-field regime) can be used to obtain this constant of proportionality for the $m_F = 0$. This will enable us to use this understanding to be able to derive this parameter for the other two sub-states.

Using the Breit-Rabi formula to calculate the energies of the $|F = 1\rangle$ and $|F = 2\rangle$ states (assuming $m = m_F$ in the lower end of the intermediate-field regime) yields:

$$E_{|F=1\rangle} = -\frac{E_{\text{hfs}}}{2(2I+1)} + g_I \mu_B m_F B - \frac{E_{\text{hfs}}}{2}\left(1 + \frac{4m_F x}{2I+1} + x^2\right)^{1/2}, \tag{4.43a}$$

$$E_{|F=2\rangle} = -\frac{E_{\text{hfs}}}{2(2I+1)} + g_I \mu_B m_F B + \frac{E_{\text{hfs}}}{2}\left(1 + \frac{4m_F x}{2I+1} + x^2\right)^{1/2}. \tag{4.43b}$$

In the case of $m_F = 0$:

$$E_{|F=2\rangle} - E_{|F=1\rangle} = E_{\text{hfs}}\left(1 + x^2\right)^{1/2}. \tag{4.44}$$

The difference in energies is only a consequence of of the hyperfine splitting and the magnetic field. Therefore, $E_{|F=2\rangle} - E_{|F=1\rangle} = E_{\text{hfs}} + E_{\text{mag}}$. Additionally, the term in brackets can be expanded around $x = 0$ as:

$$(1 + x^2)^{1/2} = 1 + \frac{x^2}{2} - \frac{x^4}{8} + ... \tag{4.45}$$

Assuming that the field is relatively weak, the higher order terms can be neglected to

Table 4.1: Parameters needed to calculate κ for the $|F=1, m_F=0\rangle \rightarrow |F=2, m_F=0\rangle$ transition of ^{87}Rb D_2 line.

$g_J(5^2S_{1/2})$	2.00233113(20)
g_I	-0.0009951414(10)
μ_B	$9.27400899(37)\times10^{-24}$ J/T = $h\times1.399624624(56)$ MHz/G
$\hbar$	$1.054571596(82)\times^{-43}$ Js
E_{hfs}	$h \times 6.83468261090429(9) \times 10^9$ Hz

obtain:

$$E_{\text{hfs}} + E_{\text{mag}} = E_{\text{hfs}}\left(1 + \frac{x^2}{2}\right), \tag{4.46}$$

leading to:

$$E_{\text{mag}} = \frac{E_{\text{hfs}}}{2}\frac{(g_J - g_I)^2\mu_B^2 B^2}{E_{\text{hfs}}^2}, \tag{4.47}$$

using the definition of x. Remembering that $E = \hbar\omega$, it is finally possible to derive the literature expression of κ as:

$$\kappa_{|F=1,m_F=0\rangle\rightarrow|F=2,m_F=0\rangle} = \frac{\omega_{|F=1,m_F=0\rangle\rightarrow|F=2,m_F=0\rangle}}{2\pi B^2} = \frac{(g_J - g_I)^2\mu_B^2}{2hE_{\text{hfs}}} = 575.15 \text{ Hz/G}^2, \tag{4.48}$$

using the values in Table 4.1. This is in line with the value quoted in [96].

From the work found in literature so far, we are in a position to calculate the linear Zeeman effect for any m_F state of ^{87}Rb interferometer and the quadratic Zeeman effect for the $m_F = 0$ by being able to obtain its constant of proportionality, κ. From now on, we will refer to the κ for the $m_F = 0$ sub-state as κ_0. However, the $|F = 1\rangle$ state has three m_F sub-states for which κ needs to be calculated. Two calculation methods are on offer - one is analytical while the other one is numerical. Although they lead to somewhat different answers; both of these can be used, in principle, for multi-modal measurements. The corresponding phase shifts and how to calculate gravity, magnetic field and magnetic field gradient from the three m_F states will also be discussed for

both of these methods.

4.2.3 Analytical κ

The first method of estimating κ will be referred to as the analytical way. In this case, we start with the energy difference of the $|F=2\rangle$ and $|F=1\rangle$ states (assuming again that towards the weak-field limit $m = m_F$):

$$E_{|F=2\rangle} - E_{|F=1\rangle} = E_{\text{hfs}}\left(1 + \frac{4m_F x}{2I+1} + x^2\right)^{1/2}, \tag{4.49}$$

where we have assumed that the m_F state is the same for both F states, i.e. $m_{|F=1\rangle} = m_{|F=2\rangle} = m_F$. This is a reasonable assumption as operating in the $m_F = 0$ sub-state in both $|F=1\rangle$ and $|F=2\rangle$ states is typical for interferometers. The equation above can be simplified using the following expansion around $x = 0$:

$$\left(1 + \frac{4m_F x}{2I+1} + x^2\right)^{1/2} = 1 + \frac{4m_F x}{2(2I+1)} + \frac{1}{8}\left(4 - \frac{16m_F^2}{(2I+1)^2}\right)x^2 + ... \tag{4.50}$$

We have only kept terms up to x^2 (and hence B^2) as the focus of our work are the linear and quadratic Zeeman effects. Additionally, since the assumption is a relatively weak magnetic field, the higher order terms become negligible. The energy difference of the two states is a consequence of the hyperfine splitting, E_{hfs}, linear Zeeman effect, E_{lin}, and the quadratic Zeeman effect, E_{quad}. Therefore, equation (4.49) can be rewritten as:

$$E_{\text{hfs}} + E_{\text{lin}} + E_{\text{quad}} = E_{\text{hfs}} + E_{\text{hfs}}\frac{4m_F x}{2(2I+1)} + \frac{E_{\text{hfs}}}{8}\left(4 - \frac{16m_F^2}{(2I+1)^2}\right)x^2. \tag{4.51}$$

From this equation, the following two identities can be deduced:

$$E_{\text{lin}} = m_F \mu_B B, \tag{4.52a}$$

$$E_{\text{quad}} = \frac{E_{\text{hfs}}}{8}\left(4 - \frac{16m_F^2}{(2I+1)^2}\right)x^2. \tag{4.52b}$$

E_{lin} agrees with the shift seen due to the linear Zeeman effect. The quadratic term can be rearranged to obtain a general expression for κ for any m_F state:

$$\kappa_{m_F} = \frac{1}{8h}\left(\frac{4(2I+1)^2 - 16m_F^2}{(2I+1)^2}\right)\frac{(g_J - g_I)^2\mu_B^2}{E_{\text{hfs}}}. \tag{4.53}$$

For $m_F = 0$, equation (4.48) is derived. Using this derivation, the $m_F = \pm 1$ states both yield the same dependence on the quadratic Zeeman effect:

$$\kappa_{\pm 1} = \frac{3}{8h}\frac{(g_J - g_I)^2\mu_B^2}{E_{\text{hfs}}}, \tag{4.54}$$

which calculates as $\kappa_1 = \kappa_{\pm 1} = 431.36$ Hz/G^2. The problem with this method is that it ignores the higher order terms of an infinite series, potentially ignoring some important effects of the other terms that are now not accounted for.

4.2.3.1 Phase Shifts

For completeness, we will now show that even if the quadratic dependence of the $m_F = \pm 1$ states is the same, it is still possible to perform a measurement of gravity, magnetic field and magnetic field gradient using these three m_F states. We will focus on the interferometer phase of each of these, referred to as Φ_0 for the $m_F = 0$ sub-state and $\Phi_{\pm 1}$ for the $m_F = \pm 1$ sub-states. Using the phase contribution equations derived

in section 2.5, these shifts become (ignoring any other systematic effects):

$$\Phi_0 = T^2\left[k_{\text{eff}}\left(g + \frac{2h}{m_{\text{Rb}}}\kappa_0 B|\nabla B|\right) - \alpha\right], \tag{4.55a}$$

$$\Phi_{+1} = T^2\left[k_{\text{eff}}\left(g + \frac{\mu_B}{m_{\text{Rb}}}|\nabla B| + \frac{2h}{m_{\text{Rb}}}\kappa_1 B|\nabla B|\right) - \alpha\right], \tag{4.55b}$$

$$\Phi_{-1} = T^2\left[k_{\text{eff}}\left(g - \frac{\mu_B}{m_{\text{Rb}}}|\nabla B| + \frac{2h}{m_{\text{Rb}}}\kappa_1 B|\nabla B|\right) - \alpha\right]. \tag{4.55c}$$

The key to using these is to find the point at which the chirp rate cancels the phase shifts exactly. As was mentioned in section 2.2, this method can be used to obtain the value of gravity. The same method can be used here, but in this case the intersection points of these also contain magnetic field information. Let us denote the intersection point for the $m_F = 0$ as α_0 and for $m_F = \pm 1$ as $\alpha_{\pm 1}$. Using a combination of these intersection points for the three m_F sub-states, it is possible to calculate gravity, magnetic field and magnetic field gradient in the following order:

$$|\nabla B| = \frac{m_{\text{Rb}}(\alpha_{+1} - \alpha_{-1})}{2k_{\text{eff}}\mu_B}, \tag{4.56a}$$

$$B = \frac{\alpha_{-1} - \alpha_0 + \frac{k_{\text{eff}}\mu_B}{m_{\text{Rb}}}|\nabla B|}{\frac{2hk_{\text{eff}}}{m_{\text{Rb}}}(\kappa_1 - \kappa_0)|\nabla B|}, \tag{4.56b}$$

$$g = \frac{\alpha_0}{k_{\text{eff}}} - \frac{2h}{m_{\text{Rb}}}\kappa_0 B|\nabla B|. \tag{4.56c}$$

4.2.4 Numerical κ

The second method to estimate κ is to use a numerical approach. The energies of the m_F sub-states of the $|F = 1\rangle$ and $|F = 2\rangle$ states are calculated using the Breit-Rabi formula. The difference of these energies is calculated as before but in this case numerically. The hyperfine splitting, E_{hfs}, and the linear Zeeman effect ($m_F\mu_B B$) are subtracted from this difference. What should remain is only the quadratic dependence

because the higher order terms should be negligible for weak fields. The resulting output of this procedure can be seen in Figure 4.12, with the B-field range chosen to be in the region of standard interferometer operation. The curves in the Figure were fitted with a polynomial equation of the form:

$$E_{\text{quad}} = E_{\text{offset}} + \xi B + \kappa B^2. \tag{4.57}$$

The legend in the figure is a reference to the m_F sub-states, e.g. 0 - 0 is the energy difference between the $m_{|F=2\rangle} = 0$ and $m_{|F=1\rangle} = 0$ sub-states. Note that the errors in the plot are the fitting errors. These are very small given the values of ξ and κ and hence register as 0 given the accuracy quoted. As this is an initial investigation of multi-modal measurements, these will be ignored and have only been left to showcase that the fits produce values with low errors.

Using this numerical approach, κ_0 was calculated as 574.96 Hz/G^2, which is different by less than 1% to the value obtained analytically. As expected, the $m_F = 0$ sub-state does not have any extra B dependence as $\xi = 0$. As this is a plot of energy differences after subtracting the hyperfine splitting and the linear Zeeman shift, this is to be expected. The $m_F = \pm 1$ energy differences are the more interesting results. The good news is that the fit for $m_F = +1$ produces $\kappa_{+1} = 431.08$ Hz/G^2 while the fit for $m_F = -1$ produces $\kappa_{-1} = 431.35$ Hz/G^2. Both of these are less than 1% different to the analytical value obtained; therefore, even in this case we will assume that $\kappa_{-1} = \kappa_{+1} = \kappa_1$. The more interesting artefact is the B dependence. Fitting the curve with only B^2 dependence did not produce a good fit and hence the B dependence had to be introduced into the fitting equation. It is not clear where this dependence comes from, especially physically. Critically, it appears that the analytical approach assumes that this energy difference (after the subtraction of the hyperfine splitting and the linear

Zeeman effect) will only increase for both $m_F = \pm 1$ for all B. However, the numerical approach highlights that while the $m_F = +1$ energy difference increases, the $m_F = -1$ energy difference decreases for the B-field range investigated. More investigation of this is definitely needed to ascertain the reason for this and whether an important factor has been missed in either approaches. However, for now, since $\xi_{+1} = 2096$ Hz/G and $\xi_{-1} =$ -2096 Hz/G, we will assume that $\xi_{-1} = -\xi_{+1}$ for the numerical approach.

It should be emphasised that the field strengths investigated here have been chosen in line with the magnetic field strengths that standard atom interferometers tend to operate in. Increasing the B field starts to change the fitted values of $\xi_{\pm 1}$ and $\kappa_{\pm 1}$. Therefore, if larger fields are to be measured, this approach should be investigated further, especially since the Breit-Rabi formula is only valid in the intermediate-field regime. In general, this method has an advantage over the analytical one in the sense that apart from assuming what the equation for the linear Zeeman effect is, no other assumptions are made. Therefore, this method is likely to be a better way of estimating κ for the $m_F \neq 0$ states. However, it does have outstanding questions that require further investigation.

4.2.4.1 Phase Shifts

In analogy with the analytical solution, the phase shifts of the different m_F sub-states are needed. The $\xi_{\pm 1}$ values pose a problem as to how these couple to the interferometer phase. In this work, we will assume that the coupling of this is in line with how the the linear and quadratic Zeeman effects couple into the interferometer phase. Therefore,

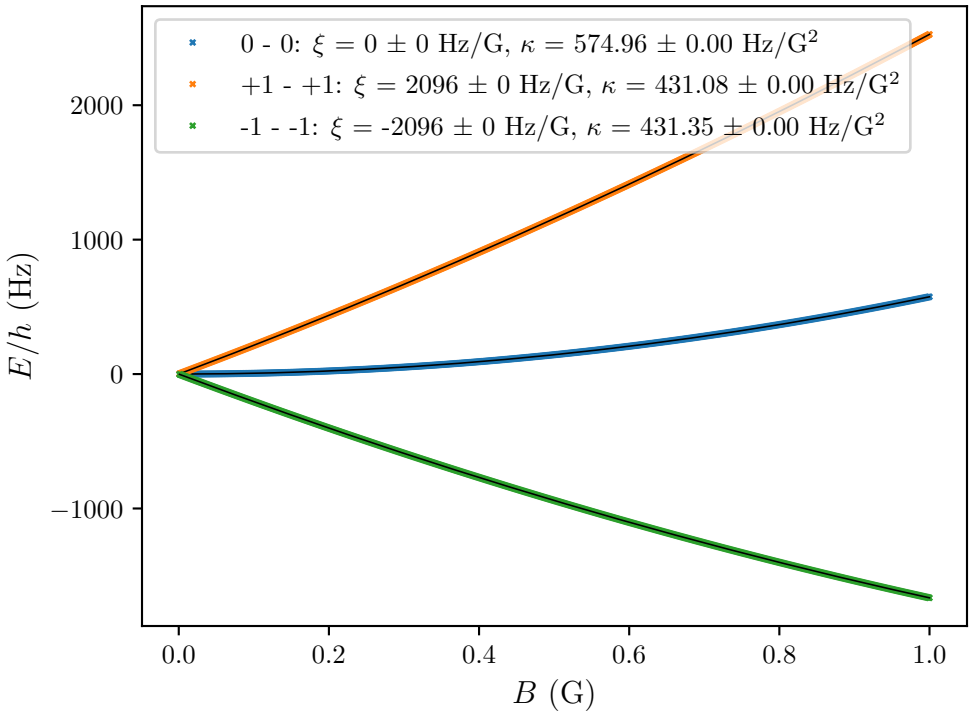


Figure 4.12: Numerically-calculated energy differences between the $m_{|F=2\rangle}$ and $m_{|F=1\rangle}$ sub-states. These are the remaining energy differences after the subtraction of the hyperfine splitting and the linear Zeeman effect. The black solid lines are the fits of these energy differences that have been used to calculate ξ and κ, which are the coefficients of the B and B^2 dependencies, respectively.

the equations for the phase shifts of the three separate m_F sub-states are:

$$\Phi_0 = T^2\left[k_{\text{eff}}\left(g + \frac{2h}{m_{\text{Rb}}}\kappa_0 B|\nabla B|\right) - \alpha\right], \tag{4.58a}$$

$$\Phi_{+1} = T^2\left[k_{\text{eff}}\left(g + \left(\frac{\mu_B + h\xi_{+1}}{m_{\text{Rb}}}\right)|\nabla B| + \frac{2h}{m_{\text{Rb}}}\kappa_1 B|\nabla B|\right) - \alpha\right], \tag{4.58b}$$

$$\Phi_{-1} = T^2\left[k_{\text{eff}}\left(g - \left(\frac{\mu_B + h\xi_{+1}}{m_{\text{Rb}}}\right)|\nabla B| + \frac{2h}{m_{\text{Rb}}}\kappa_1 B|\nabla B|\right) - \alpha\right]. \tag{4.58c}$$

Similarly to the analytical approach, gravity, magnetic field and magnetic field

gradient can be obtained in the following order:

$$|\nabla B| = \frac{m_{\mathrm{Rb}}(\alpha_{+1} - \alpha_{-1})}{2k_{\mathrm{eff}}(\mu_B + h\xi_{+1})}, \tag{4.59a}$$

$$B = \frac{\alpha_{-1} - \alpha_0 + k_{\mathrm{eff}}\left(\frac{\mu_B + h\xi_{+1}}{m_{\mathrm{Rb}}}\right)|\nabla B|}{\frac{2hk_{\mathrm{eff}}}{m_{\mathrm{Rb}}}(\kappa_1 - \kappa_0)|\nabla B|}, \tag{4.59b}$$

$$g = \frac{\alpha_0}{k_{\mathrm{eff}}} - \frac{2h}{m_{\mathrm{Rb}}}\kappa_0 B|\nabla B|. \tag{4.59c}$$

Therefore, while both of these approaches of derivation give slightly different results, with the numerical approach including an extra B dependence, it is possible to obtain all three parameters in both of these cases.

4.2.5 Quantum Projection Uncertainties

We will now try to estimate the quantum projection limits of these measurements in simple terms to see whether this work holds potential. As was touched on in section 2.2.1, the gravity uncertainty due to quantum projection noise is [43]:

$$\sigma_g = \frac{1}{k_{\mathrm{eff}}T^2\sqrt{N}}. \tag{4.60}$$

For an example of a $T = 50$ ms atom interferometer with $N = 1 \times 10^6$ atoms taking part in the interferometer, this leads to a sensitivity of $\sigma_g \simeq 3 \times 10^{-8}$ ms^{-2} per shot.

For the magnetic field gradient atom shot noise limit, we will ignore the extra $h\xi_{\pm1}/m_{\mathrm{Rb}}$ term and only consider the linear Zeeman effect. This is because the extra term is only applicable for the numerical approach and not the analytical one. Additionally, the linear Zeeman effect is the dominant effect (with a scaling factor of $\sim$1.4 MHz/G) from these two, almost three orders of magnitude bigger than this additional term. Hence ignoring it will not give any misleading or optimistic results.

Consequently, in analogy with gravity, the magnetic field gradient uncertainty due to quantum projection noise is:

$$\sigma_{|\nabla B|} = \frac{m_{\mathrm{Rb}}}{k_{\mathrm{eff}}\mu_B m_F T^2\sqrt{N}}. \tag{4.61}$$

For an example of a $T = 50$ ms atom interferometer with $N = 1 \times 10^6$ atoms taking part in the interferometer, this leads to a sensitivity of $\sigma_{|\nabla B|} \simeq 4 \times 10^{-6}$ Gm^{-1} per shot for $m_F = +1$.

The gravity and magnetic field gradient (ignoring the $h\xi_{\pm 1}/m_{\mathrm{Rb}}$ term) atom shot noise uncertainties appear to be low, meaning that it seems like it is possible to measure both of these with high sensitivity. However, more work needs to be done to check that these uncertainty limits could be reached in theory because the multi-modal measurements rely on combining different m_F measurements together. Additionally, the magnetic field uncertainty limit is not so easily obtained as the quadratic Zeeman effect is dependent on both B and $|\nabla B|$, meaning that they are coupled.

4.2.6 Summary

We have investigated the possibility of multi-modal measurements of gravity, magnetic field and magnetic field gradient using a Mach-Zehnder atom interferometer utilising stimulated Raman transitions in ^{87}Rb. This can be achieved by obtaining the chirp rate scans of the three $m_F = 0$ and $m_F = \pm 1$ sub-states and using them in combination to calculate all of these parameters. A particular challenge has been found in obtaining the quadratic Zeeman shift of an atom interferometer utilising the $m_F = \pm 1$ sub-states. Two potential methods of obtaining the coefficients of proportionality have been demonstrated. Both of these methods have their limitations but the more likely one has been highlighted. While giving different results, in both cases it is possible to

obtain the measurements of all three parameters. Calculating the simple atom shot noise limit of gravity and magnetic field gradient seems to offer promising sensitivities that can be utilised in real-world applications.

The next steps in validating this work would be to be able to measure and/or deduce the $\kappa_{\pm 1}$ and $\xi_{\pm 1}$ values to validate whether the experiment agrees with what has been derived or whether something has been missed. One simple experimental example could be to perform the measurements mentioned in preceding sections with the three m_F sub-states in a known magnetic field to check which of the methods (if either) agrees. The uncertainty limits of these parameters should also be looked at in more detail because these have been estimated in a simple way but obtaining these parameters is done by combining different measurements together. It could also be beneficial to start looking at whether it is possible to drive an interferometer with all of the three m_F sub-states simultaneously followed by individually imaging these different sub-states at the end of the sequence. This would mean that all three m_F sub-state chirp rate scans could be performed and imaged in the same experimental shot.

Chapter 5

Cross-coupling

This chapter is concerned with the simulations of the cross-coupling effect of an accelerating atom interferferometer. It is currently being drafted into a paper and hence this chapter is largely written in the style of a paper, with its own Introduction and Conclusion. However, there are still some outstanding questions with regards to this modelling prior to submission. These will be discussed and are left to be concluded following the submission of this thesis. The only addition is section 5.6, in which we will discuss outstanding work with regards to these results as well as a potential way to observe this effect using Rabi oscillations. This thesis' author is the first author of this paper, with the co-authors (Andrew Lamb, Samuel Lellouch and Michael Holynski) providing supervision, advice and feedback.

5.1 Introduction

Atom interferometers have a rich history, spanning over 25 years since their first demonstration [41]. They are appealing in a range of applications due to their precision [40]. Therefore, their uses are being investigated in fields ranging from testing the foundations of physics, such testing the equivalence principle [40, 143], to commercial quantum

technologies, such underground detection for gravity cartography [6], navigation map matching [7] and unstaffed aerial vehicle uses [144].

An atom interferometer manipulates atomic population levels using a laser(s), which allows us to create a gravity sensor. This is achieved by letting the atoms free-fall and applying a series of laser pulses at specific times. The most common interferometer to measure gravity uses a series of three pulses that coherently divide, deflect and recombine the atomic wavepackets [88]. Equation (2.31), showing the probability of atoms ending up in the excited state at the end of this sequence, can be rewritten more generally as [41, 88, 89]:

$$P = P_0 - \frac{C}{2}\cos[(\boldsymbol{k}_{\text{eff}} \cdot \boldsymbol{g} - \alpha)T^2], \tag{5.1}$$

where C is the contrast of the atom interferometer, $\boldsymbol{g}$ is the acceleration due to the gravity experienced by the atoms, $\boldsymbol{k}_{\text{eff}}$ is the effective propagation vector of the laser(s) and α is the chirp rate, i.e. the rate of change of laser frequency to account for the Doppler shift as a consequence of the atoms falling with respect to the laser(s) [41, 85].

While the use of quantum gravity sensors has been recognised, major challenges still remain to make them fully use-able in real-life applications and to expand their versatility. A key challenge is the ability to measure in dynamic conditions. Demonstrations of dynamic quantum gravimeter operation have been published [13, 74] but their capability in this regard is still an active area of research. One of the consequences of dynamic motion is that if the sensor is accelerating with a component transverse to the laser direction during the measurement, the free-falling atoms will not be subjected to this force. Given current state of the art in field deployment means that this effect is not dominant. However, as these technologies progress and their performance improves, this will lead to this effect becoming substantial. The consequence of this

cross-coupling is the loss of visibility of contrast due to the fact that the atoms move in the intensity profile of the laser beam(s). In this chapter, we investigate this effect by analysing the contrast loss and "apparent" phase shift seen. Additionally, we explore this effect for clouds with different horizontal temperatures and finish by suggesting a compensation technique utilising a quantum gravimeter in conjunction with a classical accelerometer.

5.2 Method

Let us assume that we have a three-level atom with two lower states $|a>$ and $|b>$ and an excited state $|e>$, as seen in Figure 5.1(a), where we have defined the single-photon detuning as Δ and the two-photon detuning as δ. We apply a pair of counter-propagating stimulated Raman light beams with angular frequencies ω_1 and ω_2 that couple $|a>$ with $|e>$ and $|b>$ with $|e>$, respectively [41, 85]. For this system, it can be shown that the time-dependent complex amplitudes of probability of $|a>$ and $|b>$ are [87]:

$$C_a(t_0+\tau) = e^{-i(|\boldsymbol{p}|^2/2m\hbar+\omega_a)(t_0+\tau)} e^{i(-\Omega_{\mathrm{AC}}+\delta)\tau/2} \Bigg\{ -i\frac{\Omega_{\mathrm{eff}}}{\Omega_{\mathrm{R}}} \sin\left(\frac{\Omega_{\mathrm{R}}\tau}{2}\right) e^{i(\delta t_0+\phi_{\mathrm{eff}})} c_b(t_0) + \left[\cos\left(\frac{\Omega_{\mathrm{R}}\tau}{2}\right) + i\frac{(\delta_{\mathrm{AC}}-\delta)}{\Omega_{\mathrm{R}}} \sin\left(\frac{\Omega_{\mathrm{R}}\tau}{2}\right)\right] c_a(t_0) \Bigg\}, \tag{5.2a}$$

$$C_b(t_0+\tau) = e^{-i(|\boldsymbol{p}+\hbar\boldsymbol{k}_{\mathrm{eff}}|^2/2m\hbar+\omega_b)(t_0+\tau)} e^{i(-\Omega_{\mathrm{AC}}-\delta)\tau/2} \Bigg\{ -i\frac{\Omega_{\mathrm{eff}}}{\Omega_{\mathrm{R}}} \sin\left(\frac{\Omega_{\mathrm{R}}\tau}{2}\right) e^{-i(\delta t_0+\phi_{\mathrm{eff}})} c_a(t_0) + \left[\cos\left(\frac{\Omega_{\mathrm{R}}\tau}{2}\right) - i\frac{(\delta_{\mathrm{AC}}-\delta)}{\Omega_{\mathrm{R}}} \sin\left(\frac{\Omega_{\mathrm{R}}\tau}{2}\right)\right] c_b(t_0) \Bigg\}, \tag{5.2b}$$

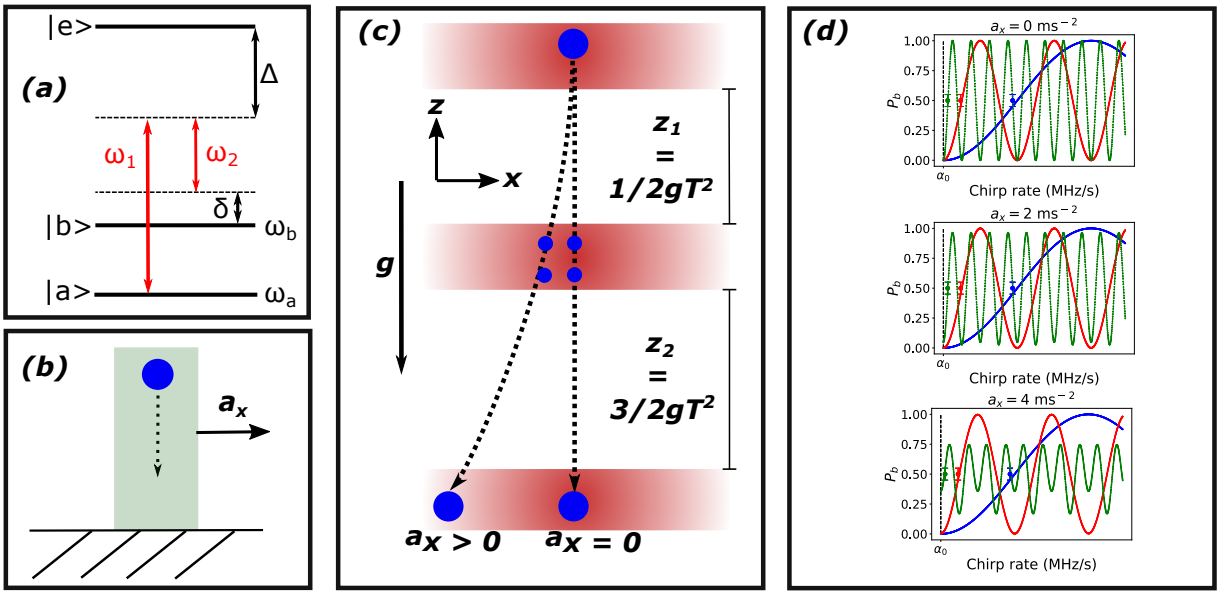


Figure 5.1: **(a)** Three-level atom diagram, showing the ground states $|a>$ and $|b>$ and the excited state $|e>$ and the two laser frequencies ω_1 and ω_2. These are detuned from $|e>$ by Δ and δ from the state $|b>$. **(b)** Diagram illustrating the acceleration, a_x, acting on the sensor head while the atoms (blue circle) are in free-fall. The atoms will not feel the force producing this acceleration during their free-fall. **(c)** If $a_x = 0$, the atomic cloud (blue circles) does not move horizontally and remains in the centre of the Gaussian intensity profile. In the case of $a_x > 0$, the atomic cloud moves in the intensity profile of the beams, reducing the contrast seen at the output. The size of the pulses is for illustrative purposes to explain the movement in the intensity profile. **(d)** α scans showing the outputs of our simulations for $a_x = 0$, $a_x = 2$ ms^{-2} and $a_x = 4$ ms^{-2} for a number of T times - 10 ms (blue), 20 ms (red) and 40 ms (green). These are plotted with a single atom and no thermal expansion. α_0 represents the value at which g is cancelled exactly and is the first value of the α scan to help with the "apparent" phase shift calculation. The shape of these will be discussed in section 5.3.

where Ω_{eff} is the effective Rabi frequency, Ω_{AC} is the total AC Stark shift, δ_{AC} is the differential AC Stark shift, Ω_{R} is the generalised Rabi frequency given by $\Omega_{\text{R}} = \sqrt{|\Omega_{\text{eff}}|^2 + (\delta_{\text{AC}} - \delta)}$. ϕ_j is the phase of the laser, and ω_a and ω_b are the internal energies of the ground and excited states, respectively [85, 87, 145].

The movement of the atoms in the laser beams as the sensor accelerates has an effect on the Rabi frequency of the transition, which can be calculated using the formula [94]:

$$\Omega_{\text{eff}} = \frac{\sqrt{I_1 I_2}}{c\epsilon_0 \hbar^2} \frac{D^2}{\Delta} \frac{\sqrt{4 - m_F^2}}{12}, \tag{5.3}$$

where I_1, I_2 are the intensities of the two laser beams (where we have set $I_2 \simeq 1.89 I_1$ to cancel the AC Stark shift given our value of $\Delta = 2\pi \times 1.4$ GHz and assuming orthogonal linear polarisations [51]), c is the speed of light, ϵ_0 is the electric constant, D is the transition dipole matrix element of the D_2 line of ^{87}Rb ($D = 3.584 \times 10^{-29}$ Cm [96]), and the fraction is a geometric factor related to the Clebsch-Gordan coefficients for ^{87}Rb, which is valid if the two laser beams have equal polarisations. In our simulations, the state $m_F = 0$ has been used, which is common practice in atom interferometry.

Assuming that the intensities of the Raman beams are set so that the AC Stark shift is cancelled, equations (5.2a) and (5.2b) reduce to [89]:

$$C_a(p, t_0 + \tau) = e^{-i\omega_a \tau} \left\{ \cos\left(\frac{\Omega_{\text{R}} \tau}{2}\right) C_a(p, t_0) - i e^{i(\omega_{\text{L}} t_0 + \phi_j)} \sin\left(\frac{\Omega_{\text{R}} \tau}{2}\right) C_b(p, t_0) \right\}, \tag{5.4a}$$

$$C_b(p, t_0 + \tau) = e^{-i\omega_b \tau} \left\{ \cos\left(\frac{\Omega_{\text{R}} \tau}{2}\right) C_b(p, t_0) - i e^{-i(\omega_{\text{L}} t_0 + \phi_j)} \sin\left(\frac{\Omega_{\text{R}} \tau}{2}\right) C_a(p, t_0) \right\}. \tag{5.4b}$$

To perform our simulations, we we have set $\omega_a = 0$, $\omega_b = 2\pi \times 6.835$ GHz and the difference in the laser frequencies, $\omega_L = \omega_1 - \omega_2 = 2\pi \times 6.835$ GHz. The fact that the AC Stark shift is cancelled and that $\delta = 0$ ($\omega_{ba} = \omega_L$) means that $\Omega_{\text{R}} = \Omega_{\text{eff}}$.

The Mach-Zehnder atom interferometer is composed of three laser pulses, each separated by interrogation time T during the free-fall of the atoms. Our simulations are performed using two approaches, both utilising equations (5.4a) and (5.4b) as the starting point. Firstly, an analytical solution was obtained using these equations by rewriting these equations as matrices and multiplying these for the three pulses and

the two free evolution times, where the free evolution times can be taken to have the same form as the laser pulses but with $\Omega_{\mathrm{R}} = 0$. The final analytical solution of the Mach-Zehnder (which can be seen derived in Appendix G) is then given by:

$$
\begin{aligned}
P_b = {} & \cos^2\left(\frac{\Omega_{\mathrm{R}1}\tau_1}{2}\right)\cos^2\left(\frac{\Omega_{\mathrm{R}2}\tau_2}{2}\right)\sin^2\left(\frac{\Omega_{\mathrm{R}3}\tau_3}{2}\right) + \sin^2\left(\frac{\Omega_{\mathrm{R}1}\tau_1}{2}\right)\sin^2\left(\frac{\Omega_{\mathrm{R}2}\tau_2}{2}\right)\cdot \\
& \sin^2\left(\frac{\Omega_{\mathrm{R}3}\tau_3}{2}\right) + \cos^2\left(\frac{\Omega_{\mathrm{R}1}\tau_1}{2}\right)\sin^2\left(\frac{\Omega_{\mathrm{R}2}\tau_2}{2}\right)\cos^2\left(\frac{\Omega_{\mathrm{R}3}\tau_3}{2}\right) + \sin^2\left(\frac{\Omega_{\mathrm{R}1}\tau_1}{2}\right)\cdot \\
& \cos^2\left(\frac{\Omega_{\mathrm{R}2}\tau_2}{2}\right)\cos^2\left(\frac{\Omega_{\mathrm{R}3}\tau_3}{2}\right) + 2\cos\Big[(T+\tau_1)(\omega_{ba}-\omega_{\mathrm{L}}) + \phi_1 - \phi_2\Big]\cdot \\
& \sin\left(\frac{\Omega_{\mathrm{R}1}\tau_1}{2}\right)\cos\left(\frac{\Omega_{\mathrm{R}1}\tau_1}{2}\right)\sin\left(\frac{\Omega_{\mathrm{R}2}\tau_2}{2}\right)\cos\left(\frac{\Omega_{\mathrm{R}2}\tau_2}{2}\right)\cos\left(\frac{2\Omega_{\mathrm{R}3}\tau_3}{2}\right) \\
& + 2\cos\Big[(T+\tau_2)(\omega_{ba}-\omega_{\mathrm{L}}) + \phi_2 - \phi_3\Big]\sin\left(\frac{\Omega_{\mathrm{R}2}\tau_2}{2}\right)\cos\left(\frac{\Omega_{\mathrm{R}2}\tau_2}{2}\right)\cdot \\
& \sin\left(\frac{\Omega_{\mathrm{R}3}\tau_3}{2}\right)\cos\left(\frac{\Omega_{\mathrm{R}3}\tau_3}{2}\right)\cos\left(\frac{2\Omega_{\mathrm{R}1}\tau_1}{2}\right) + \sin\left(\frac{\Omega_{\mathrm{R}1}\tau_1}{2}\right)\cos\left(\frac{\Omega_{\mathrm{R}1}\tau_1}{2}\right)\cdot \\
& \sin\left(\frac{\Omega_{\mathrm{R}3}\tau_3}{2}\right)\cos\left(\frac{\Omega_{\mathrm{R}3}\tau_3}{2}\right)\Bigg\{\Big[2\cos(2T+\tau_1+\tau_2)(\omega_{ba}-\omega_{\mathrm{L}}) + \phi_1 - \phi_3\Big]\cos^2\left(\frac{\Omega_{\mathrm{R}2}\tau_2}{2}\right) \\
& - 2\cos\Big[(\tau_1-\tau_2)(\omega_{ba}-\omega_{\mathrm{L}}) + \phi_3 - 2\phi_2 + \phi_1)\Big]\sin^2\left(\frac{\Omega_{\mathrm{R}2}\tau_2}{2}\right)\Bigg\},
\end{aligned}
\tag{5.5}
$$

where $\omega_{ba} = \omega_b - \omega_a$, $\Omega_{\mathrm{R}j}$ and τ_j with $j = 1, 2, 3$ identifying the three laser pulses. As these laser pulses are performed during the free-fall, we have set $\phi_1 = 0$, $\phi_2 = \frac{1}{2}kgT^2 + (\omega_L - \frac{1}{2}\alpha T)T$ and $\phi_3 = 2kgT^2 + 2(\omega_L - \alpha T)T$.

The second approach, which is numerical, also uses equations (5.4a) and (5.4b) but the complex amplitudes of probabilities are calculated numerically after each part of the sequence using matrix multiplication. The probability is only calculated on the final complex amplitudes of probabilities after including the three pulses and the two free evolutions.

As is clear from equation (5.3), to calculate the Rabi frequencies at each of the three pulses, we need to be able to calculate the intensity of the laser beam at the position of the atoms as they move in transverse direction to the laser beams. To this end, we

model the laser intensity as a 2D Gaussian, $I(x,y) = 2P/(\pi w_0^2)\exp\left(-2(x^2+y^2)/w_0^2\right)$, where P is the power in the centre of the beam and w_0 is the waist radius [146]. The simulations have assumed that the intensity variation along the z-axis is negligible compared to the intensity variation along the horizontal direction and set $y = 0$ m as the concern is only dynamics in 1D, i.e. the x-direction. The following estimations have been used: $P = 200$ mW and $w_0 = 16.95$ mm.

The simulations are not concerned with the creation of cold atoms, therefore the dynamics of magneto-optical traps and molasses are not dealt with. To simplify the issue, our simulations are performed with 10^6 atoms, which is a reasonable assumption if using a magneto-optical trap and applying a velocity-selective Raman transition. Assuming that there is no acceleration in the x-direction, a_x, during the first pulse, the initial atomic positions are randomly generated centred at $x = 0$ m and using a normalised Gaussian probability, $(2\pi\sigma^2)^{-1/2}\exp(-x^2/2\sigma^2)$, with standard deviation of $\sigma = 1$ mm. Following this, the atomic positions during the pulses are calculated using the equations of motion, taking into account a_x as well as the ballistic thermal expansion of the cloud, neglecting the time of the individual pulses themselves and only using the interrogation time T. The cloud temperature is converted into expansion velocity, $v_{\text{exp}} = \sqrt{k_B T_{\text{temp}}/m}$, where k_B is the Boltzmann constant, T_{temp} is the atomic temperature and m is the mass of the atom. v_{exp} is then used to set the scale of the Maxwell-Boltzmann distribution $\sqrt{2/\pi}v_x^2/v_{\text{exp}}^3\exp(-v_x^2/2v_{\text{exp}}^2)$, where v_x is the speed of the atoms, to obtain the speeds of all of the individual atoms - with half of these speeds given negative velocities as the cloud expands in both positive and negative x.

5.3 Results

The simulations are analysed by taking the output probability of state $|b>$ as a function of α, which are the well-known gravity fringes. This is performed for each atom individually for each horizontal acceleration, taking an average across the spatial extend of the cloud.

The contrast is taken as the height difference of the peaks, i.e. the difference between the maximum value of the oscillation and the minimum one. The contrast loss seen with increasing T and a_x can be seen in Figure 5.2 for a cloud with horizontal temperature of 2.5 μK. Limiting ourselves to the case when the centre of mass of the atomic cloud is still within the laser beam waist radius at the third pulse (as depicted by the vertical lines), there is a contrast drop seen for both $T = 40$ ms and $T = 80$ ms. For $T = 40$ ms, the contrast has dropped to 49% at the green vertical line while for $T = 80$ ms, the contrast has dropped to 59% at the yellow vertical line. Therefore, a significant contrast loss is seen even when the centre of mass of the cloud is within the laser beam. However, one caveat has to be mentioned. As was seen in Figure 5.1(d), the gravity fringes for $T = 40$ ms at $a_x \neq 0$ ms^{-2} exhibit strange behaviour that needs to be investigated as this is within the intensity profile of the laser. This strange effect appears to come from the inclusion of $\boldsymbol{g}$, α and ω_{L} dependence during each of the ϕ_1, ϕ_2 and ϕ_3. If we set $\phi_1 = \phi_2 = 0$ and $\phi_3 = (kg - \alpha)T^2$ then this strange behaviour is not observed; in this instance the contrast decreases and the centre of oscillation shifts. This behaviour needs to be investigated further to understand whether this is due to the limitation of the simulations or due to physical effects. The contrast behaviour after the cloud leaves the laser beam is attributed to the fact that the oscillations are no longer gravity fringes but rather interferometry with two pulses or one pulse. These either need further investigation as well or the work could just concentrate on keeping

the atomic cloud within the beam. It is instructive to observe that if dealing with small T (such as is the case for $T = 10$ or 20 ms in our simulations) or small a_x, it is possible to ignore the contrast loss due to this effect.

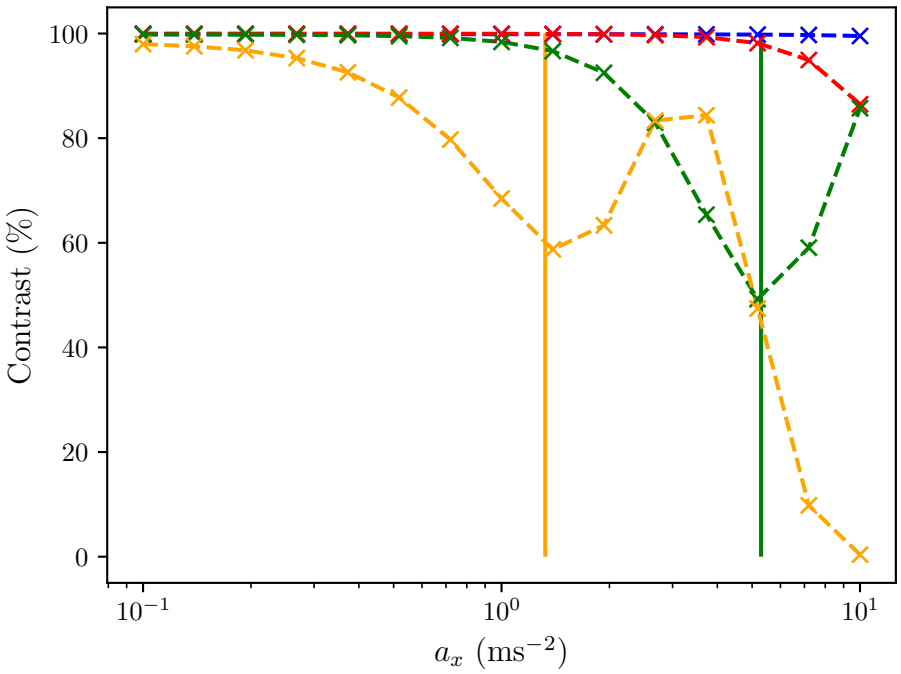


Figure 5.2: A plot showing contrast loss due to a_x for $T = 10$ ms (blue), 20 ms (red), 40 ms (green) and 80 ms (yellow) - using both the analytical (dashed line) and numerical (crosses) simulation approaches. The vertical lines show when the centre of mass of the atomic cloud at the third pulse reaches 16.95 mm, i.e. w_0.

We have also investigated the "apparent" phase shifts due to this cross-coupling effect. We imagine that we are trying to position our interferometer on the $P_b = 0.5$ line, as this is where the interferometer is the most sensitive to changes - this is a common method in atom interferometry [89]. The α scan is set so that it starts with α that exactly cancels out g, i.e. $\alpha_0 = k_{\text{eff}}g$. Taking a case of a single atom with no acceleration, we calculate the α at which the first value of $P_b = 0.5$ is present - this is taken as the reference for a perfect interferometer. Using this as a reference, we compare other cases against this reference, i.e. we calculate α at which $P_b = 0.5$

for the first time in other scenarios. If the difference in P_b between the reference and the newly calculated value is less than 0.05 (10% tolerance) then P_b is taken to be the same as reference and there is no phase shift. If the difference is larger than this tolerance, we calculate the difference in α and convert it into phase shift. If value of $P_b = 0.5$ cannot be found in the α scan of an atom then this atom is disregarded from the analysis. The reference points at which this first $P_b = 0.5$ occurs for a range of T in our simulations can be seen in the α scans in Figure 5.1(d).

The results of this analysis for an averaged atomic cloud can be seen in Figure 5.3 for a cloud with horizontal temperature of 2.5 μK. Again, even when the centre of mass is within the radius waist by the third pulse, this leads to an "apparent" phase shift of 0.56 rad for $T = 80$ ms and 0.58 rad for $T = 40$ ms. Small variation is seen for a long range of smaller accelerations, with phase shift becoming more prominent once the centre-of-mass of the cloud starts reaching the laser width at the third pulse. The behaviour past this point is once again strange, probably as before, due to the fact that the chirp rate scans produced are no longer true chirp rate scans. The limit of ~ -1.6 rad is partly due to the fact that we have assumed that the first pulse always occurs with the atoms in the centre and hence the central line of the oscillations returns to $P_b = 0.5$ for the entirety of the α scan once contrast reaches 0%. This calculation of the "apparent" phase shift is one of the outstanding questions as to its appropriateness and the tolerance used.

Lastly, we look at the dependence of the contrast loss and "apparent" phase shift on both the horizontal temperature (we have assumed that the temperature along the z-axis is zero) and a_x. These contour plots can be seen in Figure 5.4. As can be seen, this effect is more important for high temperatures and accelerations although an effect is also seen for low temperatures and a_x as well. These are instructive in understanding parameters where this effect can be ignored and where care must be taken.

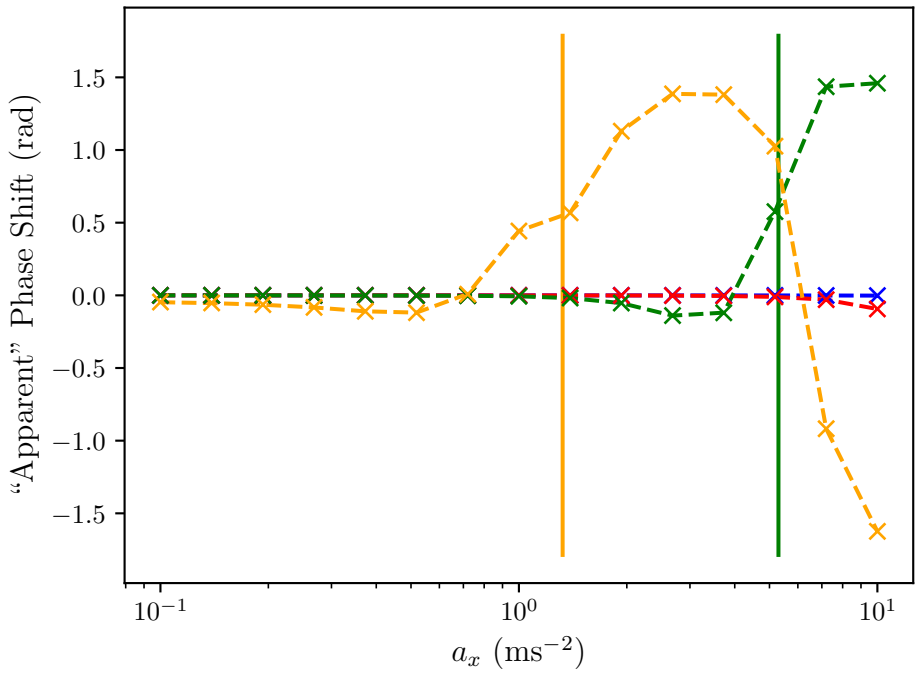
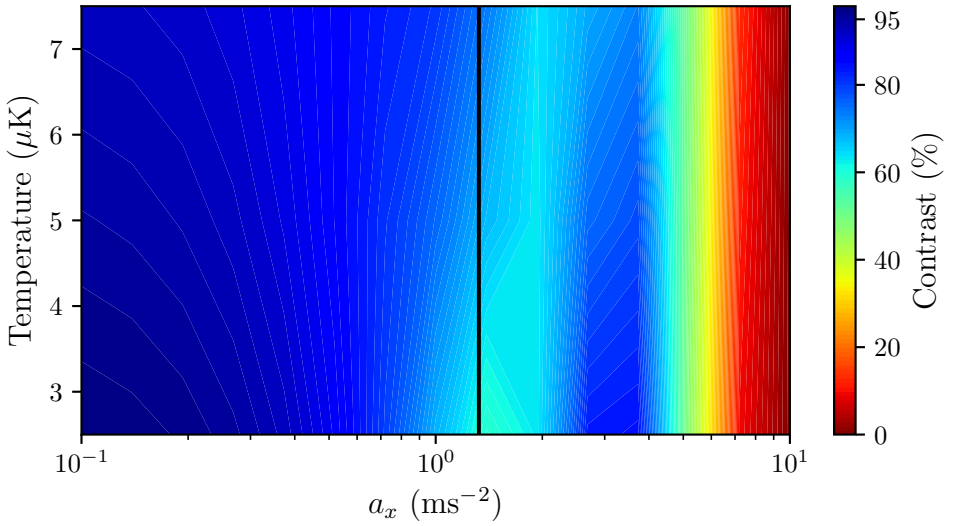


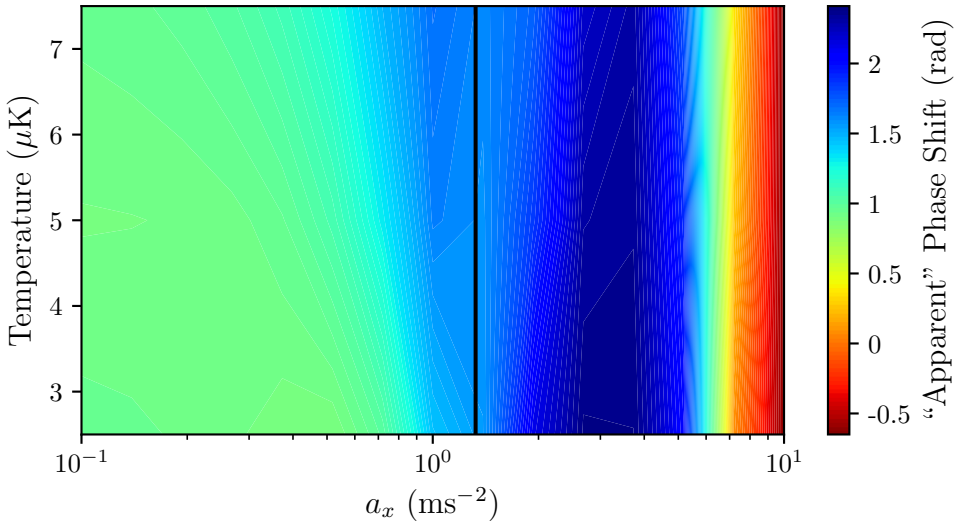
Figure 5.3: A plot showing "apparent" phase shift due to a_x for $T = 10$ ms (blue), 20 ms (red), 40 ms (green) and 80 ms (yellow) - using both the analytical (dashed line) and numerical (crosses) simulation approaches. The vertical lines show when the centre of mass of the atomic cloud at the third pulse reaches 16.95 mm, i.e. w_0.

5.4 Compensation Technique

Lastly, we investigate a simple compensation technique. To do this, we propose a hybrid sensor where we have a classical accelerometer attached to an atom interferometer gravimeter. The classical accelerometer is used to measure the horizontal acceleration in real-life, which in turn can be used to calculate the position moved during the interferometric sequence. The position moved can then be fed onto the laser. A circuit could be designed to use this information to either reduce the beam waist of the laser beam and/or increase the central power of the laser during the three pulses. In this article, we will concentrate on the latter as the reduction of beam waist requires more difficult optimisation, as we will briefly mention at the end. We will specifically



(a)



(b)

Figure 5.4: Contour plots showing the (a) contrast, and (b) "apparent" phase shift for a typical range of horizontal atomic cloud temperatures with the effect of a_x for T = 80 ms. The vertical line shows when the centre of mass of the atomic cloud at the third pulse reaches 16.95 mm, i.e. w_0.

concentrate on increasing the power of the unmultiplied laser beam, I_1, during the second and third Raman pulses using :

$$I_{\text{compensated}} = I_{\text{uncompensated}} \times \left(1 + 2\frac{\Delta x^2}{w_0^2}\right), \tag{5.6}$$

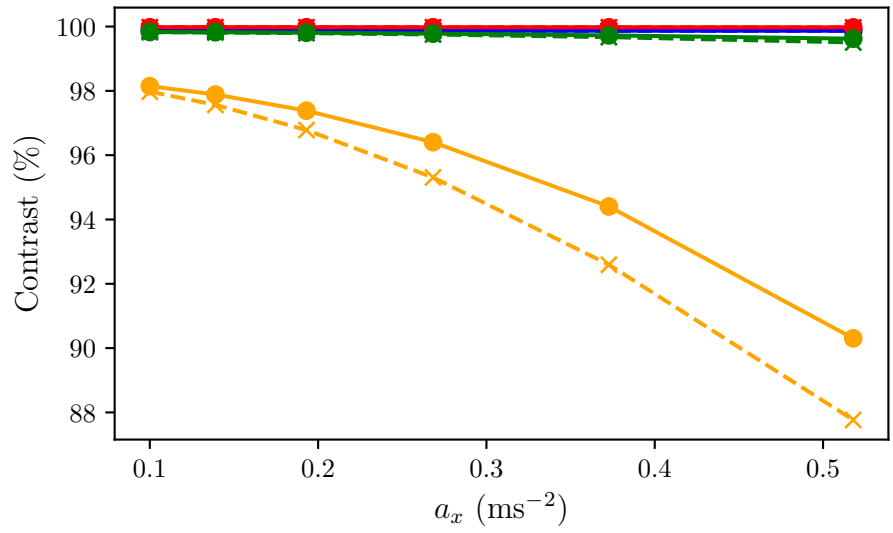
where Δx is the change in x position of the sensor between the first and second; and second and third pulses, respectively. This equation has been derived using the Gaussian intensity profile of the beam. This simple compensation technique works fairly well for small changes in Δx, recovering some of the contrast loss as well as the "apparent" phase shift as shown in Figure 5.5.

Small compensation is offered by this technique for small accelerations. For example, contrast improvement of $\sim$3% and "apparent" phase shift improvement of $\sim$25 mrad are achieved for $T = 80$ ms at 0.5 ms^{-2} for a cloud of temperature 2.5 μK if the central laser power is 1.7 times the uncompensated value (340 mW). However, obviously, increasing intensity constantly is not feasible due to real-life power limitations, and even compensating for small Δx can lead to needing large power increases so a compromise needs to be found. To characterise the power needed for compensation, assuming we are allowed a power multiplication factor, n, of I_1 relative to the original power, P_0, we can deduce the constraints of how much power we would need to compensate using:

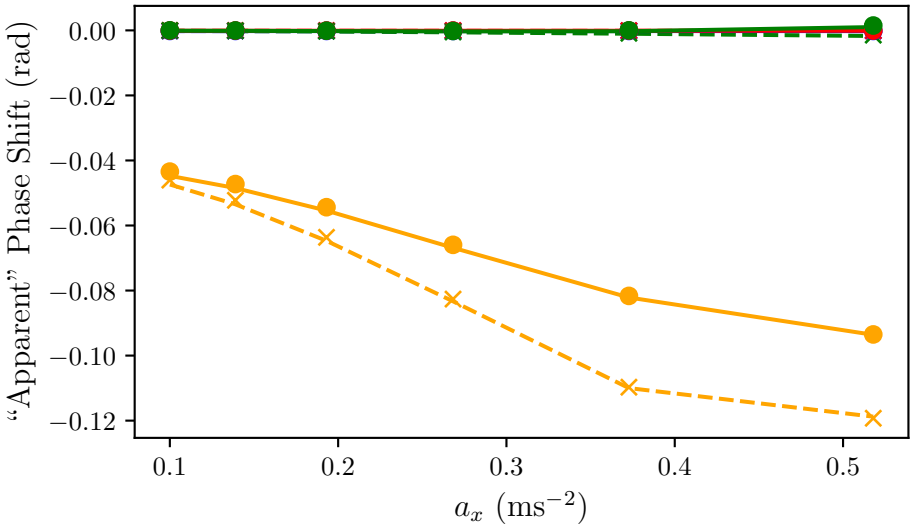
$$n = \left(1 + \frac{8a_x^2T^4}{w_0^2}\right) \cdot \exp\left(\frac{8a_x^2T^4}{w_0^2}\right). \tag{5.7}$$

Lastly, as alluded to at the beginning of this section, it is also possible to change the beam waist size as a potential compensation technique. The exact parameters of such a compensation technique would be obtained by optimising:

$$I_{\text{compensated}} = I_{\text{uncompensated}} \times \frac{w_1^2}{w_0^2} \cdot \exp\left(2\frac{\Delta x^2}{w_1^2}\right), \tag{5.8}$$



(a)



(b)

Figure 5.5: Comparison of uncompensated and compensated (a) contrast and (b) "apparent" phase shift for $T = 10$ ms (blue), 20 ms (red), 40 ms (green) and 80 ms (yellow). Analytical (dashed line for uncompensated and solid line for compensated) and numerical (crosses for uncompensated and circles for compensated) solutions are shown.

where w_1 is the waist radius of the compensated beam.

5.5 Conclusion

Atom interferometers offer promise in navigation [7, 40] while atom interferometer-based gravimeters offer great potential in geophysical applications [6]. However, one of the key challenges that remains is their ability to operate in dynamic conditions.

In this article, we have shown that acceleration transverse to the free-fall of the atoms has an effect on the output of the interferometer, both in terms of contrast loss and "apparent" phase shift, especially for high T. Nevertheless, there is a compromise here, as low temperatures and transverse accelerations could be largely robust to this effect. The "apparent" phase shift could lead to potential issues when trying to detect targets. As a result, we have proposed a potential simple compensation technique using a classical accelerometer feeding onto the Raman laser. This allows us to measure the movement of the sensor using the accelerometer, which in turn controls the Raman laser and increases the power to compensate for this. We have shown that this leads to a small contrast and "apparent" phase recovery for small accelerations but increasing the power has practical limitations. This is a simple compensation technique; alternatives include composite [147] or polychromatic pulses [148].

5.6 Outlook

The basics of the cross-coupling effects simulations have been setup. As has been highlighted, some questions still remain prior to publishing. One of these is the strange behaviour of the gravity fringes seen even when the third pulse is within w_0 - more understanding of this is required physically to see what contributes to this effect. It might be that even at this point, the atom can no longer be considered as being within the beam. As the "apparent" phase shift calculation is a consequence of the contrast

loss, resolving the aforementioned issue should also help to solidify this calculation. However, it does contain its own questions, specifically whether calculating the "apparent" phase shift this way is appropriate physically. This feeds into the rest of the work, including the horizontal temperature dependence and the compensation technique. The showcasing of the compensation technique had to be limited at 0.5 ms^{-2} because after this acceleration, the "apparent" phase shift changes from negative to positive and so combining this with the compensation technique resulted in strange results. The work to resolve these issues is currently underway by the author, with help from an expert in atom interferometery theory and so the hope is that it can be resolved relatively "soon" following the submission of this thesis. However, all the theoretical and computational infrastructure has been setup; therefore, once these are resolved and understood, new results can be obtained relatively quickly.

Apart from the aforementioned verification of these simulations by another colleague, thoughts have been given to validating/observing these results experimentally. The most obvious one is by the ability to observe the loss of contrast of the fringes. However, another way to potentially validate this is via the use of Rabi oscillations. This effect is simulated for 10^3 atoms (due to computational constraints) for 2.5 μK (horizontal temperature) cloud with the same parameters as before. This is done for various accelerations and can be seen in Figure 5.6 for Rabi oscillations 150 ms after molasses. As can be seen, the Rabi fidelity decreases with increasing acceleration and its π-time increases. This shows the possibility of validating this model with Rabi oscillations only, which are easier to perform and are less sensitive to external effects than gravity fringes.

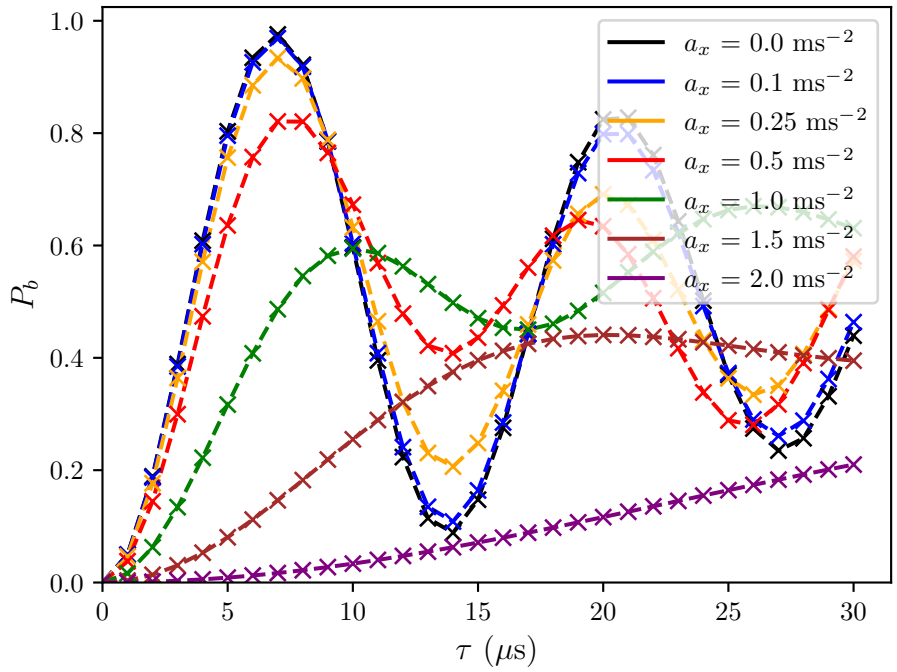


Figure 5.6: Rabi oscillations 150 ms after molasses for an atomic cloud with 10^3 atoms and horizontal temperature of 2.5 μK for a range of a_x.

Chapter 6

Atom Interferometry

Once a sufficiently cold cloud of atoms is achieved, as seen in chapter 3, interferometry can be performed. Since the sensor head has previously been able to obtain interferometry, it was decided to first obtain the interferometry with the original setup, prior to upgrades for phase shear readout. This had the added benefit that steps needed for implementation of phase shear readout could be investigated, helping with implementing this technique in other instruments (especially within our group), which was the key theme of this PhD.

6.1 Standard Interferometry

6.1.1 Raman Polarisation

In order to maximise the transition probability, the Raman beams need to be orthogonal. This is due to the fact that the effective Rabi frequency, Ω_{eff}, is given by [43]:

$$\Omega_{\text{eff}} \propto |\boldsymbol{E}_1 \times \boldsymbol{E}_2| \cdot M, \tag{6.1}$$

where $\boldsymbol{E}_{1,2}$ are the electric fields of the beams and M is the dipole matrix element. In our experiment, the laser beams are of linear polarisations, the stability of which for about an hour can be seen in Figure 6.1 (measured with PAX1000IR1/M polarimeter [149]). A very good stability with over 99% linear polarisation of both of the laser beams has been observed. However, $\pi - \pi$ transitions with $m_F = 0$ are forbidden due to selection rules. So how can linearly polarised Raman beams drive transitions with $m_F = 0$? It turns out that linear polarisation can be decomposed into circular polarisations in the vertical quantisation axis. As a result of this, the following possible combinations can drive the stimulated Raman transitions: σ^+-σ^+, σ^+-σ^-, σ^--σ^+ and σ^--σ^-. Out of these possibilities, due to the dipole transition matrix, only two of these are non-zero and will contribute to the interferometer, namely the σ^+-σ^+ and σ^--σ^- [43].

6.1.2 Detection Scheme

To detect the atoms at the end of the experimental sequence, a standard two-state detection sequence is depicted in Figure 6.2. The detection scheme is composed of seven pulses. The first pulse lasting 100 μs, I_1, only drives the cooling transition, detecting $|F = 2\rangle$ atoms only. The second pulse lasting 100 μs, I_2, drives the cooling and repump transitions, hence selecting the total number of atoms, i.e. both $|F = 1\rangle$ and $|F = 2\rangle$. The third pulse, I_3, which again drives both cooling and repump transitions, similar to I_2, is switched on for $\sim$3 ms. This pulse blows all of the atoms away from the detection region. Pulses 4 (I_4) and 5 (I_5) are the same as pulses I_1 and I_2, respectively. However, as the atoms have now been blown away, these are used to measure the background light levels. Finally, the last two pulses are the top Raman and bottom Raman lights, respectively. These are currently unused but they could be useful in Raman intensity monitoring. The final probability of the upper state ($|F = 2\rangle$) at the

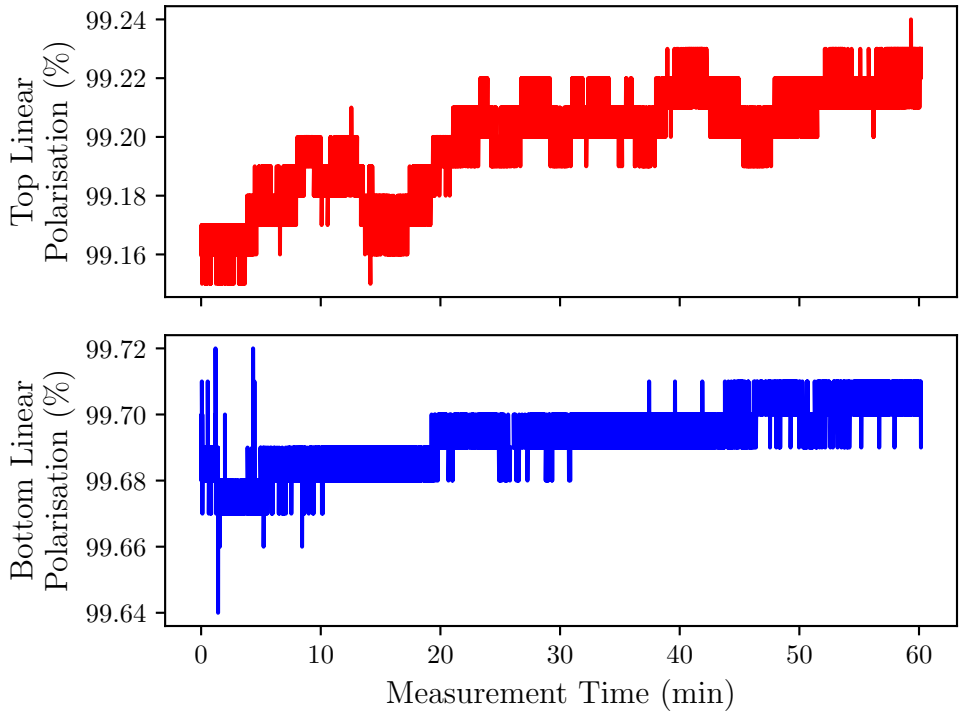


Figure 6.1: Top and bottom Raman beam linear polarisation levels prior to being fed into the telescopes. A stable and high level of linear polarisations is observed for a measurement time of about an hour.

output of a real-life interferometer is obtained using:

$$P_{|F=2\rangle} = \frac{I_1 - I_4}{I_2 - I_5}. \tag{6.2}$$

The design of the sensor head meant that the atoms should be arriving at the detection region 178 ms after molasses. However, as was seen with the lightsheets, this time of arrival was shifted somewhat, especially for the bottom chamber. Therefore, the detection start time was investigated to ensure that the best signal was still observed at this time. This characterisation can be seen in Figure 6.3. The maximum signal for both chambers is indeed observed at 178 ms after molasses, as is expected, again implying that the lightsheets are slightly misaligned. It should be mentioned that

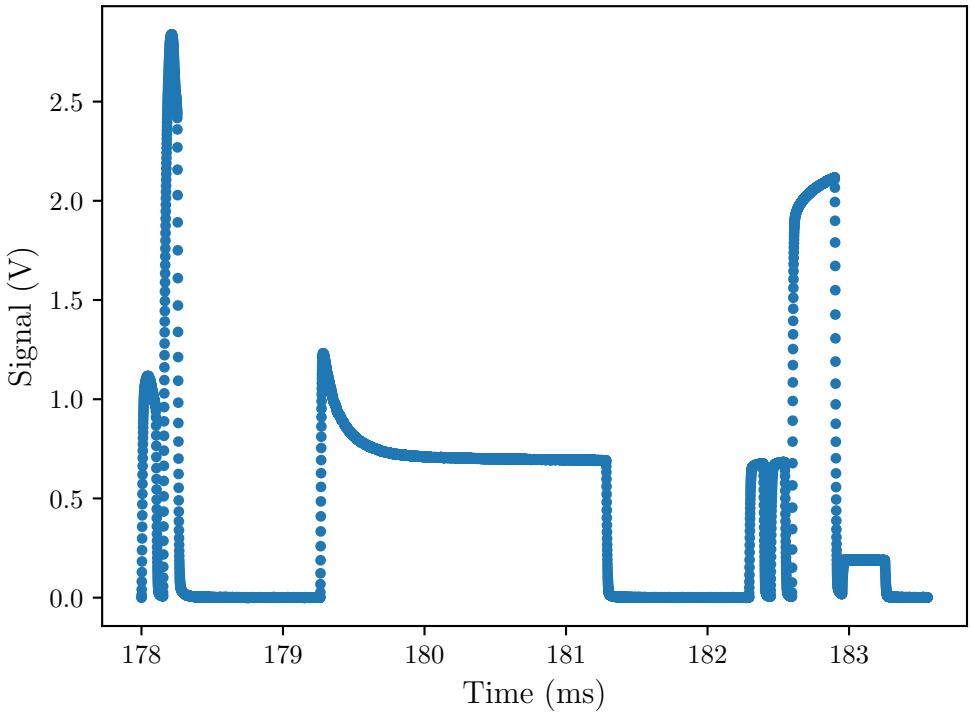


Figure 6.2: Two-state detection scheme.

this characterisation was done with cooling and repump lights after state preparation with only $|F = 1\rangle$ atoms. In the future, if possible, it would be advantageous to re-characterise this again but with the $|F = 2\rangle$ atoms.

6.1.3 Rabi Oscillations

The first step in obtaining interferometry is the ability to obtain Rabi oscillations. A series of three of these Rabi oscillations at different times after molasses (and hence heights in the chambers) can be seen in Figure 6.4. The dashed lines are the fits of these Rabi oscillations using an exponentially damped sinusoidal function. The times at which maximum probability is observed are taken to be the π-times. For the top chamber, the π-times vary from 10.15 μs at 45 ms after molasses to 11.45 μs at 143 ms after molasses - resulting in a variation of 12% from the the π-time at 45 ms. For

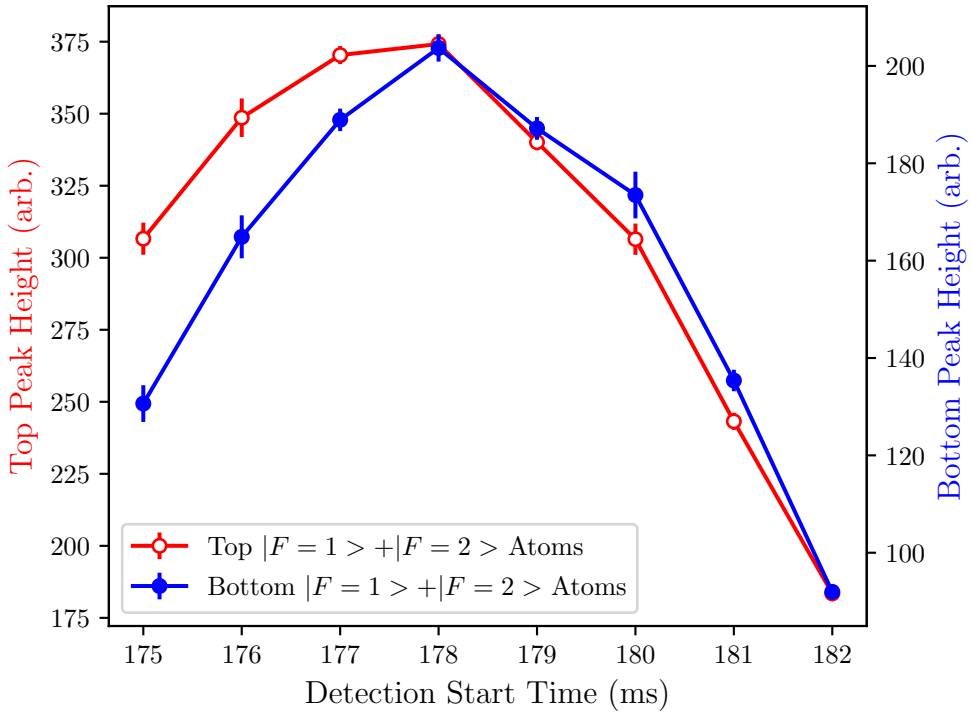


Figure 6.3: Vertical detection start time characterisation.

the bottom chamber, the π-times vary from 9.98 μs at 45 ms after molasses to 11.74 μs at 143 ms after molasses - resulting in a variation of 18% from the π-time at 45 ms. The variation of the π times in both chambers implies that the Raman beams are not perfectly aligned. One disadvantage of the original telescopes is that they have limited alignment capabilities, which should be improved with the upgrades discussed in section 6.2.

While the general shape of these Rabis is similar to the theoretical one in Figure 2.2, it is obvious that they are not identical, especially when the pulse lengths are longer. The damping of the Rabi at longer lengths is largely due to the thermal expansion of the cloud with effects such as dehoherence and spontaneous emission also playing their parts. The population ratio of these Rabi oscillations is also of interest. The height of the peak of a Rabi oscillation around π-time is referred to as fidelity. This is essentially

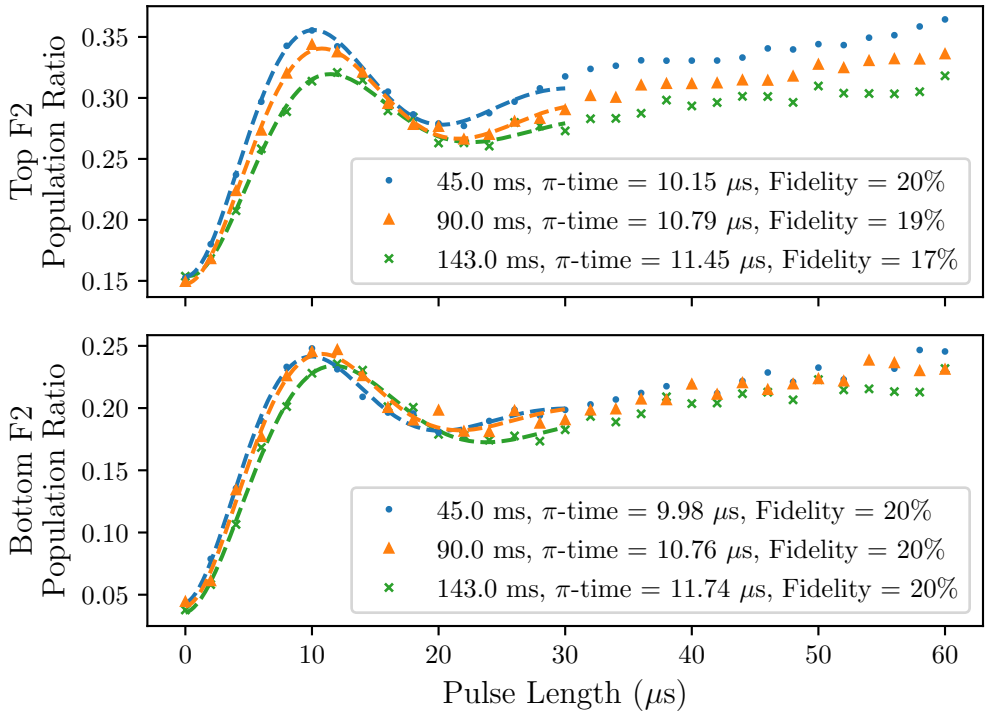


Figure 6.4: Rabi oscillations at different heights. The dashed lines are the fits using an exponentially damped sinusoidal function used to obtain the π-times. The π-times are increasing with time, implying that the Raman beams are not perfectly aligned.

a measure of the efficiency of the population transfer from $|F = 1\rangle$ to $|F = 2\rangle$. As we are preparing the Rabis in the $|F = 1\rangle$ state with three different m_F states but then only driving only the $m_F = 0$ state, this means that the maximum possible transfer is $\sim$33%. The fidelities in our case for both of the chambers are around 20% with the bottom chamber fidelities remaining constant while the top chamber shows variations. The unusual thing is that starting point of these Rabi oscillations, i.e. around pulse length of 0 μs. Theoretically, these should start at 0. However, the bottom chamber consistently starts at 0.05 while the top chamber starts at 0.15. This probably means that the even though the $|F = 2\rangle$ blowaway was optimised, it is not fully blowing all of the $|F = 2\rangle$ atoms away and so further characterisation and optimisation of this will be beneficial in the future. For completeness sake, we will mention that it is

possible to enable Rabi oscillations to theoretically reach a fidelity of 100% if extra state preparation is included to prepare all of the atoms in the $m_F = 0$ sub-state of $|F = 1\rangle$. This preparation requires the application of two π pulses, and $|F = 2\rangle$ as well as $|F = 1\rangle$ blowaways. The latter is quite difficult to implement, requiring careful tuning of frequency and power [44].

6.1.4 Spectrum Scans

Examples of a spectrum scans can be seen in Figure 6.5 at different heights. These are created by applying a Raman pulse of certain length (usually in the 8 - 10 μs region for our setup) and changing the frequency of the Raman sideband. The three peaks in the scans are the counter-propagating m_F state transitions (with the middle one being $m_F = 0$), with the separation of the peaks being due to the bias field applied onto the atoms to break the degeneracy of the sub-states. This allows to primarily drive the $m_F = 0$ transitions even without specific $m_F = 0$ state preparation. This allows the interferometer to be to be magnetically insensitive to first order, with only the quadratic Zeeman effect being of consequence. Due to the fact that these peaks are Doppler sensitive, their frequencies change as they fall through the chamber. The movement of the $m_F = \pm 1$ sub-states in comparison to the $m_F = 0$ state is due to the first order Zeeman effect. The spectrum scans can be used to characterise the chirp rate and the magnetic field seen by the atoms during their fall.

By performing spectrum scans at different heights and finding the frequency of the $m_F = 0$ state at each of these points, one can plot the frequency against the time (after molasses). This should produce a straight line where the gradient is the chirp rate, in an ideal case this would only caused by gravity. Figure 6.6 shows this chirp rate calculation for our system, obtaining a value of 25.265 MHz/s $\pm$ 0.008 MHz/s for the top chamber and 25.293 MHz/s $\pm$ 0.021 MHz/s for the bottom chamber. These

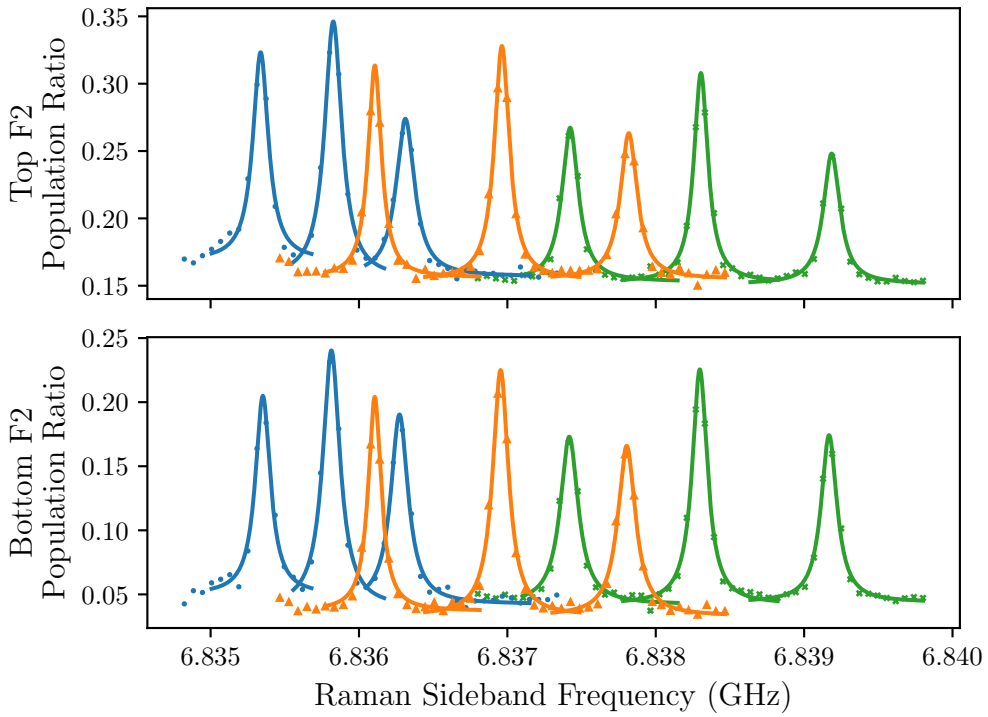


Figure 6.5: Spectrum scans at different heights with a bias coil current of 450 mA and Raman pulse length of 8 μs. The solid lines are the Lorentzian fits of these peaks.

are somewhat shifted from the expected value, which must be due to other systematic effects that are not the gravitational field. The y-intercept of this fit should be the hyperfine splitting between the $|F = 1\rangle$ and $|F = 2\rangle$ states. For both of the chambers, this has been calculated as 6.8347 GHz (with very minimal fitting errors), which agrees with the hyperfine splitting frequency in [96]. The other way to obtain this chirp rate would be to obtain the gravity fringes for different T times and finding the point at which they all intersect.

While the $m_F = 0$ sub-state can be used solely to obtain the chirp rate, it can be used in combination with the $m_F = \pm 1$ sub-states to calculate the magnetic field that the atoms experience as they fall through the chamber. The magnetic field profile within the sensor head can be calculated using the energy difference between the $m_F = 0$ and

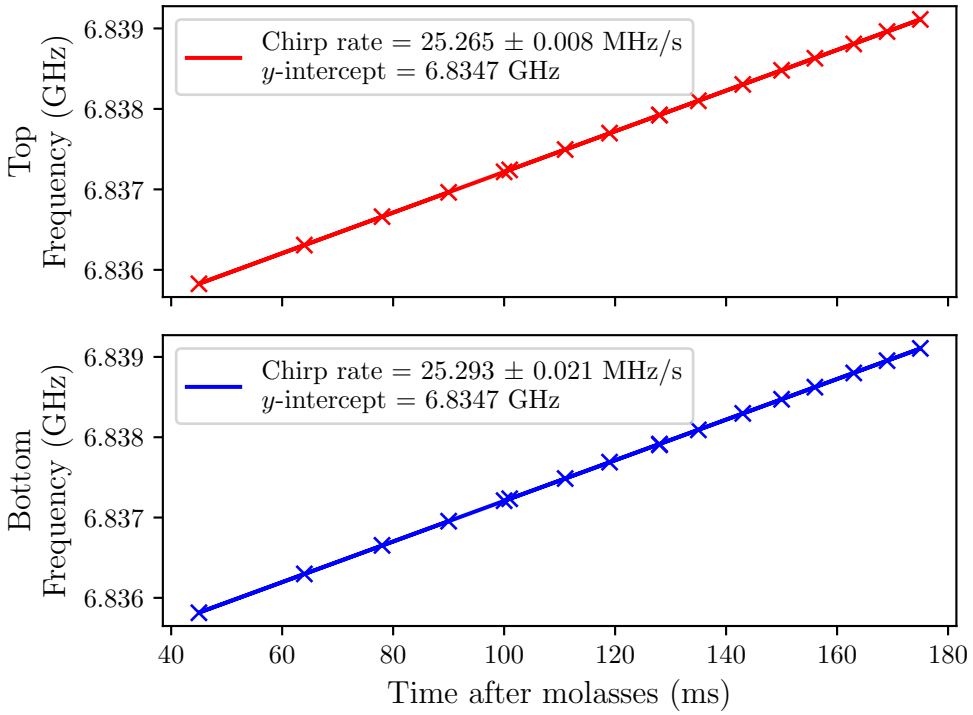


Figure 6.6: Chirp rate calculation using the $m_F = 0$ state. The calculated chirp rate values differ from the expected result, likely due to other systematic effects apart from the gravitational field.

$m_F = \pm 1$ transitions [97]:

$$B = \frac{h(\nu_{m_F=\pm 1} - \nu_{m_F=0})}{\mu_B m_{F=\pm 1}}, \tag{6.3}$$

where $\nu_{m_F=\pm 1}$ and $\nu_{m_F=0}$ are the frequencies of the corresponding sub-states. The resulting magnetic field profile as seen in our chambers can be seen in Figure 6.7, measured with coils current of 450 mA. The magnetic field profile is fairly uniform, reaching over 600 mG.

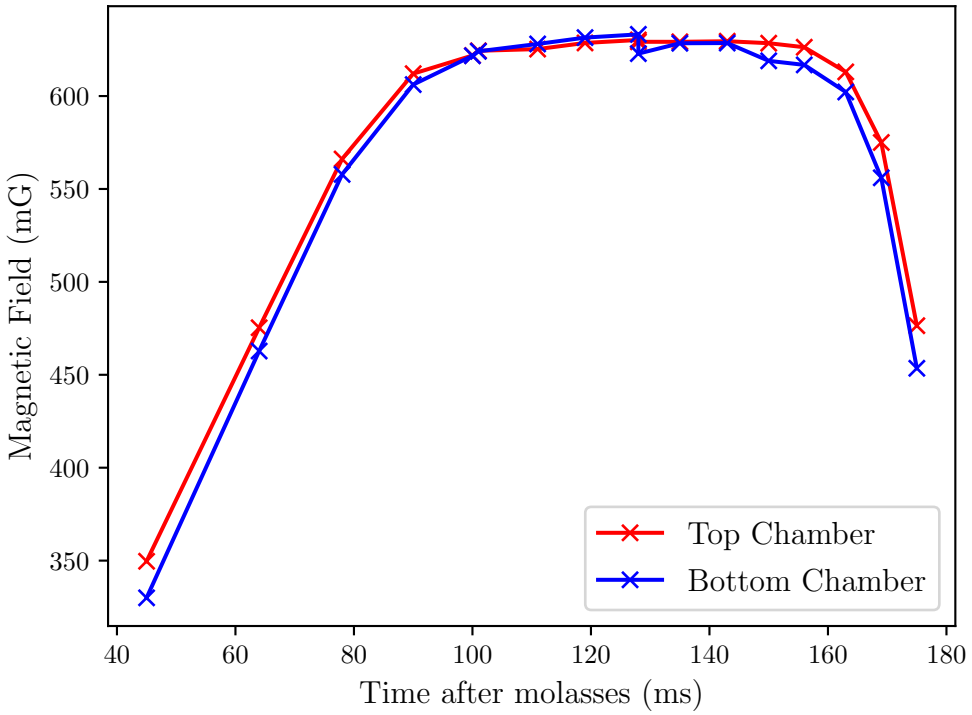


Figure 6.7: Magnetic field profile as calculated using the atoms with bias coil currents of 450 mA. While largely uniform in the central region, small variations in the magnetic field seen by the atoms is observed, most probably due to background magnetic fields and practical limitations of designing and building the bias coils.

6.1.5 Gravity Fringes

The final step in the interferometry in our setup is to use all of the information to produce the gravity fringes. The π and $\pi/2$ times can be obtained from the Rabi oscillations. The chirp rates can be obtained from the spectrum scan. Putting all of this together, one can obtain the gravity fringes. For our setup, these gravity fringe can be seen in Figure 6.8. For these measured fringes, the first pulse is 50 ms after molasses and $T = 1$ ms. Therefore, these gravity fringes use very short T time and hence do not provide high sensitivity. Additionally, the heights of the oscillations from top to bottom in both of the chambers are only $\sim$7%. There are a lot of potential systematics that could be affecting these measurements and due to time constraints,

a full investigation and optimisation of all these systematics could not be performed. One thing to mention is that the short T time is partly due to the low performance and partly due to vibrations because as T increases, vertical vibrations start to have a bigger effect. One way to reduce these is to use an isolation platform, as will be seen later on in this chapter. The other is to use both of these chambers in combination as a gravity gradiometer. This can be done by plotting both chambers' population ratios on the same plot on separate axes, e.g. top chamber on the y-axis and bottom chamber on the x-axis, to create an ellipse. This ellipse can be analysed and phase information (and hence the gravity gradient) obtained from this ellipse. This works even when high levels of vibrations are present and allows higher T times to be used. This is beyond the scope of this work but more information on ellipse fitting can be seen in [150].

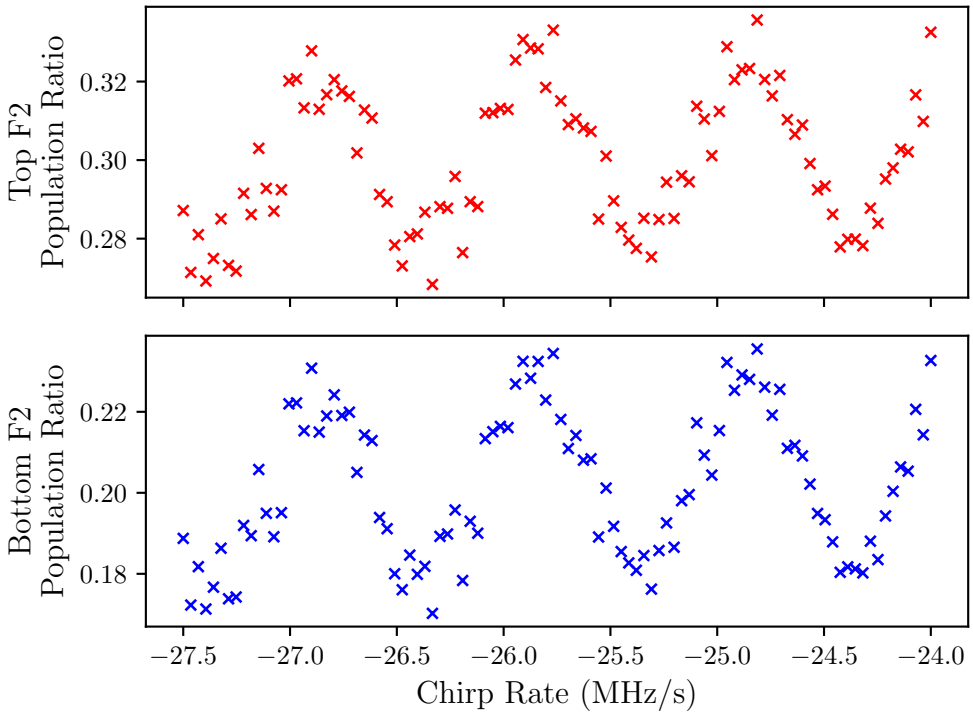


Figure 6.8: Measured gravity fringes, with the first pulse being 50 ms after molasses and with $T = 1$ ms.

6.2 Phase Shear

The intentional introduction of phase shear cannot be demonstrated with the experimental setup described in chapter 3, requiring the following upgrades:

1. **Raman Telescope**: The original Raman telescope in chapter 3 did not have the required beam tilting capability required and so a new telescope was needed.

2. **Imaging Detection**: The default detection device for the interferometry in the original setup is the photodiode. However, phase shear readout requires a spatially-enabled imaging detection. Therefore, a new camera imaging was introduced in the detection region.

As the goal of this work was to investigate the implementation of this technique, these upgrades have only been done to the top chamber to investigate the challenges presented by this implementation, with the view to potentially add the same upgrades to the bottom chamber, if needed.

6.2.1 Raman Telescope

The updated Raman telescope can be seen in Figure 6.9. The design builds on the original setup and within the constraints that are present due to the sensor head. The cooling collimator has been largely unchanged and sits in pretty much the same position as in the original telescope. The main change has been performed on the Raman end, where a more elaborate setup has been created. The Raman collimator is attached upside down to a rotating mount. The beam from this collimator travels upwards and is reflected from the first mirror, that has alignment capability. Once reflected from this first mirror, the beam travels horizontally before being reflected from a second mirror.

This mirror also provides alignment capability but more than that, it is attached to a piezo-actuated mount. This mount allows for the change of the angle of the Raman beam, enabling beam tilting. Following the reflection from this mirror, the beam then passes downwards into the lenses in the sensor head as was described in section 3.1.3. The reason that the collimator is mounted in the rotating mount is to be able to change the orientation of the polarisation of the Raman beam. However, slight issue with this design has seen found in that turning the collimator also changes how the beam hits each of the mirrors and ultimately how it couples into the sensor head. This means that changing orientation of the polarisation of the Raman beam also leads to having to re-align the beam. While a nuisance, it is not a show-stopper as it is possible to obtain both the desired orientation and good alignment within the sensor head.

The piezo-actuated mirror mount is the commercially-available Polaris K05P2 [151], which has been utilised alongside a 3-axis controller MDT693B [152]. This mount requires voltages in the range of 0 - 150 V to access the full range of angles. The controller itself can be controlled in two ways. The first way is to connect the PC to the controller via USB and set the output voltages using a bespoke Thorlabs software. The second way is by sending input voltages into the controller (in the range of 0 - 10 V) that will then output the appropriate voltages out of the controller. The latter method was implemented as it is easier to use within the experimental sequence. However, some of the following characterisations have been done with the software, which will be highlighted appropriately. The input voltages for the controller are provided by the Zotino module of ARTIQ.

To ensure that the piezo-actuated mount is able to provide the angles as per the Thorlabs specifications [151], characterisation of the angles produced with different voltages of the controller was performed, where the voltage output was controlled using the aforementioned Thorlabs software. The testing setup composed of a simple

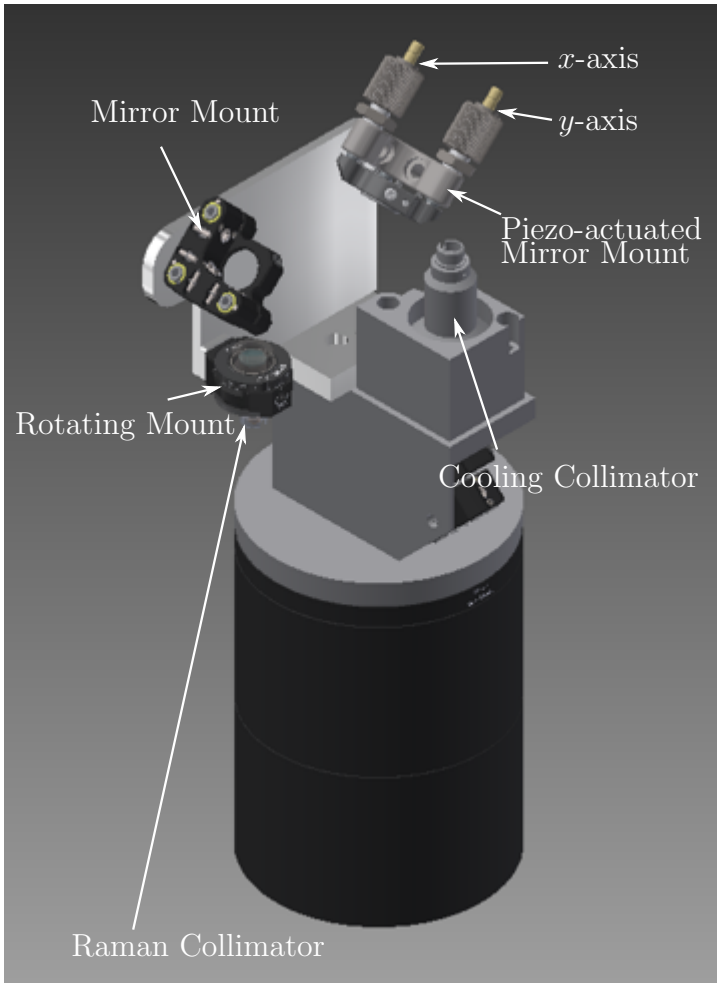
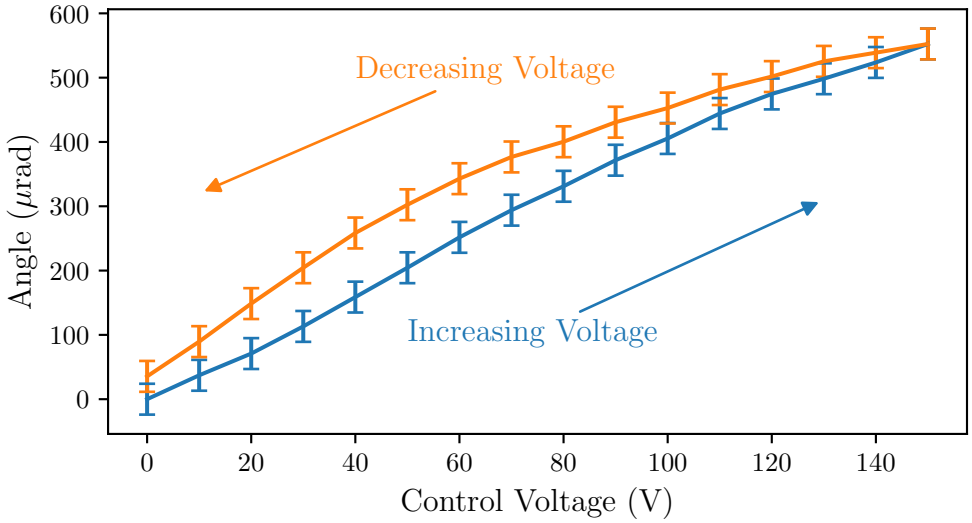
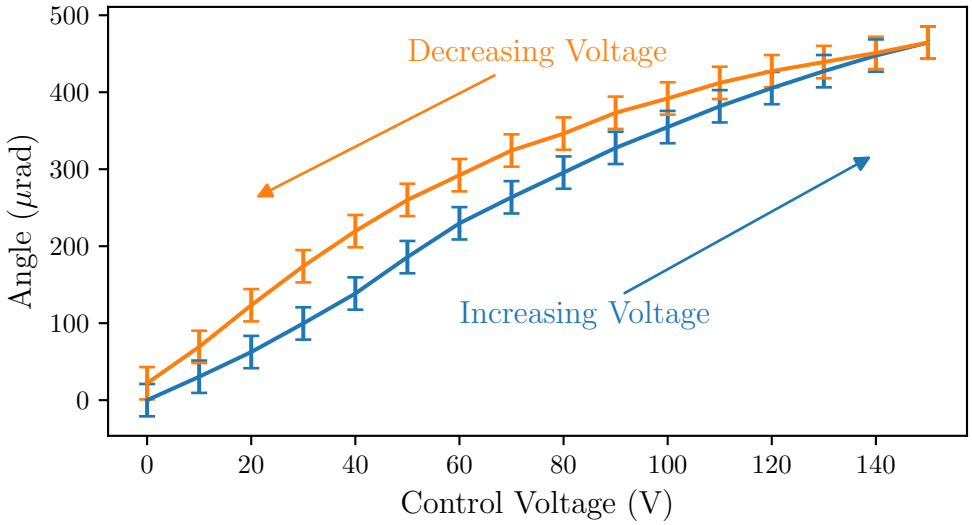


Figure 6.9: Upgraded telescope design for the implementation of beam tilting. The x- and $y-$axes will be used throughout this chapter to differentiate between the two axes that can be controlled using the piezo-actuated mirror mount.

bench-top laser that was fed into a collimator, which was fit into the piezo-actuated mount. The beam out of the collimator passed through an iris (SM1D12) that was closed as much as possible in order to obtain the smallest possible beam. The beam was incident onto a quadrature photodiode (PDP90A) that was placed 3.7 m away from the collimator. The quadrature photodiode was used to measure how much the beam has moved along either of the axes by measuring the mean voltages outputted on an oscilloscope, which was subsequently converted into an actual distance using the



(a)



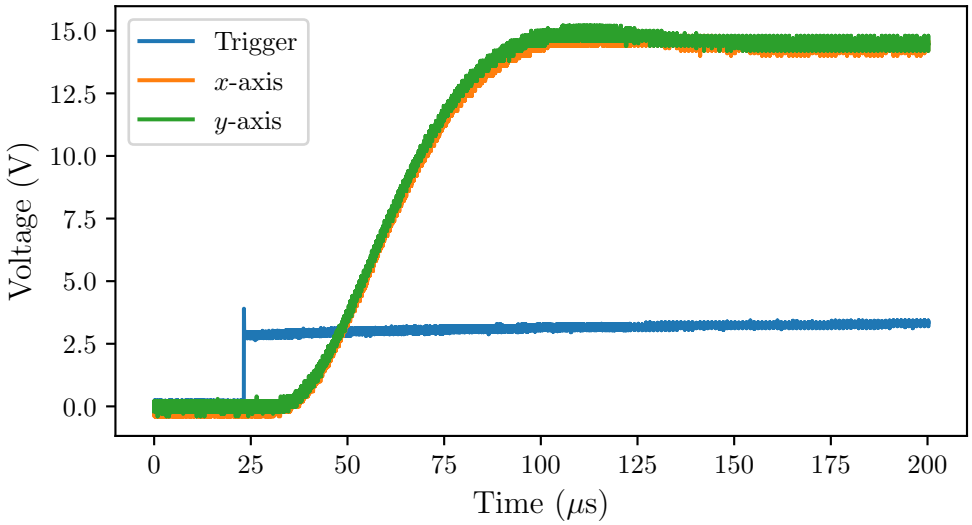
(b)

Figure 6.10: Angle as a function of the control voltage for the **(a)** x-axis and **(b)** y-axis of the Polaris K05P2 piezo-actuators, featuring hysteresis loops.

PDP90A manual [153]. Finally, the angle was obtained by using these distances while taking the geometry of the setup into consideration. The resulting calculated angles can be seen in in Figure 6.10. The errors were calculated by measuring the voltage out of the quadrature photodiode on an oscilloscope for 10 s when the laser was on

but without any voltage applied. The largest difference from the mean was then taken as the error for each of the axes. This calculates as 24 μrad for the x-axis and 21 μrad for the y-axis. The angles calculated are in agreement with the specifications and exhibit the expected hysteresis loop as the voltage is increased or decreased. It is a bit difficult to quantify the differences between the measurements and the specifications but taking the case of the highest angle for both should produce $\sim$500 μrad for both axes according to the manufacturer. However, in our measurements, the maximum angle for the x-axis is 552 μrad (10% difference from the stated value) and 465 μrad for the y-axis (7% difference from the stated value). Differences are likely to be due to the noise and measurement technique because there are other errors on measurements that have not been taken into account, such as the error on the distance between the collimator and the quadrature photodiode, uncommon vertical vibrations between measurements, manual recording of voltages, etc. While a more robust characterisation of these angles would be useful in the future, relatively good agreement is seen between the expected angles and the measured ones, giving confidence that this mount is acting as specified. The hysteresis loop is obviously of concern - in our setup we have tried to rectify this by resetting the angle to minimum in-between measurements. The other potential approach is to use an angle feedback loop, e.g. measuring the angle within the system to feedback onto the voltage applied.

To characterise the responsiveness of the MDT693B controller, input voltages from the ARTIQ were sent to the controller. The output voltages from the controller as well as a trigger from ARTIQ (timed at the same time as the input voltages) were observed on an oscilloscope. The output can be seen in Figure 6.11(a). The response of the controller is $\sim$83 μs between the trigger arriving and the voltages being outputted. Given the experimental time-frames, this should be fast enough, at least for initial demonstrations. The other responsiveness testing was to look at the response of the



(a)

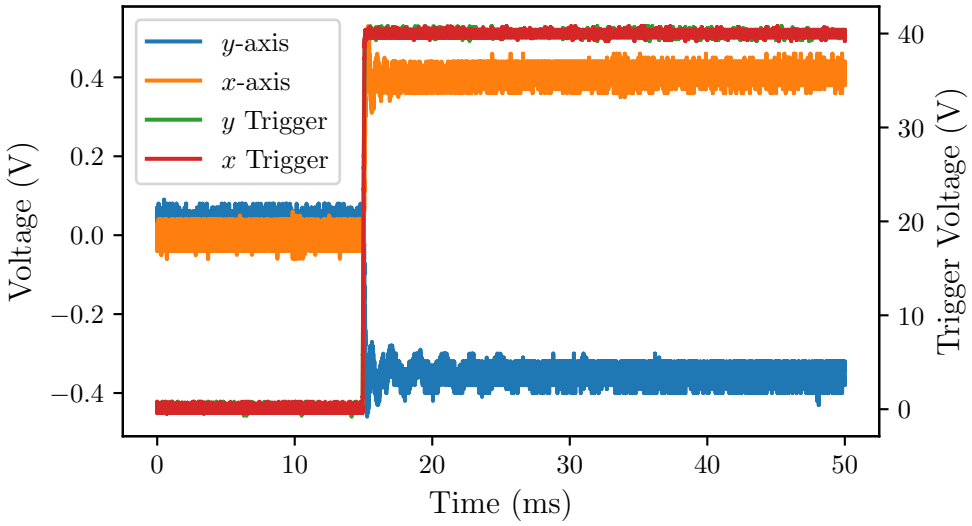


Figure 6.11: **(a)** Piezo controller response of outputting a voltage once it receives an input voltage. **(b)** Piezo-actuated mount response following the controller signal.

piezo-actuators, as this is likely the slowest part. To test this involved looking at the time response of the piezo-actuated mount once it receives the voltage from the controller. Voltages were sent from the controller using the Thorlabs software, with the signal split - one part of the signal is the trigger for that axis while the other one was used on the piezo-actuated mount. This can be seen characterised in Figure 6.11(b).

Similarly to the controller, this response is fast given our experimental requirements. The only concern is that there appear to be certain oscillations after the voltage is applied, lasting potentially for up to ∼5 - 6 ms. It looks like it takes the mount a few ms to stabilise, with the two axes having different responsiveness in terms of these oscillations (the y-axis oscillations appear to last longer than the x-axis ones). It is currently unclear whether this is due to external factors and/or the piezo-actuated mounts. Fortunately, these oscillations are relatively small in magnitude compared to the voltage difference, meaning that for initial demonstrations of this technique this should not be as critical as when sensitive measurements and fine control of the angle are required. One way to suppress this effect is to apply the voltage to the mount during the second T time, therefore, letting the angle stabilise before the last pulse is actually applied but obviously this is slightly difficult to do with short T times. Further investigation of this will be needed in the future.

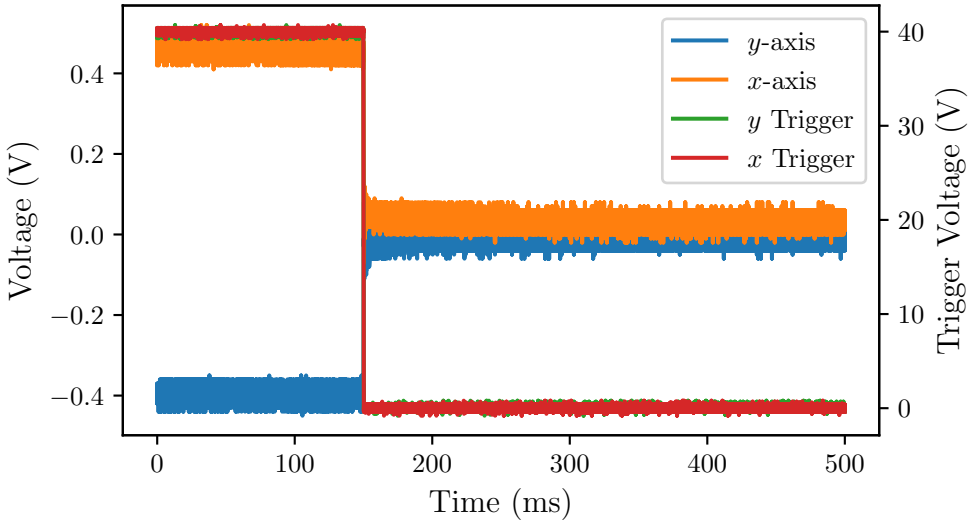


Figure 6.12: Piezo-actuated mount switching off response.

The existence of the hysteresis loop and oscillations when the voltage is increased begged the question whether unusual behaviour would also occur when the voltage into

the piezo-actuated mount is switched off. In interferometers, measurements are taken within a few seconds of each other and so an understanding needed to be gained to see if switching off the voltage in one measurement would affect the next one. The results of this characterisation can be seen in Figure 6.12. Similarly to when the voltage is applied, the response is almost instantaneous on the ms timescale. No strange effects are apparent following the switching off of the voltage. A slight decrease in the voltage is seen for the y-axis but it is not clear if this is the mount or another source of noise as it is not present for the x-axis. Additionally, this decrease is very minimal and, again, should not have an effect on initial demonstrations.

Once the Raman telescope had been upgraded, the performance of this system was characterised. The first test of this was to perform Rabi oscillations at similar points to before the upgrade, the results of which can be seen in Figure 6.13 for a set of three runs. The timings after molasses of these are not identical to the ones before the upgrade but are only different by a few ms, hence they can be compared fairly accurately. As can be seen, some misalignment is still present as the π-time increases with increasing time but the variations in both chambers have slightly improved, implying better alignment. The fidelities are a bit trickier - the top chamber fidelities have decreased while the bottom ones have increased. Part of the reason will be that the bottom dispensers are a lot newer than the top ones, and it was noticed that the MOT loading curves of the top chamber were not as good as in the past. However, even taking this into account, the performance is at least comparable prior to the telescope upgrade.

While not necessarily a factor of the system but rather of external fields, a similar analysis was performed with spectrum scans. This was done to compare whether the chirp rate and the magnetic field profile have remained unchanged. Since the system had not moved considerably between the telescope upgrades, any changes to these are likely an artefact of the telescope upgrade. Similarly to the Rabis above, a set of three

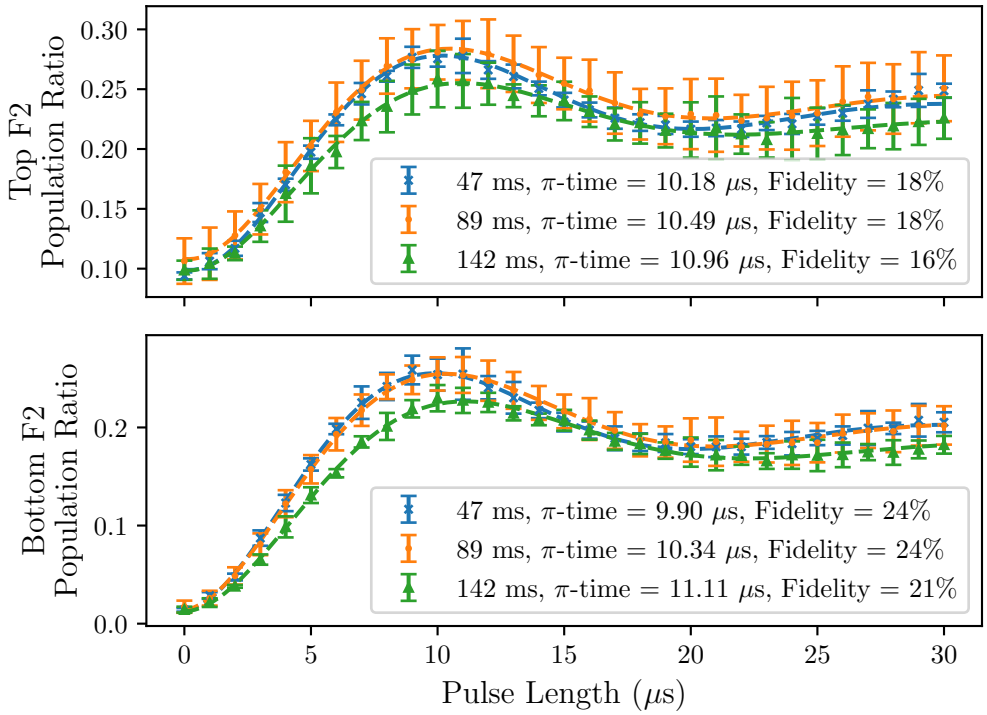
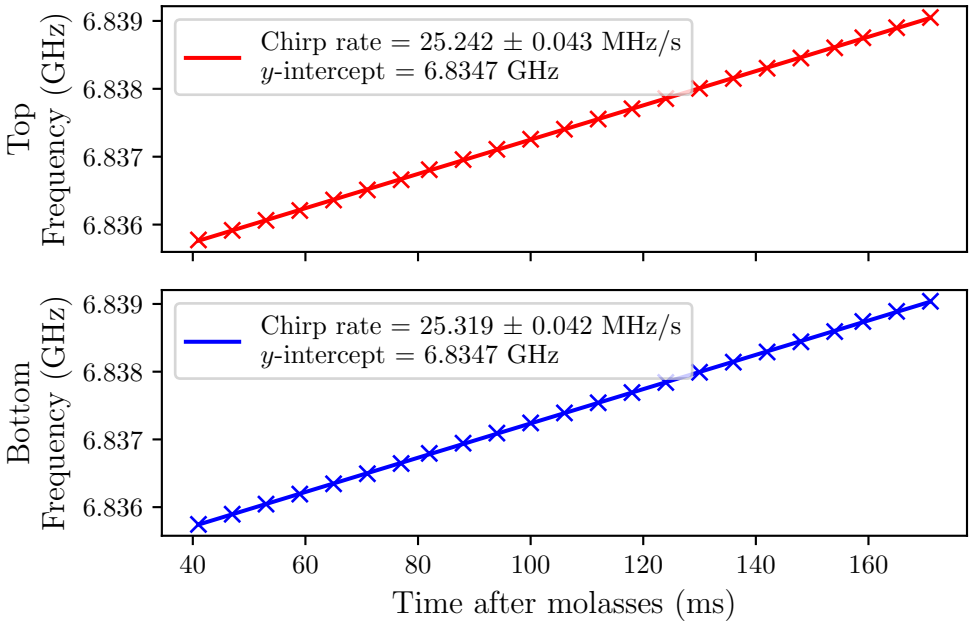


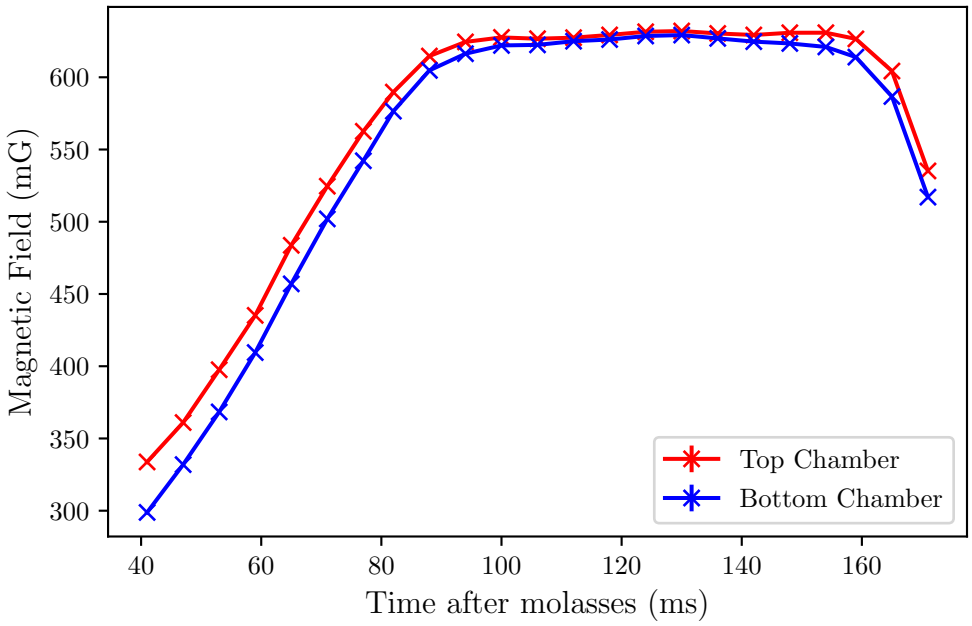
Figure 6.13: Performance of Rabis for a number of times after molasses following the Raman telescope upgrade.

measurements were taken and averaged to obtain the three m_F peaks at different times after molasses. From this, a chirp rate and the magnetic field profile of both chambers were obtained and can be seen in Figure 6.14. The chirp rates of 25.242 ± 0.043 MHz/s for the top chamber and 25.319 ± 0.042 MHz/s for the bottom chamber are within errors of the ones calculated prior to the upgrade. The magnetic field profile post upgrade is largely very similar and uniform as the field calculated prior to the upgrade. The small differences could be due to measurement noise and small changes in external magnetic fields as the measurements were taken months apart.

Lastly, as the initial plan with the phase shear readout technique was to use an average of multiple images, another concern was whether Raman intensity instability would cause issues by affecting the $|F = 2\rangle$ population ratio output because the Rabi



(a)



(b)

Figure 6.14: **(a)** Chirp rate and **(b)** magnetic field profile for the two chambers following the Raman telescope upgrade.

frequency is dependent on the product of the intensities of the two Raman beams. It is not easily possible to obtain the measurement of this intensity directly, therefore, an approach was taken to use the product of I_6 and I_7 of the two-state detection scheme (mentioned in section 6.1.2) and to treat these as the "intensity". A set of 100 measurements were taken with a pulse length of 5 μs - this meant that the Rabi oscillation was around the steepest slope and that if the intensity were affecting the $|F = 2\rangle$ population ratio, a higher intensity would result in higher ratio, and lower one in a lower ratio. The results of this analysis can be seen in Figure 6.15. While variations in both the product of I_6 and I_7 as well as the $|F = 2\rangle$ population ratio are observed, there appears to be no correlation between these two parameters.

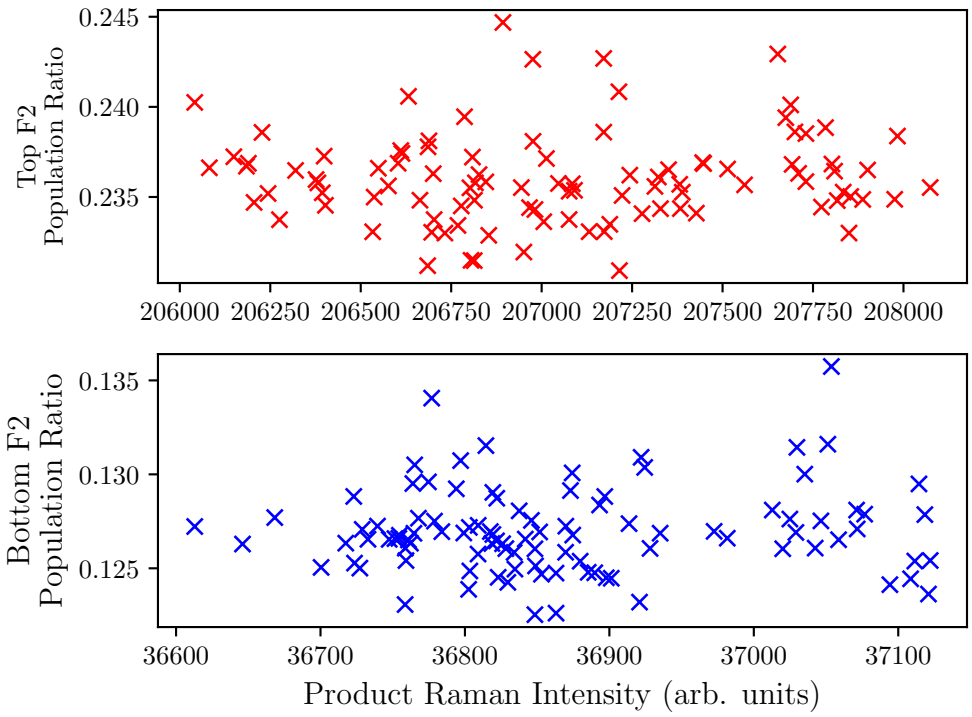


Figure 6.15: Raman intensity stability analysis using 100 shots with a pulse length of 5 μs.

6.2.2 Imaging Detection

For the imaging detection, a camera with a lens system was mounted in the detection region. The camera that was chosen is the DZK 33UX250 that includes the Sony IMX250MZR sensor [138]. This was combined with the commercially-available Computar 35 mm 1:1.4 2/3" lens [137], chosen in line with the estimated distance between the mounting of the camera and the atomic cloud.

One of the key considerations with this imaging system is the noise levels. It is possible to change the strength of the signal seen by the camera by changing the gain setting. However, this also has the effect of increasing all of the signal, including the noise. Analysing the signal-to-noise ratio showed no discernible change for different gain settings. Therefore, the lowest possible gain setting that retained a signal was found to be 20 dB. This is already quite a substantial gain and poses concerns, especially since it is no clear whether increasing the gain has any effect on the blurring of the image. To analyse the background noise that is seen with this gain setting, 50 background measurements were taken and averaged using the experimental sequence but without the MOT coils on - there is no atomic signal at the end of the sequence but light is present. The exposure time, light pulse length, etc. are the same as the ones used in the next section. The results of these measurements can be seen in Figure 6.16, showing very little noise - the maximum pixel value is 0.38 with the mean being 0.0003.

The unknown in this setup is the lens as this is a commercial one and not every information is available. An object of similar size as the estimated size of the atomic cloud was placed the estimated distance from the lens and imaged with the camera in combination with the lens. Qualitatively, the object appeared to be fairly well imaged but no quantitative analysis has been performed. This would be very beneficial to perform to ensure that the lens is able to image the cloud as expected and that

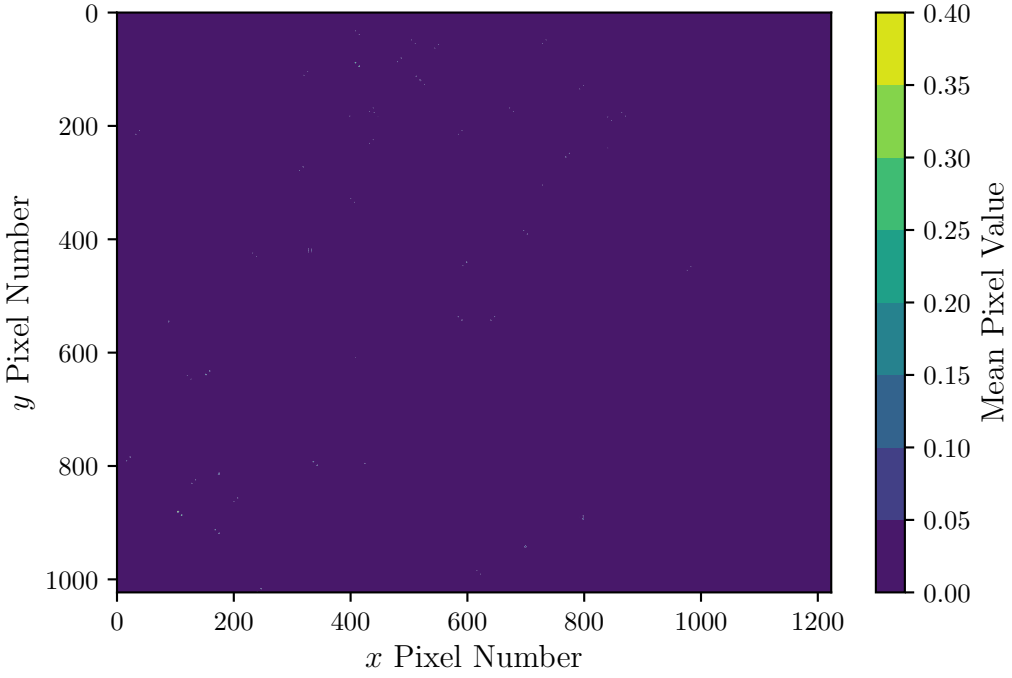


Figure 6.16: Camera background measurements of a mean of 50 images for 20 dB gain.

lens artefacts, such as depth of field, will not cause blurring that could prevent the observation of the phase shear fringes. This could be done with the standard test target plates available from Thorlabs.

That being said, a temperature measurement as well as a magnification of the lens estimation were performed. The atomic cloud was detected following molasses at detection but with slightly different detection times. The central vertical pixel of a 2D Gaussian fitting is taken as the location of the atomic cloud. Using equations of motion along the vertical axis ($z = \frac{1}{2}gt^2$), it is possible to correlate the number of pixels moved with actual distance travelled in real space. The results, together with the fit obtained can be seen in Figure 6.17(a). Earlier and latter detection times were disregarded from this analysis as it was noticed from the pictures that the cloud started leaving the

window and the full cloud was not being imaged. This results in one pixel representing 22 ± 1 μm in real space. Given this pixel size, the IMX250MZR-C sensor that comes in our camera has a pixel size of 3.45 μm along each axis, leads to a magnification of $\sim$6.4.

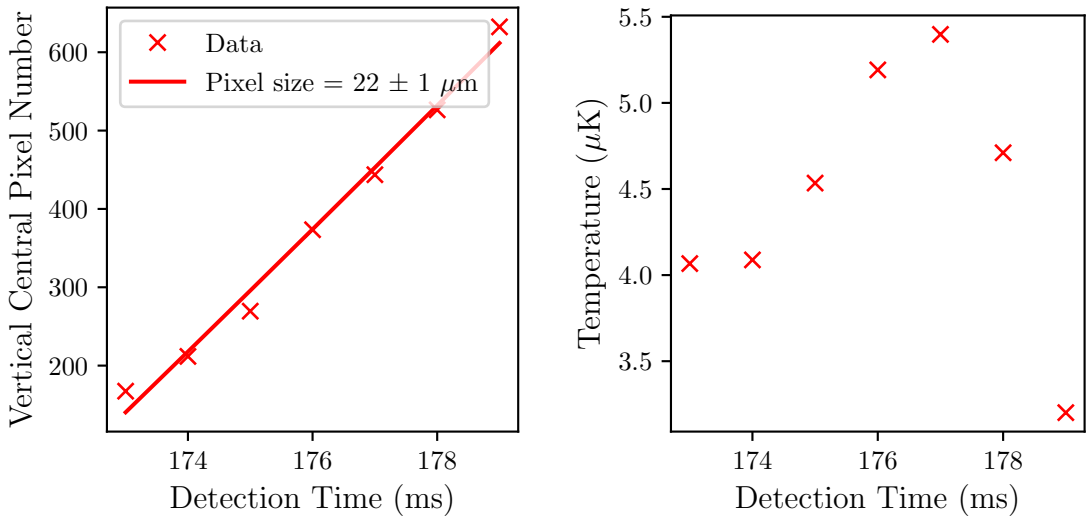


Figure 6.17: Preliminary estimate of **(a)** size per pixel and **(b)** the horizontal atomic temperature at different detection times.

Having obtained the actual representation of each pixel in real space, it is now possible to estimate the size of the cloud and hence the temperature. Once again, the atomic cloud was fitted with a 2D Gaussian but in this case we calculated the σ_f in the horizontal direction. This can be used to calculate the temperature using [154]:

$$\sigma_f^2(t) = \sigma_i^2(0) + \frac{k_B T_{\text{temp}}}{m_{\text{Rb}}} t_d^2, \tag{6.4}$$

where σ_i and σ_f are the initial and final Gaussian radii of the cloud ($\sigma_i = 1$ mm in line with section 3.4.2), k_B is the Boltzmann constant, T_{temp} is the temperature, m_{Rb} is the mass of ^{87}Rb and t_d is the detection time ($t_d = 178$ ms). The results of this analysis

for the same detection times can be seen in Figure 6.17(b). These temperatures are in the region of $\sim 4 - 5$ μK, which are roughly in agreement with the ones measured with lightsheet that were previously quoted in section 3.4.2. There are differences, however, as the values obtained in that section are a bit higher, in the region of 7-8 μK. The differences could be due to errors on the measurements performed here and/or due to slight out-of-focus imaging of the lens although it seems that the lens is relatively well-focused. As this is a preliminary estimation, it would be good to re-perform these measurements multiple times to include some statistics. Additionally, this pixel size and temperature estimations were performed towards the beginning of the implementation of the imaging detection, with multiple rounds of optimisations in-between.

6.2.3 Initial Interferometry

Due to the limitations of the camera, the detection scheme had to be modified to be able to perform single-state detection. In order to be able to give a comparison of performance, a simultaneous photodiode detection was implemented. The photodiode detection was performed by performing two pulses, as seen in Figure 6.18. Both of these pulses contain the cooling and repump lights. The first pulse is the atom signal while the second pulse is just the light background - note that in the future it might be better to include a blowaway between these pulses. The difference between the pulses is taken as the final $|F = 2\rangle$ population ratio, although unlike in two-state defection, this is not normalised. For the camera, the first pulse is used to perform the atom measurement. However, the background signal could not be performed using the second pulse as the time taken to save the camera data is in the region $\sim$0.3 - 0.6 s. To obtain the background signal for the camera, a subsequent experimental sequence is ran but without the MOT coils being switched on and using the first of these two

pulses - this was used for the camera noise analysis described in the previous section. The current optimised camera imaging detection has the camera exposure starting for 400 μs, followed by 250 μs delay followed by light pulse of 100 μs.

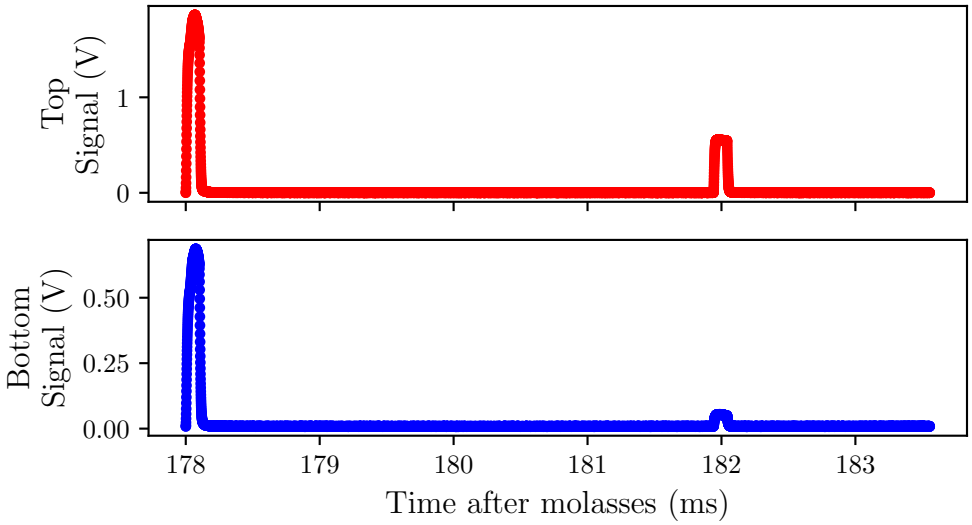


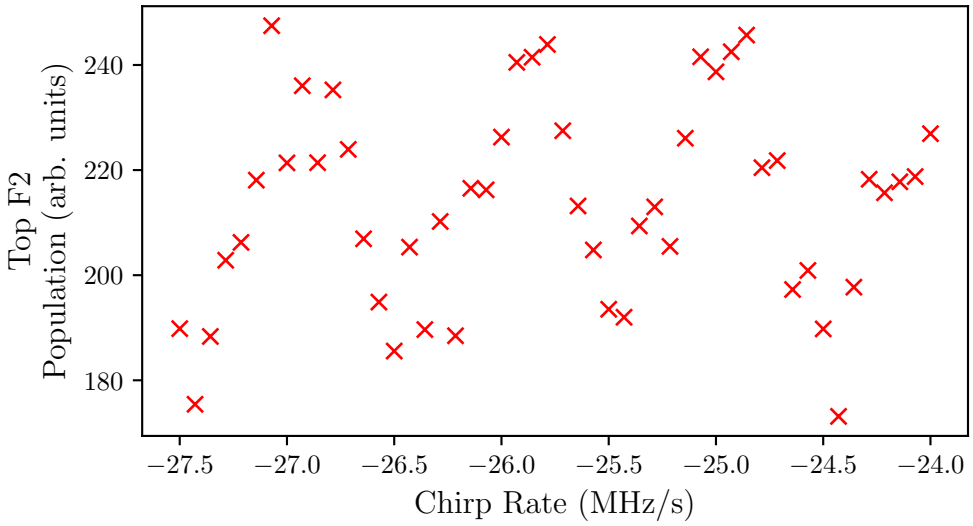
Figure 6.18: Single-state detection scheme.

An example of gravity fringes obtained using this single-state detection can be seen in Figure 6.19. Both of these are for the top chamber and use a loading time of 5 s to obtain a reasonable signal. As can be seen by comparing with section 6.1.5, these fringes are not as good or as clean as the ones obtained with two-state detection, highlighting the advantage of this method over single-state detection. As can be seen by looking at Figure 6.19(a), this is the case even with the photodiode. The camera imaging uses a 2D Gaussian fitting of the subtracted results of the imaging, where the amplitude of the Gaussian is taken the $|F = 2\rangle$ population ratio. After some data points have been excluded from the camera imaging results to get rid of outliers (three points with amplitude below 0.85), the filtered data between the camera and photodiode look fairly comparative. The outliers are interesting as they do not feature the same in the photodiode results, therefore it is unknown whether these are a remnant of the

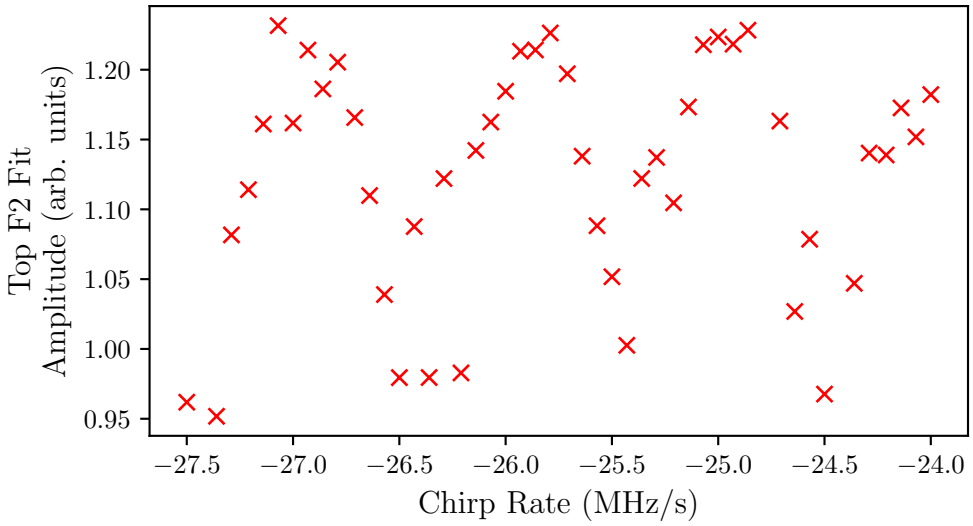
analysis method or some physical reason. This probably needs more investigation as it has been found that there are some random outliers when running these experiments. One thing to note with the camera results is the fact that in the quest to reduce the background noise as much as possible, this has meant that the signal is also very low (the maximum pixel value in the camera fringes is $\sim$1.2). As the phase shear fringes are likely to be relatively small, this signal strength likely needs to be increased.

As the plan is to use multiple phase shear measurements to average over, as well as to ensure that the system is relatively stable when demonstrating the fringes in the first instance, the system was placed on an vibration isolation platform (Table Stable TS-150 [155]) via an adapter plate. This is obviously able to improve the T times considerably as well. An example of this improvement using two-state detection for T = 10 ms (with the first pulse 50 ms after molasses) using the isolation platform can be seen in Figure 6.20 and serves to highlight the benefit of an isolation platform. We will note that the isolation platform is to be used while trying to demonstrate the fringes in the first instance. However, as the goal is to create a portable gradiometer, once these can be demonstrated, the goal is to use the fringes without any isolation platform.

Attempts were made to see whether phase shear fringes could be observed. To do this, a set of 50 images were taken and the mean of these calculated to obtain a "mean" image. A standard Python PCA library was used to analyse this image and the first two principal components were taken. The first principal component was fit with a Gaussian to obtain the cloud width while the second one was fitted with a sinusoidal pattern combined with a Gaussian to obtain the spatial frequency, in analogy with section 4.1.0.7. These can be seen for different times after molasses and for different beam tilts in Figure 6.21 for a chirp rate of -27 MHz/s to ensure that we obtain the maximum signal even with no tilt. The goal was to see whether any differences would be seen between the different times after molasses and between tilting and no tilting -



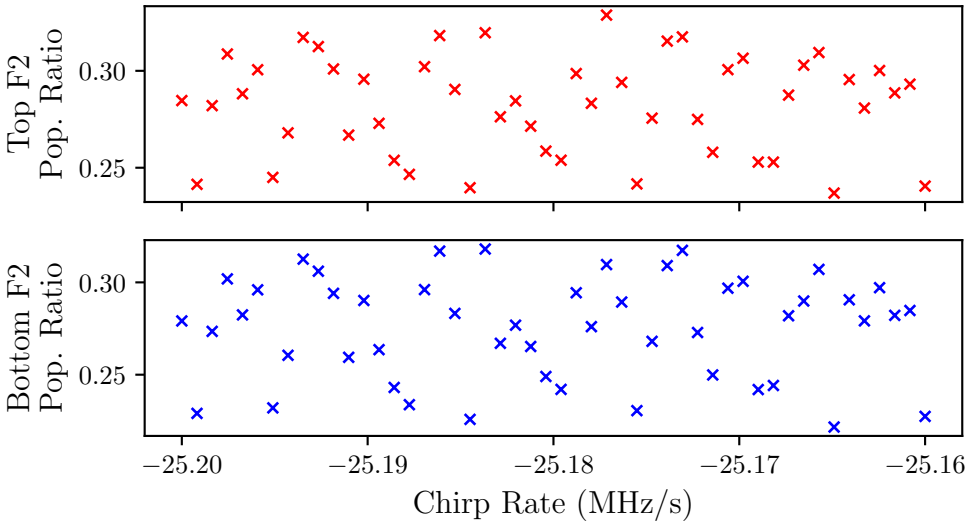
(a)



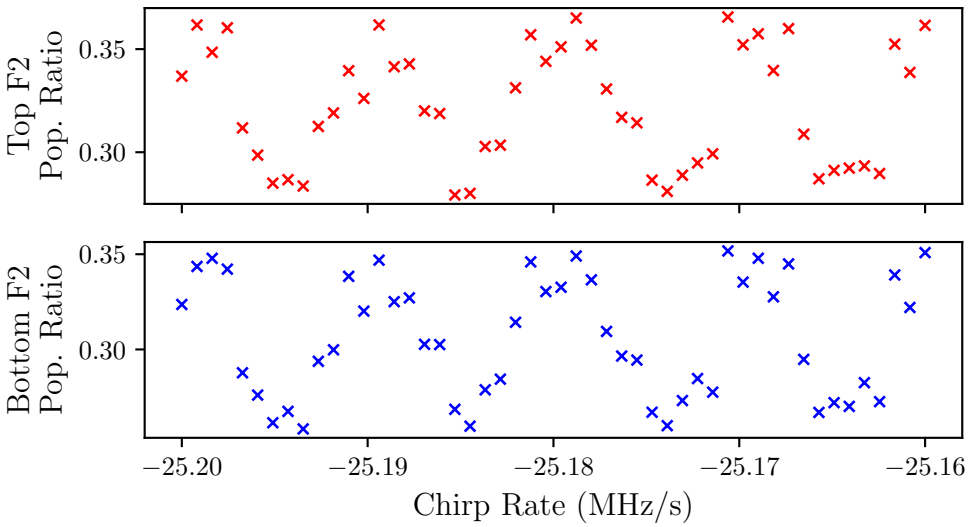
(b)

Figure 6.19: Gravity fringes using single-state detection for $T = 1$ ms with the first pulse being 40 ms after molasses as obtained with **(a)** photodiode and **(b)** camera, where the camera fringes have been filtered to ignore outliers.

it is unlikely that maximum tilt actually translates to 500 μrad tilting as there is slight misalignment - because the beam tilting spatial frequency is dependent on both of these factors. As can be seen from the figures, the radius of the Gaussian does not look



(a)



(b)

Figure 6.20: Gravity fringes utilising two-state detection **(a)** without and **(b)** with the isolation platform enabled for $T = 10$ ms and the first pulse being 50 ms after molasses. The reduction of vertical vibrations is the reason for being able to observe these fringes in **(b)** but not in **(a)**.

unreasonable but the fit is not amazing for all of these, especially for the 50 ms after molasses results and is different between the times after molasses. Similar differences

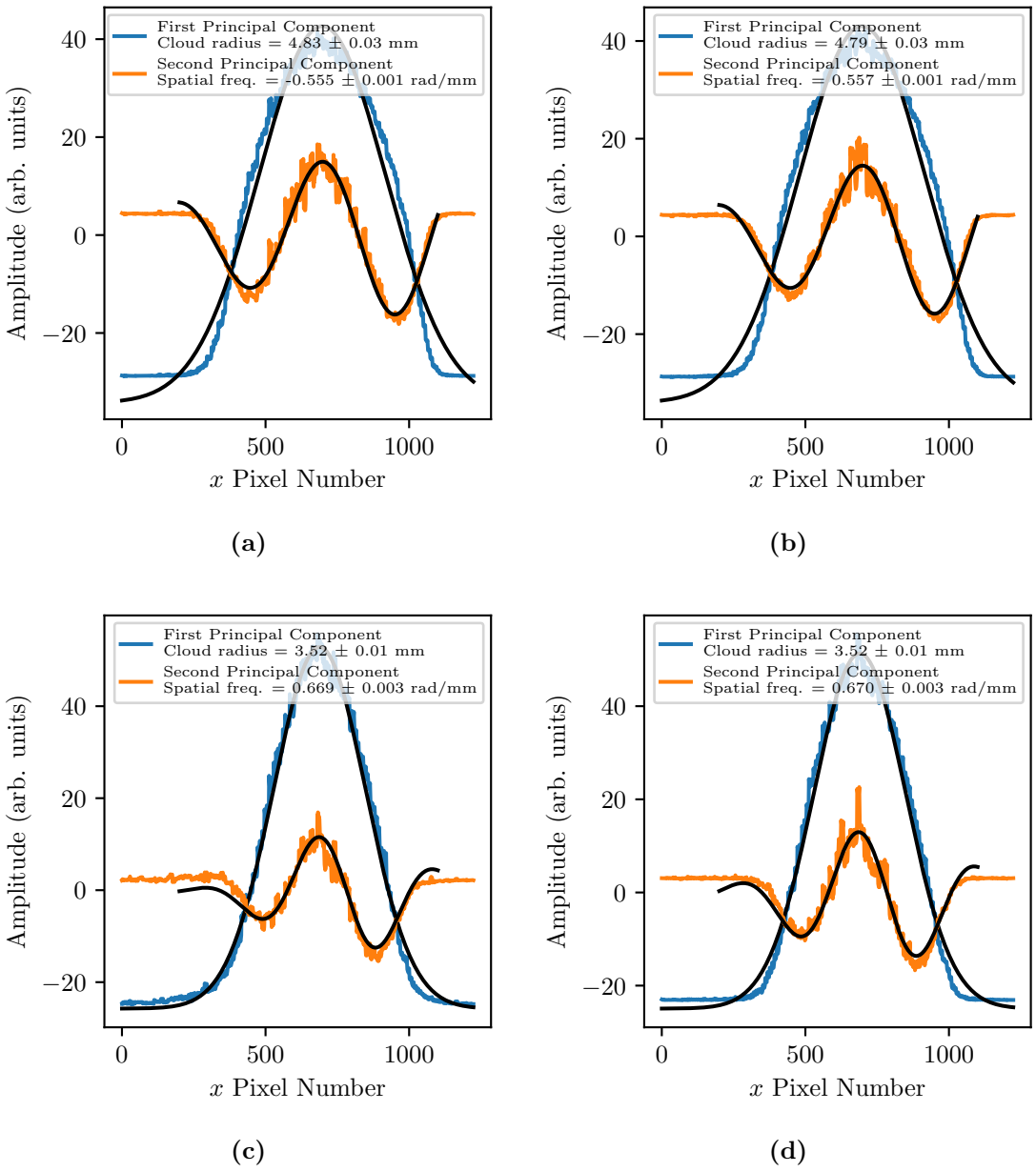


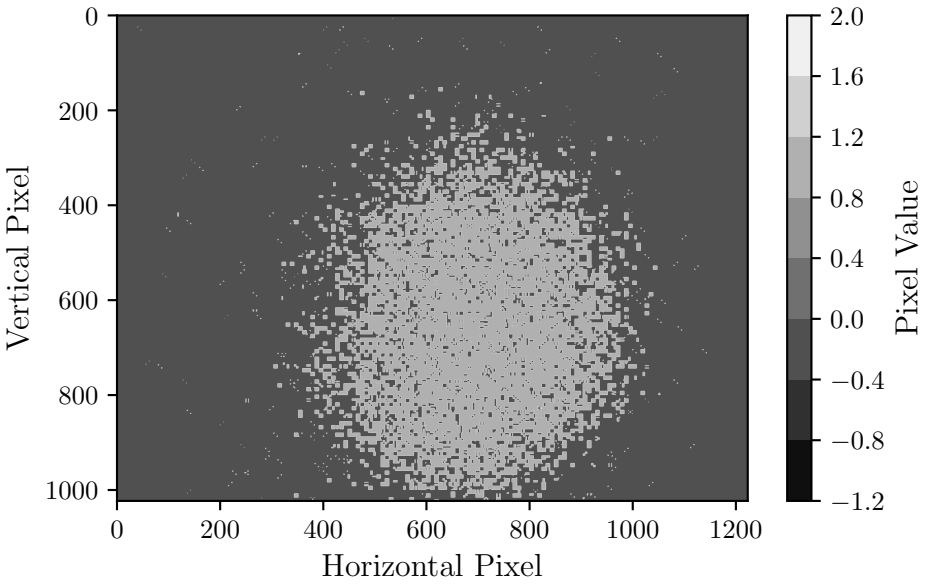
Figure 6.21: Phase shear attempts for $T = 1$ ms. **(a)** First pulse 50 ms after molasses and no beam tilt. **(b)** First pulse 50 ms after molasses and maximum beam tilts along both axes. **(c)** First pulse 150 ms after molasses and no beam tilt. **(d)** First pulse 150 ms after molasses and maximum beam tilts along both axes. The solid black lines are the fits to both of the principal components used to obtain the parameters in the legends.

between 50 and 150 ms after molasses are seen in the spatial frequency but there is no discernible difference between tilting and no tilting (this is also the case for the third principal component). Therefore, no fringes can be seen in this case. Actually looking at example images of Figure 6.22, the lack of the phase shear fringes is apparent, with almost no difference in the images seen with and without beam tilting in the subtracted image - note that the pixel values are negative in some cases due to the subtraction of the background.

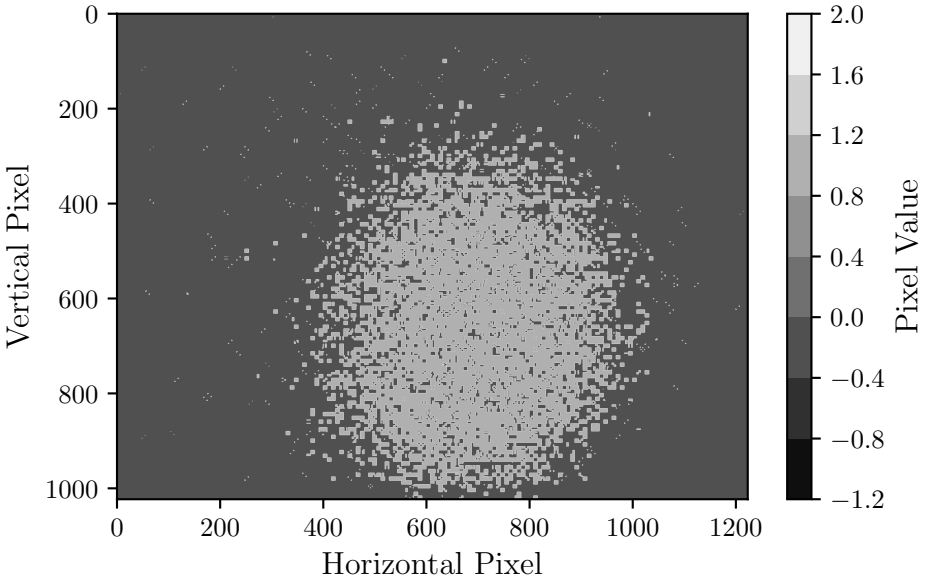
Nevertheless, we have demonstrated the steps needed to move from standard atom interferometer to building and starting to implement phase shear readout. This has included the steps and considerations needed to implement a beam tilting telescope as well as introducing camera imaging into the system. These lessons can be used on most standard atom interferometer setups, and specifically on the systems within our group. A preliminary analysis technique of these fringes utilising principal component analysis has also been created, able to be used once the fringes are seen.

6.3 Moving Platform

As the purpose of this work is to understand and investigate operation in dynamic conditions, the sensor head was placed on a linear rail with an adapter plate and the bottom of the sensor was strapped to this adapter plate, as seen in the still images in Figure 6.23. This meant that the sensor head could be moved while keeping the laser system stationary. The linear rail in question is the Parker Motion 412T07XRMSD2. It is a one-axis linear actuator and is 1200 mm in length [156]. Control of this rail is enabled using a bespoke controller shipped with the rail together with a bespoke Motion Perfect v4.3 software that utilises Trio programming language. The controller is connected to a PC via an ethernet cable, similarly to ARTIQ. As is the case with



(a)

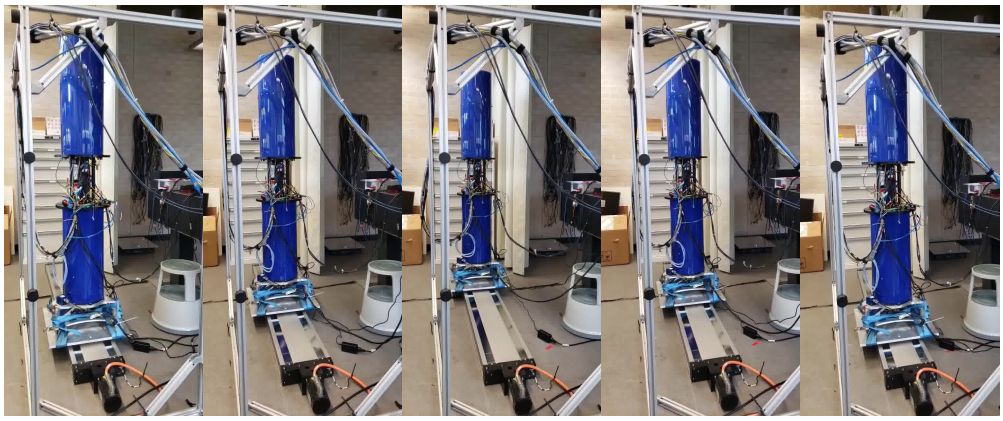


(b)

Figure 6.22: Atomic cloud image with first pulse 150 ms after molasses **(a)** without application of beam tilting and **(b)** with the application of beam tilting.

ARTIQ, the PC needs to be on the same IP network as the rail. These settings are different to the ARTIQ and hence a different PC needed to be connected to be able

to control it. ARTIQ Zotino together with a voltage amplifier was needed to be able to trigger the rail - the rail needs voltage of at least 12 - 15 V to be able to trigger it. The trigger was setup to be a part of the standard experimental sequence, and will be discussed later. As the rail works in its own internal units, a calibration had to be performed to be able to convert these internal units into metric units (16,000 internal units are equivalent to a distance of 76 cm). This can be used as a reference to set parameters, such as the desired acceleration and velocity of the rail, etc.



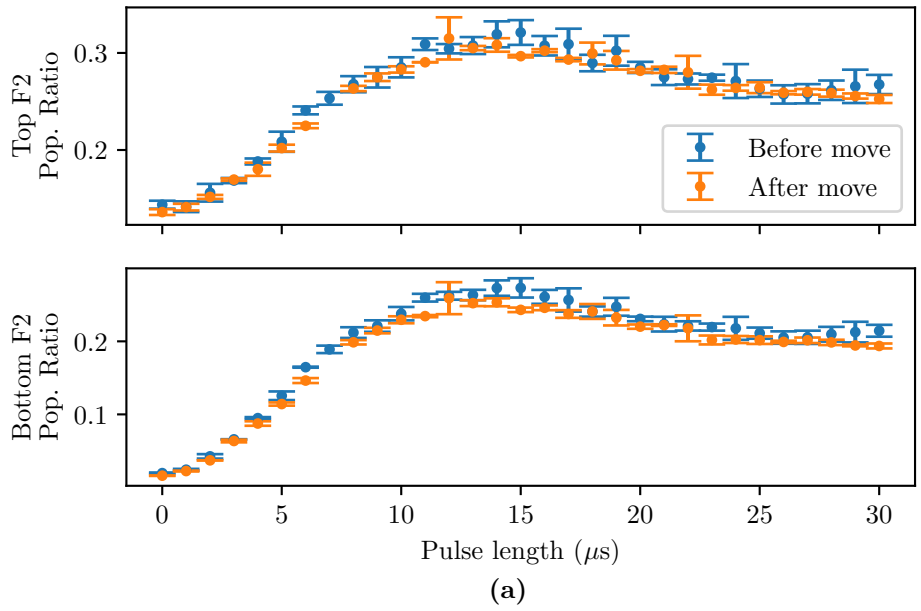
© Crown Copyright

Figure 6.23: Still images of the sensor head moving on the rail.

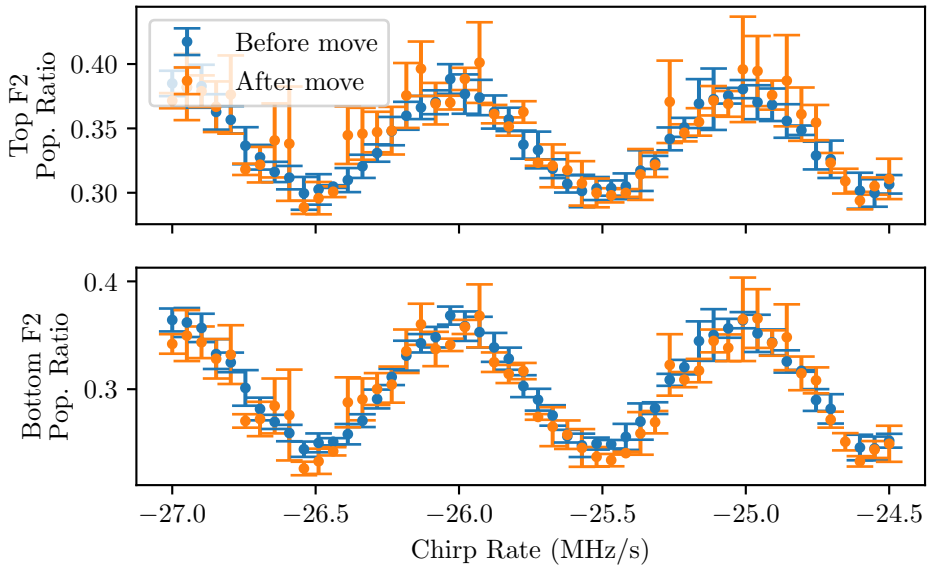
Since the sensor head is placed on the rail separately from the laser system, the umbilical cord was attached to a rigid structure around the system. This was to ensure that it is as stable and as static as possible. This was done to reduce the amount of intensity variation that might be introduced as a result of its motion. A simple first step is to make sure that if the sensor head moves and comes back to its original position, the performance is comparable. To do this, a set of three measurements were taken while the sensor head was static. The sensor head was then moved along the rail and returned back to its original location. Subsequently, a set of another three

measurements was taken. Example of this testing can be seen in Figure 6.24, where (a) shows the Rabi oscillations and (b) shows the gravity fringes using the two-state detection. The error bars represent the standard deviation of these measurements. One point had been filtered from the Rabi plot after the move as the mean was within the trend but the standard deviation was too large as one of the three measurements was higher than usual for both of the chambers. This is likely to be due to noise rather than the move because a similar point was filtered from the gravity fringes for both of the chambers but before the move. The performance before and after the move appears comparable.

The other issue with moving is the changing external environment. In general, this is not an issue in laboratory settings as the external environment is constant and can be controlled. As this experiment is located on the second floor of a research building, with different equipment present at different points of the building, a check of the chirp rate and the magnetic field seen by the atoms in the interferometry region was conducted at different points along the rail. This was unlikely to be hugely different as the distances are not huge but we wanted to verify this using the atoms to ensure that this would not cause significant issues. Spectrum scans at different points in the chamber for a few points along the chambers were taken for different locations on the rail. These were used to calculate the chirp rate as well as the magnetic field profiles at each of these locations. These can be seen superimposed in Figure 6.25 for a number of these locations investigated. The legend of distance is in reference to the same location along one side of the rail. The chirp rates calculated are very identical, with the slight differences likely an effect of relatively few measurements points as well as noise. The same is the case for the magnetic field profiles seen at each of these locations, which is potentially the more useful measurement. This means that the magnetic field profile seen by the atoms during the interferometry is largely unchanged between the locations



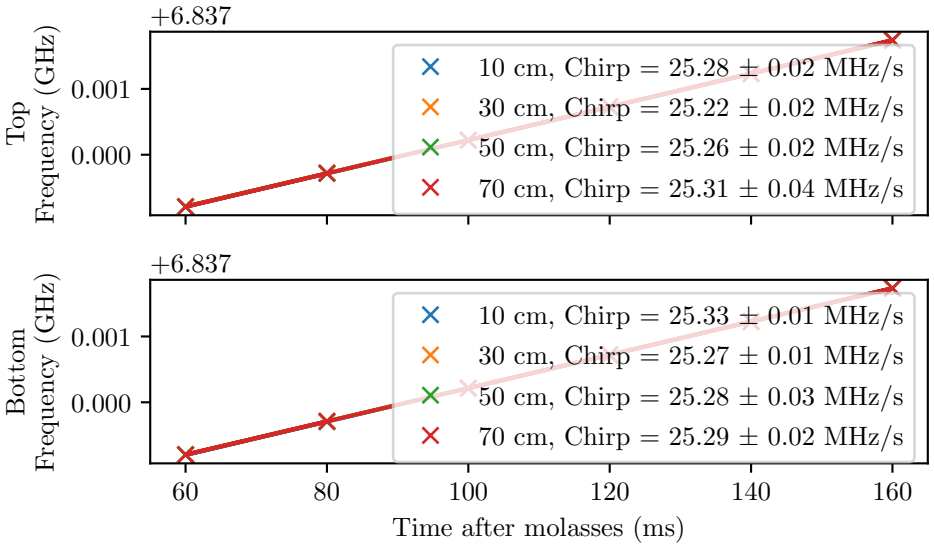
(a)



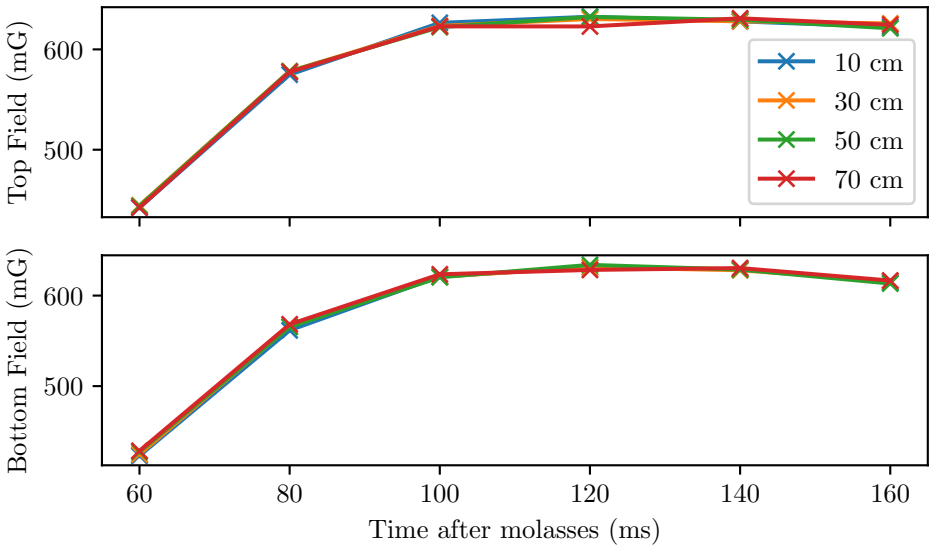
(b)

Figure 6.24: **(a)** Rabi oscillations 150 ms after molasses and **(b)** gravity fringes with $T = 1$ ms with the first pulse being 150 ms after molasses. Both of these show the results before and after moving the sensor head.

on the rail.



(a)



(b)

Figure 6.25: **(a)** Chirp rate and **(b)** magnetic field profile calculations at different locations along the rail.

A tiltmeter (Jewell Instruments JDI-200 14.5 inclinometer), which is able to measure with an accuracy of 0.015° [157], was integrated with the sensor head as well as

the experimental sequence using Python threading (parallel processing) to obtain the measurements of tilt during the sequence. This tiltmeter was attached to the bottom of the sensor head with screws, at an angle to the propagation of sensor head on the rail - therefore neither of x and y tilts perfectly represent the axis along the movement direction. However, these tilts were analysed for a set of 10 runs and the maximum and minimum tilts observed for each of these axes - these can be seen in Figure 6.26. A clear correlation is seen between the applied acceleration and the tilt measured. In general, the x-axis experiences greater tilting than the y-axis. The sensor head is not perfectly inclined as even the stationary case has an small tilt to it. Considerable tilting is seen with the higher accelerations applied, implying that strapping the sensor head to the bottom is, as expected, not a good enough way to secure the system. Therefore, a better design would be to create a more rigid structure.

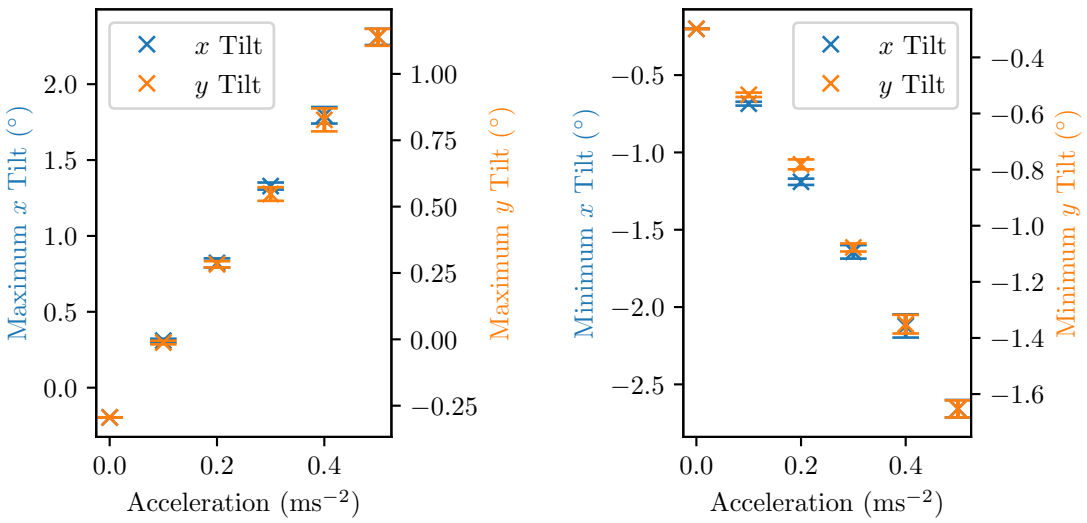


Figure 6.26: **(a)** Maximum and **(b)** minimum tilts as measured by the tiltmeter when the sensor is moving along both of the axes measured. The error bars are the standard deviation of a set of 10 measurements. A clear correlation is seen between the applied acceleration of the rail and the tilt seen by the tiltmeter.

The other classical sensor that has been integrated is the Nanometrics Titan accelerometer (Direct Current [DC] to 430 Hz; 4/2/1/0.5/0.25 V/g sensitivity ranges) [158]. The output of this accelerometer was collected by a picoscope for each of the experimental runs, from before the MOT loading until after the detection sequence at the end of the interferometry sequence. The accelerometer was mounted at the bottom of the sensor head but in this case it was strapped to it with cable ties. The y-axis was oriented in direction of the movement of the rail. The results of the applied acceleration as per the rail and the maximum measured acceleration by the accelerometer (utilising the 0.25 V/g sensitivity range) can be seen in Figure 6.27. Unlike the tiltmeter, it is very hard to draw any conclusive results from this but it appears that the applied acceleration as per the rail might not correspond to this acceleration in real-life. There are a few potential reasons for this. Firstly, the mounting with cable ties is not a good solution as this might mean that the acceleration measured by the accelerometer does not fully correspond to the acceleration seen by the sensor head. It would be useful to design and manufacture a rigid structure of mounting the accelerometer to the sensor head, similarly to the tiltmeter. Secondly, the rail has not been fully characterised yet and it is not clear how fast the triggering works and whether it can respond fast enough - the trigger was set to trigger at the end of the molasses sequence and have the desired accelerations for 0.5 s; therefore, within the experimental drop. This was chosen by trial and error as longer time-frames meant that the rail failed to work at larger accelerations due to the design limits of the rail, which will be discussed in chapter 7.

Even with the obvious areas that need improving in order to design good trials and to be fully able to utilise the rail and the peripheral instruments together, attempts of seen how moving Rabis changed with different applied accelerations were made, and examples for minimum and maximum applied accelerations can be seen in Figure 6.28. They show largely the same behaviour although the top chamber at 0.5 ms^{-2} appears

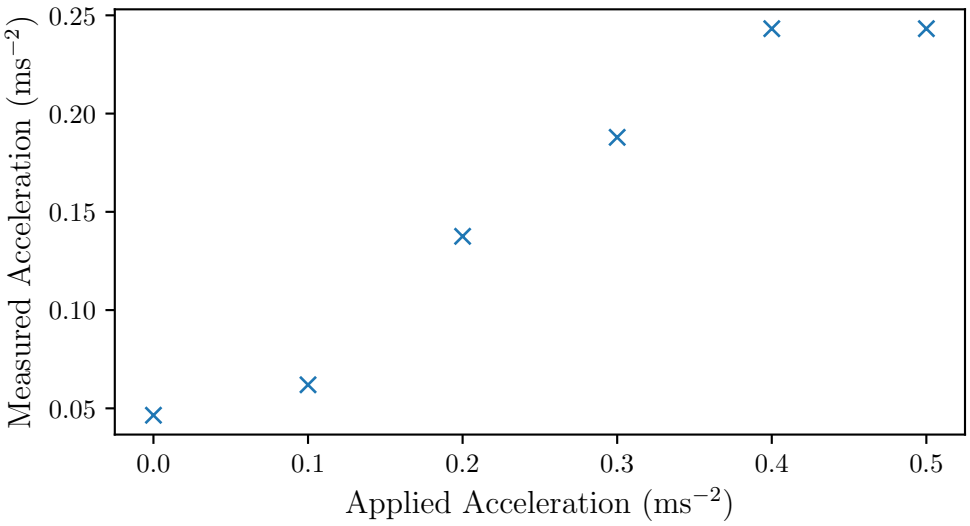


Figure 6.27: Maximum accelerations measured by the Nanometrics Titan accelerometer compared against the ones set by the rail software.

noisier. However, as additional movement has been done between these points, it could be that instability introduced due to multiple runs is the reason for this. Similar, albeit smaller, effect is also seen for the bottom chamber. More experimental runs were performed to see whether these Rabi oscillations would follow the results seen in chapter 5 (as well as gravity fringes and two pulses) but no trends were seen. Actually, in some cases, the standard deviation of the static case was higher than an accelerating one, implying low performance of the system.

However, we have now started the integration of the peripheral instruments with the atom interferometer, able to measure all of the different parameters simultaneously. This foundation serves to help the other systems in our group to transition into dynamic conditions, which is the aim of this work. Lastly, we have also demonstrated the beginnings of measuring Rabi oscillations in dynamic conditions.

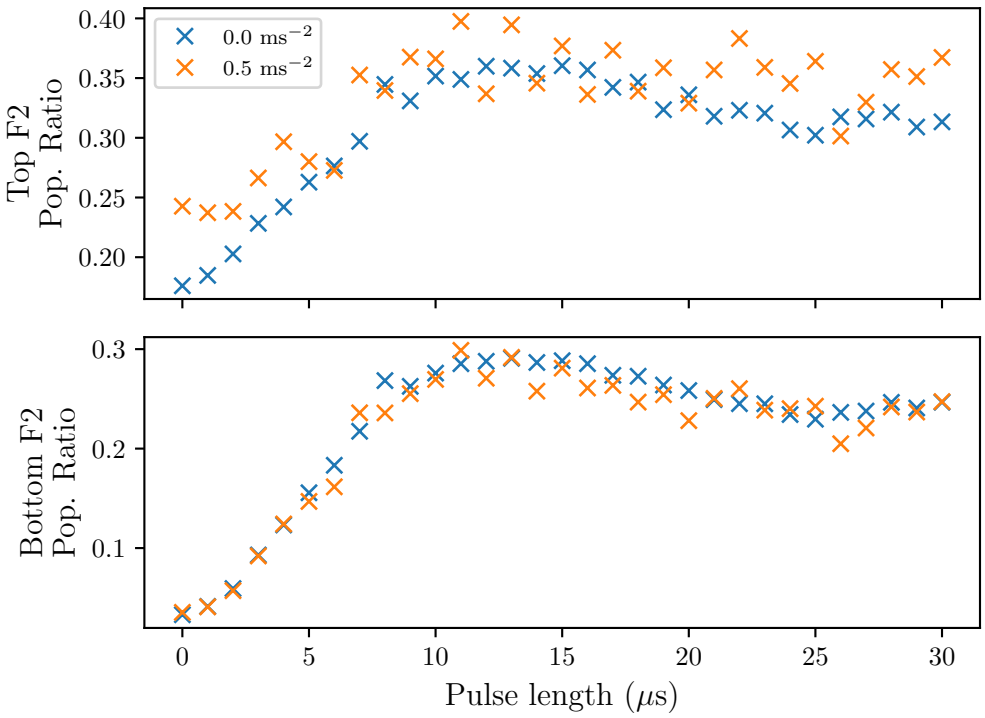


Figure 6.28: Rabi oscillations while the rail is stationary and moving.

Chapter 7

Conclusion and Outlook

The operation of atom interferometers in dynamic conditions has been investigated, with key effects discussed. Many of the known effects are currently the dominating challenges in these conditions; however, they can often be tackled with engineering solutions, such as placing the sensor on a gimbal or using sensor instrumentation to provide corrections. Above a small threshold, this is not the case for the transverse acceleration of the sensor during the experimental sequence. This poses fundamental challenges of operation, the effect of which will become more relevant as the performance of these systems improves. As a result, this cross-coupling and signal loss effect has been investigated, creating the mathematical and theoretical tools to quantify it. As an example, we have shown a contrast drop from $\sim 100\%$ to 59% for $T = 80$ ms and 49% for $T = 40$ ms (with 10^6 atoms) can be observed even when the centre-of-mass of the atoms is within the waist radius of the laser beam. There is an outstanding question as to the strange behaviour of the gravity fringes even when the atomic cloud is within the waist radius. This needs to be investigated and understood. This has an effect on the "apparent" phase shift calculations that can be performed, which also need to be checked for appropriateness and the tolerances used. In spite of that, the effect of horizontal temperature has also been investigated. A simple compensation

technique has been proposed, showing small contrast improvement as well as potential "apparent" phase shift improvement, the latter of which could potentially prove more interesting. Therefore, to close off this work, the strange behaviour of the gravity fringes needs to be understood as well as the appropriateness of the "phase shift" calculations. Once these are dealt with, the software infrastructure is ready to re-run the simulations fairly quickly. We have also proposed a way to validate these results experimentally via the use of Rabi oscillations (although the gravity fringes contrast drop could also work). The experimental validation of these findings and implementation of mitigation schemes is being planned for in future trials.

Two techniques of overcoming operation in dynamic conditions have been investigated theoretically. The first is phase shear readout, where it is possible to obtain the interferometer contrast and phase in one experimental shot. For this reason, a simple model that can simulate the fringes, combined with fluorescence and camera imaging detection has been created. It would be useful to include other additional parameters to this model, such as depth of field and other blurring mechanisms. The work on implementation of phase shear readout is informing other experimental activities, including towards implementation in trials, with the model being used to help with capturing the technical requirements. The other technique investigated is the potential of multi-modal measurements of gravity, magnetic field and magnetic field gradient using the separate m_F states to, for example, tackle the changing external magnetic field. These offer promising atom shot noise limited uncertainties of 3×10^{-8} ms^{-2} per shot for gravity and 4×10^{-6} Gm^{-1} per shot for magnetic field gradient (assuming $T = 50$ ms with 10^6 atoms). These are simple estimates and more work should be done in order to ensure that some other factors are not missed. The calculation of the quadratic effect for the $m_F = \pm 1$ states remains to be validated and is the biggest unknown with this work, with two potential ways of obtaining it presented.

Experimentally, a gravity gradiometer based using atom interferometry has been built. It is capable of producing over 10^8 atoms in the MOT, with temperatures of 7.3 $\pm$ 0.2 μK for the top chamber and 7.4 $\pm$ 1.7 μK for the bottom chamber obtained following molasses and state preparation. This has been demonstrated to perform interferometry, including short T gravity fringes. However, currently, the system suffers from low performance, with Rabi fidelities of $\sim$17% for the top chamber and $\sim$23% for the bottom chamber. The variations of π times in both chambers suggest a misalignment of the Raman beams that needs to be addressed. This low performance makes the observation of the phase shear fringes and the cross-coupling effect difficult. As the Rabi oscillation amplitudes do not reach 0, there might be an issue with the $|F = 2\rangle$ blowaway and so re-optimisation of this might be useful. Additional useful upgrade would be the inclusion of m_F state preparation to obtain higher fidelities in the Rabi oscillations.

However, the current performance of the system has allowed for valuable lessons to be learnt. With regards to the phase shear readout, the telescope swap has been successful and performance comparable prior to the upgrade has been observed. This work has shown that the piezo-actuated mounts are not trivial. They feature hysteresis loops with increasing and decreasing voltages and so it might be useful to think about ways to ensure that this does not affect measurements, e.g. by obtaining a feedback loop where the angle is measured and the appropriate voltage is applied to counterract this. The switching on of the piezo-actuated mounts also features oscillations in some cases that last a few ms. The feedback loop mentioned might be able to counteract this effect as well. When measuring the piezo-mount angles produced, significant noise has been seen. It is unclear whether this is an artefact of the mounts themselves or external vibrations. It might be useful to perform these measurements on an isolation platform (and potentially within the system if possible) to investigate this further. The addi-

tion of the camera detection has also been successful, with the performance obtained with the camera and photodiode (utilising single-state detection) being comparable. However, work still remains. The noise of the camera has been kept as low as possible, however, part of this has been at the expense of the signal seen. While Rabi oscillations and gravity fringes using this detection and single-state detection have been obtained, the maximum pixel values of $\sim$1.2 for the gravity fringes are low, likely hindering the observation of fringes. The other aspect that has not been tested is the lens system. It would be useful to quantify the effect of this by using test targets. Additionally, an analysis code for performing PCA on the experimental data has been created, able to obtain the different principal components. The exact performance of this analysis is yet untested until the fringes are obtained. It would be a useful exercise to analyse this analysis method further using the modelling in section 4.1. This model could feed into this PCA analysis and see whether the output matches the simulated input. While the modelling implies that the angles investigated should be able to produce fringes with enough spacing, blurring mechanisms could deter this and create what appears to be a single atomic cloud.

The use of atom interferometers on the linear rail has also been investigated. The movement of the sensor back and forth has not presented issues on the performance. However, when tests of performing measurements during movement for extended periods have been done, increased noise has been observed. This is believed to be partly due to motion of the umbilical cord, and partly due to movement of the sensor head itself. The integration of the peripherals sensors with the interferometer has been completed, being able to measure both the tilt experienced during the movement with a tiltmeter (showing correlation between applied acceleration and the tilt experienced) as well as the acceleration with a classical accelerometer. One issue that needs to be resolved is the difference between the applied rail acceleration and the measured

accelerometer acceleration. An improvement to the setup would be to mount the accelerometer to the sensor head more rigidly, rather than using cable ties, to ensure that the acceleration measured is correlated with the sensor head. Additionally, the tilting of the sensor head during the movement should be addressed, likely requiring better mechanical support. The biggest limitation to performing the tests has been due to the rail. By trail and error it has been found that accelerations up to $\sim$0.6/0.7 ms^{-2} can be programmed into the rail because higher accelerations cause the rail to malfunction. By confirming with the provider of the rail, it is unlikely that the rail should be able to reach velocities over 0.2 ms^{-1}. This, together with the length of the rail, means that while higher accelerations are in principle possible, these cannot be obtained for long times. This limits the use of this rail, especially for a demonstration of the cross-coupling effect. The rail itself should also be characterised more if other trials on it are to be performed, especially the response of the trigger and the movement to ensure that the time between triggering and the rail moving is adequate.

The research conducted here is being built on and used. Other experimental activities are underway to implement phase shear readout, with the modelling and lessons learnt here contributing to guide the work, while the multi-modal work has led to new doctoral research to advance it (with plans for experimental validation) and to investigate other multi-modal measurements. The work on the cross-coupling paper continues; focusing on finalising parameter values, understanding whether operating interferometers by applying phase shift on the last pulse has advantages over chirp rate scan, possible analytical calculations of the "apparent" phase shift, and other compensation techniques (e.g. beam shaping). The system in [6] has plans to perform trials in dynamic conditions; these could be used to map experimental data onto the cross-coupling work. In the meantime, this work has contributed to other theoretical and experimental work, including design of future systems and moving trials.

Appendices

Appendix A
Additional Theory

The Schrödinger equation can be solved using these substitutions, yielding for example [14, 85]:

$$\begin{aligned} &c_b(t) - c_b(t_0) = \\ &= -i\Omega_{eb}^* \int_{t_0}^{t} c_{e1}(t') e^{i\left(\frac{|\boldsymbol{p}+\hbar\boldsymbol{k}_{\mathrm{eff}}|^2 - |\boldsymbol{p}+\hbar\boldsymbol{k}_1|^2}{2m\hbar} + \omega_{be}\right)} \left(\frac{e^{i(\omega_2 t' + \phi_{2\mathrm{L}})} + e^{-i(\omega_2 t' + \phi_{2\mathrm{L}})}}{2}\right) \mathrm{d}t'. \end{aligned} \tag{A.1}$$

Since $c_{e1}(t')$ is a slowly varying amplitude, the integral of the "off-resonant" term $e^{i(\omega_{be}+\omega_2)t'}$ will be much smaller than the integral of the "resonant term" $e^{i(\omega_{be}-\omega_2)t'}$. Adopting the "rotating wave approximation" (RWA) and considering only the "resonant term" [43, 85, 90]:

$$i\dot{c}_a(t) = \frac{\Omega_{ea}^*}{2} \exp\{i[\Delta \cdot t - \phi_{1\mathrm{L}}]\} c_e(t), \tag{A.2a}$$

$$i\dot{c}_b(t) = \frac{\Omega_{eb}^*}{2} \exp\{i[(\Delta - \delta)t - \phi_{2\mathrm{L}}]\} c_e(t), \tag{A.2b}$$

$$i\dot{c}_e(t) = \frac{\Omega_{ea}}{2} \exp\{-i[\Delta \cdot t - \phi_{1\mathrm{L}}]\} c_a(t) + \frac{\Omega_{eb}}{2} \exp\{-i[(\Delta - \delta)t - \phi_{2\mathrm{L}}]\} c_b(t). \tag{A.2c}$$

These are essentially a set of coupled first-order differential equations for $c_a(t), c_e(t)$ and $c_b(t)$. If the detunings $\omega_1 - (\omega_e - \omega_a)$ and $\omega_2 - (\omega_e - \omega_b)$ are much larger than the Rabi frequencies, the coefficients $c_k(t)$ vary slowly compared to the explicitly time-dependent terms. Therefore, the coefficients for the state $|e\rangle$ can be adiabatically eliminated. This leaves only a couple of equations for a two-level system in an external

driving field [43, 85, 90]:

$$i\dot{c}_a(t) = \frac{|\Omega_{ea}|^2}{4\Delta} c_a(t) + \frac{\Omega_{ea}^* \Omega_{eb}}{4(\Delta - \delta)} \exp\{i[\delta \cdot t + \phi_{2\mathrm{L}} - \phi_{1\mathrm{L}}]\} c_b(t), \tag{A.3a}$$

$$i\dot{c}_b(t) = \frac{\Omega_{eb}^* \Omega_{ea}}{4\Delta} \exp\{-i[\ \delta \cdot t + \phi_{2\mathrm{L}} - \phi_{1\mathrm{L}}]\} c_a(t) + \frac{|\Omega_{eb}|^2}{4(\Delta - \delta)} c_b(t). \tag{A.3b}$$

These equations can be simplified using the following substitutions [90]:

$$\begin{aligned} &\Omega_a^{\mathrm{AC}} = \frac{|\Omega_{ea}|^2}{4\Delta}, \qquad \Omega_b^{\mathrm{AC}} = \frac{|\Omega_{eb}|^2}{4(\Delta - \delta)}, \qquad \Omega_{\mathrm{eff}} = \frac{\Omega_{eb}^* \Omega_{ea}}{2\Delta}, \\ &\phi_{\mathrm{eff}} = \phi_{1\mathrm{L}} - \phi_{2\mathrm{L}}, \quad \delta_{\mathrm{AC}} = \Omega_b^{\mathrm{AC}} - \Omega_a^{\mathrm{AC}}, \qquad \Omega_{\mathrm{AC}} = \Omega_b^{\mathrm{AC}} + \Omega_a^{\mathrm{AC}}, \end{aligned} \tag{A.4}$$

as well as the fact that $\Delta >> \delta$. Applying these definitions yields [43, 90]:

$$i\dot{c}_a(t) = \Omega_a^{\mathrm{AC}} c_a(t) + \frac{\Omega_{\mathrm{eff}}^*}{2} \exp\{i[\delta \cdot t - \phi_{\mathrm{eff}}]\} c_b(t), \tag{A.5a}$$

$$i\dot{c}_b(t) = \frac{\Omega_{\mathrm{eff}}}{2} \exp\{-i[\delta \cdot t - \phi_{\mathrm{eff}}]\} c_a(t) + \Omega_b^{\mathrm{AC}} c_b(t). \tag{A.5b}$$

To be able to solve these differential equations, another substitution is used [85, 90]:

$$c_a(t) = s_a(t) \exp\left[\frac{i(\delta - \Omega_{\mathrm{AC}})t}{2}\right], \tag{A.6a}$$

$$c_b(t) = s_b(t) \exp\left[\frac{i(-\delta - \Omega_{\mathrm{AC}})t}{2}\right]. \tag{A.6b}$$

This transformation describes a quantum state in terms of a state rotating around the z-axis with frequency δ coupled with a uniform shift of the energy scale of $\hbar(\Omega_b - \Omega_a)/2$ and allows for the removal of the time dependency in the off-diagonal terms [90]:

$$\begin{aligned} i\dot{s}_a(t) &= \frac{1}{2}\Big[s_a(t)(\delta - \delta_{\mathrm{AC}}) + s_b(t)\Omega_{\mathrm{eff}} e^{-i\phi_{\mathrm{eff}}}\Big], \\ i\dot{s}_b(t) &= \frac{1}{2}\Big[s_a(t)\Omega_{\mathrm{eff}} e^{i\phi_{\mathrm{eff}}} - s_b(t)(\delta - \delta_{\mathrm{AC}})\Big]. \end{aligned} \tag{A.7}$$

This system can be relatively easily solved in mathematics but is beyond the scope of this work. The result are the complex amplitudes of equation (2.14).

Appendix B
Phase Noise

There are many noise sources that affect the measurement of Φ. The two main ones that we will concentrate on in this appendix are:

1) **Raman Laser Phase Noise**: This is the residual noise between the two Raman lasers [51].

2) **Mechanical Setup**: In standard interferometer geometries, Raman beam enters the sensor head vertically from the top and is reflected by a mirror at the bottom of the sensor head. Vertical vibrations of the mirror will cause a change in overlap of the beams, leading to a phase noise [51]. Our geometry contains two independent Raman telescopes, feeding into the sensor head from both top and bottom. In this case, treating the top telescope as a reference point, any vibrations of the bottom telescope to this reference will result in phase noise similar to the vibrations of the mirror.

B.1 Sensitivity Function

Sensitivity function describes how different systematic effects, as well as Raman laser phase noise, couple into the interferometer [70]. An infinitesimal step in Raman laser phase $\delta\phi$ results in a change $\delta P(\delta\phi, t)$ of the interferometer probability. The definition of the sensitivity function is given by these parameters as [51]:

$$g_s(t) = 2 \lim_{\delta\phi \to 0} \frac{\delta P(\delta\phi, t)}{\delta\phi}. \tag{B.1}$$

The default operating mode of interferometer has them operating at mid-fringe (i.e. $\Phi = \frac{\pi}{2}$) because this is when the interferometer is the most sensitive. However, this also means that the interferometer is the most sensitive to interferometry phase fluctuations. Assuming perfect contrast, a small phase jump, $\delta\phi$, leads to [43, 51]:

$$P(\delta\phi, t) = \frac{1 - \cos(\pi/2 + \delta\Phi(\delta\phi, t))}{2} \approx \frac{1 + \delta\Phi(\delta\phi, t)}{2}, \tag{B.2}$$

using the identity $\cos(\pi/2 \pm x) = \mp\sin(x)$, followed by Taylor expansion and using $\sin(x) \sim x$ as $x \to 0$. This equation can be substituted into equation (B.1) to obtain [43, 51]:

$$g_s(t) = \lim_{\delta\phi \to 0} \frac{\delta\Phi(\delta\phi, t)}{\delta\phi}. \tag{B.3}$$

If the Raman pulses are ignored (as their length can be considered negligible), $\delta\phi$ can only occur outside of the interferometer, yielding $g_s = 0$, or between the pulses [51].

Equation (2.27) can be rewritten as [43]:

$$\Phi = \phi(0) - 2\phi(T) + \phi(2T) \tag{B.4}$$

to help derive the sensitivity function. If the fluctuation happens during the first free evolution (still keeping the assumption that the interferometer is kept at mid-fringe and hence $\Phi \approx \pi/2$), the phase jump will also affect the phases of the second and third pulses. If we assume that the laser phase noise does not happen during the pulses themselves, the interferometry phase becomes [43]:

$$\Phi + \delta\Phi = \phi(0) - 2[\phi(T) + \delta\phi] + [\phi(2T) + \delta\phi] = \frac{\pi}{2} - \delta\phi, \tag{B.5}$$

leading to $\delta\Phi = -\delta\phi$. Hence, one then obtains g_s = -1 for $0 < t < T$. Similar calculation can be performed if the phase jump happens during the second interferometry free evolution [43]:

$$\delta\Phi = \phi(0) - 2\phi(T) + [\phi(2T) + \delta\phi] = \pi/2 + \delta\phi, \tag{B.6}$$

and $\delta\Phi = +\delta\phi$, which leads to $g_s = +1$ for $T < t < 2T$ [43].

If $\delta\phi$ happens during the Raman pulse, the matrix of the pulse must be used to derive the sensitivity function within the pulse. The pulse is then a product of the matrix before $\delta\phi$ and a matrix after $\delta\phi$. The precise matrices derivation of this function is beyond the scope of this work. The equation for this sensitivity function has been shown to have the form [51, 86]:

$$g_s(t) = \begin{cases} 0 & t < -T - 2\tau \\ \sin(\Omega_{\mathrm{R}}(t+T)) & -T - 2\tau < t < -T - \tau \\ -1 & -T - \tau < t < -\tau \\ \sin(\Omega_{\mathrm{R}} t) & \tau < t < \tau \\ 1 & \tau < t < T + \tau \\ \sin(\Omega_{\mathrm{R}}(t-T)) & T + \tau < t < T + 2\tau \\ 0 & T + 2\tau < t, \end{cases} \tag{B.7}$$

and can be seen plotted in Figure B.1. It is an odd function around the central π pulse.

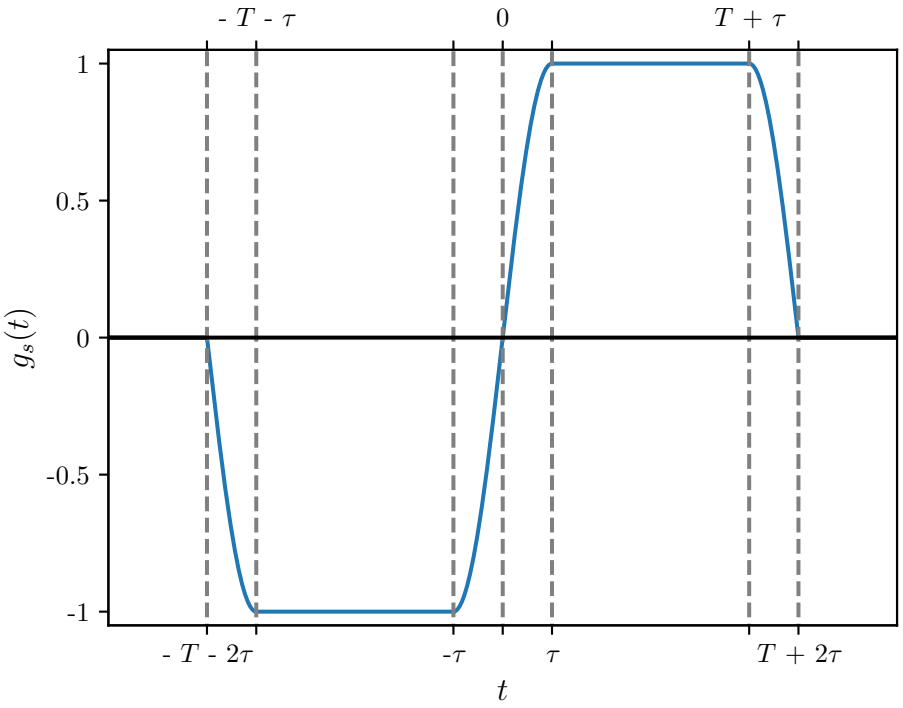


Figure B.1: Sensitivity function, $g_s(t)$, as a function of time, showing the odd symmetry.

B.2 Laser Phase Noise

In this section, we largely follow the work performed in [86] to derive the final transfer function of an interferometer.

The sensitivity function can be used to calculate the effect of a phase evolution $\phi(t)$ on the final interferometer output using [51, 86]:

$$\delta\Phi = \int_{-\infty}^{+\infty} g_s(t)\ \mathrm{d}\phi(t) = \int_{-\infty}^{+\infty} g_s(t)\frac{\mathrm{d}\phi(t)}{\mathrm{d}t}\ \mathrm{d}t. \tag{B.8}$$

Assuming a phase noise of $\phi(t) = A_0\cos(\omega_0 t + \psi)$ together with equation (B.8), the interferometer phase as a result can be calculated using [43, 51, 86]:

$$\delta\Phi = A_0\omega_0 \int_{-\infty}^{+\infty} -g_s(t)\sin(\omega_0 t + \psi)\ \mathrm{d}t. \tag{B.9}$$

The Fourier Transform of $g_s(t)$ is given by [86]:

$$G(\omega) = \int_{-\infty}^{+\infty} e^{-i\omega t} g_s(t)\ \mathrm{d}t, \tag{B.10}$$

where it is possible to replace $e^{-i\omega t}$ with $\cos(\omega t) - i\sin(\omega t)$. Here, we have to realise that $g_s(t)$ is odd, therefore, the integral $g_s(t) \times \cos(\omega t)$ is zero, simplifying the above equation to [86]:

$$G(\omega) = \int_{-\infty}^{+\infty} -i\sin(\omega t) g_s(t)\ \mathrm{d}t. \tag{B.11}$$

Thus equation (B.9) can be rewritten using identity $\sin(\omega_0 t + \psi) = \sin(\omega_0 t)\cos(\psi) + \cos(\omega_0 t)\sin(\psi)$. Realising that the integral of the latter is null, the following is obtained [86]:

$$\delta\Phi = A_0\omega_0 \int_{-\infty}^{+\infty} -g_s(t)\sin(\omega_0 t)\cos(\psi)\ \mathrm{d}t, \tag{B.12}$$

and finally the following can be deduced [86]:

$$|\delta\Phi| = A_0\omega_0\cos(\psi)|G(\omega_0)|. \tag{B.13}$$

Assuming a random distribution of the phase modulation allows us to average this phase modulation by calculating the RMS of the interferometer phase [51]:

$$\delta\Phi^{\mathrm{RMS}} = \sqrt{\frac{1}{2\pi}\int_{-\pi}^{\pi} |\delta\Phi|^2\ \mathrm{d}\psi} = \frac{A_0}{\sqrt{2}}\omega_0|G(\omega_0)|. \tag{B.14}$$

In the presence of a phase noise spectral density, the variance of the interferometric phase fluctuations becomes [86]:

$$\sigma_\Phi^2 = \int_0^{+\infty} |\omega G(\omega_0)|^2 S_\Phi(\omega)\ \frac{\mathrm{d}\omega}{2\pi}, \tag{B.15}$$

where $S_\Phi(\omega)$ is the power spectral density (PSD) of the phase noise of the Raman laser and $H_\Phi(\omega) = |\omega G(\omega)|$ is referred to as the transfer function of the interferometer [51]. The Fourier transform of the sensitivity function can be evaluated as [89]:

$$G(\omega) = \frac{4i\Omega_{\mathrm{R}}}{\omega^2 - \Omega_{\mathrm{R}}^2}\sin\left(\frac{\omega(T+2\tau)}{2}\right)\left[\cos\left(\frac{\omega(T+2\tau)}{2}\right) + \frac{\Omega_{\mathrm{R}}}{\omega}\sin\left(\frac{\omega T}{2}\right)\right], \tag{B.16}$$

which gives the expression for the transfer function [51]:

$$|H_\Phi(\omega)|^2 = \left| \frac{-4\Omega_\mathrm{R}}{\omega^2 - \Omega_\mathrm{R}^2} \sin\left(\frac{\omega(T+2\tau)}{2}\right) \times \left[\cos\left(\frac{\omega(T+2\tau)}{2}\right) + \frac{\Omega_\mathrm{R}}{\omega}\sin\left(\frac{\omega T}{2}\right)\right]\right|^2. \tag{B.17}$$

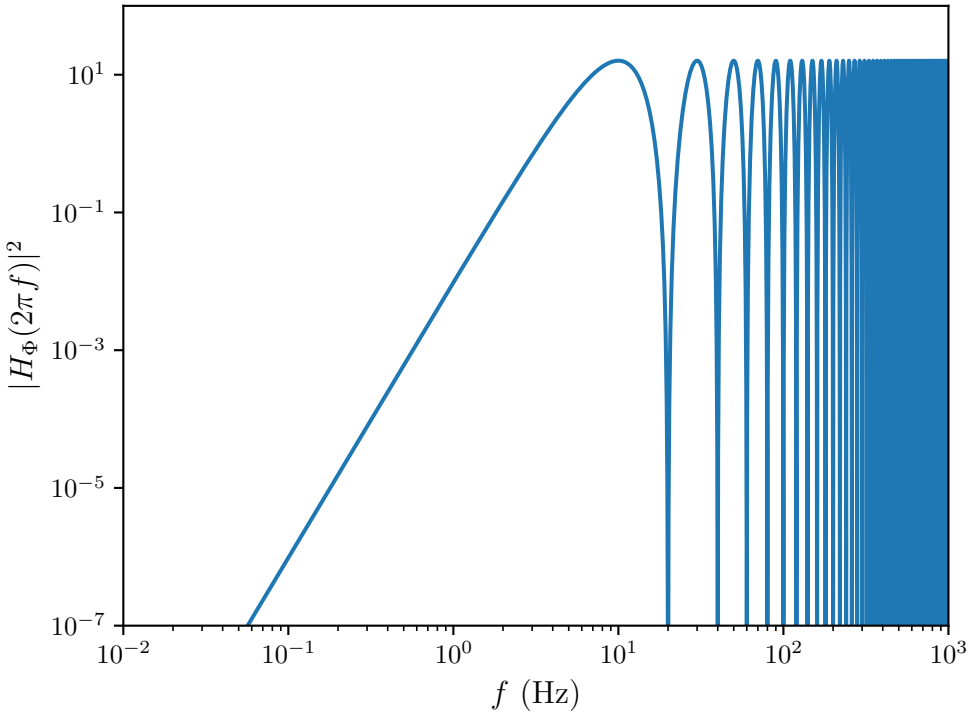


Figure B.2: Plot of $|H_\phi(\omega)|^2$ for $T = 50$ ms and $\tau = 15$ μs.

This transfer function can be seen in Figure B.2 and is also sometimes referred to as a weighting function, acting as a band pass filter [43]. Due to the T and τ dependence, it is possible to tune the interferometer's response to Raman laser phase noise. Decreasing T would decrease the sensitivity to low-requency noise but would also serve to decrease the sensitivity of the interfeormeter due to its T^2 dependence. On the other hand, longer τ can limit high frequency noise but this would also make the Raman pulses very velocity-selective, and hence affect the atom number in the interferometer. Therefore, a compromise of these parameters is needed [51].

B.3 Vibrational Phase Noise

In most standard atom interferometers, a beam enters the chamber from the top and retro-reflected by a mirror at the bottom. In our setup, we have two telescopes feeding light from the top and bottom. However, if the top telescope is treated as a reference, any vibration on the bottom telescope that is not common to the top telescope will introduce a phase shift [51], seen pictured in Figure B.3. Therefore, the sensitivity function due to this vibration is defined as [43]:

$$g_a(t) = 2 \lim_{\delta a \to 0} \frac{\delta P(\delta a, t)}{\delta a}. \tag{B.18}$$

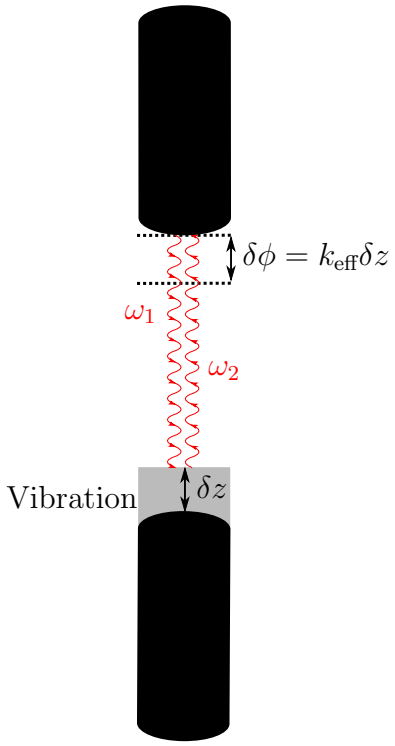


Figure B.3: Vibration-induced phase noise. The relative phase between the two lasers changes depending on the displacement.

If there is an infinitesimal displacement, δz, the phase of the bottom beam is changed by $\delta\phi = 2k_i\delta z \approx k_{\text{eff}}\delta z$. Therefore, $g_a(t)$ can be expressed as [43]:

$$g_a(t) = \frac{\mathrm{d}^2 g_z(t)}{\mathrm{d}t^2} = \frac{1}{k_{\text{eff}}} \frac{\mathrm{d}^2 g_s(t)}{\mathrm{d}t^2}. \tag{B.19}$$

The PSD of the Raman phase noise induced by the vibration can be written as [43]:

$$S_\Phi(\omega) = k_{\text{eff}}^2 S_z(\omega) = k_{\text{eff}}^2 \frac{S_a(\omega)}{\omega^4}, \tag{B.20}$$

where $S_a(\omega)$ is the PSD of the vertical vibrations. The corresponding interferometry phase noise due to vibrations can be evaluated by [43]:

$$\sigma_\Phi = \sqrt{\int_0^{+\infty} |H_\Phi(\omega)|^2 \frac{k_{\text{eff}}^2}{\omega^4} S_a(\omega)\, \mathrm{d}\omega}. \tag{B.21}$$

The resulting vibration noise transfer function is given by [51]:

$$|H_a(\omega)|^2 = |H_\Phi(\omega)|^2 \cdot \frac{|k_{\text{eff}}|^2}{\omega^4}, \tag{B.22}$$

and hence the equation can be rewritten as [51]:

$$\sigma_\Phi = \sqrt{\int_0^{+\infty} |H_a(\omega)|^2 S_a(\omega)\, \mathrm{d}\omega}. \tag{B.23}$$

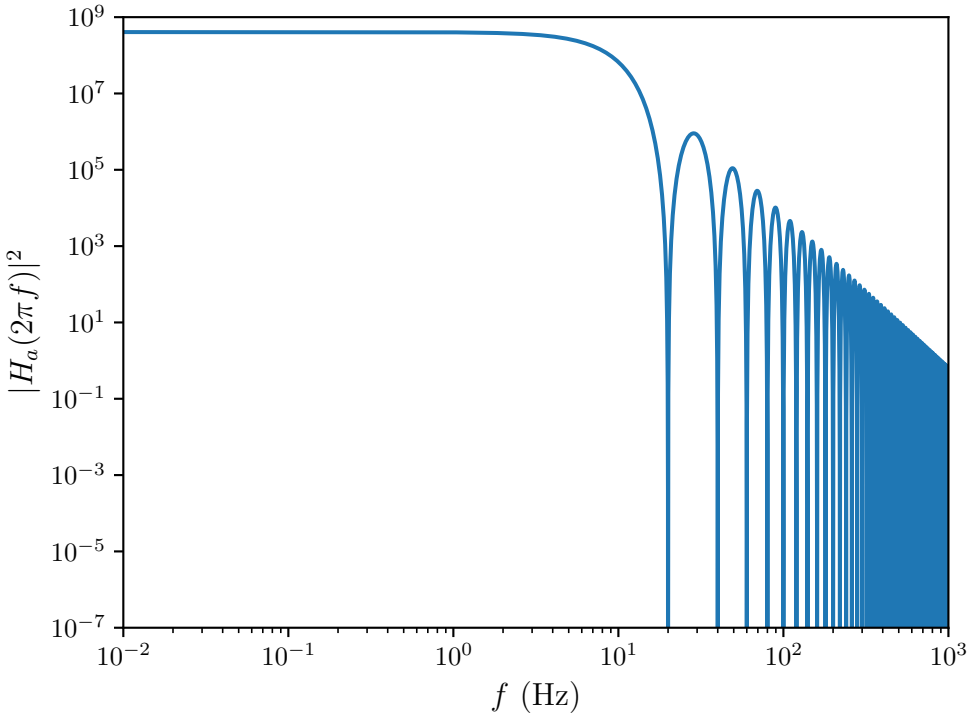


Figure B.4: Plot of $|H_a(\omega)|^2$ for $T = 50$ ms and $\tau = 15$ μs.

The plot of this transfer function can be seen in Figure B.4. This function acts as a low pass filter that mainly lets vibrations through below a certain frequency. Increasing T makes the interferometer less sensitive to low frequency vibrations and, as the interferometer phase difference is proportional to T^2, it also increases the interferometer's sensitivity. However, increasing T also means that more vibrations will be coupled into the measurement and can increase the overall vibrational phase noise. As a consequence of all these considerations, a compromise on the value of T has to be reached [51].

In the case of a gravity gradiometer, a differential transfer function can be defined as [70]:

$$H_d(\omega) = H_a^1(\omega) - H_a^2(\omega), \tag{B.24}$$

where H_a^1 and H_a^2 are the vibration transfer functions of the two interferometers. The differential transfer function has a more complicated frequency dependence than the single case. If the two interferometers have wavevectors k_1 and k_2, satisfying $k_1 = (1-\epsilon)^2 k_2$ (with $\epsilon << 1$), and are symmetrically overlapped in time [70]:

$$\begin{aligned} |H_d(\omega)| \sim k_{\text{eff}}(T_1^2 - T_2^2)\text{sinc}\left(\frac{\omega(T_1+T_2)}{2}\right)\text{sinc}\left(\frac{\omega(T_1-T_2)}{2}\right) \\ - 2\epsilon k_1 T_2^2 \text{sinc}^2\left(\frac{\omega T_2}{2}\right), \end{aligned} \tag{B.25}$$

where T_1 and T_2 are the T times of the two interferometers. In the case of $\epsilon = 0$, i.e. $k_1 = k_2$, the first term dominates, being zero for all frequencies if $T_1 = T_2$. This represents a simultaneous gravity gradiometer with identical T times [70], and is valid for our instrument. This illustrates the ability of gravity gradiometers to suppress vibrations when operating simultaneously and utilising the same element (and hence laser frequencies).

B.4 Response Function

There is another function that is able to quantify the effect of vibrations onto the interferometer phase. This function can be used to project vibrations present at different times of the interferometer sequence onto the interferometer phase. To discuss this response function, we can again use $\delta\phi = k_{\text{eff}} z(t)$. The phase of the interferometer then becomes [70]:

$$\Phi_{\text{vib}} = \int_{-\infty}^{\infty} w(t)\, a_{\text{vib}}(t)\, \mathrm{d}t = k_{\text{eff}} \int_{-\infty}^{\infty} f(t)\, a_{\text{vib}}(t)\, \mathrm{d}t, \tag{B.26}$$

where $a_{\text{vib}}(t)$ is the acceleration of the bottom telescope due to vibrations, $w(t) = k_{\text{eff}} f(t)$ is a time-dependent weight function for these accelerations, and $f(t)$ is called

the response function of the interferometer. $f(t)$ is derived using [70]:

$$f(t) = -\int_0^t g_s(t)\ \mathrm{d}t. \tag{B.27}$$

and can be shown to have the form [70]:

$$f(t) = \begin{cases} 0 & t < -T - 2\tau \\ \frac{1}{\Omega_\mathrm{R}}[1 - \cos(\Omega_\mathrm{R} t)] & -T - 2\tau < t < -T - \tau \\ t - \tau + \frac{1}{\Omega_\mathrm{R}} & -T - \tau < t < -\tau \\ T + \frac{1}{\Omega_\mathrm{R}}[1 - \cos(\Omega_\mathrm{R}(t - \tau))] & \tau < t < \tau \\ 2T + 3\tau + \frac{1}{\Omega_\mathrm{R}} - t & \tau < t < T + \tau \\ \frac{1}{\Omega_\mathrm{R}}[1 - \cos(\Omega_\mathrm{R}(t - 2T))] & T + \tau < t < T + 2\tau \\ 0 & T + 2\tau < t. \end{cases} \tag{B.28}$$

This function describes how strongly vibrations contribute to the interferometer phase at time t. It is triangle-shaped, as shown in Figure B.5. This can be explained by the fact that at the edges of the interferometer, the wave-packet separations are minimum and hence vibrations almost couple the same for both. However, in the central point of the interferometer, these separations are maximum, and so the largest effect of vibrations on the interferometer is seen [70].

Similarly to section B.3, the gradiometer configuration can be analysed. In this case, the difference in phase due to vibrations during the interferometer sequence is given by [70]:

$$\Phi^d_\mathrm{vib} = \Phi_1 - \Phi_2 = \int_{-\infty}^{\infty} w_d(t)\ a_\mathrm{vib}(t)\ \mathrm{d}t, \tag{B.29}$$

where the differential weight function, $w_d(t)$, is given by the difference between the single weight functions [70]:

$$w_d(t) = w_1(t) - w_2(t) = k_1 f_1(t) - k_2 f_2(t). \tag{B.30}$$

In the case of the same species gradiometer, $k_1 = k_2$. Additionally, if the two interferometers operate simultaneously, $T_1 = T_2$ and $\tau_1 = \tau_2$. This means that $w_d(t) = 0$ for all values of time, corresponding to a perfect common mode rejection of vibrations [70].

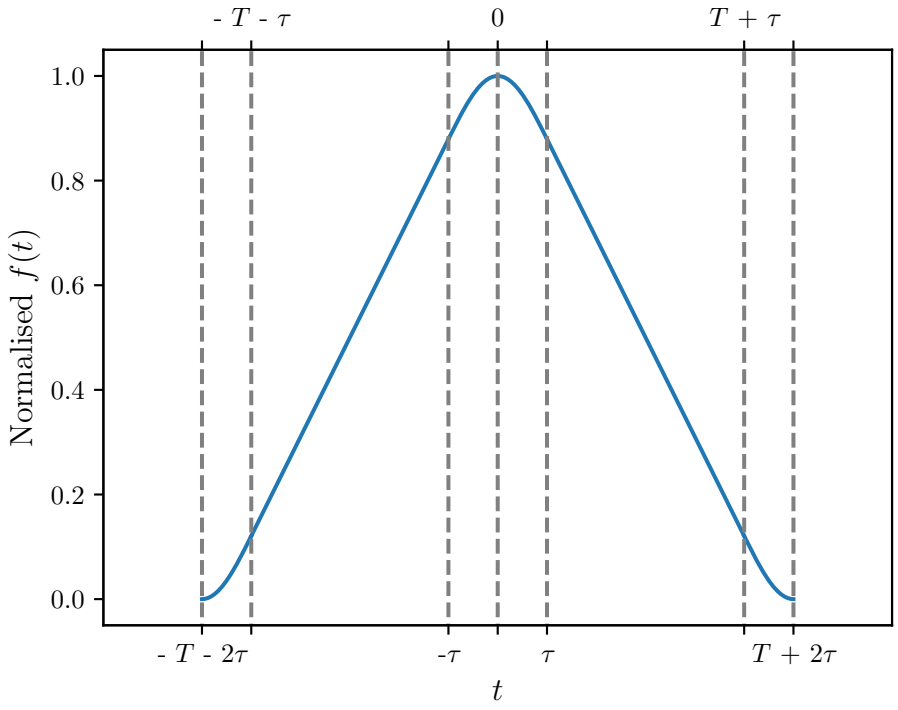


Figure B.5: Triangle-shaped response function of an atom interferometer.

Appendix C

^{87}Rb Transitions

C.1 $\sigma^- - \sigma^-$ Raman Transitions

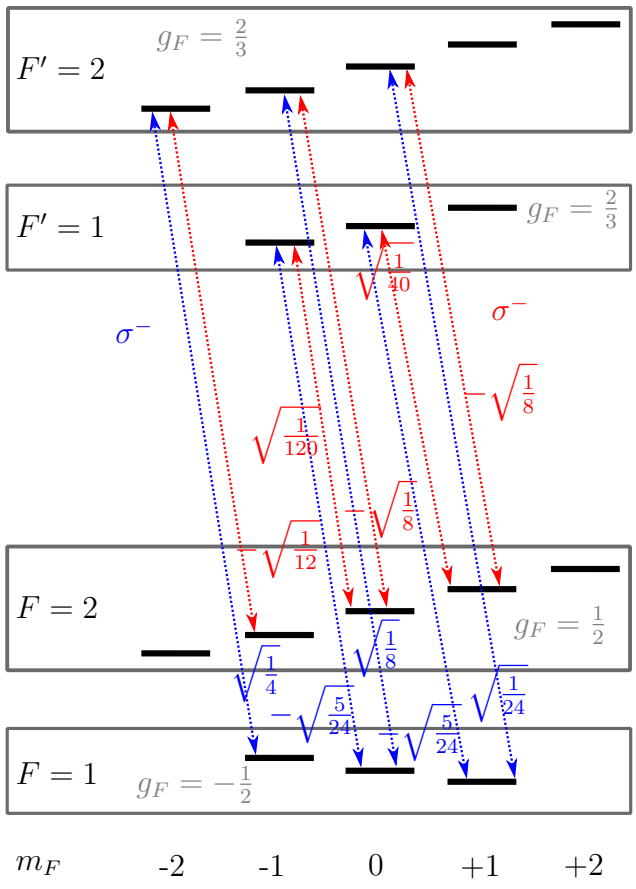


Figure C.1: $\sigma^- - \sigma^-$ transitions (and their Clebsch-Gordan coefficients) between $|5^2S_{1/2}; F = 1\rangle$ and $|5^2S_{1/2}; F = 2\rangle$ via $|5^2P_{3/2}; F' = 1\rangle$ and $|5^2P_{3/2}; F' = 2\rangle$.

C.2 $\pi - \pi$ Raman Transitions

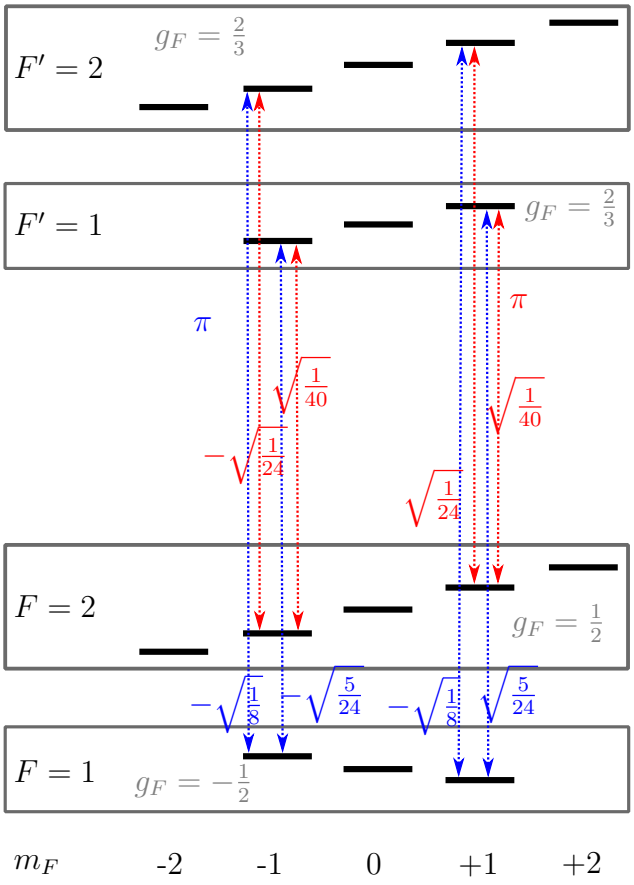


Figure C.2: $\pi - \pi$ transitions (and their Clebsch-Gordan coefficients) between $|5^2S_{1/2}; F = 1\rangle$ and $|5^2S_{1/2}; F = 2\rangle$ via $|5^2P_{3/2}; F' = 1\rangle$ and $|5^2P_{3/2}; F' = 2\rangle$.

Appendix D

Barrell Connectors Cleaning Procedure for Vacuum

When the dispensers have been used up and need to be replaced, the vacuum of the science chamber needs to be broken. The barrell connectors that are used to attach the dispensers to the power feedthrough need to be cleaned and replaced. The procedure for cleaning these barrell connectors is as follows:

1. Rinse a glass beaker with tap water until it does not froth.
2. Pour 1% liquinox and tap water into beaker and sonicate for 15 minutes.
3. Rinse the beaker with tap water in the same way as step 1.
4. 15 minute ultrasonic bath with clean hot tap water.
5. Rinse with distilled water.
6. Clean connectors for 1 hour (4 $\times$ 15 minutes) in a ultrasonic bath using $\sim$3% neutracon and distilled water mix.
7. Rinse by hand with distilled water a few times until no soap bubbles are visible. Clean in ultrasonic bath for 1 hour (4 $\times$ 15 minutes) using distilled water, changing the water every 15 minutes.
8. 1 hour (4 $\times$ 15 min) ultrasonic bath using acetone, leave to dry after pouring off.
9. 1 hour (4 $\times$ 15 min) ultrasonic bath using isopropanol. Remove from bath and place on clean foil.
10. Bake at 150°C in vacuum overnight.

Once this procedure is completed, the connectors can be placed inside of the vacuum chamber.

Appendix E

Doubler Response and 1560 nm AOM

Prior to committing to the laser system design, an investigation of two areas of this laser design was carried out. The first was the response of SHG 5 with low input powers. Assuming 2 W out of EDFA 5, and BS 5 (50:50) that has 90% efficiency, means that only ∼0.9 W of light would be fed into EOM 1. Assuming 50% efficiency of this EOM meant that the input power into SHG 5 would be around 450 mW (∼26.5 dBm), which is just over 20% of the EDFA 5 power. The question was whether this EDFA was needed or whether it could be eliminated and replaced with, for example, a pre-amp stage.

The second investigation involved the use of the 1560 nm AOMs as opposed to the 780 nm alternatives, which is the common mode of operation within our group. These 1560 nm provided two potential benefits:

1. 1560 nm AOMs are more efficient than 780 nm, and
2. any leaked light out of the AOMs will be caught by the frequency doublers, removing any spontaneous emission effects without the need for high loss optical switches.

However, it was unknown whether the SHG performance would suffer due to the pulsing of high-power light into the crystals, potentially causing thermal cycling and local heating. The other concern was whether these 1560 nm AOMs, in combination with the SHGs, would respond fast enough.

The frequency doubler was characterised using a laser seed, EDFA and SHG chain, as seen in Figure E.1. The power out of the EDFA was varied; hence changing the input power into the SHG. At each different EDFA power, the frequency doubler temperature was optimised. The results of this characterisation can be seen in Figure E.2. Using the power measured before (1) and after (2) the doubler, the efficiency of the doubler was calculated. The efficiency of the doubler increases with increasing input power up to ∼28 dBm, after which the efficiency saturates at just over 60%. Given the low

efficiency at low input powers, it was decided to proceed with using EDFA 5, which meant we would get an estimated input power of ∼26 dBm, obtaining an efficiency of ∼50% of the doubler.



Figure E.1: Frequency doubler testing setup.

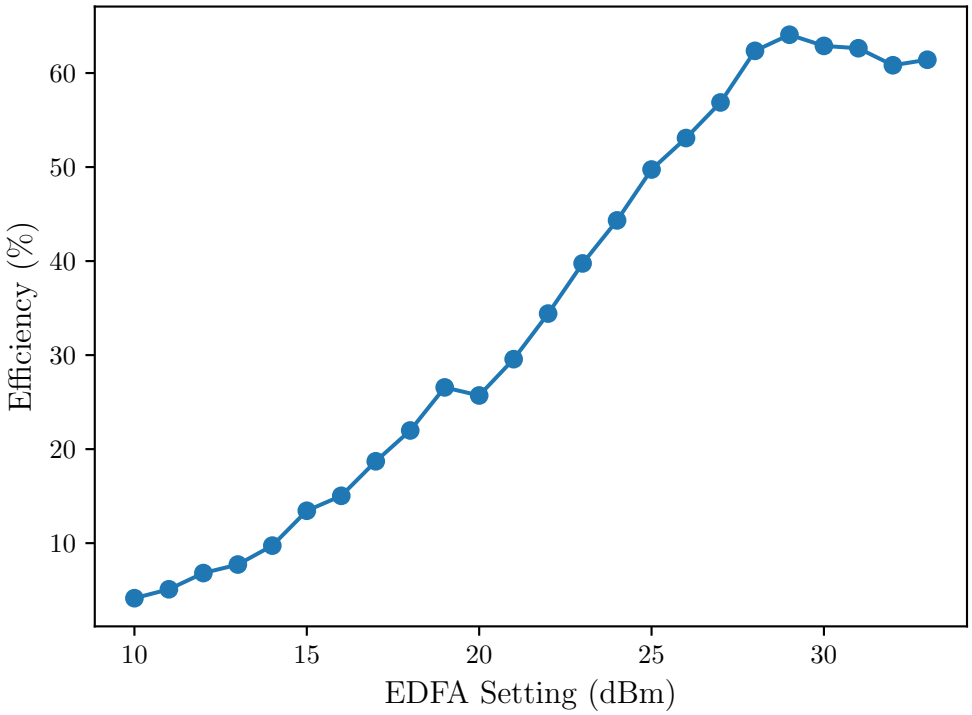


Figure E.2: Frequency doubler power response as a function of the input power.

The characterisations of the 1560 nm AOMs compared to the 780 nm AOMs were carried out with similar setups. These involved similar optical chains to the above, composed of a laser seed, EDFA, and AOM/SHG, seen in Figure E.3. The order of the last two components was chosen based on the whether it was a 1560 nm or 780 nm AOM. The RF chains feeding onto the AOMs were different between the setups but in both cases provided the appropriate power and frequency for both. Similarly to the doubler response characterisation, for a given EDFA setting, the frequency doubler temperature was optimised to obtain the maximum power output. The response was

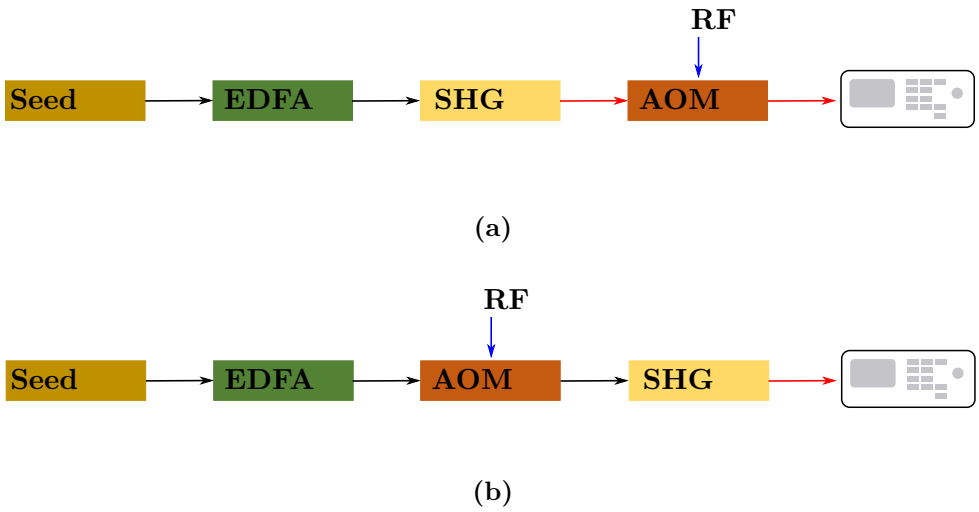
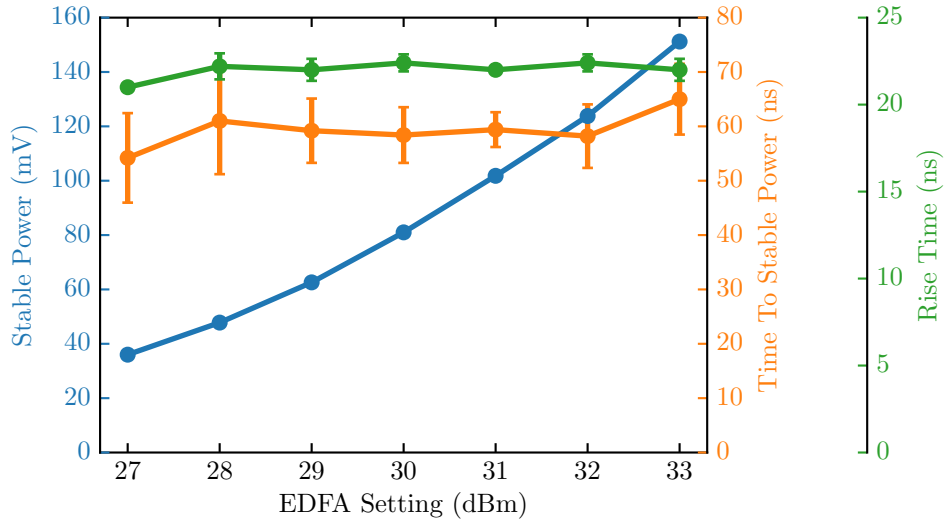


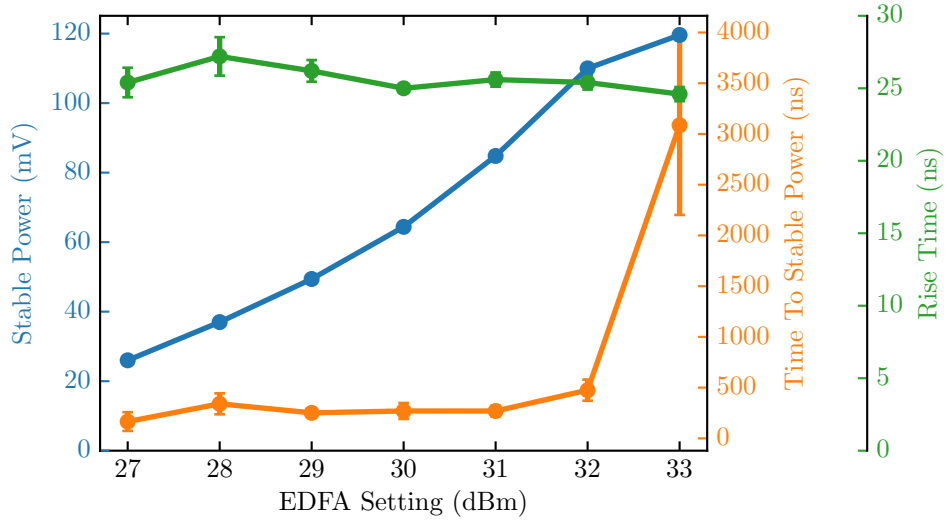
Figure E.3: **(a)** 780 nm AOM setup and **(b)** 1560 nm AOM setup.

tested by switching the RF on and off to create a square pulse of length of ∼10 μs, with the response after the chain recorded by an oscilloscope and subsequently analysed. RF power of up to ∼2 W was used for this characterisation for both the 1560 nm and 780 nm AOMs. The analysed results can be seen in Figure E.4.

As this data was collected on different days and the optical setup was different for both of these tests (meaning potentially different fibre couplings), care and consideration must be taken when comparing the stable power between the results. Additionally, the fibres had to be connected and disconnected a few times at each EDFA setting even within the same characterisation. However, even with these considerations taken into account, comparable stable powers are obtained between the designs. As is expected, increasing the EDFA power results in a higher stable power. Overall, the results for the 780 nm AOMs are better. The rise time is comparable for both types of AOMs, although generally 780 nm is better by a few ns. The time to stable power is better for the 780 nm AOMs. The highest time for stable power is at 33 dBm, reaching ∼65 ns. For 1560 nm AOMs, the minimum time to stable power is ∼165 ns at 27 dBm. This clearly shows the better time response of the 780 nm over the 1560 nm AOMs. Additionally, the standard deviation of the 780 nm is better, showing less variation for the 780 nm AOM compared to the 1560 nm equivalent. The time to stable power at 33 dBm for the 1560 nm AOM is very interesting and the actual plots of the whole testing pulses show that the power seems to be still rising, which begs the question as to whether it has reached the stable power in the time investigated. While these results show that the 780 nm AOMs perform slightly better, the response of the 1560 nm AOMs is more than fast enough given our experimental timings. Therefore, given the aforementioned benefits, the design with the 1560 nm AOMs was adopted. Since 33 dBm driving RF seems to give spurious results, an operating driving power of ∼32 dBm was chosen because the stable power difference is ∼10% but the time to stable power is significantly better than for ∼33 dBm.



(a)



(b)

Figure E.4: **(a)** 780 nm AOM results and **(b)** 1560 nm AOM results. The error bars represent the standard deviation of a set of five measurements.

Appendix F
ARTIQ Characterisation

F.1 Trigger

The ARTIQ module used in this instrument contains four Bayonet Neill–Concelman (BNC) input/output transistor-transistor logic connections (TTLs). These can be configured to be either "IN" or "OUT". By default, these four TTLs are configured to be "IN" - changing them to be "OUT" is possible but would require some hardware changes. As this capability was not required, these have been left unused for now.

In addition to the four TTLs mentioned, there are also four BNC TTL outputs. These are specifically output channels and hence do not require any hardware changes. These four channels were used to switch on and off the dispensers and the MOT coils during the experimental sequence. On top of that, there are also 16 SubMiniature version A (SMA) TTL outputs. These were used to trigger various parts of our laser, such as RF switches, data collection triggers, etc.

The response of the ARTIQ triggers was characterised to understand whether it is fit-for-purpose in this regard. A set of four triggers was implemented and the resulting output as observed on oscilloscope was compared with what was programmed. These results can be seen in Figure F.1. The first and second triggers in this characterisation consisted of a delay of 2 μs, with the same delay present between the second and third/fourth triggers. No delay was programmed between the third and fourth triggers. The results show the fast response of the ARTIQ triggers, which is more than sufficient for the triggering needs of our experimental sequence. However, one issue found with these triggers is that when they are switched on, they reach $\sim$3 V (reaching $\sim$4 V on the order of a few ms). This has meant that triggering certain devices does not work properly as the voltages reached are not high enough. Fortunately, this has not affected the components used in our experimental setup.

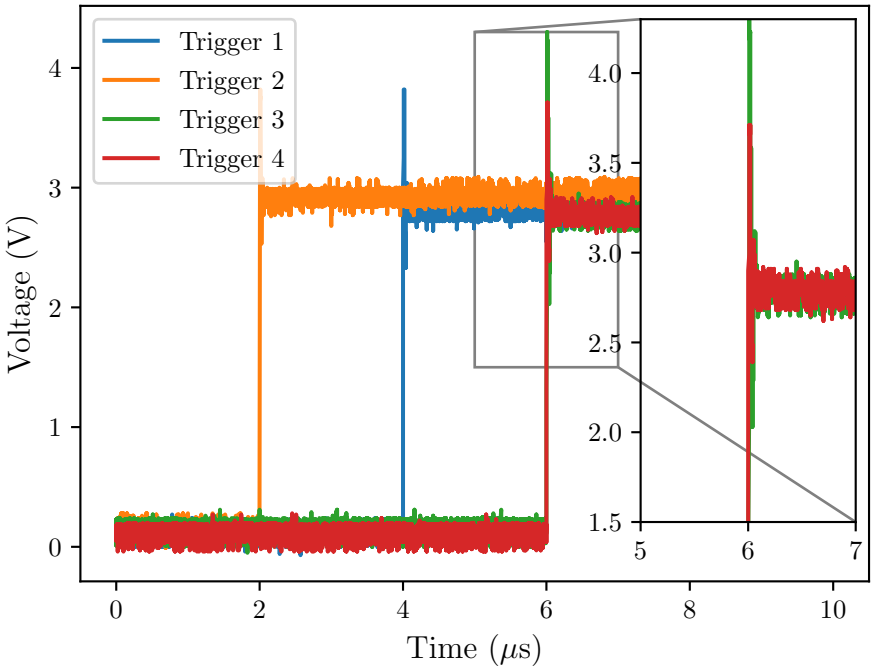


Figure F.1: Characterisation of the ARTIQ triggering response.

F.2 Variable Voltage

This ARTIQ also includes Zotino (model: AD5372BCPZ), which is a 32 channel, 16-bit digital-to-analog converter (DAC) with eight analogue channel outputs able to provide voltages up to ±10 V [124]. As with the triggering in section F.1, Zotino response characterisation was performed, the results of which can be seen in Figure F.2(a). A control trigger was used to measure this response. Channel 3 and Channel 4 refer to the ports of the Zotino used in this characterisation. A delay of 1 μs was programmed between the control trigger and the analogue outputs of the Zotino being switched on. However, the delay seen is actually longer than was programmed. It takes time to see any response from the Zotino (∼8 - 9 μs), with even more time needed to reach the programmed voltage out of the channels - these were +9.9 V for Channel 3 and +5 V for Channel 4. Since it takes longer for Channel 3 to reach the programmed value compared to Channel 4, it can be deduced that the desired voltage has an effect on the time of the rise. Fortunately, these delays are short given the timings of our experimental sequence (on the order of ∼ms) and can also be compensated for, if needed. Therefore, they should pose no huge problem in the use of this capability in our experimental setup.

There are two things to note with the Zotino. Firstly, while the data specifications

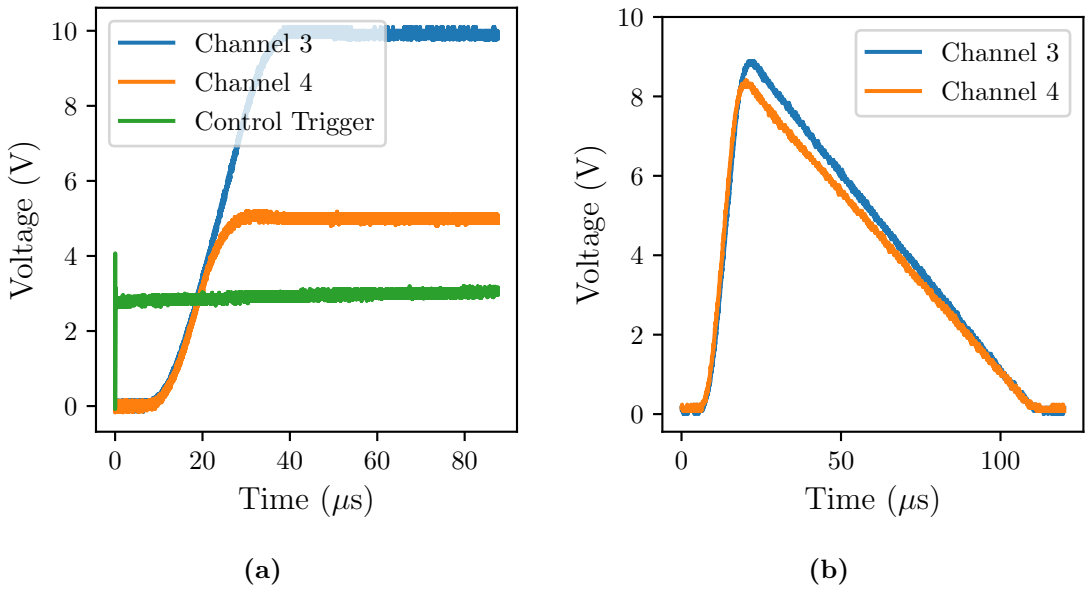


Figure F.2: **(a)** Variable voltage response and **(b)** variable voltage ramps.

for Zotino say that the range of output voltages is ±10 V [124], in actuality this is not quite the case. Setting the value of the Zotino to +10 V produces negative voltages. Therefore, a voltage of +9.9 V was used as the maximum output possible from the Zotino. Secondly, an issue was identified when connecting the Zotino to standard Mini-Circuits RF variable attenuators - a significant voltage drop was observed when the Zotino output was connected to these RF components and a non-zero voltage was programmed. This is thought to be a consequence of impedance mismatch - the impedance of Zotino is 470 Ω [124]. For example, programming one of the Zotino channels to have 0 V output produced an actual voltage out of the socket of -0.008 V, and when connected to the variable attenuator, a voltage of -0.004 V was measured. Setting the channel output to +9.9 V, actual voltage out of the socket was measured as +9.89 V, but this dropped to +5.930 V once connected to the variable attenuator. As a result, for the time-being, RF variable attenuators 1 and 2 are controlled with standard power supplies and only variable attenuators 3, 4 and 5 are controlled by ARTIQ. A possible upgrade in the future would be the inclusion of voltage amplifiers.

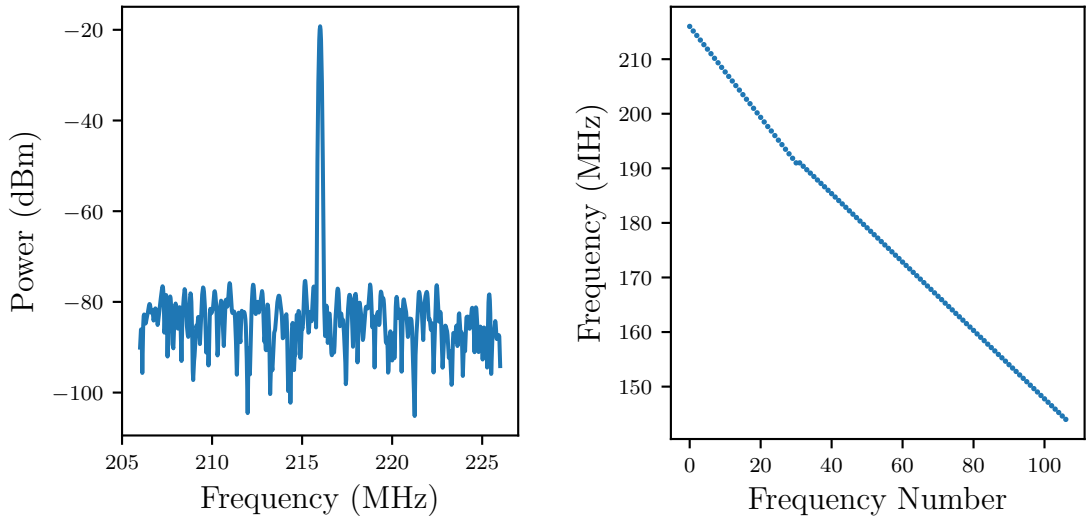
While flexibility in controlling the variable attenuators statically is one of the uses of our Zotino, the other one is to perform power ramps during the molasses sequence. As is explained in more detail in section 3.4.2, the cooling light power needs to be controlled, requiring the ability to perform voltage ramps. Essentially, there needs to be a capability to control the percentage power out of the variable attenuators using the variable attenuators' control voltages. A characterisation of the voltage ramps using ARTIQ was performed. Using channels 3 and 4, in line with the variable attenuators 3 and 4 used to control the power going into AOMs 3 and 4, the corresponding voltage

ramps can be observed in Figure F.2(b). The ramps are composed of 40 voltage steps in 104 μs for channel 3 and 105 μs for channel 4 - the step sizes and timings needed to be optimised for each separately as the percentage power out of each arms is not exactly identical. These ramps are relatively smooth, which is the desired effect.

F.3 RF Frequency

ARTIQ has the ability to generate RF frequencies using its own synthesiser board Urukul. This board utilises either the AD9910 or AD9912 synthesiser boards. Our ARTIQ uses the former of these boards and has 10 RF output channels able to provide frequencies of up to 400 MHz [125]. This meant that ARTIQ was chosen as the low frequency generation source in the RF. This has simplified the work as it has meant that no bespoke code needed to be programmed to be able to integrate individual boards with the experimental sequence, which has accelerated the development progress.

The first RF characterisation was to ensure that the right frequencies can be output at sufficient powers. An example of this frequency output can be seen in Figure F.3(a). The programmed frequency for this was 216 MHz, and the outputted spectrum is a clean spectrum at this frequency with power of ∼-19.2 dBm. This has meant that high amplification is needed in the RF chains that use the ARTIQ frequencies. A stability measurement of this frequency was performed over 1 hour with no change in frequency observed, highlighting good stability.



(a) **(b)**

Figure F.3: **(a)** RF spectrum of Urukul output of 216 MHz. **(b)** Frequency ramps characterisation, where frequency number refers to the position of the frequency in the ramps (105 frequencies feature in the two ramps).

Similarly to the variable voltages, frequency ramps are also needed for the molasses sequence. While Urukul should have the capability to perform frequency ramps with internal commands, this was found to not work. Therefore, bespoke code for frequency ramps was created and characterised. The ramps chosen for characterisation were roughly in line with the ones required for the molasses sequence, composed of a faster ramp and a slower ramp. The faster ramp consisted of 216 MHz $\rightarrow$ 191 MHz shift in 30 steps in 1.5 ms. The slower ramp used 191 MHz $\rightarrow$ 144 MHz in 75 steps in 13 ms. During each run, each subsequent frequency in the ramps was triggered to ensure that the frequency output was stable. Completing every frequency in both ramps once constituted one run. To test this fully and to ensure stability over a longer period, 27 of these runs were completed (27 runs with each run containing 105 frequencies). The mean value of each of these frequencies can be seen in Figure F.3(b). It is not obvious but these are plotted with their standard deviations, which highlights the stability of RF frequency output of ARTIQ over a period of $\sim$14 hours.

F.4 Summary

The implementation of ARTIQ within our system has had challenges. The first challenge that has already been mentioned is that while the triggers are fast, the voltage provided ($\sim$3 V) is not always high enough to trigger some devices. It has been fortunate that the components used in this experimental setup have not suffered from this issue. The second challenge has been the voltage drop seen when the Zotino is connected to standard RF Mini-Circuits variable attenuators.

Another challenge has been troubleshooting ARTIQ timing errors. The buffer on the Kasli chip of the ARTIQ can only store a certain amount of data. Sending it numerous commands at one time causes timing errors, with the most common being "RTIOUnderflow Error". This is caused by the ARTIQ thinking that a command has been set in the past (this mechanism is not fully clear to the author). The challenge with this error is that it is not clear how to debug this - no clear information is provided. The best solution that has been found is to use the delay command. However, due to the lack of clarity from the error, it is not clear where the delays should be placed or how long they should last. Therefore, a significant amount of trial and error has to be done to resolve these. This has been seen to also affect triggering in some instances, as these will sometimes not work but will also not produce an error. Using the ARTIQ direct memory access module has been found to be a way to deal with this issue at times, but not always. As the ARTIQ develops further, and our group's knowledge of ARTIQ improves, it would be beneficial to find an efficient way to deal with these problems.

Lastly, a paid license is needed to keep ARTIQ up-to-date and to be able to use the hardware with the newest software. This involves flashing the hardware with a new repository so that it is able to utilise this newest software. If this license is not paid, the repository is archived and is not updated. This means that newer versions of the

software cannot be used. Very old repositories are not stored by M-Labs, meaning that it is useful to keep a backup to ensure that this is not lost, especially if the license is not being paid. This flashing is not always trivial.

Overall, ARTIQ does offer great advantages for atom interferometry experiments because it can provide a plethora of functionality required for an integrated setup in one standard, commercial setup. This means that less time needs to be invested by researchers to integrate different components together, giving them more time to perform interesting experiments. The fact that it can be tailored to the experimental requirements is also advantageous as is the fact that since it is integrated, different researchers within a group are able to create a homogeneous use of this control package, helping each other with progressing their respective experiments. As it is constantly being upgraded, the author expects that the challenges mentioned beforehand will slowly start to disappear, only enhancing the advantages of ARTIQ.

Appendix G

Analytical Solution of Mach-Zehnder

G.1 Atomic State Evolution

The total matrix of evolution is:

$$M_{\text{total}} = M_{\text{third pulse}} M_{\text{second evolution}} M_{\text{second pulse}} M_{\text{first evolution}} M_{\text{first pulse}}. \tag{G.1}$$

If the atoms start in the lower state $|a\rangle$ at $t = 0$, the evolution becomes:

$$\begin{pmatrix} C_a(t_f) \\ C_b(t_f) \end{pmatrix} = M_{\text{total}} \begin{pmatrix} 1 \\ 0 \end{pmatrix}. \tag{G.2}$$

The evolution matrix is given by [89]:

$$M_p(t_0, t, \Omega_R, \phi) = \begin{pmatrix} e^{-i\omega_a(t-t_0)} \cos(\frac{\Omega_R}{2}(t-t_0)) & -ie^{-i\omega_a(t-t_0)} e^{i(\omega_L t_0+\phi)} \sin(\frac{\Omega_R}{2}(t-t_0)) \\ -ie^{-i\omega_b(t-t_0)} e^{-i(\omega_L t_0+\phi)} \sin(\frac{\Omega_R}{2}(t-t_0)) & e^{-i\omega_b(t-t_0)} \cos(\frac{\Omega_R}{2}(t-t_0)) \end{pmatrix}, \tag{G.3}$$

where we can define $t_{\pi/2} = \frac{\pi}{2\times\Omega_R}$ and $t_\pi = \frac{\pi}{\Omega_R}$.

G.1.1 First Pulse

The first pulse matrix is given by:

$$M_{\text{first pulse}} = M_p(0, t_1, \Omega_{R1}, \phi_1) = \begin{pmatrix} e^{-i\omega_a(t_1)} \cos(\frac{\Omega_{R1}}{2}(t_1)) & -ie^{-i\omega_a(t_1)} e^{i(\phi_1)} \sin(\frac{\Omega_{R1}}{2}(t_1)) \\ -ie^{-i\omega_b(t_1)} e^{-i(\phi_1)} \sin(\frac{\Omega_{R1}}{2}(t_1)) & e^{-i\omega_b(t_1)} \cos(\frac{\Omega_{R1}}{2}(t_1)) \end{pmatrix}, \tag{G.4}$$

which results in the following state population:

$$M_{\text{first pulse}} \begin{pmatrix} 1 \\ 0 \end{pmatrix} = \begin{pmatrix} e^{-i\omega_a(t_1)} \cos(\frac{\Omega_{R1}}{2}(t_1)) \\ -ie^{-i\omega_b(t_1)} e^{-i(\phi_1)} \sin(\frac{\Omega_{R1}}{2}(t_1)) \end{pmatrix}. \tag{G.5}$$

G.1.2 First Free Evolution

This is followed by the first free evolution matrix:

$$M_{\text{first evolution}} = M_p(t_1, T+t_1, 0, \phi_{T1}) = \begin{pmatrix} e^{-i\omega_a(T)} & 0 \\ 0 & e^{-i\omega_b(T)} \end{pmatrix}, \tag{G.6}$$

which results in the following state population:

$$M_{\text{first evolution}} M_{\text{first pulse}} \begin{pmatrix} 1 \\ 0 \end{pmatrix} = \begin{pmatrix} e^{-i\omega_a(T+t_1)} \cos(\frac{\Omega_{R1}}{2}(t_1)) \\ -ie^{-i\omega_b(T+t_1)} e^{-i(\phi_1)} \sin(\frac{\Omega_{R1}}{2}(t_1)) \end{pmatrix}. \tag{G.7}$$

G.1.3 Second Pulse

This is followed by the second pulse matrix:

$$\begin{aligned} &M_{\text{second pulse}} = M_p(T+t_1, T+t_1+t_2, \Omega_{R2}, \phi_2) = \\ &\begin{pmatrix} e^{-i\omega_a(t_2)} \cos(\frac{\Omega_{R2}}{2}(t_2)) & -ie^{-i\omega_a(t_2)} e^{i(\omega_L(T+t_1)+\phi_2)} \sin(\frac{\Omega_{R2}}{2}(t_2)) \\ -ie^{-i\omega_b(t_2)} e^{-i(\omega_L(T+t_1)+\phi_2)} \sin(\frac{\Omega_{R2}}{2}(t_2)) & e^{-i\omega_b(t_2)} \cos(\frac{\Omega_{R2}}{2}(t_2)) \end{pmatrix}, \end{aligned} \tag{G.8}$$

which results in the following state population:

$$\begin{aligned} &M_{\text{second pulse}} M_{\text{first evolution}} M_{\text{first pulse}} \begin{pmatrix} 1 \\ 0 \end{pmatrix} = \\ &\begin{pmatrix} e^{-i\omega_a(T+t_1+t_2)} \cos(\frac{\Omega_{R1}}{2}(t_1)) \cos(\frac{\Omega_{R2}}{2}(t_2)) - e^{-i(\omega_a(t_2)+\omega_b(T+t_1))} e^{i(\omega_L(T+t_1)+\phi_2-\phi_1)} \sin(\frac{\Omega_{R1}}{2}(t_1)) \sin(\frac{\Omega_{R2}}{2}(t_2)) \\ -ie^{-i(\omega_a(T+t_1)+\omega_b(t_2))} e^{-i(\omega_L(T+t_1)+\phi_2)} \cos(\frac{\Omega_{R1}}{2}(t_1)) \sin(\frac{\Omega_{R2}}{2}(t_2)) - ie^{-i(\omega_b(T+t_1+t_2))} e^{-i(\phi_1)} \sin(\frac{\Omega_{R1}}{2}(t_1)) \cos(\frac{\Omega_{R2}}{2}(t_2)) \end{pmatrix}. \end{aligned} \tag{G.9}$$

G.1.4 Second Free Evolution

This is followed by the second free evolution matrix:

$$M_{\text{second evolution}} = M_p(T+t_1+t_2, 2T+t_1+t_2, 0, \phi_{T2}) = \begin{pmatrix} e^{-i\omega_a(T)} & 0 \\ 0 & e^{-i\omega_b(T)} \end{pmatrix}, \tag{G.10}$$

which results in the following state population:

$$\begin{aligned} &M_{\text{second evolution}} M_{\text{second pulse}} M_{\text{first evolution}} M_{\text{first pulse}} \begin{pmatrix} 1 \\ 0 \end{pmatrix} = \\ &\begin{pmatrix} e^{-i\omega_a(2T+t_1+t_2)} \cos(\frac{\Omega_{R1}}{2}(t_1)) \cos(\frac{\Omega_{R2}}{2}(t_2)) - e^{-i(\omega_a(T+t_2)+\omega_b(T+t_1))} e^{i(\omega_L(T+t_1)+\phi_2-\phi_1)} \sin(\frac{\Omega_{R1}}{2}(t_1)) \sin(\frac{\Omega_{R2}}{2}(t_2)) \\ -ie^{-i(\omega_a(T+t_1)+\omega_b(T+t_2))} e^{-i(\omega_L(T+t_1)+\phi_2)} \cos(\frac{\Omega_{R1}}{2}(t_1)) \sin(\frac{\Omega_{R2}}{2}(t_2)) - ie^{-i(\omega_b(2T+t_1+t_2))} e^{-i(\phi_1)} \sin(\frac{\Omega_{R1}}{2}(t_1)) \cos(\frac{\Omega_{R2}}{2}(t_2)) \end{pmatrix}. \end{aligned} \tag{G.11}$$

G.1.5 Third Pulse

This is followed by the third pulse matrix:

$$\begin{aligned} &M_{\text{third pulse}} = M_p(2T+t_1+t_2, 2T+t_1+t_2+t_3, \Omega_{R3}, \phi_3) = \\ &\begin{pmatrix} e^{-i\omega_a(t_3)} \cos(\frac{\Omega_{R3}}{2}(t_3)) & -ie^{-i\omega_a(t_3)} e^{i(\omega_L(2T+t_1+t_2)+\phi_3)} \sin(\frac{\Omega_{R3}}{2}(t_3)) \\ -ie^{-i\omega_b(t_3)} e^{-i(\omega_L(2T+t_1+t_2)+\phi_3)} \sin(\frac{\Omega_{R3}}{2}(t_3)) & e^{-i\omega_b(t_3)} \cos(\frac{\Omega_{R3}}{2}(t_3)) \end{pmatrix}, \end{aligned} \tag{G.12}$$

which results in the following state population:

$$M_{\text{third pulse}} M_{\text{second evolution}} M_{\text{second pulse}} M_{\text{first evolution}} M_{\text{first pulse}} \begin{pmatrix} 1 \\ 0 \end{pmatrix} = \begin{pmatrix} \text{Top Term} \\ \text{Bottom Term} \end{pmatrix}, \tag{G.13}$$

with:

$$\text{Top Term} = \begin{pmatrix} e^{-i\omega_a(2T+t_1+t_2+t_3)} \cos(\frac{\Omega_{R1}}{2}(t_1)) \cos(\frac{\Omega_{R2}}{2}(t_2)) \cos(\frac{\Omega_{R3}}{2}(t_3)) \\ -e^{-i(\omega_a(T+t_2+t_3)+\omega_b(T+t_1))} e^{i(\omega_L(T+t_1)+\phi_2-\phi_1)} \sin(\frac{\Omega_{R1}}{2}(t_1)) \sin(\frac{\Omega_{R2}}{2}(t_2)) \cos(\frac{\Omega_{R3}}{2}(t_3)) \\ -e^{-i(\omega_a(T+t_1+t_3)+\omega_b(T+t_2))} e^{i(\omega_L(T+t_2)-\phi_2+\phi_3)} \cos(\frac{\Omega_{R1}}{2}(t_1)) \sin(\frac{\Omega_{R2}}{2}(t_2)) \sin(\frac{\Omega_{R3}}{2}(t_3)) \\ -e^{-i(\omega_a(t_3)+\omega_b(2T+t_1+t_2))} e^{i(\omega_L(2T+t_1+t_2)+\phi_3-\phi_1)} \sin(\frac{\Omega_{R1}}{2}(t_1)) \cos(\frac{\Omega_{R2}}{2}(t_2)) \sin(\frac{\Omega_{R3}}{2}(t_3)) \end{pmatrix} \tag{G.14}$$

and:

$$\text{Bottom Term} = \begin{pmatrix} -ie^{-i(\omega_a(2T+t_1+t_2)+\omega_b(t_3))}e^{-i(\omega_L(2T+t_1+t_2)+\phi_3)}\cos(\frac{\Omega_{R1}}{2}(t_1))\cos(\frac{\Omega_{R2}}{2}(t_2))\sin(\frac{\Omega_{R3}}{2}(t_3)) \\ +ie^{-i(\omega_a(T+t_2)+\omega_b(T+t_1+t_3))}e^{-i(\omega_L(T+t_2)+\phi_3-\phi_2+\phi_1)}\sin(\frac{\Omega_{R1}}{2}(t_1))\sin(\frac{\Omega_{R2}}{2}(t_2))\sin(\frac{\Omega_{R3}}{2}(t_3)) \\ -ie^{-i(\omega_a(T+t_1)+\omega_b(T+t_2+t_3))}e^{-i(\omega_L(T+t_1)+\phi_2)}\cos(\frac{\Omega_{R1}}{2}(t_1))\sin(\frac{\Omega_{R2}}{2}(t_2))\cos(\frac{\Omega_{R3}}{2}(t_3)) \\ -ie^{-i(\omega_b(2T+t_1+t_2+t_3))}e^{-i(\phi_1)}\sin(\frac{\Omega_{R1}}{2}(t_1))\cos(\frac{\Omega_{R2}}{2}(t_2))\cos(\frac{\Omega_{R3}}{2}(t_3)) \end{pmatrix}, \quad \text{(G.15)}$$

G.2 Probabilities

These complex amplitudes derived up to this point can be used to calculate the probabilities after each stage of the Mach-Zehnder sequence, which will be done in the next sections.

G.2.1 Probability of Excited State After First Pulse

Using the complex amplitudes, the probability of the upper state $|b\rangle$ after the first pulse can be derived as:

$$P_b = \sin^2(\frac{\Omega_{R1}}{2}(t_1)), \quad \text{(G.16)}$$

which are the Rabi oscillations.

G.2.2 Probability of Excited State After First Free Evolution

Using the complex amplitudes, the probability of the upper state $|b\rangle$ after the first free evolution can be derived as:

$$P_b = \sin^2(\frac{\Omega_{R1}}{2}(t_1)), \quad \text{(G.17)}$$

which is the same result as the probability after the first pulse.

G.2.3 Testing $\pi/2$ and π times

Using $t_{\pi/2} = \frac{\pi}{2\times\Omega_R}$, $P_b = \frac{1}{2}$, as expected; while using $t_\pi = \frac{\pi}{\Omega_R}$, $P_b = 1$, as expected.

G.2.4 Probability of Excited State After Second Pulse

Using the complex amplitudes, the probability of the upper state $|b\rangle$ after the second pulse can be derived as:

$$P_b = [-ie^{-i(\omega_a(T+t_1)+\omega_b t_2)}e^{-i(\omega_L(T+t_1)+\phi_2)}\cos(\frac{\Omega_{R1}}{2}(t_1))\sin(\frac{\Omega_{R2}}{2}(t_2)) - ie^{-i(\omega_b(T+t_1+t_2))}e^{-i\phi_1}\sin(\frac{\Omega_{R1}}{2}(t_1))\cos(\frac{\Omega_{R2}}{2}(t_2))]$$
$$[+ie^{+i(\omega_a(T+t_1)+\omega_b t_2)}e^{+i(\omega_L(T+t_1)+\phi_2)}\cos(\frac{\Omega_{R1}}{2}(t_1))\sin(\frac{\Omega_{R2}}{2}(t_2)) + ie^{+i(\omega_b(T+t_1+t_2))}e^{+i\phi_1}\sin(\frac{\Omega_{R1}}{2}(t_1))\cos(\frac{\Omega_{R2}}{2}(t_2))], \quad \text{(G.18)}$$

$$P_b = \cos^2(\frac{\Omega_{R1}}{2}(t_1))\sin^2(\frac{\Omega_{R2}}{2}(t_2)) + \sin^2(\frac{\Omega_{R1}}{2}(t_1))\cos^2(\frac{\Omega_{R2}}{2}(t_2)) + \cos(\frac{\Omega_{R1}}{2}(t_1))\sin(\frac{\Omega_{R2}}{2}(t_2))\sin(\frac{\Omega_{R1}}{2}(t_1))\cos(\frac{\Omega_{R2}}{2}(t_2))$$
$$[+e^{-i(\omega_a(T+t_1)+\omega_b t_2)-i(\omega_L(T+t_1)+\phi_2)}e^{+i(\omega_b(T+t_1+t_2))}e^{+i\phi_1} + e^{-i(\omega_b(T+t_1+t_2))}e^{-i\phi_1}e^{+i(\omega_a(T+t_1)+\omega_b t_2)}e^{+i(\omega_L(T+t_1))+i\phi_2}], \quad \text{(G.19)}$$

$$P_b = \cos^2(\frac{\Omega_{R1}}{2}(t_1))\sin^2(\frac{\Omega_{R2}}{2}(t_2)) + \sin^2(\frac{\Omega_{R1}}{2}(t_1))\cos^2(\frac{\Omega_{R2}}{2}(t_2)) + \cos(\frac{\Omega_{R1}}{2}(t_1))\sin(\frac{\Omega_{R2}}{2}(t_2))\sin(\frac{\Omega_{R1}}{2}(t_1))\cos(\frac{\Omega_{R2}}{2}(t_2))$$
$$[+e^{-i\omega_a(T+t_1)+i\omega_b(T+t_1)+i(\phi_1-\phi_2)-i\omega_L(T+t_1)} + e^{+i\omega_a(T+t_1)-i\omega_b(T+t_1)-i(\phi_1-\phi_2)+i\omega_L(T+t_1)}], \quad \text{(G.20)}$$

$$P_b = \cos^2(\frac{\Omega_{R1}}{2}(t_1))\sin^2(\frac{\Omega_{R2}}{2}(t_2)) + \sin^2(\frac{\Omega_{R1}}{2}(t_1))\cos^2(\frac{\Omega_{R2}}{2}(t_2)) + \cos(\frac{\Omega_{R1}}{2}(t_1))\sin(\frac{\Omega_{R2}}{2}(t_2))\sin(\frac{\Omega_{R1}}{2}(t_1))\cos(\frac{\Omega_{R2}}{2}(t_2))$$
$$[+e^{+i(-\omega_a(T+t_1)+\omega_b(T+t_1)+\phi_1-\phi_2-\omega_L(T+t_1))} + e^{-i(-\omega_a(T+t_1)+\omega_b(T+t_1)+\phi_1-\phi_2-\omega_L(T+t_1))}], \tag{G.21}$$

finally, resulting in:

$$P_b = \cos^2(\frac{\Omega_{R1}}{2}(t_1))\sin^2(\frac{\Omega_{R2}}{2}(t_2)) + \sin^2(\frac{\Omega_{R1}}{2}(t_1))\cos^2(\frac{\Omega_{R2}}{2}(t_2)) +$$
$$2\cos[(T+t_1)(\omega_b-\omega_a)+\phi_1-\phi_2-\omega_L(T+t_1)]\cos(\frac{\Omega_{R1}}{2}(t_1))\sin(\frac{\Omega_{R2}}{2}(t_2))\sin(\frac{\Omega_{R1}}{2}(t_1))\cos(\frac{\Omega_{R2}}{2}(t_2)). \tag{G.22}$$

G.2.5 Probability of Excited State After Second Free Evolution

Using the complex amplitudes, the probability of the upper state $|b\rangle$ after the second free evolution can be derived as:

$$P_b = [-ie^{-i(\omega_a(T+t_1)+\omega_b(T+t_2))}e^{-i(\omega_L(T+t_1)+\phi_2)}\cos(\frac{\Omega_{R1}}{2}(t_1))\sin(\frac{\Omega_{R2}}{2}(t_2)) - ie^{-i(\omega_b(2T+t_1+t_2))}e^{-i\phi_1}\sin(\frac{\Omega_{R1}}{2}(t_1))\cos(\frac{\Omega_{R2}}{2}(t_2))]$$
$$[+ie^{+i(\omega_a(T+t_1)+\omega_b(T+t_2))}e^{+i(\omega_L(T+t_1)+\phi_2)}\cos(\frac{\Omega_{R1}}{2}(t_1))\sin(\frac{\Omega_{R2}}{2}(t_2)) + ie^{+i(\omega_b(2T+t_1+t_2))}e^{+i\phi_1}\sin(\frac{\Omega_{R1}}{2}(t_1))\cos(\frac{\Omega_{R2}}{2}(t_2))], \tag{G.23}$$

$$P_b = \cos^2(\frac{\Omega_{R1}}{2}(t_1))\sin^2(\frac{\Omega_{R2}}{2}(t_2)) + \sin^2(\frac{\Omega_{R1}}{2}(t_1))\cos^2(\frac{\Omega_{R2}}{2}(t_2)) + \cos(\frac{\Omega_{R1}}{2}(t_1))\sin(\frac{\Omega_{R2}}{2}(t_2))\sin(\frac{\Omega_{R1}}{2}(t_1))\cos(\frac{\Omega_{R2}}{2}(t_2))$$
$$[+e^{-i(\omega_a(T+t_1)+\omega_b(T+t_2))-i(\omega_L(T+t_1)+\phi_2)}e^{+i(\omega_b(2T+t_1+t_2))}e^{+i\phi_1} + e^{-i(\omega_b(2T+t_1+t_2))}e^{-i\phi_1}e^{+i(\omega_a(T+t_1)+\omega_b(T+t_2))}e^{+i(\omega_L(T+t_1))+i\phi_2}], \tag{G.24}$$

$$P_b = \cos^2(\frac{\Omega_{R1}}{2}(t_1))\sin^2(\frac{\Omega_{R2}}{2}(t_2)) + \sin^2(\frac{\Omega_{R1}}{2}(t_1))\cos^2(\frac{\Omega_{R2}}{2}(t_2)) + \cos(\frac{\Omega_{R1}}{2}(t_1))\sin(\frac{\Omega_{R2}}{2}(t_2))\sin(\frac{\Omega_{R1}}{2}(t_1))\cos(\frac{\Omega_{R2}}{2}(t_2))$$
$$[+e^{-i\omega_a(T+t_1)+i\omega_b(T+t_1)+i(\phi_1-\phi_2)-i\omega_L(T+t_1)} + e^{+i\omega_a(T+t_1)-i\omega_b(T+t_1)-i(\phi_1-\phi_2)+i\omega_L(T+t_1)}], \tag{G.25}$$

$$P_b = \cos^2(\frac{\Omega_{R1}}{2}(t_1))\sin^2(\frac{\Omega_{R2}}{2}(t_2)) + \sin^2(\frac{\Omega_{R1}}{2}(t_1))\cos^2(\frac{\Omega_{R2}}{2}(t_2)) + \cos(\frac{\Omega_{R1}}{2}(t_1))\sin(\frac{\Omega_{R2}}{2}(t_2))\sin(\frac{\Omega_{R1}}{2}(t_1))\cos(\frac{\Omega_{R2}}{2}(t_2))$$
$$[+e^{+i(-\omega_a(T+t_1)+\omega_b(T+t_1)+\phi_1-\phi_2-\omega_L(T+t_1))} + e^{-i(-\omega_a(T+t_1)+\omega_b(T+t_1)+\phi_1-\phi_2-\omega_L(T+t_1))}], \tag{G.26}$$

finally, resulting in:

$$P_b = \cos^2(\frac{\Omega_{R1}}{2}(t_1))\sin^2(\frac{\Omega_{R2}}{2}(t_2)) + \sin^2(\frac{\Omega_{R1}}{2}(t_1))\cos^2(\frac{\Omega_{R2}}{2}(t_2)) +$$
$$2\cos[(T+t_1)(\omega_b-\omega_a)+\phi_1-\phi_2-\omega_L(T+t_1)]\cos(\frac{\Omega_{R1}}{2}(t_1))\sin(\frac{\Omega_{R2}}{2}(t_2))\sin(\frac{\Omega_{R1}}{2}(t_1))\cos(\frac{\Omega_{R2}}{2}(t_2)). \tag{G.27}$$

This is the same as the probability after the second pulse.

G.2.6 Probability of Excited State After Third Pulse

Lastly, using the complex amplitudes, the probability of the upper state $|b\rangle$ after the third pulse can be derived as:

$$\begin{aligned}
P_b = [&-ie^{-i(\omega_a(2T+t_1+t_2)+\omega_b(t_3))}e^{-i(\omega_L(2T+t_1+t_2)+\phi_3)}\cos(\frac{\Omega_{R1}}{2}(t_1))\cos(\frac{\Omega_{R2}}{2}(t_2))\sin(\frac{\Omega_{R3}}{2}(t_3))\\
&+ie^{-i(\omega_a(T+t_2)+\omega_b(T+t_1+t_3))}e^{-i(\omega_L(T+t_2)+\phi_3-\phi_2+\phi_1)}\sin(\frac{\Omega_{R1}}{2}(t_1))\sin(\frac{\Omega_{R2}}{2}(t_2))\sin(\frac{\Omega_{R3}}{2}(t_3))\\
&-ie^{-i(\omega_a(T+t_1)+\omega_b(T+t_2+t_3))}e^{-i(\omega_L(T+t_1)+\phi_2)}\cos(\frac{\Omega_{R1}}{2}(t_1))\sin(\frac{\Omega_{R2}}{2}(t_2))\cos(\frac{\Omega_{R3}}{2}(t_3))\\
&-ie^{-i(\omega_b(2T+t_1+t_2+t_3))}e^{-i(\phi_1)}\sin(\frac{\Omega_{R1}}{2}(t_1))\cos(\frac{\Omega_{R2}}{2}(t_2))\cos(\frac{\Omega_{R3}}{2}(t_3))]\\
[&+ie^{+i(\omega_a(2T+t_1+t_2)+\omega_b(t_3))}e^{+i(\omega_L(2T+t_1+t_2)+\phi_3)}\cos(\frac{\Omega_{R1}}{2}(t_1))\cos(\frac{\Omega_{R2}}{2}(t_2))\sin(\frac{\Omega_{R3}}{2}(t_3))\\
&-ie^{+i(\omega_a(T+t_2)+\omega_b(T+t_1+t_3))}e^{+i(\omega_L(T+t_2)+\phi_3-\phi_2+\phi_1)}\sin(\frac{\Omega_{R1}}{2}(t_1))\sin(\frac{\Omega_{R2}}{2}(t_2))\sin(\frac{\Omega_{R3}}{2}(t_3))\\
&+ie^{+i(\omega_a(T+t_1)+\omega_b(T+t_2+t_3))}e^{+i(\omega_L(T+t_1)+\phi_2)}\cos(\frac{\Omega_{R1}}{2}(t_1))\sin(\frac{\Omega_{R2}}{2}(t_2))\cos(\frac{\Omega_{R3}}{2}(t_3))\\
&+ie^{+i(\omega_b(2T+t_1+t_2+t_3))}e^{+i(\phi_1)}\sin(\frac{\Omega_{R1}}{2}(t_1))\cos(\frac{\Omega_{R2}}{2}(t_2))\cos(\frac{\Omega_{R3}}{2}(t_3))],
\end{aligned} \tag{G.28}$$

where with rewriting the coefficients, it is possible to derive:

$$\begin{aligned}
P_b = [&a\cos(\frac{\Omega_{R1}}{2}(t_1))\cos(\frac{\Omega_{R2}}{2}(t_2))\sin(\frac{\Omega_{R3}}{2}(t_3))+b\sin(\frac{\Omega_{R1}}{2}(t_1))\sin(\frac{\Omega_{R2}}{2}(t_2))\sin(\frac{\Omega_{R3}}{2}(t_3))\\
&+c\cos(\frac{\Omega_{R1}}{2}(t_1))\sin(\frac{\Omega_{R2}}{2}(t_2))\cos(\frac{\Omega_{R3}}{2}(t_3))+d\sin(\frac{\Omega_{R1}}{2}(t_1))\cos(\frac{\Omega_{R2}}{2}(t_2))\cos(\frac{\Omega_{R3}}{2}(t_3))]\\
[&a^*\cos(\frac{\Omega_{R1}}{2}(t_1))\cos(\frac{\Omega_{R2}}{2}(t_2))\sin(\frac{\Omega_{R3}}{2}(t_3))+b^*\sin(\frac{\Omega_{R1}}{2}(t_1))\sin(\frac{\Omega_{R2}}{2}(t_2))\sin(\frac{\Omega_{R3}}{2}(t_3))\\
&+c^*\cos(\frac{\Omega_{R1}}{2}(t_1))\sin(\frac{\Omega_{R2}}{2}(t_2))\cos(\frac{\Omega_{R3}}{2}(t_3))+d^*\sin(\frac{\Omega_{R1}}{2}(t_1))\cos(\frac{\Omega_{R2}}{2}(t_2))\cos(\frac{\Omega_{R3}}{2}(t_3))].
\end{aligned} \tag{G.29}$$

Multiplying these equations leads to:

$$\begin{aligned}
P_b = &aa^*\cos^2(\frac{\Omega_{R1}}{2}(t_1))\cos^2(\frac{\Omega_{R2}}{2}(t_2))\sin^2(\frac{\Omega_{R3}}{2}(t_3))\\
&+bb^*\sin^2(\frac{\Omega_{R1}}{2}(t_1))\sin^2(\frac{\Omega_{R2}}{2}(t_2))\sin^2(\frac{\Omega_{R3}}{2}(t_3))\\
&+cc^*\cos^2(\frac{\Omega_{R1}}{2}(t_1))\sin^2(\frac{\Omega_{R2}}{2}(t_2))\cos^2(\frac{\Omega_{R3}}{2}(t_3))\\
&+dd^*\sin^2(\frac{\Omega_{R1}}{2}(t_1))\cos^2(\frac{\Omega_{R2}}{2}(t_2))\cos^2(\frac{\Omega_{R3}}{2}(t_3))\\
&+ab^*\cos(\frac{\Omega_{R1}}{2}(t_1))\cos(\frac{\Omega_{R2}}{2}(t_2))\sin^2(\frac{\Omega_{R3}}{2}(t_3))\sin(\frac{\Omega_{R1}}{2}(t_1))\sin(\frac{\Omega_{R2}}{2}(t_2))\\
&+ac^*\cos^2(\frac{\Omega_{R1}}{2}(t_1))\cos(\frac{\Omega_{R2}}{2}(t_2))\sin(\frac{\Omega_{R3}}{2}(t_3))\sin(\frac{\Omega_{R2}}{2}(t_2))\cos(\frac{\Omega_{R3}}{2}(t_3))\\
&+ad^*\cos(\frac{\Omega_{R1}}{2}(t_1))\cos^2(\frac{\Omega_{R2}}{2}(t_2))\sin(\frac{\Omega_{R3}}{2}(t_3))\sin(\frac{\Omega_{R1}}{2}(t_1))\cos(\frac{\Omega_{R3}}{2}(t_3))\\
&+ba^*\cos(\frac{\Omega_{R1}}{2}(t_1))\cos(\frac{\Omega_{R2}}{2}(t_2))\sin^2(\frac{\Omega_{R3}}{2}(t_3))\sin(\frac{\Omega_{R1}}{2}(t_1))\sin(\frac{\Omega_{R2}}{2}(t_2))\\
&+bc^*\sin(\frac{\Omega_{R1}}{2}(t_1))\sin^2(\frac{\Omega_{R2}}{2}(t_2))\sin(\frac{\Omega_{R3}}{2}(t_3))\cos(\frac{\Omega_{R1}}{2}(t_1))\cos(\frac{\Omega_{R3}}{2}(t_3))\\
&+bd^*\sin^2(\frac{\Omega_{R1}}{2}(t_1))\sin(\frac{\Omega_{R2}}{2}(t_2))\sin(\frac{\Omega_{R3}}{2}(t_3))\cos(\frac{\Omega_{R2}}{2}(t_2))\cos(\frac{\Omega_{R3}}{2}(t_3))\\
&+ca^*\cos^2(\frac{\Omega_{R1}}{2}(t_1))\cos(\frac{\Omega_{R2}}{2}(t_2))\sin(\frac{\Omega_{R3}}{2}(t_3))\sin(\frac{\Omega_{R2}}{2}(t_2))\cos(\frac{\Omega_{R3}}{2}(t_3))\\
&+cb^*\sin(\frac{\Omega_{R1}}{2}(t_1))\sin^2(\frac{\Omega_{R2}}{2}(t_2))\sin(\frac{\Omega_{R3}}{2}(t_3))\cos(\frac{\Omega_{R1}}{2}(t_1))\cos(\frac{\Omega_{R3}}{2}(t_3))\\
&+cd^*\cos(\frac{\Omega_{R1}}{2}(t_1))\sin(\frac{\Omega_{R2}}{2}(t_2))\cos^2(\frac{\Omega_{R3}}{2}(t_3))\sin(\frac{\Omega_{R1}}{2}(t_1))\cos(\frac{\Omega_{R2}}{2}(t_2))\\
&+da^*\cos(\frac{\Omega_{R1}}{2}(t_1))\cos^2(\frac{\Omega_{R2}}{2}(t_2))\sin(\frac{\Omega_{R3}}{2}(t_3))\sin(\frac{\Omega_{R1}}{2}(t_1))\cos(\frac{\Omega_{R3}}{2}(t_3))\\
&+db^*\sin^2(\frac{\Omega_{R1}}{2}(t_1))\sin(\frac{\Omega_{R2}}{2}(t_2))\sin(\frac{\Omega_{R3}}{2}(t_3))\cos(\frac{\Omega_{R2}}{2}(t_2))\cos(\frac{\Omega_{R3}}{2}(t_3))\\
&+dc^*\cos(\frac{\Omega_{R1}}{2}(t_1))\sin(\frac{\Omega_{R2}}{2}(t_2))\cos^2(\frac{\Omega_{R3}}{2}(t_3))\sin(\frac{\Omega_{R1}}{2}(t_1))\cos(\frac{\Omega_{R2}}{2}(t_2)),
\end{aligned} \tag{G.30}$$

$$
\begin{aligned}
P_b = &\cos^2(\frac{\Omega_{R1}}{2}(t_1))\cos^2(\frac{\Omega_{R2}}{2}(t_2))\sin^2(\frac{\Omega_{R3}}{2}(t_3)) \\
&+\sin^2(\frac{\Omega_{R1}}{2}(t_1))\sin^2(\frac{\Omega_{R2}}{2}(t_2))\sin^2(\frac{\Omega_{R3}}{2}(t_3)) \\
&+\cos^2(\frac{\Omega_{R1}}{2}(t_1))\sin^2(\frac{\Omega_{R2}}{2}(t_2))\cos^2(\frac{\Omega_{R3}}{2}(t_3)) \\
&+\sin^2(\frac{\Omega_{R1}}{2}(t_1))\cos^2(\frac{\Omega_{R2}}{2}(t_2))\cos^2(\frac{\Omega_{R3}}{2}(t_3)) \\
&+\cos(\frac{\Omega_{R1}}{2}(t_1))\cos(\frac{\Omega_{R2}}{2}(t_2))\sin^2(\frac{\Omega_{R3}}{2}(t_3))\sin(\frac{\Omega_{R1}}{2}(t_1))\sin(\frac{\Omega_{R2}}{2}(t_2))(ab^* + ba^*) \\
&+\cos^2(\frac{\Omega_{R1}}{2}(t_1))\cos(\frac{\Omega_{R2}}{2}(t_2))\sin(\frac{\Omega_{R3}}{2}(t_3))\sin(\frac{\Omega_{R2}}{2}(t_2))\cos(\frac{\Omega_{R3}}{2}(t_3))(ac^* + ca^*) \\
&+\cos(\frac{\Omega_{R1}}{2}(t_1))\cos^2(\frac{\Omega_{R2}}{2}(t_2))\sin(\frac{\Omega_{R3}}{2}(t_3))\sin(\frac{\Omega_{R1}}{2}(t_1))\cos(\frac{\Omega_{R3}}{2}(t_3))(ad^* + da^*) \\
&+\sin(\frac{\Omega_{R1}}{2}(t_1))\sin^2(\frac{\Omega_{R2}}{2}(t_2))\sin(\frac{\Omega_{R3}}{2}(t_3))\cos(\frac{\Omega_{R1}}{2}(t_1))\cos(\frac{\Omega_{R3}}{2}(t_3))(bc^* + cb^*) \\
&+\sin^2(\frac{\Omega_{R1}}{2}(t_1))\sin(\frac{\Omega_{R2}}{2}(t_2))\sin(\frac{\Omega_{R3}}{2}(t_3))\cos(\frac{\Omega_{R2}}{2}(t_2))\cos(\frac{\Omega_{R3}}{2}(t_3))(bd^* + db^*) \\
&+\cos(\frac{\Omega_{R1}}{2}(t_1))\sin(\frac{\Omega_{R2}}{2}(t_2))\cos^2(\frac{\Omega_{R3}}{2}(t_3))\sin(\frac{\Omega_{R1}}{2}(t_1))\cos(\frac{\Omega_{R2}}{2}(t_2))(cd^* + dc^*).
\end{aligned}
\tag{G.31}
$$

Multiplying and simplifying the coefficients leads to:

$$
\begin{aligned}
ab^* + ba^* &= [-ie^{-i(\omega_a(2T+t_1+t_2)+\omega_b(t_3))}e^{-i(\omega_L(2T+t_1+t_2)+\phi_3)}][-ie^{+i(\omega_a(T+t_2)+\omega_b(T+t_1+t_3))}e^{+i(\omega_L(T+t_2)+\phi_3-\phi_2+\phi_1)}]+ \\
&+ [ie^{+i(\omega_a(2T+t_1+t_2)+\omega_b(t_3))}e^{i(\omega_L(2T+t_1+t_2)+\phi_3)}][+ie^{-i(\omega_a(T+t_2)+\omega_b(T+t_1+t_3))}e^{-i(\omega_L(T+t_2)+\phi_3-\phi_2+\phi_1)}] \\
&= -e^{+i((\omega_b-\omega_a)(T+t_1)-\omega_L(T+t_1)+\phi_1-\phi_2)} - e^{-i((\omega_b-\omega_a)(T+t_1)-\omega_L(T+t_1)+\phi_1-\phi_2)} \\
&= -2\cos((\omega_b-\omega_a)(T+t_1)-\omega_L(T+t_1)+\phi_1-\phi_2),
\end{aligned}
\tag{G.32}
$$

$$
\begin{aligned}
ac^* + ca^* &= [-ie^{-i(\omega_a(2T+t_1+t_2)+\omega_b(t_3))}e^{-i(\omega_L(2T+t_1+t_2)+\phi_3)}][+ie^{+i(\omega_a(T+t_1)+\omega_b(T+t_2+t_3))}e^{+i(\omega_L(T+t_1)+\phi_2)}]+ \\
&+ [ie^{+i(\omega_a(2T+t_1+t_2)+\omega_b(t_3))}e^{i(\omega_L(2T+t_1+t_2)+\phi_3)}][-ie^{-i(\omega_a(T+t_1)+\omega_b(T+t_2+t_3))}e^{-i(\omega_L(T+t_1)+\phi_2)}] \\
&= +e^{+i((\omega_b-\omega_a)(T+t_2)-\omega_L(T+t_2)+\phi_2-\phi_3)} + e^{-i((\omega_b-\omega_a)(T+t_2)-\omega_L(T+t_2)+\phi_2-\phi_3)} \\
&= +2\cos((\omega_b-\omega_a)(T+t_2)-\omega_L(T+t_2)+\phi_2-\phi_3),
\end{aligned}
\tag{G.33}
$$

$$
\begin{aligned}
ad^* + da^* &= [-ie^{-i(\omega_a(2T+t_1+t_2)+\omega_b(t_3))}e^{-i(\omega_L(2T+t_1+t_2)+\phi_3)}][+ie^{+i(\omega_b(2T+t_1+t_2+t_3))}e^{+i(\phi_1)}]+ \\
&+ [ie^{+i(\omega_a(2T+t_1+t_2)+\omega_b(t_3))}e^{i(\omega_L(2T+t_1+t_2)+\phi_3)}][-ie^{-i(\omega_b(2T+t_1+t_2+t_3))}e^{-i(\phi_1)}] \\
&= +e^{+i((\omega_b-\omega_a)(2T+t_1+t_2)-\omega_L(2T+t_1+t_2)+\phi_1-\phi_3)} + e^{-i((\omega_b-\omega_a)(2T+t_1+t_2)-\omega_L(2T+t_1+t_2)+\phi_1-\phi_3)} \\
&= +2\cos((\omega_b-\omega_a)(2T+t_1+t_2)-\omega_L(2T+t_1+t_2)+\phi_1-\phi_3),
\end{aligned}
\tag{G.34}
$$

$$
\begin{aligned}
bc^* + cb^* &= [+ie^{-i(\omega_a(T+t_2)+\omega_b(T+t_1+t_3))}e^{-i(\omega_L(T+t_2)+\phi_3-\phi_2+\phi_1)}][+ie^{+i(\omega_a(T+t_1)+\omega_b(T+t_2+t_3))}e^{+i(\omega_L(T+t_1)+\phi_2)}]+ \\
&+ [-ie^{+i(\omega_a(T+t_2)+\omega_b(T+t_1+t_3))}e^{+i(\omega_L(T+t_2)+\phi_3-\phi_2+\phi_1)}][-ie^{-i(\omega_a(T+t_1)+\omega_b(T+t_2+t_3))}e^{-i(\omega_L(T+t_1)+\phi_2)}] \\
&= -e^{-i((\omega_b-\omega_a)(t_1-t_2)-\omega_L(t_1-t_2)+\phi_3-2\phi_2+\phi_1)} - e^{+i((\omega_b-\omega_a)(t_1-t_2)-\omega_L(t_1-t_2)+\phi_3-2\phi_2+\phi_1)} \\
&= -2\cos((\omega_b-\omega_a)(t_1-t_2)-\omega_L(t_1-t_2)+\phi_3-2\phi_2+\phi_1)),
\end{aligned}
\tag{G.35}
$$

$$
\begin{aligned}
bd^* + db^* &= [+ie^{-i(\omega_a(T+t_2)+\omega_b(T+t_1+t_3))}e^{-i(\omega_L(T+t_2)+\phi_3-\phi_2+\phi_1)}][+ie^{+i(\omega_b(2T+t_1+t_2+t_3))}e^{+i(\phi_1)}]+ \\
&+ [-ie^{+i(\omega_a(T+t_2)+\omega_b(T+t_1+t_3))}e^{+i(\omega_L(T+t_2)+\phi_3-\phi_2+\phi_1)}][-ie^{-i(\omega_b(2T+t_1+t_2+t_3))}e^{-i(\phi_1)}] \\
&= -e^{+i((\omega_b-\omega_a)(T+t_2)-\omega_L(T+t_2)+\phi_2-\phi_3)} - e^{-i((\omega_b-\omega_a)(T+t_2)-\omega_L(T+t_2)+\phi_2-\phi_3)} \\
&= -2\cos((\omega_b-\omega_a)(T+t_2)-\omega_L(T+t_2)+\phi_2-\phi_3)),
\end{aligned}
\tag{G.36}
$$

$$
\begin{aligned}
cd^* + dc^* &= [-ie^{-i(\omega_a(T+t_1)+\omega_b(T+t_2+t_3))}e^{-i(\omega_L(T+t_1)+\phi_2)}][+ie^{+i(\omega_b(2T+t_1+t_2+t_3))}e^{+i(\phi_1)}]+ \\
&+ [+ie^{+i(\omega_a(T+t_1)+\omega_b(T+t_2+t_3))}e^{+i(\omega_L(T+t_1)+\phi_2)}][-ie^{-i(\omega_b(2T+t_1+t_2+t_3))}e^{-i(\phi_1)}] \\
&= +e^{+i((\omega_b-\omega_a)(T+t_1)-\omega_L(T+t_1)+\phi_1-\phi_2)} + e^{-i((\omega_b-\omega_a)(T+t_1)-\omega_L(T+t_1)+\phi_1-\phi_2)} \\
&= +2\cos((\omega_b-\omega_a)(T+t_1)-\omega_L(T+t_1)+\phi_1-\phi_2)).
\end{aligned}
\tag{G.37}
$$

Substituting these coefficients into the original equation yields:

$$
\begin{aligned}
P_b = {} & \cos^2(\frac{\Omega_{R1}}{2}(t_1))\cos^2(\frac{\Omega_{R2}}{2}(t_2))\sin^2(\frac{\Omega_{R3}}{2}(t_3)) + \sin^2(\frac{\Omega_{R1}}{2}(t_1))\sin^2(\frac{\Omega_{R2}}{2}(t_2))\sin^2(\frac{\Omega_{R3}}{2}(t_3)) \\
& + \cos^2(\frac{\Omega_{R1}}{2}(t_1))\sin^2(\frac{\Omega_{R2}}{2}(t_2))\cos^2(\frac{\Omega_{R3}}{2}(t_3)) + \sin^2(\frac{\Omega_{R1}}{2}(t_1))\cos^2(\frac{\Omega_{R2}}{2}(t_2))\cos^2(\frac{\Omega_{R3}}{2}(t_3)) \\
& - 2\cos((\omega_b-\omega_a)(T+t_1)-\omega_L(T+t_1)+\phi_1-\phi_2)\cos(\frac{\Omega_{R1}}{2}(t_1))\cos(\frac{\Omega_{R2}}{2}(t_2))\sin^2(\frac{\Omega_{R3}}{2}(t_3))\sin(\frac{\Omega_{R1}}{2}(t_1))\sin(\frac{\Omega_{R2}}{2}(t_2)) \\
& + 2\cos((\omega_b-\omega_a)(T+t_2)-\omega_L(T+t_2)+\phi_2-\phi_3)\cos^2(\frac{\Omega_{R1}}{2}(t_1))\cos(\frac{\Omega_{R2}}{2}(t_2))\sin(\frac{\Omega_{R3}}{2}(t_3))\sin(\frac{\Omega_{R2}}{2}(t_2))\cos(\frac{\Omega_{R3}}{2}(t_3)) \\
& + 2\cos((\omega_b-\omega_a)(2T+t_1+t_2)-\omega_L(2T+t_1+t_2)+\phi_1-\phi_3)\cos(\frac{\Omega_{R1}}{2}(t_1))\cos^2(\frac{\Omega_{R2}}{2}(t_2))\sin(\frac{\Omega_{R3}}{2}(t_3))\sin(\frac{\Omega_{R1}}{2}(t_1))\cos(\frac{\Omega_{R3}}{2}(t_3)) \\
& - 2\cos((\omega_b-\omega_a)(t_1-t_2)-\omega_L(t_1-t_2)+\phi_3-2\phi_2+\phi_1))\sin(\frac{\Omega_{R1}}{2}(t_1))\sin^2(\frac{\Omega_{R2}}{2}(t_2))\sin(\frac{\Omega_{R3}}{2}(t_3))\cos(\frac{\Omega_{R1}}{2}(t_1))\cos(\frac{\Omega_{R3}}{2}(t_3)) \\
& - 2\cos((\omega_b-\omega_a)(T+t_2)-\omega_L(T+t_2)+\phi_2-\phi_3))\sin^2(\frac{\Omega_{R1}}{2}(t_1))\sin(\frac{\Omega_{R2}}{2}(t_2))\sin(\frac{\Omega_{R3}}{2}(t_3))\cos(\frac{\Omega_{R2}}{2}(t_2))\cos(\frac{\Omega_{R3}}{2}(t_3)) \\
& + 2\cos((\omega_b-\omega_a)(T+t_1)-\omega_L(T+t_1)+\phi_1-\phi_2))\cos(\frac{\Omega_{R1}}{2}(t_1))\sin(\frac{\Omega_{R2}}{2}(t_2))\cos^2(\frac{\Omega_{R3}}{2}(t_3))\sin(\frac{\Omega_{R1}}{2}(t_1))\cos(\frac{\Omega_{R2}}{2}(t_2)),
\end{aligned}
\tag{G.38}
$$

$$
\begin{aligned}
P_b = {} & \cos^2(\frac{\Omega_{R1}}{2}(t_1))\cos^2(\frac{\Omega_{R2}}{2}(t_2))\sin^2(\frac{\Omega_{R3}}{2}(t_3)) + \sin^2(\frac{\Omega_{R1}}{2}(t_1))\sin^2(\frac{\Omega_{R2}}{2}(t_2))\sin^2(\frac{\Omega_{R3}}{2}(t_3)) \\
& + \cos^2(\frac{\Omega_{R1}}{2}(t_1))\sin^2(\frac{\Omega_{R2}}{2}(t_2))\cos^2(\frac{\Omega_{R3}}{2}(t_3)) + \sin^2(\frac{\Omega_{R1}}{2}(t_1))\cos^2(\frac{\Omega_{R2}}{2}(t_2))\cos^2(\frac{\Omega_{R3}}{2}(t_3)) \\
& + 2\cos((\omega_b-\omega_a)(T+t_1)-\omega_L(T+t_1)+\phi_1-\phi_2)[-\cos(\frac{\Omega_{R1}}{2}(t_1))\cos(\frac{\Omega_{R2}}{2}(t_2))\sin^2(\frac{\Omega_{R3}}{2}(t_3))\sin(\frac{\Omega_{R1}}{2}(t_1))\sin(\frac{\Omega_{R2}}{2}(t_2)) \\
& + \cos(\frac{\Omega_{R1}}{2}(t_1))\sin(\frac{\Omega_{R2}}{2}(t_2))\cos^2(\frac{\Omega_{R3}}{2}(t_3))\sin(\frac{\Omega_{R1}}{2}(t_1))\cos(\frac{\Omega_{R2}}{2}(t_2))] \\
& + 2\cos((\omega_b-\omega_a)(T+t_2)-\omega_L(T+t_2)+\phi_2-\phi_3)[\cos^2(\frac{\Omega_{R1}}{2}(t_1))\cos(\frac{\Omega_{R2}}{2}(t_2))\sin(\frac{\Omega_{R3}}{2}(t_3))\sin(\frac{\Omega_{R2}}{2}(t_2))\cos(\frac{\Omega_{R3}}{2}(t_3)) \\
& - \sin^2(\frac{\Omega_{R1}}{2}(t_1))\sin(\frac{\Omega_{R2}}{2}(t_2))\sin(\frac{\Omega_{R3}}{2}(t_3))\cos(\frac{\Omega_{R2}}{2}(t_2))\cos(\frac{\Omega_{R3}}{2}(t_3))] \\
& + \sin(\frac{\Omega_{R1}}{2}(t_1))\cos(\frac{\Omega_{R1}}{2}(t_1))\sin(\frac{\Omega_{R3}}{2}(t_3))\cos(\frac{\Omega_{R3}}{2}(t_3))[2\cos((\omega_b-\omega_a)(2T+t_1+t_2)-\omega_L(2T+t_1+t_2)+\phi_1-\phi_3)\cos^2(\frac{\Omega_{R2}}{2}(t_2)) \\
& - 2\cos((\omega_b-\omega_a)(t_1-t_2)-\omega_L(t_1-t_2)+\phi_3-2\phi_2+\phi_1))\sin^2(\frac{\Omega_{R2}}{2}(t_2))],
\end{aligned}
\tag{G.39}
$$

$$
\begin{aligned}
P_b = {} & \cos^2(\frac{\Omega_{R1}}{2}(t_1))\cos^2(\frac{\Omega_{R2}}{2}(t_2))\sin^2(\frac{\Omega_{R3}}{2}(t_3)) + \sin^2(\frac{\Omega_{R1}}{2}(t_1))\sin^2(\frac{\Omega_{R2}}{2}(t_2))\sin^2(\frac{\Omega_{R3}}{2}(t_3)) \\
& + \cos^2(\frac{\Omega_{R1}}{2}(t_1))\sin^2(\frac{\Omega_{R2}}{2}(t_2))\cos^2(\frac{\Omega_{R3}}{2}(t_3)) + \sin^2(\frac{\Omega_{R1}}{2}(t_1))\cos^2(\frac{\Omega_{R2}}{2}(t_2))\cos^2(\frac{\Omega_{R3}}{2}(t_3)) \\
& + 2\cos((\omega_b-\omega_a)(T+t_1)-\omega_L(T+t_1)+\phi_1-\phi_2)\sin(\frac{\Omega_{R1}}{2}(t_1))\cos(\frac{\Omega_{R1}}{2}(t_1))\sin(\frac{\Omega_{R2}}{2}(t_2))\cos(\frac{\Omega_{R2}}{2}(t_2)) \\
& \times[-\sin^2(\frac{\Omega_{R3}}{2}(t_3))+\cos^2(\frac{\Omega_{R3}}{2}(t_3))] \\
& + 2\cos((\omega_b-\omega_a)(T+t_2)-\omega_L(T+t_2)+\phi_2-\phi_3)\sin(\frac{\Omega_{R2}}{2}(t_2))\cos(\frac{\Omega_{R2}}{2}(t_2))\sin(\frac{\Omega_{R3}}{2}(t_3))\cos(\frac{\Omega_{R3}}{2}(t_3)) \\
& \times[\cos^2(\frac{\Omega_{R1}}{2}(t_1))-\sin^2(\frac{\Omega_{R1}}{2}(t_1))] \\
& + \sin(\frac{\Omega_{R1}}{2}(t_1))\cos(\frac{\Omega_{R1}}{2}(t_1))\sin(\frac{\Omega_{R3}}{2}(t_3))\cos(\frac{\Omega_{R3}}{2}(t_3))[2\cos((\omega_b-\omega_a)(2T+t_1+t_2)-\omega_L(2T+t_1+t_2)+\phi_1-\phi_3)\cos^2(\frac{\Omega_{R2}}{2}(t_2)) \\
& - 2\cos((\omega_b-\omega_a)(t_1-t_2)-\omega_L(t_1-t_2)+\phi_3-2\phi_2+\phi_1))\sin^2(\frac{\Omega_{R2}}{2}(t_2))].
\end{aligned}
\tag{G.40}
$$

Using the identity $\cos^2(x) - \sin^2(x) = \cos(2x)$, it is possible to simplify this further:

$$\begin{aligned}
P_b = &\cos^2(\frac{\Omega_{R1}}{2}(t_1))\cos^2(\frac{\Omega_{R2}}{2}(t_2))\sin^2(\frac{\Omega_{R3}}{2}(t_3)) + \sin^2(\frac{\Omega_{R1}}{2}(t_1))\sin^2(\frac{\Omega_{R2}}{2}(t_2))\sin^2(\frac{\Omega_{R3}}{2}(t_3)) \\
&+ \cos^2(\frac{\Omega_{R1}}{2}(t_1))\sin^2(\frac{\Omega_{R2}}{2}(t_2))\cos^2(\frac{\Omega_{R3}}{2}(t_3)) + \sin^2(\frac{\Omega_{R1}}{2}(t_1))\cos^2(\frac{\Omega_{R2}}{2}(t_2))\cos^2(\frac{\Omega_{R3}}{2}(t_3)) \\
&+ 2\cos((\omega_b - \omega_a)(T + t_1) - \omega_L(T + t_1) + \phi_1 - \phi_2)\sin(\frac{\Omega_{R1}}{2}(t_1))\cos(\frac{\Omega_{R1}}{2}(t_1))\sin(\frac{\Omega_{R2}}{2}(t_2))\cos(\frac{\Omega_{R2}}{2}(t_2))\cos(\frac{\Omega_{R3}}{2}(2t_3)) \\
&+ 2\cos((\omega_b - \omega_a)(T + t_2) - \omega_L(T + t_2) + \phi_2 - \phi_3)\sin(\frac{\Omega_{R2}}{2}(t_2))\cos(\frac{\Omega_{R2}}{2}(t_2))\sin(\frac{\Omega_{R3}}{2}(t_3))\cos(\frac{\Omega_{R3}}{2}(t_3))\cos(\frac{\Omega_{R1}}{2}(2t_1)) \\
&+ \sin(\frac{\Omega_{R1}}{2}(t_1))\cos(\frac{\Omega_{R1}}{2}(t_1))\sin(\frac{\Omega_{R3}}{2}(t_3))\cos(\frac{\Omega_{R3}}{2}(t_3))[2\cos((\omega_b - \omega_a)(2T + t_1 + t_2) - \omega_L(2T + t_1 + t_2) + \phi_1 - \phi_3)\cos^2(\frac{\Omega_{R2}}{2}(t_2)) \\
&- 2\cos((\omega_b - \omega_a)(t_1 - t_2) - \omega_L(t_1 - t_2) + \phi_3 - 2\phi_2 + \phi_1))\sin^2(\frac{\Omega_{R2}}{2}(t_2))].
\end{aligned} \tag{G.41}$$

Using the other relation of $\omega_L = \omega_b - \omega_a$, we obtain:

$$\begin{aligned}
P_b = &\cos^2(\frac{\Omega_{R1}}{2}(t_1))\cos^2(\frac{\Omega_{R2}}{2}(t_2))\sin^2(\frac{\Omega_{R3}}{2}(t_3)) + \sin^2(\frac{\Omega_{R1}}{2}(t_1))\sin^2(\frac{\Omega_{R2}}{2}(t_2))\sin^2(\frac{\Omega_{R3}}{2}(t_3)) \\
&+ \cos^2(\frac{\Omega_{R1}}{2}(t_1))\sin^2(\frac{\Omega_{R2}}{2}(t_2))\cos^2(\frac{\Omega_{R3}}{2}(t_3)) + \sin^2(\frac{\Omega_{R1}}{2}(t_1))\cos^2(\frac{\Omega_{R2}}{2}(t_2))\cos^2(\frac{\Omega_{R3}}{2}(t_3)) \\
&+ 2\cos(\phi_1 - \phi_2)\sin(\frac{\Omega_{R1}}{2}(t_1))\cos(\frac{\Omega_{R1}}{2}(t_1))\sin(\frac{\Omega_{R2}}{2}(t_2))\cos(\frac{\Omega_{R2}}{2}(t_2))\cos(\frac{\Omega_{R3}}{2}(2t_3)) \\
&+ 2\cos(\phi_2 - \phi_3)\sin(\frac{\Omega_{R2}}{2}(t_2))\cos(\frac{\Omega_{R2}}{2}(t_2))\sin(\frac{\Omega_{R3}}{2}(t_3))\cos(\frac{\Omega_{R3}}{2}(t_3))\cos(\frac{\Omega_{R1}}{2}(2t_1)) \\
&+ \sin(\frac{\Omega_{R1}}{2}(t_1))\cos(\frac{\Omega_{R1}}{2}(t_1))\sin(\frac{\Omega_{R3}}{2}(t_3))\cos(\frac{\Omega_{R3}}{2}(t_3))[2\cos(\phi_1 - \phi_3)\cos^2(\frac{\Omega_{R2}}{2}(t_2)) \\
&- 2\cos(\phi_3 - 2\phi_2 + \phi_1))\sin^2(\frac{\Omega_{R2}}{2}(t_2))].
\end{aligned} \tag{G.42}$$

G.2.7 Recovering Mach-Zehnder Equation

Using the derivation above, it is now possible to obtain the standard Mach-Zehnder equation. Assuming the same Rabi frequency for all three pulses, i.e. $\Omega_{R1} = \Omega_{R2} = \Omega_{R3} = \Omega_R$ and $t_1 = t_3 = 1/2 \times t_2$:

$$\begin{aligned}
P_b = &\cos^2(\frac{\Omega_R}{2}(t_1))\cos^2(\frac{\Omega_R}{2}(2 \times t_1))\sin^2(\frac{\Omega_R}{2}(t_1)) + \sin^2(\frac{\Omega_R}{2}(t_1))\sin^2(\frac{\Omega_R}{2}(2 \times t_1))\sin^2(\frac{\Omega_R}{2}(t_1)) \\
&+ \cos^2(\frac{\Omega_R}{2}(t_1))\sin^2(\frac{\Omega_R}{2}(2 \times t_1))\cos^2(\frac{\Omega_R}{2}(t_1)) + \sin^2(\frac{\Omega_R}{2}(t_1))\cos^2(\frac{\Omega_R}{2}(2 \times t_1))\cos^2(\frac{\Omega_R}{2}(t_1)) \\
&+ 2\cos(\phi_1 - \phi_2)\sin(\frac{\Omega_R}{2}(t_1))\cos(\frac{\Omega_R}{2}(t_1))\sin(\frac{\Omega_R}{2}(2 \times t_1))\cos(\frac{\Omega_R}{2}(2 \times t_1))\cos(\frac{\Omega_R}{2}(2t_1)) \\
&+ 2\cos(\phi_2 - \phi_3)\sin(\frac{\Omega_R}{2}(2 \times t_1))\cos(\frac{\Omega_R}{2}(2 \times t_1))\sin(\frac{\Omega_R}{2}(t_1))\cos(\frac{\Omega_R}{2}(t_1))\cos(\frac{\Omega_R}{2}(2 \times t_1)) \\
&+ \sin(\frac{\Omega_R}{2}(t_1))\cos(\frac{\Omega_R}{2}(t_1))\sin(\frac{\Omega_R}{2}(t_1))\cos(\frac{\Omega_R}{2}(t_1))[2\cos(\phi_1 - \phi_3)\cos^2(\frac{\Omega_R}{2}(2 \times t_1)) \\
&- 2\cos(\phi_3 - 2\phi_2 + \phi_1))\sin^2(\frac{\Omega_R}{2}(2 \times t_1))],
\end{aligned} \tag{G.43}$$

$$\begin{aligned}
P_b = &2\cos^2(\frac{\Omega_R}{2}(t_1))\cos^2(\frac{\Omega_R}{2}(2t_1))\sin^2(\frac{\Omega_R}{2}(t_1)) + \sin^2(\frac{\Omega_R}{2}(2t_1))[\sin^4(\frac{\Omega_R}{2}(t_1)) + \cos^4(\frac{\Omega_R}{2}(t_1))] \\
&+ 2\cos(\phi_1 - \phi_2)\sin(\frac{\Omega_R}{2}(t_1))\cos(\frac{\Omega_R}{2}(t_1))\sin(\frac{\Omega_R}{2}(2t_1))\cos^2(\frac{\Omega_R}{2}(2t_1)) + \\
&2\cos(\phi_2 - \phi_3)\sin(\frac{\Omega_R}{2}(t_1))\cos(\frac{\Omega_R}{2}(t_1))\sin(\frac{\Omega_R}{2}(2t_1))\cos^2(\frac{\Omega_R}{2}(2t_1)) \\
&+ \sin^2(\frac{\Omega_R}{2}(t_1))\cos^2(\frac{\Omega_R}{2}(t_1))[2\cos(\phi_1 - \phi_3)\cos^2(\frac{\Omega_R}{2}(2t_1)) - 2\cos(\phi_3 - 2\phi_2 + \phi_1))\sin^2(\frac{\Omega_R}{2}(2t_1))],
\end{aligned} \tag{G.44}$$

$$\begin{aligned}
P_b = &2\cos^2(\frac{\Omega_R}{2}(t_1))\cos^2(\frac{\Omega_R}{2}(2t_1))\sin^2(\frac{\Omega_R}{2}(t_1)) + \sin^2(\frac{\Omega_R}{2}(2t_1))[\sin^4(\frac{\Omega_R}{2}(t_1)) + \cos^4(\frac{\Omega_R}{2}(t_1))] \\
&+ 2\sin(\frac{\Omega_R}{2}(t_1))\cos(\frac{\Omega_R}{2}(t_1))\sin(\frac{\Omega_R}{2}(2t_1))\cos^2(\frac{\Omega_R}{2}(2t_1))[\cos(\phi_1 - \phi_2) + \cos(\phi_2 - \phi_3)] \\
&+ 2\sin^2(\frac{\Omega_R}{2}(t_1))\cos^2(\frac{\Omega_R}{2}(t_1))[\cos(\phi_1 - \phi_3)\cos^2(\frac{\Omega_R}{2}(2t_1)) - \cos(\phi_3 - 2\phi_2 + \phi_1))\sin^2(\frac{\Omega_R}{2}(2t_1))].
\end{aligned} \tag{G.45}$$

It is now possible to substitute the following relations in the above equation:

$$\Omega_R t_1 = \frac{\pi}{2}, \tag{G.46}$$

$$\frac{\Omega_R}{2} t_1 = \frac{\Omega_R}{2} \frac{\pi}{2 \times \Omega_R} = \frac{\pi}{4}, \tag{G.47}$$

and:

$$\frac{\Omega_R}{2} \times 2t_1 = \frac{\Omega_R}{2} \frac{\pi}{\Omega_R} = \frac{\pi}{2}, \tag{G.48}$$

to obtain:

$$\begin{aligned} P_b = {} & 2\cos^2(\frac{\pi}{4})\cos^2(\frac{\pi}{2})\sin^2(\frac{\pi}{4}) + \sin^2(\frac{\pi}{2})[\sin^4(\frac{\pi}{4}) + \cos^4(\frac{\pi}{4})] + 2\sin(\frac{\pi}{4})\cos(\frac{\pi}{4})\sin(\frac{\pi}{2})\cos^2(\frac{\pi}{2})[\cos(\phi_1 - \phi_2) + \cos(\phi_2 - \phi_3)] \\ & + 2\sin^2(\frac{\pi}{4})\cos^2(\frac{\pi}{4})[\cos(\phi_1 - \phi_3)\cos^2(\frac{\pi}{2}) - \cos(\phi_3 - 2\phi_2 + \phi_1))\sin^2(\frac{\pi}{2})]. \end{aligned} \tag{G.49}$$

Calculating all of these using:

$$\sin^2(\frac{\pi}{4}) = \frac{1}{2}, \tag{G.50}$$

$$\cos^2(\frac{\pi}{4}) = \frac{1}{2}, \tag{G.51}$$

$$\sin^2(\frac{\pi}{2}) = 1, \tag{G.52}$$

and:

$$\cos^2(\frac{\pi}{2}) = 0, \tag{G.53}$$

to obtain:

$$P_b = 0 + 1 \times [\frac{1}{4} + \frac{1}{4}] + 0 + 2 \times \frac{1}{2} \times \frac{1}{2}[0 - \cos(\phi_3 - 2\phi_2 + \phi_1) \times 1], \tag{G.54}$$

and finally:

$$P_b = \frac{1}{2} - \frac{1}{2}\cos(\phi_3 - 2\phi_2 + \phi_1), \tag{G.55}$$

which when rewritten as:

$$P_b = \frac{1}{2}[1 - \cos(\phi_3 - 2\phi_2 + \phi_1)]. \tag{G.56}$$

is clearly the same result as standard Mach-Zehnder result.

Bibliography

[1] R. P. Feynman, R. B. Leighton, and M. Sands, *The Feynman lectures on physics, Vol. I: The new millennium edition: mainly mechanics, radiation, and heat*, vol. 1. Basic books, 2011.

[2] W. Torge, "Gravimetry de gruyter," *New York: New York*, 1989.

[3] W. Torge, J. Müller, and R. Pail, *Geodesy*. de Gruyter, 2023.

[4] B. D. Tapley, S. Bettadpur, J. C. Ries, P. F. Thompson, and M. M. Watkins, "Grace measurements of mass variability in the earth system," *science*, vol. 305, no. 5683, pp. 503–505, 2004.

[5] B. Wu, D. Zhu, B. Cheng, L. Wu, K. Wang, Z. Wang, Q. Shu, R. Li, H. Wang, X. Wang, *et al.*, "Dependence of the sensitivity on the orientation for a free-fall atom gravimeter," *Optics Express*, vol. 27, no. 8, pp. 11252–11263, 2019.

[6] B. Stray, A. Lamb, A. Kaushik, J. Vovrosh, A. Rodgers, J. Winch, F. Hayati, D. Boddice, A. Stabrawa, A. Niggebaum, *et al.*, "Quantum sensing for gravity cartography," *Nature*, vol. 602, no. 7898, pp. 590–594, 2022.

[7] B. Adams, C. Macrae, M. Entezami, K. Ridley, A. Kubba, Y.-H. Lien, S. Kinge, and K. Bongs, "The development of a high data rate atom interferometric gravimeter (hidrag) for gravity map matching navigation," in *2021 IEEE International Symposium on Inertial Sensors and Systems (INERTIAL)*, pp. 1–4, 2021.

[8] J. Clark, "An absolute determination of the acceleration due to gravity," *Philosophical Transactions of the Royal Society of London. Series A, Mathematical and Physical Sciences*, vol. 238, no. 787, pp. 65–123, 1939.

[9] J. P. Schwarz, D. S. Robertson, T. M. Niebauer, and J. E. Faller, "A free-fall determination of the newtonian constant of gravity," *science*, vol. 282, no. 5397, pp. 2230–2234, 1998.

[10] O. Francis, "Performance assessment of the relative gravimeter scintrex cg-6," *Journal of Geodesy*, vol. 95, no. 10, p. 116, 2021.

[11] I. Marson, "A short walk along the gravimeters path," *International Journal of Geophysics*, vol. 2012, 2012.

[12] A. Peters, K. Y. Chung, and S. Chu, "High-precision gravity measurements using atom interferometry," *Metrologia*, vol. 38, no. 1, p. 25, 2001.

[13] Y. Bidel, N. Zahzam, C. Blanchard, A. Bonnin, M. Cadoret, A. Bresson, D. Rouxel, and M. Lequentrec-Lalancette, "Absolute marine gravimetry with matter-wave interferometry," *Nature communications*, vol. 9, no. 1, pp. 1–9, 2018.

[14] C. V. Rammeloo, *Optimisation of a compact cold-atoms interferometer for gravimetry*. PhD thesis, University of Birmingham, 2018.

[15] "Scintrex CG 5." `https://scintrexltd.com/wp-content/uploads/2017/02/CG-5-Manual-Ver_8.pdf`. Online, Last accessed on 05/06/2023.

[16] "Scintrex CG 6." `https://scintrexltd.com/wp-content/uploads/2018/04/CG-6-Operations-Manual-RevB.pdf`. Online, Last accessed on 05/06/2023.

[17] U. Riccardi, S. Rosat, and J. Hinderer, "On the accuracy of the calibration of superconducting gravimeters using absolute and spring sensors: a critical comparison," *Pure and Applied Geophysics*, vol. 169, pp. 1343–1356, 2012.

[18] "Scintrex RG1." `https://scintrexltd.com/product/rg-1-remote-operating-gravity-meter/`. Online, Last accessed on 06/06/2023.

[19] "Scintrex Gravilog." `https://scintrexltd.com/product/gravilog-slim-hole-gravity-probe/`. Online, Last accessed on 21/06/2023.

[20] M. Hauth, C. Freier, V. Schkolnik, A. Peters, H. Wziontek, and M. Schilling, "Atom interferometry for absolute measurements of local gravity," in *Atom interferometry*, pp. 557–603, IOS Press, 2014.

[21] T. Niebauer, R. Billson, B. Ellis, B. Mason, D. van Westrum, and F. Klopping, "Simultaneous gravity and gradient measurements from a recoil-compensated absolute gravimeter," *Metrologia*, vol. 48, no. 3, p. 154, 2011.

[22] "Micro-g LaCoste FG5X." `https://microglacoste.com/`. Online, Last accessed on 06/06/2023.

[23] "Micro-g Lacoste gA10." `https://microglacoste.com/product/a10-outdoor-absolute-gravimeter/`. Online, Last accessed on 21/06/2023.

[24] "Micro-g Lacoste gA10 User Manual." https://microglacoste.com/wp-content/uploads/2021/02/A-10-Manual-web.pdf. Online, Last accessed on 21/06/2023.

[25] "Micro-g Lacoste gPhonex." https://microglacoste.com/product/gphonex-gravimeter/. Online, Last accessed on 21/06/2023.

[26] "Micro-g Lacoste gPhonex User Manual." https://microglacoste.com/wp-content/uploads/2017/06/gPhoneX-manual.pdf. Online, Last accessed on 21/06/2023.

[27] "Micro-g Lacoste sea iii." https://microglacoste.com/product/sea-iii-marine-gravity-system/. Online, Last accessed on 21/06/2023.

[28] "Micro-g Lacoste tags 7." https://microglacoste.com/product/tags-7-dynamic-gravity-meter/. Online, Last accessed on 21/06/2023.

[29] "Dynamic Gravity Systems AT1A." https://www.dynamicgravitysystems.com/products/AT1A. Online, Last accessed on 21/06/2023.

[30] "Gravity Systems AT1M." https://www.dynamicgravitysystems.com/products/AT1M. Online, Last accessed on 21/06/2023.

[31] "Gravity Systems AT1U." https://www.dynamicgravitysystems.com/products/AT1U. Online, Last accessed on 21/06/2023.

[32] "Dynamic Gravity Systems AT1L." https://www.dynamicgravitysystems.com/products/AT1L. Online, Last accessed on 21/06/2023.

[33] "GF Instruments LG-1 Galileo." http://www.gfinstruments.cz/index.php?menu=gi&smenu=grav&cont=grav_&ear=ts. Online, Last accessed on 06/06/2023.

[34] "iGrav GWR Instruments." https://www.gwrinstruments.com/pdf/igrav-brochure.pdf. Online, Last accessed on 05/06/2023.

[35] R. Warburton, H. Pillai, and R. Reineman, "Initial results with the new gwr igrav superconducting gravity meter," in *Extended Abstract Presented at 2nd Asia Workshop on Superconducting Gravimetry Taipei, Taiwan*, 2010.

[36] J. Hinderer, D. Crossley, and R. Warburton, "Gravimetric methods-superconducting gravity meters," *Planets and Moons. Treatise on Geophysics*, vol. 10, pp. 65–122, 2007.

[37] A. Krasnov, A. Sokolov, and L. Elinson, "A new air-sea shelf gravimeter of the chekan series," *Gyroscopy and Navigation*, vol. 5, no. 3, pp. 131–137, 2014.

[38] L. Zheleznyak, V. Koneshov, A. Krasnov, A. Sokolov, and L. Elinson, "The results of testing the chekan gravimeter at the leningrad gravimetric testing area," *Izvestiya. Physics of the Solid Earth*, vol. 51, no. 2, p. 315, 2015.

[39] R. Middlemiss, A. Samarelli, D. Paul, J. Hough, S. Rowan, and G. Hammond, "Measurement of the earth tides with a mems gravimeter," *Nature*, vol. 531, no. 7596, pp. 614–617, 2016.

[40] K. Bongs, M. Holynski, J. Vovrosh, P. Bouyer, G. Condon, E. Rasel, C. Schubert, W. P. Schleich, and A. Roura, "Taking atom interferometric quantum sensors from the laboratory to real-world applications," *Nature Reviews Physics*, vol. 1, no. 12, pp. 731–739, 2019.

[41] M. Kasevich and S. Chu, "Measurement of the gravitational acceleration of an atom with a light-pulse atom interferometer," *Applied Physics B*, vol. 54, no. 5, pp. 321–332, 1992.

[42] P. Cheinet, *Conception et réalisation d'un gravimètre à atomes froids*. PhD thesis, Université Pierre et Marie Curie-Paris VI, 2006.

[43] L. Zhu, *A cold atoms gravimeter for use in absolute gravity comparisons*. PhD thesis, University of Birmingham, 2018.

[44] B. Stray, *A portable cold atom gravity gradiometer with field application performance*. PhD thesis, University of Birmingham, 2021.

[45] "Muquans." `https://www.muquans.com/product/absolute-quantum-gravimeter/`. Online, Last accessed on 21/06/2023.

[46] V. Ménoret, P. Vermeulen, N. Le Moigne, S. Bonvalot, P. Bouyer, A. Landragin, and B. Desruelle, "Gravity measurements below 10- 9 g with a transportable absolute quantum gravimeter," *Scientific reports*, vol. 8, no. 1, pp. 1–11, 2018.

[47] "AOSense." `https://aosense.com/products/atom-optic-sensors/gravimeter/`. Online, Last accessed on 21/06/2023.

[48] "Lockheed Martin."
https://www.lockheedmartin.com/content/dam/lockheed-martin/rms/documents/gravity-gradiometry/LM-Gravity-Systems-brochure.pdf.
Online, Last accessed on 17/09/2023.

[49] D. Difrancesco, "Gravity gradiometry developments at Lockheed Martin," in *EGS - AGU - EUG Joint Assembly*, EGS - AGU - EUG Joint Assembly, p. 1069, Apr. 2003.

[50] C. Freier, M. Hauth, V. Schkolnik, B. Leykauf, M. Schilling, H. Wziontek, H.-G. Scherneck, J. Müller, and A. Peters, "Mobile quantum gravity sensor with unprecedented stability," in *Journal of physics: conference series*, vol. 723, p. 012050, IOP Publishing, 2016.

[51] M. Schmidt, *A mobile high-precision gravimeter based on atom interferometry*. PhD thesis, Mathematisch-Naturwissenschaftlichen Fakultät I der Humboldt-Universität zu Berlin, 2011.

[52] P. Cheinet, F. Pereira Dos Santos, T. Petelski, J. Le Gouët, J. Kim, K. Therkildsen, A. Clairon, and A. Landragin, "Compact laser system for atom interferometry," *Applied Physics B*, vol. 84, pp. 643–646, 2006.

[53] A. Louchet-Chauvet, T. Farah, Q. Bodart, A. Clairon, A. Landragin, S. Merlet, and F. P. Dos Santos, "The influence of transverse motion within an atomic gravimeter," *New Journal of Physics*, vol. 13, no. 6, p. 065025, 2011.

[54] P. Gillot, O. Francis, A. Landragin, F. P. Dos Santos, and S. Merlet, "Stability comparison of two absolute gravimeters: optical versus atomic interferometers," *Metrologia*, vol. 51, no. 5, p. L15, 2014.

[55] T. Farah, C. Guerlin, A. Landragin, P. Bouyer, S. Gaffet, F. Pereira Dos Santos, and S. Merlet, "Underground operation at best sensitivity of the mobile lne-syrte cold atom gravimeter," *Gyroscopy and Navigation*, vol. 5, pp. 266–274, 2014.

[56] J. Lautier, L. Volodimer, T. Hardin, S. Merlet, M. Lours, F. Pereira Dos Santos, and A. Landragin, "Hybridizing matter-wave and classical accelerometers," *Applied Physics Letters*, vol. 105, no. 14, p. 144102, 2014.

[57] Y. Bidel, O. Carraz, R. Charrière, M. Cadoret, N. Zahzam, and A. Bresson, "Compact cold atom gravimeter for field applications," *Applied Physics Letters*, vol. 102, no. 14, p. 144107, 2013.

[58] B. Wu, Z. Wang, B. Cheng, Q. Wang, A. Xu, and Q. Lin, "The investigation of a μgal-level cold atom gravimeter for field applications," *Metrologia*, vol. 51, no. 5, p. 452, 2014.

[59] Q.-Y. Wang, Z.-Y. Wang, Z.-J. Fu, and Q. Lin, "Investigation of the thermal adaptability for a mobile cold atom gravimeter," *Chinese Physics B*, vol. 25, no. 12, p. 123701, 2016.

[60] Z. Fu, B. Wu, B. Cheng, Y. Zhou, K. Weng, D. Zhu, Z. Wang, and Q. Lin, "A new type of compact gravimeter for long-term absolute gravity monitoring," *Metrologia*, vol. 56, no. 2, p. 025001, 2019.

[61] R. A. Nyman, G. Varoquaux, F. Lienhart, D. Chambon, S. Boussen, J.-F. Clément, T. Müller, G. Santarelli, F. Pereira Dos Santos, A. Clairon, *et al.*, "Ice: a transportable atomic inertial sensor for test in microgravity," *Applied Physics B*, vol. 84, pp. 673–681, 2006.

[62] R. Geiger, V. Ménoret, G. Stern, N. Zahzam, P. Cheinet, B. Battelier, A. Villing, F. Moron, M. Lours, Y. Bidel, *et al.*, "Detecting inertial effects with airborne matter-wave interferometry," *Nature communications*, vol. 2, no. 1, pp. 1–7, 2011.

[63] B. Barrett, P.-A. Gominet, E. Cantin, L. Antoni-Micollier, A. Bertoldi, B. Battelier, P. Bouyer, J. Lautier, and A. Landragin, "Mobile and remote inertial sensing with atom interferometers," *arXiv preprint arXiv:1311.7033*, 2013.

[64] B. Barrett, A. Bertoldi, and P. Bouyer, "Inertial quantum sensors using light and matter," *Physica Scripta*, vol. 91, no. 5, p. 053006, 2016.

[65] A. V. Rakholia, H. J. McGuinness, and G. W. Biedermann, "Dual-axis high-data-rate atom interferometer via cold ensemble exchange," *Physical Review Applied*, vol. 2, no. 5, p. 054012, 2014.

[66] J. Lee, R. Ding, J. Christensen, R. R. Rosenthal, A. Ison, D. P. Gillund, D. Bossert, K. H. Fuerschbach, W. Kindel, P. S. Finnegan, *et al.*, "A compact cold-atom interferometer with a high data-rate grating magneto-optical trap and a photonic-integrated-circuit-compatible laser system," *Nature Communications*, vol. 13, no. 1, p. 5131, 2022.

[67] H. J. McGuinness, A. V. Rakholia, and G. W. Biedermann, "High data-rate atom interferometer for measuring acceleration," *Applied Physics Letters*, vol. 100, no. 1, 2012.

[68] D. Becker, M. D. Lachmann, S. T. Seidel, H. Ahlers, A. N. Dinkelaker, J. Grosse, O. Hellmig, H. Müntinga, V. Schkolnik, T. Wendrich, *et al.*, "Space-borne bose–einstein condensation for precision interferometry," *Nature*, vol. 562, no. 7727, pp. 391–395, 2018.

[69] S. Merlet, J. Le Gouët, Q. Bodart, A. Clairon, A. Landragin, F. P. Dos Santos, and P. Rouchon, "Operating an atom interferometer beyond its linear range," *Metrologia*, vol. 46, no. 1, p. 87, 2009.

[70] B. Barrett, L. Antoni-Micollier, L. Chichet, B. Battelier, P. Gominet, A. Bertoldi, P. Bouyer, and A. Landragin, "Correlative methods for dual-species quantum tests of the weak equivalence principle," *New Journal of Physics*, vol. 17, no. 8, p. 085010, 2015.

[71] P. Cheiney, L. Fouché, S. Templier, F. Napolitano, B. Battelier, P. Bouyer, and B. Barrett, "Navigation-compatible hybrid quantum accelerometer using a kalman filter," *Physical Review Applied*, vol. 10, no. 3, p. 034030, 2018.

[72] B. Barrett, L. Antoni-Micollier, L. Chichet, B. Battelier, T. Lévèque, A. Landragin, and P. Bouyer, "Dual matter-wave inertial sensors in weightlessness," *Nature communications*, vol. 7, no. 1, pp. 1–9, 2016.

[73] B. Battelier, B. Barrett, L. Fouché, L. Chichet, L. Antoni-Micollier, H. Porte, F. Napolitano, J. Lautier, A. Landragin, and P. Bouyer, "Development of compact cold-atom sensors for inertial navigation," in *Quantum optics*, vol. 9900, pp. 21–37, SPIE, 2016.

[74] Y. Bidel, N. Zahzam, A. Bresson, C. Blanchard, M. Cadoret, A. V. Olesen, and R. Forsberg, "Absolute airborne gravimetry with a cold atom sensor," *Journal of Geodesy*, vol. 94, no. 2, pp. 1–9, 2020.

[75] A. Sugarbaker, S. M. Dickerson, J. M. Hogan, D. M. Johnson, and M. A. Kasevich, "Enhanced atom interferometer readout through the application of phase shear," *Physical review letters*, vol. 111, no. 11, p. 113002, 2013.

[76] S. M. Dickerson, J. M. Hogan, A. Sugarbaker, D. M. Johnson, and M. A. Kasevich, "Multiaxis inertial sensing with long-time point source atom interferometry," *Physical review letters*, vol. 111, no. 8, p. 083001, 2013.

[77] P. Asenbaum, C. Overstreet, T. Kovachy, D. D. Brown, J. M. Hogan, and M. A. Kasevich, "Phase shift in an atom interferometer due to spacetime curvature across its wave function," *Physical review letters*, vol. 118, no. 18, p. 183602, 2017.

[78] C. Overstreet, P. Asenbaum, T. Kovachy, R. Notermans, J. M. Hogan, and M. A. Kasevich, "Effective inertial frame in an atom interferometric test of the equivalence principle," *Physical review letters*, vol. 120, no. 18, p. 183604, 2018.

[79] P. Asenbaum, C. Overstreet, M. Kim, J. Curti, and M. A. Kasevich, "Atom-interferometric test of the equivalence principle at the 10- 12 level," *Physical Review Letters*, vol. 125, no. 19, p. 191101, 2020.

[80] Y.-J. Chen, A. Hansen, M. Shuker, R. Boudot, J. Kitching, and E. A. Donley, "Robust inertial sensing with point-source atom interferometry for interferograms spanning a partial period," *Optics Express*, vol. 28, no. 23, pp. 34516–34529, 2020.

[81] D. Yankelev, C. Avinadav, N. Davidson, and O. Firstenberg, "Atom interferometry with thousand-fold increase in dynamic range," *Science Advances*, vol. 6, no. 45, p. eabd0650, 2020.

[82] C. Avinadav, D. Yankelev, M. Shuker, O. Firstenberg, and N. Davidson, "Rotation sensing with improved stability using point-source atom interferometry," *Physical Review A*, vol. 102, no. 1, p. 013326, 2020.

[83] J. Wang, J. Tong, W. Xie, Z. Wang, Y. Feng, and X. Wang, "Enhanced readout from spatial interference fringes in a point-source cold atom inertial sensor," *Sensors*, vol. 23, no. 11, p. 5071, 2023.

[84] J. Li, G. RM da Silva, W. C. Huang, M. Fouda, J. Bonacum, T. Kovachy, and S. M. Shahriar, "High sensitivity multi-axes rotation sensing using large momentum transfer point source atom interferometry," *Atoms*, vol. 9, no. 3, p. 51, 2021.

[85] P. R. Berman, *Atom interferometry*. Academic press, 1997.

[86] G. Rosi, *Precision gravity measurements with atom interferometry*. PhD thesis, UNIVERSITÀ DEGLI STUDI DI PISA, 2012.

[87] D. S. Weiss, B. C. Young, and S. Chu, "Precision measurement of $\hbar/m$ cs based on photon recoil using laser-cooled atoms and atomic interferometry," *Applied physics B*, vol. 59, pp. 217–256, 1994.

[88] M. Kasevich and S. Chu, "Atomic interferometry using stimulated raman transitions," *Phys. Rev. Lett.*, vol. 67, pp. 181–184, Jul 1991.

[89] P. Cheinet, B. Canuel, F. P. Dos Santos, A. Gauguet, F. Yver-Leduc, and A. Landragin, "Measurement of the sensitivity function in a time-domain atomic interferometer," *IEEE Transactions on instrumentation and measurement*, vol. 57, no. 6, pp. 1141–1148, 2008.

[90] G. Lamporesi, "Determination of the gravitational constant by atom interferometry," *Theses. UNIVERSITÀ DEGLI STUDI DI FIRENZE, déc*, 2006.

[91] H. J. Metcalf and P. van der Straten, *Laser Cooling and Trapping*. Springer Science+Business Media, LLC, 1999.

[92] C. J. Foot, *Atomic physics*, vol. 7. OUP Oxford, 2004.

[93] J. Dalibard and C. Cohen-Tannoudji, "Laser cooling below the doppler limit by polarization gradients: simple theoretical models," *JOSA B*, vol. 6, no. 11, pp. 2023–2045, 1989.

[94] J. Bateman, A. Xuereb, and T. Freegarde, "Stimulated raman transitions via multiple atomic levels," *Physical Review A*, vol. 81, no. 4, p. 043808, 2010.

[95] B. King, "Angular momentum coupling and rabi frequencies for simple atomic transitions," *arXiv preprint arXiv:0804.4528*, 2008.

[96] D. A. Steck, "Rubidium 87 d line data," 2001.

[97] A. Corney, *Atomic and laser spectroscopy*. Clarendon Press Oxford, 1978.

[98] J. M. Hogan, D. Johnson, and M. A. Kasevich, "Light-pulse atom interferometry," *arXiv preprint arXiv:0806.3261*, 2008.

[99] A. Trimeche, B. Battelier, D. Becker, A. Bertoldi, P. Bouyer, C. Braxmaier, E. Charron, R. Corgier, M. Cornelius, K. Douch, *et al.*, "Concept study and preliminary design of a cold atom interferometer for space gravity gradiometry," *Classical and Quantum Gravity*, vol. 36, no. 21, p. 215004, 2019.

[100] M. Langlois, R. Caldani, A. Trimeche, S. Merlet, and F. P. Dos Santos, "Differential phase extraction in dual interferometers exploiting the correlation between classical and quantum sensors," *Physical Review A*, vol. 96, no. 5, p. 053624, 2017.

[101] A. G. Hinton, *Development of a transportable cold atom gradiometer*. PhD thesis, University of Birmingham, 2016.

[102] J. M. Mcguirk, G. Foster, J. Fixler, M. Snadden, and M. Kasevich, "Sensitive absolute-gravity gradiometry using atom interferometry," *Physical Review A*, vol. 65, no. 3, p. 033608, 2002.

[103] F. P. Dos Santos, "Differential phase extraction in an atom gradiometer," *Physical Review A*, vol. 91, no. 6, p. 063615, 2015.

[104] J. B. Fixler, *Atom interferometer-based gravity gradiometer measurements*. Yale University, 2003.

[105] D. Savoie, M. Altorio, B. Fang, L. Sidorenkov, R. Geiger, and A. Landragin, "Interleaved atom interferometry for high-sensitivity inertial measurements," *Science advances*, vol. 4, no. 12, p. eaau7948, 2018.

[106] M. Altorio, *Novel atom interferometry techniques for a cold-atom gyroscope of large Sagnac area*. PhD thesis, Sorbonne université, 2019.

[107] K. Bongs, R. Launay, and M. A. Kasevich, "High-order inertial phase shifts for time-domain atom interferometers," *Applied Physics B*, vol. 84, pp. 599–602, 2006.

[108] T. G. Petelski, *Atom interferometers for precision gravity measurements*. PhD thesis, Paris 6, 2005.

[109] F. Sorrentino, Q. Bodart, L. Cacciapuoti, Y.-H. Lien, M. Prevedelli, G. Rosi, L. Salvi, and G. Tino, "Sensitivity limits of a raman atom interferometer as a gravity gradiometer," *Physical review A*, vol. 89, no. 2, p. 023607, 2014.

[110] H. Kleinpoppen, "Constituents of matter, atoms, molecules, nuclei and particles, p142, ed," *Bergmann/Schaefer, Copyright Walter de Gruyer, Berlin, New York*, 1997.

[111] C. Champenois, M. Büchner, R. Delhuille, R. Mathevet, C. Robilliard, C. Rizzo, and J. Vigué, "Matter neutrality test using a mach-zehnder interferometer," *The Hydrogen Atom: Precision Physics of Simple Atomic Systems*, pp. 554–563, 2001.

[112] A. A. Lamb, *Cold atom gravity gradiometer for field applications*. PhD thesis, University of Birmingham, 2019.

[113] "SAES Dispensers." `https://www.saesgetters.com/products-functions/products/dispensers/alkali-metals-dispensers`. Online, Last accessed on 20/03/2023.

[114] "MuMetal Shields." `https://magneticshields.co.uk/`. Online, Last accessed on 20/03/2023.

[115] M. E. Rudd and J. Craig, "Optimum spacing of square and circular coil pairs," *Review of Scientific Instruments*, vol. 39, no. 9, pp. 1372–1374, 1968.

[116] J. Vovrosh, G. Voulazeris, P. G. Petrov, J. Zou, Y. Gaber, L. Benn, D. Woolger, M. M. Attallah, V. Boyer, K. Bongs, *et al.*, "Additive manufacturing of magnetic shielding and ultra-high vacuum flange for cold atom sensors," *Scientific Reports*, vol. 8, no. 1, pp. 1–10, 2018.

[117] "Stefan Mayer Instruments Fluxmaster." `https://www.stefan-mayer.com/en/products/magnetometers-and-sensors/fluxmaster.html`. Online, Last accessed on 20/03/2023.

[118] F. W. Sears, M. W. Zemansky, H. D. Young, and R. A. Freedman, *Sears and Zemansky's University Physics: With Modern Physics: Technology Update*. Pearson, 2014.

[119] "NKT Photonics." https://www.nktphotonics.com/. Online, Last accessed on 04/09/2023.

[120] D. McCarron, S. King, and S. Cornish, "Modulation transfer spectroscopy in atomic rubidium," *Measurement science and technology*, vol. 19, no. 10, p. 105601, 2008.

[121] G. Ritt, G. Cennini, C. Geckeler, and M. Weitz, "Laser frequency offset locking using a side of filter technique," *Applied Physics B*, vol. 79, pp. 363–365, 2004.

[122] "ARTIQ." http://m-labs.hk/experiment-control/artiq/. Online, Last accessed on 18/02/2023.

[123] "ARTIQ User Manual." https://m-labs.hk/artiq/manual/core_device.html?highlight=kasli. Online, Last accessed on 23/05/2023.

[124] "Zotino." https://creotech.pl/product/zotino/. Online, Last accessed on 16/03/2023.

[125] "Urukul." https://creotech.pl/product/urukul/. Online, Last accessed on 16/03/2023.

[126] M. Holynski, *Creating a two dimensional cold mixture experiment*. PhD thesis, University of Birmingham, 2012.

[127] "MOT Photodiode." https://www.thorlabs.com/thorproduct.cfm?partnumber=FDS100. Online, Last accessed on 10/08/2023.

[128] T. M. Brzozowski, M. Maczynska, M. Zawada, J. Zachorowski, and W. Gawlik, "Time-of-flight measurement of the temperature of cold atoms for short trap-probe beam distances," *Journal of Optics B: Quantum and Semiclassical Optics*, vol. 4, no. 1, p. 62, 2002.

[129] A. Sugarbaker, *Atom Interferometry in 10 m fountain*. PhD thesis, Stanford University, 2014.

[130] K. S. Hardman, P. J. Everitt, G. D. McDonald, P. Manju, P. B. Wigley, M. Sooriyabandara, C. C. Kuhn, J. E. Debs, J. D. Close, and N. P. Robins, "Simultaneous precision gravimetry and magnetic gradiometry with a bose-einstein condensate: a high precision, quantum sensor," *Physical review letters*, vol. 117, no. 13, p. 138501, 2016.

[131] S. M. Dickerson, J. M. Hogan, A. Sugarbaker, D. M. Johnson, and M. A. Kasevich, "Supplemental materials: Multiaxis inertial sensing with long-time point source atom interferometry," *Physical review letters*, vol. 111, no. 8, p. 083001, 2013.

[132] P. Asenbaum, C. Overstreet, T. Kovachy, D. D. Brown, J. M. Hogan, and M. A. Kasevich, "Supplemental material: Phase shift in an atom interferometer due to spacetime curvature across its wave function," *Physical review letters*, vol. 118, no. 18, p. 183602, 2017.

[133] P. Arora, S. Purnapatra, A. Acharya, R. Kumar, and A. Sen Gupta, "Measurement of temperature of atomic cloud using time-of-flight technique," *Mapan*, vol. 27, pp. 31–39, 2012.

[134] S. R. Segal, Q. Diot, E. A. Cornell, A. A. Zozulya, and D. Z. Anderson, "Revealing buried information: Statistical processing techniques for ultracold-gas image analysis," *Physical Review A*, vol. 81, no. 5, p. 053601, 2010.

[135] W. Ketterle, D. S. Durfee, and D. Stamper-Kurn, "Making, probing and understanding bose-einstein condensates," *arXiv preprint cond-mat/9904034*, 1999.

[136] E. Rocco, R. Palmer, T. Valenzuela, V. Boyer, A. Freise, and K. Bongs, "Fluorescence detection at the atom shot noise limit for atom interferometry," *New Journal of Physics*, vol. 16, no. 9, p. 093046, 2014.

[137] "Camera Lens." `https://computar.com/product/705/M3514-MP`. Online, Last accessed on 11/09/2023.

[138] "Camera Manual." `https://s1-dl.theimagingsource.com/api/2.5/packages/documentation/manual-trm/trmdzk33ux250/6d3d7de5-d345-5e45-860f-4237f58b4b30/trmdzk33ux250.en_US.pdf`. Online, Last accessed on 15/06/2023.

[139] "Camera Noise Simulations." `http://kmdouglass.github.io/posts/modeling-noise-for-image-simulations/`. Online, Last accessed on 18/06/2023.

[140] "Thorlabs - Camera Noise." `https://www.thorlabs.com/newgrouppage9.cfm?objectgroup_id=10773#:~:text=Dark%20Shot%20Noise%20(%CF%83D,excited%20into%20the%20conduction%20band)`. Online, Last accessed on 15/06/2023.

[141] "Sensor Dark Noise and Read Noise." `https://www.ximea.com/en/products/usb-31-gen-1-with-sony-cmos-xic/mc050mg-sy?gad=1&gclid=Cj0KCQjw7aqkBhDPARIsAKGa0oJfQA_Gy2yFf7Pw2qbnv2q0IC4lbPY9he2biDL3wcD4i5Sh3hvdKZ0aAlHzEALw_wcB`. Online, Last accessed on 15/06/2023.

[142] "Analog-to-digital units." `https://www.princetoninstruments.com/learn/camera-fundamentals/gain#:~:`

text=When%20a%20sensor%20detects%20a,or%20the%20'gray%20level'. Online, Last accessed on 22/08/2023.

[143] L. Zhou, S. Long, B. Tang, X. Chen, F. Gao, W. Peng, W. Duan, J. Zhong, Z. Xiong, J. Wang, Y. Zhang, and M. Zhan, "Test of equivalence principle at 10^{-8} level by a dual-species double-diffraction raman atom interferometer," *Phys. Rev. Lett.*, vol. 115, p. 013004, Jul 2015.

[144] L. Earl, J. Vovrosh, M. Wright, D. Roberts, J. Winch, M. Perea-Ortiz, A. Lamb, F. Hayati, P. Griffin, N. Metje, *et al.*, "Demonstration of a compact magneto-optical trap on an unstaffed aerial vehicle," *Atoms*, vol. 10, no. 1, p. 32, 2022.

[145] K. Moler, D. S. Weiss, M. Kasevich, and S. Chu, "Theoretical analysis of velocity-selective raman transitions," *Physical Review A*, vol. 45, no. 1, p. 342, 1992.

[146] A. E. Siegman, *Lasers*. University science books, 1986.

[147] J. Saywell, M. Carey, M. Belal, I. Kuprov, and T. Freegarde, "Optimal control of raman pulse sequences for atom interferometry," *Journal of Physics B: Atomic, Molecular and Optical Physics*, vol. 53, no. 8, p. 085006, 2020.

[148] S. Lellouch, O. Ennis, R. Haditalab, M. Langlois, and M. Holynski, "Polychromatic atom optics for atom interferometry," *EPJ Quantum Technology*, vol. 10, no. 1, pp. 1–16, 2023.

[149] "Polarimeter." https://www.thorlabs.com/thorproduct.cfm?partnumber=PAX1000IR1/M. Online, Last accessed on 25/09/2023.

[150] G. Foster, J. Fixler, J. McGuirk, and M. Kasevich, "Method of phase extraction between coupled atom interferometers using ellipse-specific fitting," *Optics letters*, vol. 27, no. 11, pp. 951–953, 2002.

[151] "Piezo Actuators." https://www.thorlabs.com/thorproduct.cfm?partnumber=POLARIS-K05P2. Online, Last accessed on 18/06/2023.

[152] "Piezo Controller." https://www.thorlabs.com/thorproduct.cfm?partnumber=MDT693B. Online, Last accessed on 25/09/2023.

[153] "Quadrature Photodetector." https://www.thorlabs.com/thorproduct.cfm?partnumber=PDP90A. Online, Last accessed on 31/08/2023.

[154] S. Pradhan and B. Jagatap, "Measurement of temperature of laser cooled atoms by one-dimensional expansion in a magneto-optical trap," *Review of Scientific Instruments*, vol. 79, no. 1, 2008.

[155] "Isolation Platform." `http://tablestable.com/en/products/view/14/`. Online, Last accessed on 14/09/2023.

[156] "Parker Motion Linear Rail User Manual." `https://www.parkermotion.com/Support/Product_Manuals/412XR_Manual.pdf`. Online, Last accessed on 24/05/2023.

[157] "Jewell Instruments Tiltmeter." `https://www.jewellinstruments.com/wp-content/uploads/MI14A_JDI.pdf`. Online, Last accessed on 24/05/2023.

[158] "Nanometrics Titan." `https://nanometrics.ca/products/accelerometers/titan`. Online, Last accessed on 24/05/2023.